Developing Superparamagnetic Iron Oxide Nanoparticles as Targeted Cancer Nanomedicine

Maha Ramadan Amin Abdollah

A thesis submitted to University College London for the degree of Doctor of Philosophy in the School of Life and Medical Sciences, Faculty of Medical Sciences

UCL Cancer Institute

University College London

January 2016

Declaration of Originality

I, Maha Ramadan Amin Abdollah, confirm that the work presented in this thesis is my own. Where information has been derived from other sources, I confirm that this has been indicated in the thesis.

……

……

Abstract

Superparamagnetic Iron Oxide Nanoparticles (SPIONs) have unique properties with potential application in targeted cancer treatment; including the ability to generate heat when placed in an external alternating magnetic field. However, challenges such as rapid circulatory clearance by the reticuloendothelial system (RES), the need for effective functionalisation with cancer-targeting agents and heterogeneity of SPIONs, remain to be overcome. The work in this thesis aims to develop SPIONs by addressing these challenges.

Ferucarbotran (Resovist®), a clinically approved MRI contrast SPION with excellent heating potential was investigated. Three main hypotheses were tested; that RES uptake of SPIONs could be blocked *in vitro* and *in vivo*, that specific targeting could be achieved by functionalising SPIONs with non-immunoglobulin cancer-targeting proteins and that product heterogeneity could be addressed by physical separation.

Studies included: (i) Interactions of SPIONs with different cell types (ii) Blocking cell uptake using polysaccharide derivatives (iii) Conjugation strategies to link SPIONs to near-infrared dyes to trace their blood levels (iv) Enhancing the circulatory retention of SPIONs via RES blocking (v) Site-specific conjugation methods to functionalise SPIONs with cancer targeting protein (vi) Cellular- and immuno-assays to test the binding of functionalised SPIONs to target antigen (vii) Size exclusion chromatography (SEC) to fractionate SPIONs.

Results showed that Ferucarbotran was unspecifically internalised by all tested cell lines. A range of sulfated polysaccharides were shown to block this uptake *in vitro* and *in vivo* leading to prolonged circulatory times. Ferucarbotran was successfully functionalised with cancer-targeting protein and bound specifically to target antigen in ELISA. Cellular assays with a range of cell lines revealed the generalised altered behaviour of SPIONs upon surface modification with proteins. SEC successfully fractionated Ferucarbotran into more homogeneous products with improved heating properties.

In conclusion, these results are consistent with the proposed hypotheses and form a platform for addressing the challenges of SPIONs-based cancer nanomedicine.

Table of Contents

List of Figures

List of Tables

List of Equations

List of Abbreviations

293T	Human Embryonic Kidney cells
293T-EGFR	Human Embryonic Kidney cells transduced with EGFR
A375	Human melanoma cell line
AMF	Alternating magnetic field
APC	Allophycocyanin
BMPH	N-β-maleimidopropionic acid hydrazide
BSA	Bovine serum albumin
COOH	Carboxyl groups
CO_2	Carbon dioxide
CLSM	Confocal Laser Scanning Microscopy
D	Hydrodynamic diameter
D-40	Dextran 40
D-70	Dextran 70
Da	Daltons
DARPin	Designed Ankyrin Repeat Protein
DBCO	Dibenzocyclooctyne
dH_2O	Double-distilled water
DLS	Dynamic Light Scattering
DMEM	Dulbecco's Modified Eagle Medium
DMSO	Dimethyl sulfoxide
DSO4 8	Dextran sulfate sodium salt 8
DSO4 500	Dextran sulfate sodium salt 500
DTT	Dithiothreitol
E69	Anti-EGFR DARPin
EDC	1-ethyl-3-(3-dimethylaminopropyl) carbodiimide hydrochloride
EDTA	Ethylenediaminetetraacetic acid
EGF	Epidermal Growth Factor
EGFR	Epidermal Growth Factor Receptor
EGFRvIII	Epidermal Growth Factor Receptor variant three
ELISA	Enzyme-Linked Immunosorbent Assay
EU	Europe
FBS	Foetal bovine serum
FDA	US Food and Drug Administration
FC	Ferucarbotran
FC-E69	Ferucarbotran conjugated to E69

FC-G3	Ferucarbotran conjugated to G3
FDA	US Food and Drug Administration
Fe	Iron
FPLC	Fast protein liquid chromatography
g	Gram
G3	Anti-HER2 DARPin
GBM	Glioblastoma Multiforme
GMP	Good Manufacturing Practice
HCl	Hydrochloric acid
HER2	Human Epidermal Growth Factor Receptor 2
HRP	Horseradish peroxidase
HRTEM	High resolution transmission electron microscopy
ILP	Intrinsic Loss Power
J-5	Dextran sulfate sodium sulphur 18
J-18	Dextran sulfate sodium sulphur 5
KDa	Kilo Daltons
kHz	Kilo Hertz
LS174T	Human colorectal carcinoma
M	Molar
MBq	Megabecquerel
MES	2-(4-morpholino) ethanesulphonic
mgFe/ml	milligrams iron per millilitre
mM	Millimolar
MPa	Mega Pascal
MRI	Magnetic Resonance Imaging
mV	Millivolts
MW	Molecular weight
NaOH	Sodium hydroxide
NHS	N-hydroxysulfosuccinimide
NH_2	Amine group
NIR	Near infrared
nM	Nanomolar
nm	Nanometres
NM	Nanomag-D-spio-NH_2
NSCs	Neural Stem Cells
OH	Hydroxyl group
OPD	O-phenylenediamine dihydrochloride

PBS	Phosphate Buffered Saline
PBS/T	Phosphate Buffered Saline + 0.1 % Tween 20
PDI	Polydispersity Index
PEG	Poly ethylene glycol
pgFe/cell	Picogram iron per cell
PK	Pharmacokinetics
PVDF	Polyvinylidene difluoride
RAW 264.7	Murine monocytes/macrophages cell line
RES	Reticuloendothelial system
rh EGF	Recombinant human Epidermal Growth Factor
rh bFGF	Recombinant human basic fibroblast growth factor
RIPA	RadioImmunoPrecipitation Assay
RT	Room temperature
SAR	Specific absorption rate
ScFv	Single chain fragment variable
SDS	Sodium dodecyl sulfate
SDS-PAGE	Sodium dodecyl sulfate polyacrylamide gel electrophoresis
SEC	Size Exclusion Chromatography
SH	Thiol (sulfhydryl) group
SPIONs	Superparamagnetic Iron Oxide Nanoparticles
SupT1-NT	non-transduced human lymphoblastic leukaemia cell line
SupT1-EGFR	SupT1 cells transduced with EGFR
SupT1-EGFRvIII	SupT1 cells transduced with EGFR variant three
T2	Transverse relaxation
^{99m}Tc	Technetium-99m
TEM	Transmission Electron Microscopy
TEMED	Tetramethylethylenediamine
µgFe/ml	Micrograms iron per millilitre
U-251 MG	Human glioblastoma cell line
U-87 MG	Human glioblastoma cell line
v/v	Volume per volume
w/v	Weight per volume
WHO	World Health Organisation

Acknowledgements

First and foremost I would like to thank God for giving me the patience, resilience and strength to sail through my PhD. I am also extremely grateful to my supervisor Professor Kerry Chester for believing in me and welcoming me in her laboratory. I am very thankful for her constant encouragement, guidance and patience with me. I would also like to thank my supervisory committee of Professor Quentin Pankhurst, Dr Paul Mulholland and Dr Shane Minogue for their constant help and support throughout my PhD. I am also very thankful to everyone in Kerry Chester's research group especially the postdoctoral researchers: Dr Berend Tolner, Dr Enrique Miranda Rota and Dr Jenny Yeung for their constant support and guidance. I am also grateful to all my fellow PhD students and technicians in our laboratory.

I am also grateful to Professor Barbara Pedley and Matthew Robson for their help in animal studies. Thanks to Dr Martin Pule for providing EGFR-transduced cell lines, Professor Paolo Salomoni and Dr Sara Galavotti for their help with the neural stem cells work, Dr Paul Southern and Dr Joseph Bear for their help in the characterisation of SPIONs. I am also grateful to Dr Rafael de Rosales (King's College London) for his help with the SPECT/CT imaging experiments. Thanks to Dr Tammy Kalber for her scientific help throughout the project.

This work would not have been possible without support from the Seventh Framework Program (FP7) for DARPin Targeted Magnetic Hyperthermic Therapy for Glioblastoma (DARTRIX Contract No. 234870) and the Physical Sciences Research Council (EPSRC) Grand Challenge. I am also very grateful to UCL Overseas Research Scholarships (ORS) and UCL Global Excellence Scholarships for funding my PhD. I am also thankful to Meito Sangyo co., Japan for the helpful discussions and for providing Ferucarbotran and dextran sulfates. I would also like to thank the Comprehensive Cancer Imaging Centre (CCIC), Celia Abrahams and the Mothers and Daughters Committee for supporting the project.

Finally, I would like to thank my mother who comforted me through countless number of crying Skype calls and helped me get through my PhD, my father and my sister for all their love and support throughout the most challenging time of my life. I am tremendously grateful for my family and friends for their constant encouragement and for always believing in me.

Dedication

This thesis is dedicated to my beloved mother; I am nothing without your constant love, support and prayers.

إلى أمي الحبيبة، انا لا شيئ بدون حبك و دعمك و دعواتك المستمرة.

Chapter 1

Introduction

Maha Abdollah

1.1 Nanotechnology and Nanomedicine

The term nano is derived from the Latin word *nanus* or Greek *nanos* meaning dwarf (Riehemann *et al*, 2009). The famous physicist Richard Feynman is considered the father of nanotechnology who was the first to highlight the concepts and ideas of nanoscience and nanotechnology in his talk "There's Plenty of Room at the Bottom" given at the American Physical Society in Caltech on the 29th of December 1959. Feynman, although did not use the term nanotechnology, envisioned that scientists would be able to control and manipulate very small particles at the atomic and molecular levels (Feynman, 1960; Scheinberg *et al*, 2010; Toumey, 2009). It was not until a decade later that Professor Norio Taniguchi used the term nanotechnology. The modern nanotechnology era began with the development of the scanning tunnelling microscope in 1981 that enabled scientists to visualise individual atoms (Toumey, 2009).

A range of definitions have been proposed for the term "Nanotechnology" in the literature but generally it is the science concerned with particles in the size range of 0.1 to 100 nm; where 1 nm is a billionth (10^{-9}) of a meter. The US National Nanotechnology Initiative (NNI) has defined it as:

"Nanotechnology is concerned with materials and systems whose structures and components exhibit novel and significantly improved physical, chemical and biological properties, phenomena and processes due to their nanoscale size" (National Nanotechnology Initiative, 2000; Riehemann *et al*, 2009; Weissig *et al*, 2014).

Nevertheless, since 2000 this definition has been an area of controversy due to the 100 nm limitation, which has no solid scientific basis, with many nanoparticles being developed above that "cut off" (Etheridge *et al*, 2013; Kreyling *et al*, 2010). A consensus about the definition of a "nanoparticle" or "nanomaterial" is still under debate, nevertheless a definition by the European commission has been proposed as follows (Bleeker *et al*, 2013; EU, 2011):

" 'Nanomaterial' means a natural, incidental or manufactured material containing particles, in an unbound state or as an aggregate or as an agglomerate and where, for 50% or more of the particles in the number size distribution, one or more external dimensions is in the size range 1 nm-100 nm."

The European commission further defined ‘particles’, ‘agglomerates’ and ‘aggregates’ as follows (EU, 2011):

“ ’Particle’ means a minute piece of matter with defined physical boundaries; ‘agglomerate’ means a collection of weakly bound particles or aggregates where the resulting external surface area is similar to the sum of the surface areas of the individual components; ‘aggregate’ means a particle comprising of strongly bound or fused particles.”

Nanomedicine is a term, which describes the application of nanotechnology concepts to a range of medical applications. The unique physical and chemical characteristics of nanomedicine promise advantage over other conventional therapies in the ability to control and manipulate processes happening at the nanometre scale with great precision and in real time (Riehemann *et al*, 2009). Nanomedicine involves two distinct phenomena occurring at the nanoscale: transitions in the physicochemical properties of the nanoparticles and changes occurring due to their physiological interactions (Etheridge *et al*, 2013). Nanomedicine includes the development of nanoparticles and nanostructures to be used in a wide range of applications in both diagnosis and therapy (theranostics). In practice, nanomedicines can provide fast, convenient and inexpensive tools for molecular diagnostics, follow-up, imaging, treatments and much more (Riehemann *et al*, 2009).

1.2 Evolution of nanomedicine

The study of colloidal systems (i.e. systems containing nanosized components) was developed 50 years ago and the use of colloidal “nano” particles dates back to the late 1960s. For example anthracyclins were encapsulated in phospholipid vesicles (liposomes) in order to reduce their cardiotoxicity, nevertheless the term “nano” only appeared after the year 2000 in the liposomes literature (Weissig *et al*, 2014). Later in the 1980s the formulation of liposomes was further improved to increase the circulatory half-life by making them less visible to the reticuloendothelial system (RES) via “stealth” modifications (e.g. polyethylene glycol (PEG) coating) (Kamaly *et al*, 2012). The first approved nanodrug liposome came much later in 1995 with the approval of Doxil® by the US Food and Drug Administration (FDA) (Weissig *et al*, 2014). The introduction of iron oxide nanoparticles later followed and they were mainly approved by the FDA as contrast agents in magnetic resonance imaging

(MRI) (e.g. Feridex® was approved in 1996) (Kamaly *et al*, 2012; Weissig *et al*, 2014).

The application of nanotechnology in medicine is expected to greatly influence the landscape of pharmaceutical and biotechnological industries (Kamaly *et al*, 2012). An extensive analysis of the current state of nanomedicine in 2012 by (Etheridge *et al*, 2013) has identified 67 commercially available nanodevices and 33 marketed nanotherapeutics. Furthermore, 122 therapeutics and 25 devices are currently in 789 ongoing clinical trials (Etheridge *et al*, 2013; Weissig *et al*, 2014). It was found that almost two-thirds of nanotherapies are currently under investigation for cancer treatment while the rest are being developed or has been approved for infectious diseases, cardiac disorders, immune disorders, hormonal disorders, degenerative disorders, among others (Etheridge *et al*, 2013). A full list of all clinically approved nanopharmaceuticals are reviewed in (Weissig *et al*, 2014) and a list of nanopharmaceuticals under development are reviewed in (Weissig & Guzman-Villanueva, 2015).

1.3 Targeting nanomedicines to cancer cells

Despite the recent advances in cancer diagnosis and therapy, Cancer Research UK has reported that 161,823 deaths from cancer has occurred in the UK in 2012 (Cancer Research UK, 2012), while in the US, cancer is considered the second most common cause of mortality (American Cancer Society, 2013).

Passive and active targeting strategies have been employed to develop nanomedicines for cancer diagnosis and therapy (Figure 1.1). A list of clinically approved anti-cancer nanoparticles is shown in Table 1.1.

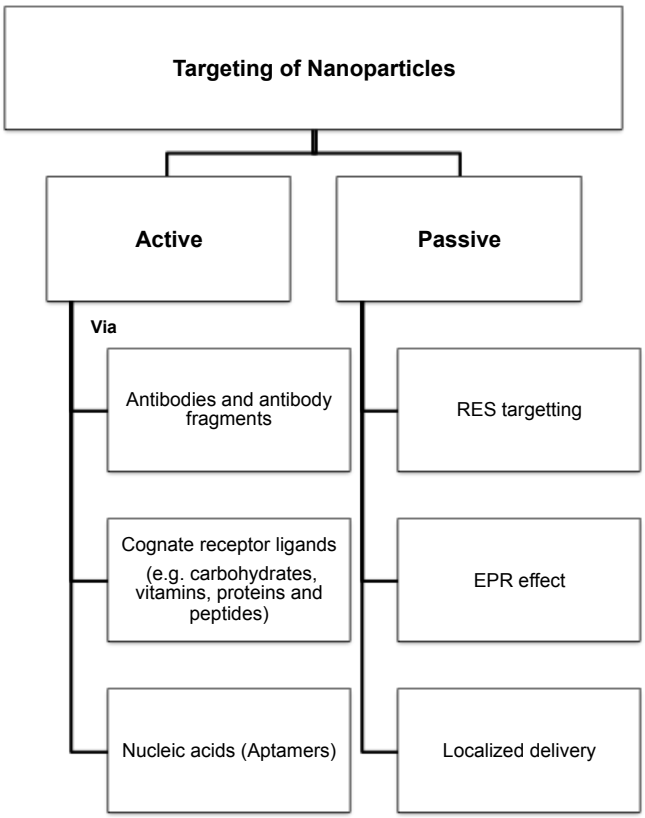

Figure 1.1: Targeting strategies for nanoparticles.

Nanoparticles could be actively (via antibodies, ligands or nucleic acids) or passively (via EPR, RES or intratumoural delivery) targeted to tumour cells. EPR: enhanced permeability and retention effect, RES: reticuloendothelial system. Figure modified from (Parveen *et al*, 2012).

1.3.1 Passive targeting

1.3.1.1 The Enhanced Permeability and Retention (EPR) effect

EPR exploits one of the main hallmarks of cancer cells; the ability to induce angiogenesis (formation of new blood vessels) (Hanahan & Weinberg, 2000; Hanahan & Weinberg, 2011). Most tumours have immature, dense and leaky vasculature caused by their rapid development in response to tumour pro-angiogenic signals (e.g. vascular endothelial growth factor (VEGF)) (Chauhan & Jain, 2013; Peer *et al*, 2007; Xu *et al*, 2015). Leaky junctions in tumour vasculature can allow entities from 100 to 500 nm to extravasate into tumours. On the contrary, normal vasculature has tight junctions between their endothelial cells that only allow particles less than 2 nm to cross (Xu *et al*, 2015) (Figure 1.2).

The EPR effect is the ability of tumour blood vessels to retain large molecules due to 3 factors: (a) leaky properties of tumour vasculature, (b) poor clearance resulting

from ineffective lymphatic drainage and (c) the minute size of the nanoparticles. This phenomenon provides a unique pharmacokinetic privilege to passively target nanomedicines to tumours thus reducing toxicity to normal tissues (Chauhan & Jain, 2013; Peer *et al*, 2007; Xu *et al*, 2015).

The EPR effect relies on increasing the circulatory time of drugs to increase tumour accumulation, which in most cases has been achieved by PEGylation (i.e. surface coating of nanoparticles with polyethylene glycol (PEG)) to reduce opsonisation (i.e. binding of plasma proteins) and rapid clearance by the reticuloendothelial system (RES) (e.g. Doxil®) (Chauhan & Jain, 2013; Peer *et al*, 2007). Furthermore, for the nanoparticles to effectively extravasate into tumours they should be smaller than 400 nm with some studies showing that a diameter less than 200 nm is more effective (Peer *et al*, 2007).

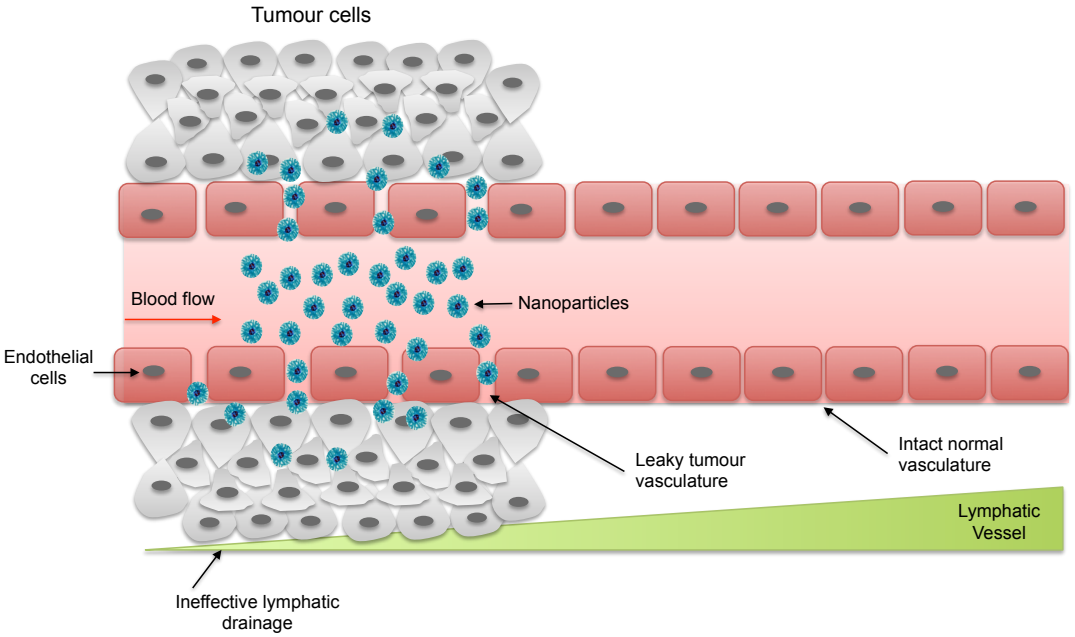

Figure 1.2: The Enhanced Permeability and Retention effect

Nanoparticles (blue carriers) can passively localise to tumours by extravasation through the leaky tumour vasculature and get retained there due to the faulty lymphatic drainage. Figure adapted from (Peer *et al*, 2007).

1.3.1.2 The Reticuloendothelial System

The monocytic-phagocytic system (MPS) or, as commonly known, the reticuloendothelial system (RES) comprises of the endothelial cells lining the blood vessels and the professional macrophages within tissues, for example (Iio & Wagner Jr, 1963; Lanza *et al*, 2004):

- Kupffer cells in the liver
- Free and fixed macrophages in the spleen and lymph nodes
- Alveolar and intravascular macrophages in lungs
- Histiocytes in connective tissues
- Microglia in the nervous system
- Osteoclasts in bone and bone marrow

The liver is one of the main organs of the RES where Kupffer cells, the resident liver macrophages, constitute 80-90% of the total tissue macrophages (Bilzer *et al*, 2006). Kupffer cells, situated alongside the endothelial cells in the lumen of liver sinusoids, play a vital role in host defence and are programed to internalize pathogens and other foreign substances (Bilzer *et al*, 2006) including nanoparticles (Shubayev *et al*, 2009). Consequently, typical biodistribution of nanoparticles following administration is 80-90% in the liver, 5-8% in the spleen and 1-2% in the bone marrow (Shubayev *et al*, 2009).

The rapid clearance of nanoparticles by the RES has been clinically exploited to deliver therapies (e.g. liposomes and iron oxide nanoparticles) to RES organs. For instance some immunomodulatory anti-cancer drugs can be targeted to the RES in order to stimulate cell mediated or humoral immune responses against cancer cells (Allen & Martin, 2004). Examples of non-PEGylated liposomes who exploit this approach include Myocet® and Mepact™ (Allen & Martin, 2004; Kager *et al*, 2010). Another type of nanoparticles, which mainly rely on these professional phagocytes for their mode of action, are iron oxide nanoparticles. They are either used as iron supplements or MRI contrast agents (Akinc & Battaglia, 2013). Iron oxide nanoparticles are further discussed in section 1.6.3.

1.3.1.3 Localised delivery

Another approach to deliver nanoparticles to cancer cells is by direct injection into tumours. Nanoparticles can either act as carriers to deliver drugs to tumour cells or

they can be used to deliver heat therapy. Nanotherm® is an example of a nanoparticle directly injected into brain tumours to allow the delivery of localised heat therapy (Maier-Hauff *et al*, 2007; Maier-Hauff *et al*, 2011). Heat therapy is further discussed in section 1.6.4. Another example is DepoCyt®, a cytarabine liposomal injection, directly injected into the cerebrospinal fluid (CSF) for intrathecal treatment of lymphomatous meningitis (McClune *et al*, 2005).

1.3.2 Active targeting

Despite the efforts done to passively target nanoparticles to cancer cells via the EPR effect and PEGylation, the RES is still the main fate of most systemically administered nanoparticles (90% or more will be retained within the liver and spleen) (Xu *et al*, 2015). The functionalisation of nanoparticles with a targeting moiety that is able to bind to overexpressed cancer-specific biomarkers might provide better accumulation of nanoparticles within the tumour and reduce off-target side effects (Xu *et al*, 2015). This could be accomplished either via: (i) electrostatic adsorption of the targeting moiety to the surface of nanoparticles, (ii) covalent linkage via a chemical reaction or (iii) via an adapter molecule (e.g. biotin and streptavidin interaction) (Arruebo *et al*, 2009). Ideally cancer cells should have 10^4-10^5 copies of the target surface marker (antigen or receptor) per cell. Binding of the nanoparticles might then induce receptor-mediated endocytosis and the release of the drug from nanocarriers (Peer *et al*, 2007). Alternatively, non-internalising receptors might encourage a bystander killing effect to neighbouring cancer cells (Peer *et al*, 2007).

Targeting agents can be divided into antibodies and their fragments, nucleic acids (aptamers) or cognate receptor ligands (e.g. carbohydrates, vitamins and peptides) (Figure 1.1) (Parveen *et al*, 2012; Peer *et al*, 2007).

Despite the promising findings seen in various pre-clinical studies with targeted nanoparticles (reviewed in (Kamaly *et al*, 2012)) with some ligand-targeted nanoparticles progressing to clinical trials (reviewed in (van der Meel *et al*, 2013)), the overall results of these studies remain inconclusive and unclear. This can be accounted to the lack of understanding of the interactions of nanoparticles with physiological proteins and the formation of protein coronas, which might mask the targeting moiety on the surface of the nanoparticles when administered *in vivo* (Xu *et al*, 2015).

Table 1.1: Clinically approved nanoparticles for cancer therapy

Table modified from (Dawidczyk *et al*, 2014a; Dawidczyk *et al*, 2014b; Parveen *et al*, 2012; Weissig *et al*, 2014)

Name	Class	Nanoparticle	Drug	Target cancer	D nm	Targeting approach	Problem addressed/MOA	Approval and additional references
Doxil®	Liposomes	PEGylated "stealth" liposome	Doxorubicin	Ovarian cancer, multiple myeloma, Kaposi's sarcoma	100 nm	EPR, PEG coating help evade RES	Reduce cardiotoxicity and adverse effects of the drug	FDA 1995 (Barenholz, 2012)
Myocet® (Caelyx®)		Non-PEGylated liposome		Metastatic breast cancer	180 nm	RES	Same as above+ drug depots in RES for slow release	EU 2000 (Leonard *et al*, 2009)
DaunoXome®		Non-PEGylated liposome	Daunorubicin citrate	Kaposi's sarcoma	50 nm	EPR	Reduce drug toxicity and side effects	FDA 1996 (Forssen & Ross, 1994)
Marqibo®			Vincristine sulfate	Acute lymphoid leukemia	100 nm		Improve PK of drug without increasing toxicity	FDA 2012 (Silverman & Deitcher, 2013)
DepoCyt®		Multivesicular liposomes	Cytarabine	Neoplastic meningitis	20 μm*	Intrathecal injection	Sustained release of the drug in the CSF for 14 days	FDA 1999/2007 (Murry & Blaney, 2000)

D: diameter; MOA: mode of action; EPR: enhanced permeability and retention effect; FDA: US Food and Drug Administration; RES: reticuloendothelial system; PEG: polyethylene glycol; PK: pharmacokinetics; CSF: cerebrospinal fluid.

*Classified as nanopharmaceuticals based on the presence of nanosized chambers within the drug (Weissig *et al*, 2014).

Continuation of Table 1.1

Name	Class	Nanoparticle	Drug	Target cancer	D	Targeting approach	Problem addressed/MOA	Approval and additional references
Mepact™	Liposomes	Large multilamellar liposomes	Mifamurtide	Non-metastasizing resectable osteaosarcoma	n/a	RES	Immunostimulant drug anchored in liposomal bilayer	EU 2000 (Kager *et al*, 2010)
Abraxane® (NAB-paclitaxel)	Protein carrier	Bovine serum albumin non-specifically bound to the drug	Paclitaxel	NSCL and metastatic breast cancer	130 nm	EPR	Overcome the low solubility of the drug, therefore; Eliminates the need for toxic solvent (Cremophor) Improve efficacy and decrease cytotoxicity	FDA 2005 (Green *et al*, 2006)
Opaxio® (Xyotax™)	Polymer nanoparticles	Polyglutamate solid nanoparticles; drug released by enzymatic hydrolysis of nanoparticle		Glioblastoma	n/a			FDA 2012 (Shaffer *et al*, 2007)
Nanoxel	Micelle	Nanoparticle delivery system for paclitaxel (amphiphilic micelles)		Breast and ovarian cancer	80 nm			India (Brahmachari *et al*, 2011)
Genexol®		Drug encapsulated in PEG-Poly (D, L-lactide) micelles		Metastatic breast and pancreatic cancer	20-50 nm		Same as above+ sustained release of the drug	South Korea 2001 (Kim *et al*, 2004)

D: diameter; MOA: mode of action; n/a: not available; EPR: enhanced permeability and retention effect; FDA: US Food and Drug Administration; EU: Europe; PEG: polyethylene glycol; NAB: nanoparticles albumin bound; NSCLC: non-small cell lung cancer

Continuation of Table 1.1

Name	Class	Nanoparticle	Drug	Target cancer	D	Targeting approach	Problem addressed/MOA	Approval and additional references
Nanotherm®	SPIONs	Aminosilane-coated SPIONs	n/a	Glioblastoma, prostate and pancreatic cancer	15 nm	Intratumoural injection	Thermal ablation	EU 2013 (Thiesen & Jordan, 2008)
Megace® ES	Nanocrystals	No carrier: the drug itself is formulated as nanocrystals	Megestrol actetae	Breast Cancer	n/a	Unknown but may interact with progesterone and glucocorticoid receptors	Enhance the solubility and bioavailability of the drug. Reduce viscosity.	FDA 2005 (Junghanns & Müller, 2008; McNeil, 2009)
Eligard®	Polymer-based	PLGH polymer nanoparticles	Leuprolide	Advanced prostate cancer	n/a	None	Sustained drug release	FDA 2002 (Sartor, 2003)
Oncaspar®		PEG polymer nanoparticles	PEGylated L-aspiraginase	ALL	n/a	PEG increase half-life of the drug	Decrease allergic reaction to the drug and reduce frequency of administration	FDA 1994 (Dinndorf *et al*, 2007; Lammers *et al*, 2008)
Zinostatin stimalamer®	Conjugate protein	Anti-tumour drug conjugated to styrene maleic acid copolymer	Neocarzinostatin	Primary hepatocellular carcinoma	n/a	EPR	Improve drug PK and PD, prolong $T_{1/2}$	Japan 1994 (Greish *et al*, 2003).

D: diameter; MOA: mode of action; SPIONs: Superparamagnetic iron oxide nanoparticles; n/a: not available; FDA: US Food and Drug Administration; EU: Europe; PEG: polyethylene glycol; PLGH: poly-(D,L-lactide-co-glycolide); ALL: Acute Lymphoblastic Leukaemia; PK: pharmacokinetics, PD: pharmacodynamics, $T_{1/2}$: half-life; ALL: Acute Lymphoblastic Leukaemia; EPR: enhanced permeability and retention effect.

Continuation of Table 1.1

Name	Class	Nanoparticle	Drug	Target cancer	D	Targeting approach	Problem addressed/MOA	Approval and additional references
Ontak®	Conjugate protein	Drug conjugated to interleukin-2 (IL-2) binding subunit	Fragment A of Diphtheria toxin	Primary cutaneous T-cell lymphoma	n/a	Active targeting via IL-2 binding subunit	Fusion protein target IL-2 receptor where toxin is released following internalisation	FDA 1999 (Foss, 2000)
Gendicine®	Virosomes	Recombinant Adenovirus expressing wild type P53	Gene therapy	Head and neck squamous cell carcinoma	n/a	Adenoviral vector	Adenovirus infects the target cells to insert P53 gene in the tumour cell genome	China 2003 (Pearson *et al*, 2004)
Rexin-G®		Retroviral vector	Cytocidal cyclin G1 construct	All solid tumours	100 nm	Retrovirus particle engineered with collagen binding motif	Targets collagenous matrix proteins on tumours then the drug blocks endogenous cyclin-G1 causing cell cycle arrest	Philippines 2007 (Gordon & Hall, 2010)

D: diameter; MOA: mode of action; n/a: not applicable; FDA: US Food and Drug Administration

1.4 Cellular interactions of nanoparticles

The interaction of nanoparticles with cells and biological barriers is strongly influenced by nanoparticle characteristics such as surface chemistry, composition, size, shape and charge. These variables affect the way in which the nanoparticles are internalised by cells (Sahay *et al*, 2010a). For instance, if nanoparticles are conjugated to a ligand, the functionalised nanoparticles will interact with the corresponding receptor on the cell surface leading to receptor-mediated endocytosis. Otherwise, nanoparticles can be internalised via the various endocytic pathways utilised by the cell to transport extracellular cargos to the inside of the cells (Chou *et al*, 2011; Conner & Schmid, 2003).

The plasma membrane lies at the interface of all cell-nanoparticle interactions. It consists of a phospholipid bilayer embedded with domains of lipids, carbohydrates and membrane proteins. Proteins embedded within the bilayer perform a range of functions including the transport of molecules and cell-cell recognitions. The membrane coordinates the entry and exit of biomolecules to and from the cell thus segregating the intracellular milieu (cytoplasm) from the extracellular environment (Cooper, 2000). The complexity of the plasma membrane can be accounted to: its flexibility, as it is a non-rigid structure that can deform, and its heterogeneity making the membrane different from one area to another (Nel *et al*, 2009). Furthermore, plasma membranes are not passive, they might secret ions, proteins or other molecules in reaction to the binding of the nanoparticles to the cell surface (Nel *et al*, 2009).

In order to develop more efficient nanomedicines, our understanding of the interactions of nanoparticles at the cellular levels is crucial. Furthermore, in order to effectively deliver nanomedicines into the cells and the targeted organelles, it is of great importance to try and understand what happens at the plasma membrane interface (Nel *et al*, 2009). The interaction between individual nanoparticles as well as the solvent medium in a colloidal solution is governed by a number of attractive forces (e.g. Van Der Waals and depletion) and repulsive forces (e.g. electrostatic) added to that, other short-range forces including solvation and electrosteric forces. However, upon contact with a biological system the situation becomes far more complicated, as nanoparticles might interact with surface ligands, soluble proteins, excreted cellular products, hydrophobic as well as polar regions on the cell surface. All of which will change the way these nanoparticles behave in a biological setting

(Nel *et al*, 2009). Therefore, in order to effectively deliver nanoparticles inside the cells, they have to be able to transverse the plasma membrane utilising the various endocytic pathways (Sahay *et al*, 2010a).

Endocytosis is the process by which macromolecules are carried into the cell in membrane-bound vesicles derived by the invagination and pinching-off of pieces of the plasma membrane. It can be broadly divided into 2 main types: phagocytosis (cell eating for large particles) and pinocytosis or fluid phase-endocytosis (cell drinking for small particles) (Conner & Schmid, 2003). The main characteristics of each type is summarised in Table 1.2 and Figure 1.3.

Table 1.2: Summary of the different endocytic pathways.

Information summarised from (Chou *et al*, 2011; Conner & Schmid, 2003; Verma & Stellacci, 2010).

<table>
<tr><th colspan="6">Endocytosis</th></tr>
<tr><th colspan="5">Pinocytosis</th><th>Phagocytosis</th></tr>
<tr><td>Definition</td><td colspan="4">Cell drinking of fluids and solutes, also known as fluid phase uptake.
Pinocytosis can be subdivided into:</td><td rowspan="3">Cell eating of large solid particles such as bacteria, yeast or remnants of dead cells.
Mainly conducted by specialised cells including monocytes, macrophages and neutrophils.</td></tr>
<tr><td>Subtypes</td><td>Macropinocytosis</td><td>Caveolae-mediated endocytosis</td><td>Clathrin-mediated endocytosis</td><td>Clathrin- and caveolin-independent endocytosis</td></tr>
<tr><td>Brief description</td><td>Large fluid pockets are trapped by formation of membrane protrusions</td><td>Flask shaped invaginations</td><td>Coated pits formed by assembly of cytosolic proteins mainly clathrin</td><td>Mechanisms poorly understood</td></tr>
<tr><td>Endocytic vesicle formed</td><td>Macropinosomes
> 1 μm</td><td>Caveosomes
~50-80 nm</td><td>Clathrin coated vesicles (CCV)
~ 120 nm</td><td>Unknown</td><td>Phagosomes of variable sizes dependent on the particle engulfed</td></tr>
</table>

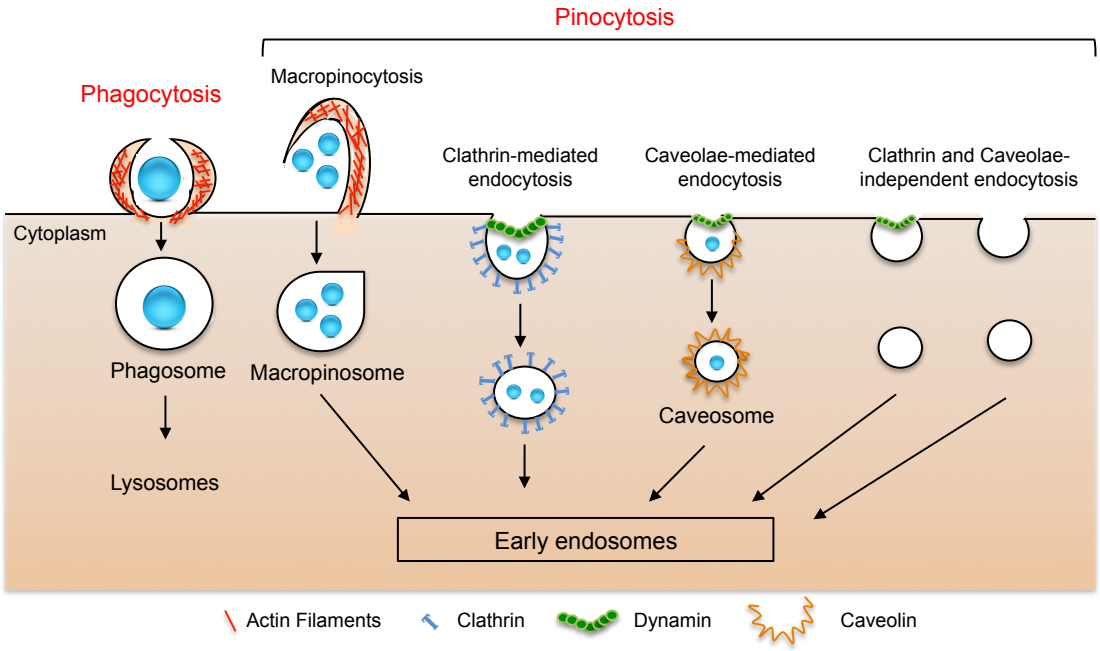

Figure 1.3: Mechanisms of endocytosis

Endocytosis can be divided into phagocytosis (for large molecules) and pinocytosis (for small molecules). The illustration shows the different endocytic pathways by which molecules can enter the cells; each endocytic process is mechanistically distinct from the other. Phagocytosis and macropinocytosis are dependent on actin while clathrin and caveolae dependent endocytosis rely on dynamin to engulf molecules (Chou *et al*, 2011; Conner & Schmid, 2003).

1.4.1 Factors affecting cellular interactions of nanoparticles

1.4.1.1 Size

The size of the nanoparticles is a paramount factor determining cellular interactions and routes of endocytosis, although the polydispersity of most nanoparticle preparations makes it difficult to define exactly which pathways are responsible (Sahay *et al*, 2010a). Another important factor is protein opsonisation which can lead to particle aggregation and subsequent loss in size control (Akinc & Battaglia, 2013). Whilst it is generally agreed that nanoparticles should have a minimum diameter of 40 to 60 nm to achieve cellular uptake, realistically it is more complicated as most internalisation processes occur by more than one pathway, some of which are size-independent (e.g. macropinocytosis) (Akinc & Battaglia, 2013).

Although phagocytosis is associated with uptake of large particles (> 1 μm), it has been reported that smaller nanoparticles can be internalised via this pathway specifically by professional phagocytic cells such as macrophages and monocytes (Akinc & Battaglia, 2013; Fischer *et al*, 2010; Lunov *et al*, 2011). Also, macropinocytosis can occur with relatively big nanoparticles (up to 1 μm). Whereas, clathrin mediated endocytosis can internalise particles in the size range of 10 to 300 nm (Akinc & Battaglia, 2013). Generally, clathrin mediated endocytosis has been accounted for the uptake of nanoparticles by non-specialised mammalian cells (Blanco *et al*, 2015). Although caveosomes are approximately 50-60 nm in diameter (Conner & Schmid, 2003), suggesting that they can only carry cargos of small nanoparticles, Wang *et al* showed that caveolae-mediated endocytosis facilitate the entry of nanoparticles in the 100 nm range (Wang *et al*, 2009).

Size is also a crucial determinant of the fate of nanoparticles *in vivo* affecting extravasation, circulation times, immunogenicity, targeting, internalisation, intracellular trafficking, metabolism, degradation, clearance and uptake mechanisms as described in Figure 1.4 (Blanco *et al*, 2015; Mitragotri & Lahann, 2009). Therefore, depending on the intended biomedical application the size of the nanoparticles could be tailored (Blanco *et al*, 2015; Mitragotri & Lahann, 2009).

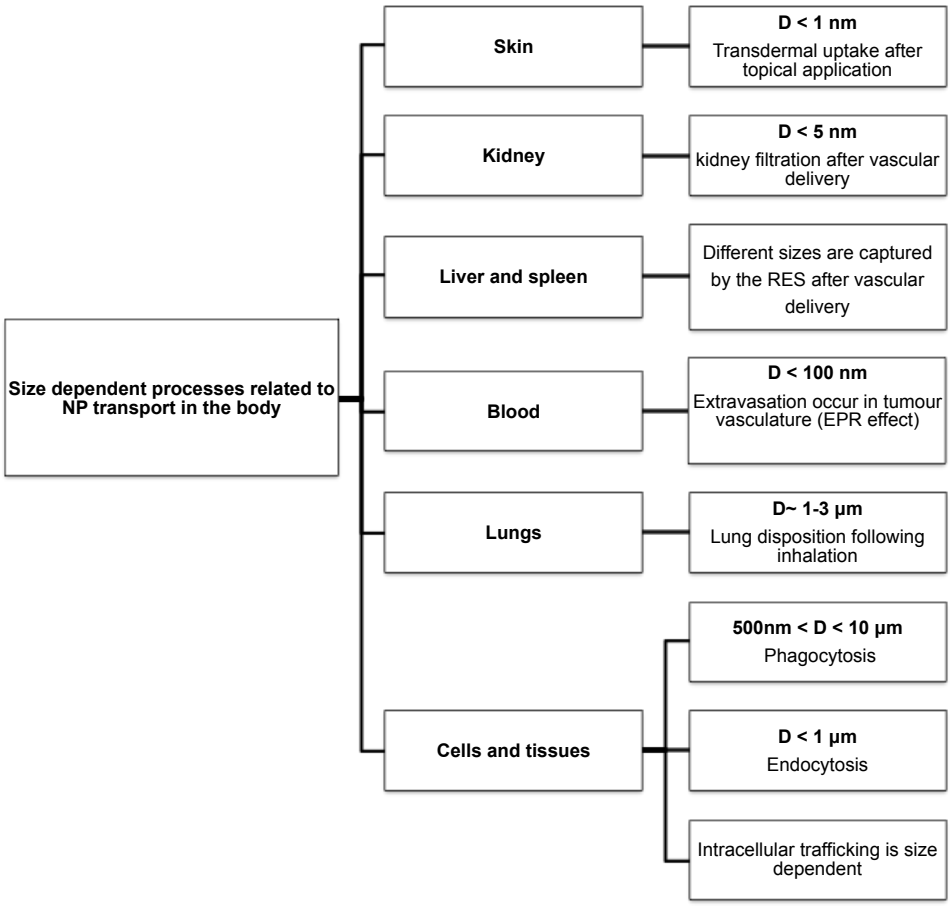

Figure 1.4: Effect of the size of nanoparticles on their uptake in the body

NP: nanoparticles; D: hydrodynamic diameter; Figure modified from (Mitragotri & Lahann, 2009).

1.4.1.2 Charge

Surface charge is another crucial factor in determining nanoparticle uptake. The cell membrane is negatively charged, suggesting that positively charged nanoparticles would be more efficiently taken up than neutral or anionic nanoparticles due to the electrostatic attractions between the particles and the negatively charged proteoglycans on the cell surface (Akinc & Battaglia, 2013; Albanese *et al*, 2012; Blanco *et al*, 2015; Sahay *et al*, 2010a). Furthermore, cationic nanoparticles are known to be cytotoxic while anionic and neutral ones are relatively safe (Akinc & Battaglia, 2013).

The surface charge of nanoparticles is measured by the zeta potential which is the magnitude of the electrostatic potential at the electrical double layer surrounding a nanoparticle in solution (Clogston & Patri, 2011). When in contact with biological environments (e.g. serum), the surface charge of nanoparticles might be altered due

to the adsorption of proteins to the particle surface forming a corona (Albanese *et al*, 2012; Sahay *et al*, 2010a). Since the type of protein corona formed around nanoparticles is dependent on the initial surface charge, studies comparing positively and negatively charged nanoparticles should be cautiously interpreted because they might be actually describing the effect of different corona compositions (Albanese *et al*, 2012).

Most data available suggests that positively charged nanoparticles are mainly internalised via clathrin-mediated endocytosis with some utilising macropinocytosis, whereas strongly cationic nanoparticles may use caveolae-mediated endocytosis (Sahay *et al*, 2010a). Nonetheless, Perumal *et al* reported that cationic and neutral dendrimers were internalised via clathrin- and caveolin-independent endocytosis while, their anionic counterparts were internalised by caveolae mediated endocytosis (Perumal et al, 2008). Similarly, cellular entry of negatively charged nanoparticles (e.g. Doxil®) has been mainly attributed to caveolae-mediated endocytosis (Sahay *et al*, 2010b). While the mechanism of uptake of neutral nanoparticles is generally still unclear (Sahay *et al*, 2010a). It has been also shown that the extent of cellular internalisation of nanoparticles is dependent on the cell type. For instance Jordan *et al* have shown that fibroblasts tend to take up negatively charged nanoparticles more than positive ones while tumour cells tend to have opposite preferences with higher uptake of positive nanoparticles (Jordan *et al*, 1999).

1.4.1.3 Shape

It has been shown that both the shape and the angle at which the nanoparticles encounter the cells can determine if the nanoparticles will be internalised. For instance, a nanoparticle in the shape of an elliptical disc will be internalised by macrophages if they are in contact with the pointed end of the disc but not with its flat region (Mitragotri & Lahann, 2009). This can be explained in terms of surface area because when macrophages are challenged with a large surface area they fail to internalise the particles and instead spread around them (Akinc & Battaglia, 2013). While others showed that gold nanospheres with diameters of 14 nm and 74 nm were 3 times preferentially internalised by HeLa cells than 14 X 74 nm cylindrical nanorods (Chithrani *et al*, 2006). Similar findings by Barua *et al* have revealed that even with targeting with an anti-HER2 antibody (Trastuzumab), cylindrical nanorods achieved higher specificity to HER2 expressing cell lines and less unspecific uptake

when compared to their spherical counterparts (nanospheres) and nanodiscs (Barua *et al*, 2013).

Generally, it has been suggested that non-spherical nanoparticles could provide a good alternative for drug delivery as they might adhere better to the vasculature. Furthermore, they can align or tumble in the presence of blood flow rendering them less prone to rapid clearance and having longer half-lives (Blanco *et al*, 2015).

1.4.1.4 Surface coating and design

The choice of the surface chemistry of nanoparticles aims to maintain their dispersibility in biological solutions and keep the nanoparticles biocompatible so they do not induce toxic effects when administered *in vivo* (Akinc & Battaglia, 2013; Albanese *et al*, 2012). The evolution of nanoparticles coat design can be divided into 3 generations as seen in Figure 1.5 (Albanese *et al*, 2012).

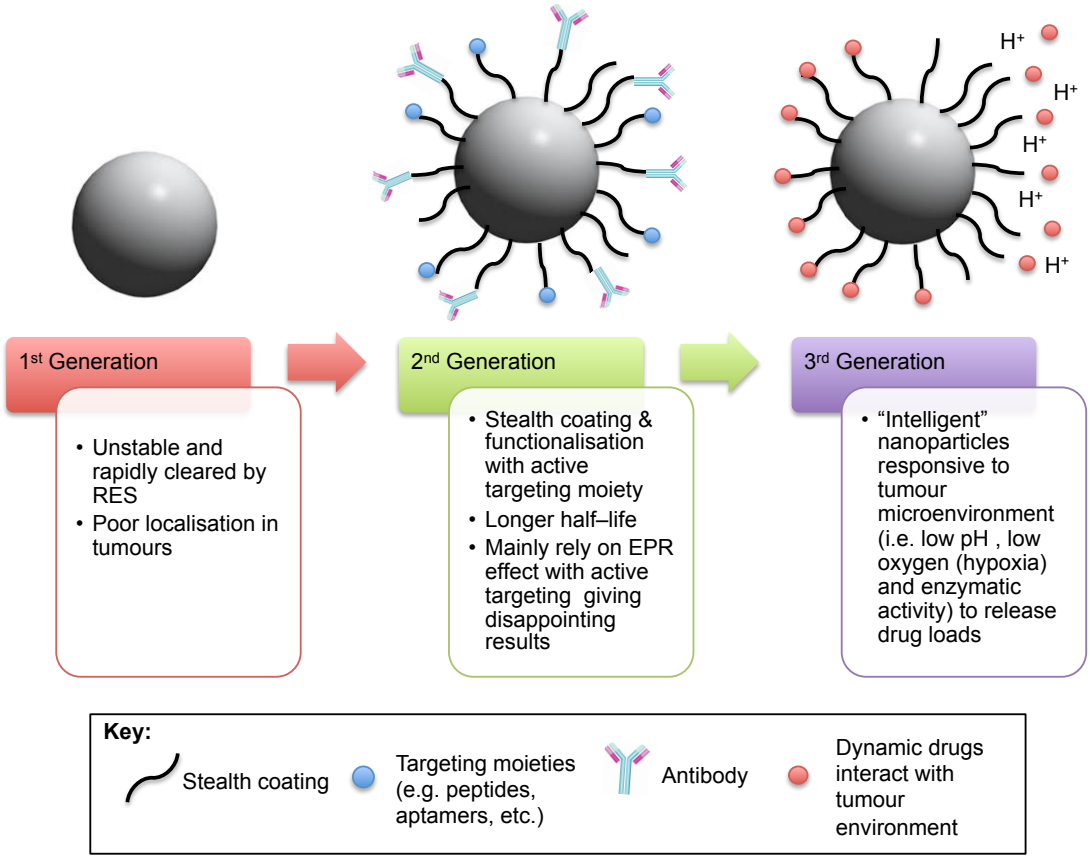

Figure 1.5: Evolution of nanoparticles design

The first generation nanoparticles were functionalised with basic non-stealth surface coatings that had poor colloidal stability leading to their aggregation in cell culture media and also their rapid removal from the circulation by the RES (Albanese *et al*, 2012).

The second generation nanoparticles involved optimisation of the surface coating to improve pharmacokinetics, reduce opsonisation and prolong circulation times (Albanese *et al*, 2012). Many approaches have been developed to sterically prevent both the hydrophobic and electrostatic interactions between nanoparticles and the various components of the blood (Fan *et al*, 2011; Gabizon, 2001; Gaur *et al*, 2000; Gupta & Gupta, 2005; Shubayev *et al*, 2009). This was achieved by surface coating of nanoparticles with brush-like structures to generate repulsive steric forces (Leckband & Israelachvili, 2001), reduce the protein corona (Li & Huang, 2010) and thus protect nanoparticles from recognition by macrophages (Moghimi & Szebeni, 2003). In addition, these coatings also maintain inter-particle stability by reducing Van der Waals attractive forces between individual nanoparticles (Moghimi & Szebeni, 2003).

The desired brush-like surface has been created by a number of soluble polymers, either non-ionic surfactants or zwitterions (Albanese *et al*, 2012; Alcantar *et al*, 2000; Barrett *et al*, 2001; Huang *et al*, 2010; Ishihara *et al*, 1999; Kitano *et al*, 2010; Lemarchand *et al*, 2004; Zalipsky *et al*, 1996). Some examples are listed below:

- Polyethylene glycol (PEG)
- Polysaccharides (e.g. dextran, heparin, chitosan, etc.)
- Poly N-vinyl pyrrolidone (PVP)
- Poly vinyl alcohol (PVA)
- Poly (2-methyl-2-oxazoline) (PMOXA)
- Poly (2-ethyl-2-oxazoline) (PEOXA),
- Poly (2-methacryloyloxyethyl phosphorylcholine) (PMPC)
- Poly (sulfobetaine methacrylate) (PSBMA)

Coating of nanoparticles with brush-like dense polysaccharides layer (e.g. dextran, chitosan, heparin and starch) has resulted in sterically inhibiting the binding of proteins to the surface of nanoparticles (Lemarchand *et al*, 2004). For instance dextran and heparin coated PMMA (poly methyl methacrylate) nanoparticles showed a prolonged half-life when compared to naked ones (Passirani *et al*, 1998). On the contrary, studies done with dextran coated iron oxide nanoparticles showed that they are rapidly removed by the RES despite their dextran coating; nevertheless, their half-life was prolonged when the size of these nanoparticles was reduced to below 50 nm (Chouly *et al*, 1996). These findings highlight the complexity of nanoparticles interaction with biological systems which is dependent on a combination of factors rather than a single parameter (Lemarchand *et al*, 2004).

In summary, PEGylation of nanoparticles is widely considered to be the gold standard for biomedical applications since its introduction in the early 1990s as an alternative coating for liposomes (Li & Huang, 2010). Surface coating with PVP, PMPC and PMOXA are viewed as appropriate alternatives (Akinc & Battaglia, 2013). Ideally stealth-coated nanoparticles should not be opsonised and thus should escape the RES to remain long enough in the circulation to penetrate the leaky tumour vasculature via the EPR effect. However, “stealthing” of nanoparticles is usually not fully effective, leading to loss of nanoparticles to the RES (Li & Huang, 2010).

Another approach to improve nanoparticle localisation into tumours is functionalisation with targeting moieties (see section 1.3.2). Nevertheless, the over reliance on the EPR effect as well as the lack of improved tumour accumulation following targeting has led to the development of the third generation nanoparticles (Shmeeda *et al*, 2009).

Third generation nanoparticles includes “intelligent” particles that interact with biological cues such as low pH, hypoxia or matrix metalloproteinases in the tumour microenvironment. For example, Poon *et al* have developed nanoparticles with multi-layers; the first stealth PEG layer is deshielded in the low pH of the hypoxic tumour regions to reveal a positively charged poly-L-lysine layer readily taken up by tumour cells (Poon *et al*, 2011). While Sarkar *et al* coated liposomes with collagen-mimetic peptides that are enzymatically cleaved by matrix metalloproteinase (MMP-9) to release the liposomal cargo at the tumour site (Sarkar *et al*, 2007). Importantly,

since the cargo of the intelligent nanoparticles is released by the tumour, they remain protected from the RES organs and toxic side effects are reduced (Albanese *et al*, 2012).

1.5 Biocompatibility of nanoparticles

The Nanotechnology Characterisation Laboratory (NCL) and the National Cancer Institute (NCI) have assessed studies investigating more than 130 different types of nanoparticles (e.g. quantum dots, metal oxides, polymers, liposomes, dendrimers and gold colloids) and concluded that size, surface charge and hydrophobicity (dispersibility) of the nanoparticles are the three main parameters governing the biocompatibility of nanomaterials. The three parameters have been assessed independently for effect on biocompatibility and a colour coded phase diagram was used to represent the data (see Figure 3 in (McNeil, 2009)). Interpretation of the phase diagram has revealed that hydrophobic nanoparticles (with low dispersibility) can be considered relatively safe as the RES rapidly clears them from the circulation while hydrophilic particles should be made of biodegradable material to maintain their biocompatibility. Surface charge, independent of the other factors, can also affect the interaction of nanoparticles *in vivo*. Cationic nanoparticles were shown to be more cytotoxic (i.e. low biocompatibility) and can induce haemolysis and platelet aggregation when compared to anionic and neutral particles. Finally the size of the particles affects their clearance (see Figure 1.4), with small particles (<8 nm) mainly excreted via the kidney and larger ones (> 200 nm) mainly being trapped within the liver Kupffer cells. Intermediate size nanoparticles (~20-100nm) can penetrate the leaky tumour vasculature and get retained within the tumour (i.e. via the EPR effect) (Khandare *et al*, 2012; McNeil, 2009; Nel *et al*, 2009).

In conclusion, even though many studies have attempted to define the rules affecting cellular uptake of nanoparticles, the exact mechanisms are still unclear and appear to vary from one nanoparticle to the other. When all the factors (e.g. size, charge, coatings, shape, protein corona composition etc.) are combined together an added level of complexity is observed, suggesting that a case-by-case examination for each nanoparticle will be the best approach. For instance minor modification to the particles' size or surface chemistry can dramatically affect their physiological response (McNeil, 2009).

1.6 Superparamagnetic Iron Oxide Nanoparticles (SPIONs)

SPIONs typically consist of an insoluble iron oxide magnetic core and a biocompatible hydrophilic surface coating to solubilize the core. The magnetic core is composed of magnetite (Fe_3O_4) and maghemite ($Y\text{-}Fe_2O_3$) crystals. The coating can be made of synthetic or natural polymers, including dextran or its derivatives (carboxydextran, carboxymethylated dextran or starch), polyethylene glycol (PEG), alginate and poly vinyl pyrrolidone (PVP) (Rosen *et al*, 2012; Weissleder *et al*, 2014).

SPIONs can be created with a wide range of hydrodynamic diameters depending on the intended use. Usually the term SPIONs refers to nanoparticles with a hydrodynamic diameter greater than 50 nm. Particles smaller than 50 nm are referred to as ultrasmall SPIONs (USPIONs) and particles of diameters less than 10 nm are called very small SPIONs (VSPIONs) (Weissig *et al*, 2014).

The miniaturisation of the iron oxide cores to the nanoscale (usually < 20 nm) leads to the development of unique magnetic properties, specifically superparamagnetism. This unique phenomenon occurs due to the reduction of the core sizes leading to each nanoparticle acting as a single magnetic domain that appears to retain no magnetisation upon the removal of a magnetic field (Karimi *et al*, 2013; Kievit & Zhang, 2011; Rosen *et al*, 2012).

1.6.1 Clinical applications

The superparamagnetic properties of SPIONs (Gupta *et al*, 2007) provide a versatile platform for different biomedical applications ranging from diagnosis to therapy (Krishnan, 2010). These applications include magnetic resonance imaging (MRI) (Bonnemain, 1998b; Hamm *et al*, 1994; Lawaczeck *et al*, 1997; Reimer & Balzer, 2003; Sun *et al*, 2008), hyperthermia (Denardo & Denardo, 2008; Maier-Hauff *et al*, 2007; Maier-Hauff *et al*, 2011; Plotkin *et al*, 2006; Vauthier *et al*, 2011; Wust *et al*, 2002), drug delivery (De Jong & Borm, 2008; Dobson, 2006; Gupta & Gupta, 2005), stem cell labelling and tracking (Loebinger *et al*, 2009b; Mailänder *et al*, 2008; Park *et al*, 2008), tissue repair and cell separation (Gupta & Gupta, 2005).

1.6.2 Magnetic Resonance Imaging (MRI)

The most well established clinical use of SPIONs is as MRI contrast agents. A range of SPIONs with different coatings and sizes have been clinically approved for this purpose (Rosen *et al*, 2012). For example AMI 121 (Lumirem® or Gastromark®), a 300 nm silicon-coated SPION, is used orally for imaging the gastrointestinal tract (Bonnemain, 1998a). While Sinerem®, a dextran coated 30 nm SPION, was the first agent to be introduced for lymph node imaging which is an important tool in cancer staging (Bonnemain, 1998a). Endorem® (Feridex® in US) and Resovist® (Ferucarbotran) have been used in the detection of cancerous lesions in liver and spleen (Chachuat & Bonnemain, 1995; Reimer & Balzer, 2003). Both Endorem® and Resovist® have a dextran coating, and rely on their preferential uptake by healthy RES tissues with minimal uptake by tumour cells due to their impaired phagocytic system. Thus, when these organs are imaged with T2-weighted MRI, a signal loss (i.e. darkening) of the normal tissues is observed while cancerous lesions appear brighter facilitating their detection (Di Marco *et al*, 2007; Rosen *et al*, 2012).

A list of clinically approved MRI contrast SPIONs is reviewed in (Weissig *et al*, 2014) while those undergoing testing in different clinical trials are reviewed in (Weissig & Guzman-Villanueva, 2015).

1.6.3 SPIONs and the RES

The rapid clearance of SPIONs from the circulation by the RES is dependent on many factors such as the hydrodynamic diameter, surface charge and coating (Chouly *et al*, 1996). The mechanism of uptake of dextran-coated SPIONs (e.g. Ferucarbotran, Feridex® (Endorem®)) by macrophages has been investigated in a number of studies and various mechanisms and receptors have been explored (Chao *et al*, 2012a; Lunov *et al*, 2010b; Raynal *et al*, 2004; Yang *et al*, 2011). Lunov *et al* have investigated a range of endocytic pathways including: macropinocytosis, pinocytosis, phagocytosis, clathrin- and caveolae-mediated endocytosis, and uptake by scavenger receptors (Lunov *et al*, 2010a). While Yang *et al* studied clathrin- and caveolae-mediated endocytosis, macropinocytosis among other pathways (Yang *et al*, 2011). Most studies indicated that scavenger receptors class A (Chao *et al*, 2012a; Chao *et al*, 2012b; Lunov *et al*, 2010b; Raynal *et al*, 2004; Yang *et al*, 2011) and clathrin-mediated endocytosis (Lunov *et al*, 2010b; Yang *et al*, 2011) are responsible for the uptake of dextran-coated SPIONs by macrophages. While, Chao *et al* examined the role of carbohydrate recognition pathways and showed that

mannose receptors (Lectin-like receptors CD206) and SIGNR1 receptors are not involved in the uptake of dextran coated SPIONs although they mediate the uptake of bacterial polysaccharides such as dextrans (Chao *et al*, 2012a).

1.6.3.1 Scavenger receptors

Scavenger receptors (SR) were first identified in 1979 by Goldstein and Brown (Brown & Goldstein, 1979). There are 8 different classes of these receptors named class A to H mainly found on dendritic cells, macrophages, and some endothelial cells (Love & Jones, 2013). These receptors were first associated with the internalisation of oxidized low-density lipoproteins (oxLDL) which have been implicated in the pathogenesis of atherosclerosis (Canton *et al*, 2013). This superfamily of receptors is now sub-classed under the membrane-bound pattern recognition receptors (PRRs) and can recognise an extremely diverse and wide range of ligands (Canton *et al*, 2013). SR play a critical role in multiple macrophage functions including phagocytosis, cell adhesion, host defence and production of reactive oxygen species (Kelley *et al*, 2014). SR have also been implicated in the pathophysiology of a number of diseases, for instance: atherosclerosis, diabetes type II and Alzheimer's disease (Canton *et al*, 2013; Love & Jones, 2013). An extensive review of ligands and tissue distribution of scavenger receptors is discussed in (Canton *et al*, 2013).

Class A scavenger receptors

The class A scavenger receptor subfamily is of particular interest as they have been shown to be responsible for the uptake of dextran-coated SPIONs by macrophages (Chao *et al*, 2012a; Chao *et al*, 2012b; Lunov *et al*, 2010b; Raynal *et al*, 2004; Yang *et al*, 2011). These receptors are homo trimeric transmembrane proteins with long extracellular C-terminus and a short cytoplasmic tail (Kelley *et al*, 2014). As with other members of this superfamily, class A scavenger receptors play a critical role in both the innate immunity and host defence as well as in the pathogenesis pathways of many diseases (e.g. atherosclerosis, endotoxemia, stroke, inflammation and coronary artery disease) (Kelley *et al*, 2014).

The class A scavenger receptors can be subdivided into 5 subtypes (Kelley *et al*, 2014; Love & Jones, 2013):

- SR-AI/II: expressed by most macrophages
- Macrophage receptor with a collagenous structure (MARCO): limited to macrophages of the spleen marginal zone
- Cellular response protein (CSR): increased expression seen in cells in response to oxidative stimuli
- Scavenger receptor with C-type lectin (SRCL): mainly on endothelial cells and is not expressed by macrophages
- Scavenger receptor A5 (SCARA5): found on epithelia and not expressed on macrophages.

Scavenger receptor class A is a multi-functional receptor that can bind to a variety of ligands such as: polyanionic macromolecules (e.g. dextran sulfate, heparin, polyinosinic acid and fucoidan), modified lipoproteins, bacteria and apoptotic cells (Kelley *et al*, 2014; Platt & Gordon, 2001; Raynal *et al*, 2004). Dextran sulfate is known to be an efficient blocker of this receptor (Patel *et al*, 1983; Yoshinobu *et al*, 1994).

1.6.4 Magnetic hyperthermia

A property with potential use in cancer therapy is the ability of SPIONs to produce heat when put in an external alternating magnetic field. This phenomenon results from the conversion of electromagnetic energy into thermal energy (Cherukuri *et al*, 2010). The heat generated by SPIONs can cause not only the direct death of cancer cells but also sensitise them to the effect of chemotherapy and radiotherapy (Thiesen & Jordan, 2008; Wust *et al*, 2002).

The use of heat to treat illnesses is not a new concept. In fact it has been exploited since the time of Hippocrates (460–370 BC) who believed that any illness could be treated by heating the patient's body (Ito *et al*, 2005). Many approaches have been developed to deliver heat to cancerous tissues, for example local hyperthermia, interstitial and endocavitary hyperthermia, regional hyperthermia and part-body hyperthermia, whole-body hyperthermia and hyperthermic isolated limb perfusion

(reviewed in (Wust *et al*, 2002)). Furthermore, a wide number of clinical trials utilising hyperthermia therapy in combination with radiotherapy and/or chemotherapy have been conducted for the treatment of breast, CNS, gynaecological, head and neck and skin cancers (reviewed in (Mallory *et al*, 2015; Wust *et al*, 2002)). Despite the presence of effectiveness in some of these trials, local and systemic side effects persist (Wust *et al*, 2002). Two main drawbacks arise: (a) the difficulty of heating the tumours to the intended temperatures without causing damage to the nearby normal tissues (Ito *et al*, 2005) and (b) the need to develop non-invasive real-time temperature monitoring systems (Mallory *et al*, 2015). The first drawback can be overcome by localised hyperthermic treatments exploiting the unique magnetic properties of SPIONs while the second problem is still to be overcome. Moreover, SPIONs provide an exciting alternative for hyperthermia owing to their unique properties of being injectable, nontoxic and biocompatible (Ito *et al*, 2005).

Gordon *et al* were the first to introduce the use of magnetic nanoparticles to deliver inducible localised hyperthermia in 1979 by injecting dextran magnetite directly into mammary carcinomas in Sprague Dawley rats (Gordon *et al*, 1979; Ito *et al*, 2005). Since then many pre-clinical studies have tested the use of magnetic nanoparticles for hyperthermia. Some of which rely on direct injection of nanoparticles near or inside the tumours (Thiesen & Jordan, 2008) while others target the nanoparticles using monoclonal antibodies towards antigens expressed on cancer cells (Denardo & Denardo, 2008).

1.7 Resovist®

The main SPION investigated in this thesis is Ferucarbotran, the active ingredient of Resovist®. Resovist® was clinically approved as a T2 MRI contrast agent to detect focal liver cancerous lesions (Reimer & Balzer, 2003). Resovist® has an average hydrodynamic diameter of 60 nm and consists of a mixture of magnetite-Fe_3O_4 and maghemite-γFe_2O_3 crystals embedded in a carboxydextran shell to provide stability and biocompatibility of the nanoparticles both in solution and *in vivo* (Gupta *et al*, 2007; Reimer & Balzer, 2003) (see Figure 1.6).

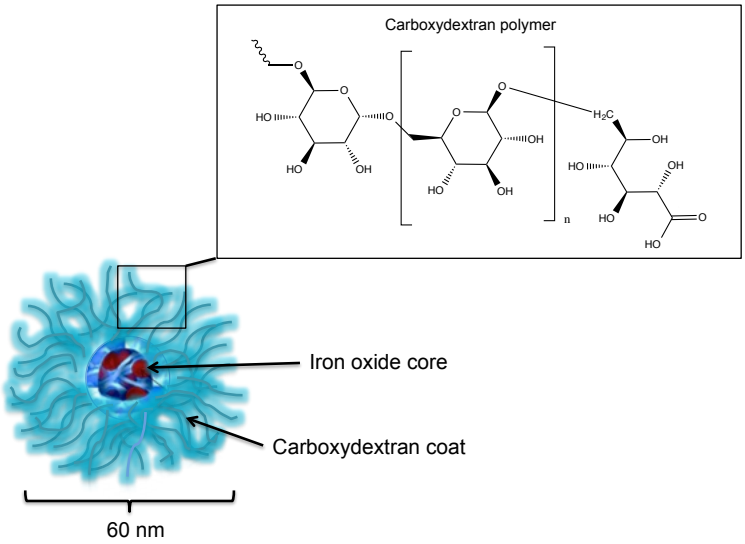

Figure 1.6: Schematic presentation of Resovist®

The nanoparticles are made up of Magnetite–Fe_3O_4 and Maghemite–γFe_2O_3 core surrounded by a watery carboxydextran coat made up of multiple carboxylated glucose units (inset). The particles have an average hydrodynamic diameter of 60 nm with core size of 4.2 nm.

Resovist® has been tested both *in vitro* and *in vivo* and showed promising heating ability. Temperatures as high as 72.4^{0}C and 45^{0}C-59.9^{0}C were achieved *in vitro* and *in vivo* respectively (Hao-Yu *et al*, 2007; Takamatsu *et al*, 2008; Tseng *et al*, 2009). *In vivo* experiments performed on CT-26 colon carcinoma xenografts in mice showed effective tumour shrinkage (Hao-Yu *et al*, 2007; Tseng *et al*, 2009) when heated to 46^{0}C (Tseng *et al*, 2009). In these studies temperatures up to 55^{0}C were achieved within the tumours (Tseng *et al*, 2009). In another study rabbits with renal VX2 carcinoma implanted in their kidneys were used. Here, intra-arterial selective hyperthermia was achieved using transcatheter arterial embolization (TAE) with Ferucarbotran (Takamatsu *et al*, 2008). Tumours were heated to 45^{0}C for 20 minutes leading to increased apoptosis when compared to control tumours (Takamatsu *et al*, 2008).

Therefore, Resovist® is considered an excellent candidate for clinical development in hyperthermia due to its well documented safety profile with few reported side effects in pre-clinical studies (Lawaczeck *et al*, 1997) and in patients (Balzer T, 1996; Hamm *et al*, 1994; Kehagias *et al*, 2001; Reimer & Balzer, 2003; Reimer *et al*, 1995; Shamsi *et al*, 1998).

1.7.1 Resovist® Pharmacokinetics

Resovist® has a distribution half-life of 3.9 to 5.8 minutes and an elimination half-life of 2.4-3.6 hours. Approximately 80% of the injected dose of Resovist® rapidly accumulates in the liver within minutes following its injection (Reimer & Balzer, 2003). Furthermore, after 6 hours of intravenous administration the nanoparticles are exclusively taken up by liver Kupffer cells (Reimer & Balzer, 2003). The rapid clearance of Resovist® and other dextran coated SPIONs by the RES (Chouly *et al*, 1996) represent a pharmacokinetic challenge that limits the use of these SPIONs for non-imaging applications.

1.8 Hyperthermia for glioblastoma

One of the most developed areas of SPIONs-based hyperthermia therapy in cancer is for the treatment of glioblastoma. Glioblastoma multiform (GBM) (WHO Grade IV) is one of the deadliest and most aggressive types of brain tumours; it is also the most common type of glial tumours, accounting for 60% of gliomas (Hoelzinger *et al*, 2007). The standard of care for GBM is surgical resection followed by radiotherapy with concurrent chemotherapy with temozolomide (TMZ, Temodar®) and a further 6 months of maintenance temozolomide (Stupp *et al*, 2005). Despite decades of research, the median survival of glioblastoma sufferers is only 14.6 months with no standard treatment for recurrent/relapsed patients resulting in very poor prognosis and high morbidity and mortality rates (Silva *et al*, 2011). These clinical outcomes highlight the urgent need for novel treatment approaches for GBM and magnetic hyperthermia represents a promising budding field.

Clinical studies have shown that hyperthermia could promote GBM cell death, reduce tumour mass and increase survival (Silva *et al*, 2011). MagForce®, a German nanomedicine company, was the first to introduce the clinical use of 15 nm positively charged aminosilane coated iron oxide nanoparticles (NanoTherm™) for cancer hyperthermia. Preclinical studies on glioma cell lines and cerebral cortical neurons have revealed preferential uptake of NanoTherm™ by tumour cells (Jordan *et al*, 1999). While *in vivo* animal studies performed on a rat glioma intracranial model comparing Resovist® with NanoTherm™ revealed prolonged survival with NanoTherm™. The researchers concluded that this could be explained by the rapid diffusion of Resovist® to the surrounding tissues and thus the dissipation of the generated heat. However, histological studies done on rat brains did not investigate

the cell types containing SPIONs (e.g. tumour cells, microglia, neurons, etc.) (Jordan *et al*, 2006).

The promising preclinical results, mentioned above, have led to phase I and II clinical trials involving the direct intratumoural injection of Nanotherm™ into brain tumour lesions. The therapy proved to be safe and well tolerated by GBM patients (Maier-Hauff *et al*, 2011; Plotkin *et al*, 2006) and clinical trials in glioblastoma, prostate, oesophageal and pancreatic cancers are ongoing (MagForce, 2015). Interestingly, post-mortem studies performed on treated patients with glioblastoma revealed the presence of nanoparticles aggregates mainly in brain macrophages with minor localisation into tumour cells (van Landeghem *et al*, 2009). These findings highlight the importance of studying the interaction of SPIONs with components of the tumour microenvironment.

Similar to other tumours, the tumour microenvironment of glioblastoma includes a wide range of cells (e.g. vascular cells, neural progenitor cells, microglia and immune cells) (Charles *et al*, 2011). Of particular interest are microglial cells, which constitute 30% of the brain tumour mass (Charles *et al*, 2011) and the tumour associated macrophages (the resident macrophages of the tumour) which promote tumorigenesis, invasion and metastasis, tumour survival and proliferation (Garris & Pittet, 2013). In addition, glioblastoma cells were reported to communicate with nearby normal brain parenchyma (astrocytes, oligodendrocytes and neurons) via secreted molecules that can facilitate tumour invasion and malignant progression (Hoelzinger *et al*, 2007). Therefore, even with intratumoural injection of SPIONs into GBM tumours, SPIONs are faced with an array of cells that might internalise them and thus deprive the main tumour core from the heating effect of the activated SPIONs. Consequently, *in vitro* and *in vivo* assays investigating the uptake of SPIONs by tumour cells and components of the microenvironment become crucial.

1.9 Targeting SPIONs to cancer cells

Mainly SPIONs have been passively targeted to the RES for imaging purposes (see sections 1.3.1.2, 1.6.2 and 1.6.3). However, active targeting has been achieved by covalently linking SPIONs to various targeting moieties to facilitate specific uptake by cancer cells. Targeting agents include small molecules (such as folate, arginylglycylaspartic acid (RGD) and transferrin), monoclonal antibodies, antibody fragments and aptamers. A comprehensive list of all targeting strategies for SPIONs

is reviewed in (Kamaly *et al*, 2012; Rosen *et al*, 2012) and some examples are discussed below.

1.9.1 Small molecules

Folate receptors (FR) are cysteine rich cell surface glycoproteins that bind to folates, there are 3 types of folate receptors: α, β and γ (Chen *et al*, 2013). Folate is a generic term that describes folic acid (vitamin B_9) and structurally related compounds. Folates play an important role in DNA synthesis, DNA repair, DNA methylation and cell division (Kelemen, 2006). Folate receptors are exciting targets for the development of cancer specific therapies for two main reasons: (a) the preferential overexpression of folate receptors (mainly FR α) on cancer cells (e.g. ovarian, epithelial, cervical, lung, kidney and brain tumours) and their limited expression in normal tissues (Kelemen, 2006); (b) folic acid is a cheap and a structurally stable small peptide (441 Da) that can be conjugated to drugs, nanoparticles or diagnostic markers while maintaining its binding ability to the receptor (Zwicke *et al*, 2012). Folate ligands (e.g. antibodies or folates) have been conjugated to different types of SPIONs (Rosen *et al*, 2012) and were shown to bind specifically *in vitro* and *in vivo* (Chen *et al*, 2008; Choi *et al*, 2004; Fan *et al*, 2011; Kalber *et al*, 2011; Sonvico *et al*, 2005; Sun *et al*, 2006).

Transferrin receptors are another example of potential therapeutic targets for cancer nanomedicines. Transferrin receptor (TfR or CD71) is a membrane bound glycoprotein that mediates the uptake of iron by cells via transferrin (Daniels *et al*, 2012; Ponka & Lok, 1999). Transferrin is a small peptide (80 KDa) that has iron chelating properties and regulates the transport, storage and utilisation of iron by cells (Ponka & Lok, 1999). Similar to folate receptors, TfR are overexpressed by many cancers (e.g. squamous cell carcinomas, liver, breast and pancreatic cancers) with low levels in normal tissues (Daniels *et al*, 2006a; Daniels *et al*, 2006b). SPIONs labelled with transferrin were used for MR imaging and were found to specifically localise to TfR positive tumours (Högemann-Savellano *et al*, 2003). While Kresse *et al* functionalised USPIO with human transferrin that were shown to localise to mammary carcinomas overexpressing TfR *in vivo* as detected with MRI (Kresse *et al*, 1998).

1.9.2 Aptamers

Aptamers are a class of nucleic acid molecules formed of short single strands of DNA or RNA oligonucleotides that fold to form secondary and tertiary 3-D structures. Aptamers are synthesised to bind targets with high affinity and specificity and can be considered as the nucleic acid equivalents of antibodies (Ni *et al*, 2011). Aptamers can also be engineered to have effective functional groups to facilitate conjugation to nanoparticles (Jayasena, 1999; Rosen *et al*, 2012) and aptamer-SPION conjugates have been developed to target cancer cells. For instance Wang *et al* synthesised SPIONs functionalised with aptamers targeting prostate-specific membrane antigen (PSMA). The functionalised SPIONs were specifically internalised by prostate cancer cells suggesting their potential use for prostate cancer imaging and therapy (Wang *et al*, 2008). While in a study done by Herr *et al* aptamer-SPION conjugates were used for leukemic cancer cell extraction from blood samples using magnetic cell separation techniques (Herr *et al*, 2006). Similarly, Bamrungsap *et al* used aptamer-conjugated magnetic nanoparticles for very sensitive selective cancer cell detection in a variety of biological fluids (e.g. foetal bovine serum (FBS), human plasma and whole blood) (Bamrungsap *et al*, 2012).

1.9.3 Antibodies and antibody fragments

Antibodies (immunoglobulins) are the most established targeting agents currently available. As seen in Figure 1.7, a basic IgG 1 antibody (~ 150 KDa) is a Y-shaped molecule consisting of four polypeptide chains: 2 identical heavy chains (H) (~50 KDa) and 2 identical light chains (L) (~ 25 KDa) held together by covalent disulphide bonds and non-covalent bonds. The heavy chain is made up of 4 distinct regions (domains) while the light chain has two domains. Three out of the four domains of the heavy chain and two out of the three domains of light chains were found to be constant among antibody chains of the same isotype, consequently named constant domains (C) (Janeway *et al*, 2001). On the contrary, the terminal domain of each chain was found to vary greatly between different antibodies, thus named variable domains (V). The paired V_H and V_L terminal domains of the antibody determine its specificity and renders two antigen binding sites on each antibody (Janeway *et al*, 2001).

Whole Y-shaped antibodies could be fragmented by proteolytic digestion into different moieties: (i) the two arms; named fragment antigen binding (Fab)

containing the variable fragments (Fv) and (ii) the trunk; named the fragment crystallizable (Fc) region (Nelson & Reichert, 2009). The Fc region was observed to readily crystallize, hence the nomenclature (Janeway *et al*, 2001; Nelson & Reichert, 2009). The Fc fragment lacks antigen binding activity but plays an important role in the biological effector function of the antibody by inducing antibody-dependent cellular cytotoxicity (ADCC) and complement-dependent cytotoxicity (CDC) (Sathish *et al*, 2013).

The rapid development in recombinant antibody technology has led to the generation of different varieties of antibody fragments (examples are shown in Figure 1.7). Each antibody fragment has unique physicochemical properties (e.g. molecular weight, affinity, half-life, etc.) that determine its pharmacokinetic and pharmacodynamic behaviour and could be tailored according to the intended use (Nelson, 2010).

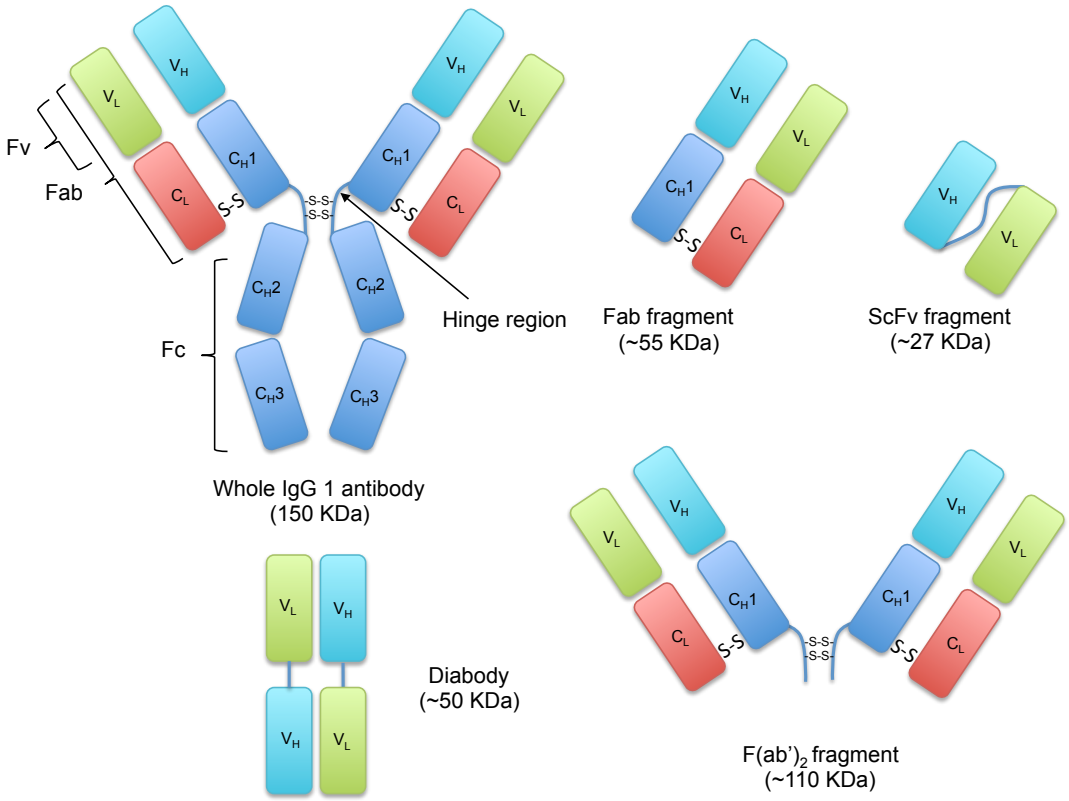

Figure 1.7: Structure of a whole IgG 1 antibody and examples of some antibody fragments

C= Constant domain; V= Variable domain; H= Heavy chain; L= Light chain; S-S= Disulfide bond; Fc= fragment crystallizable; Fab= fragment antigen binding region; Fv= variable fragment and ScFv=single chain fragment variable.

Since a number of antibodies have been approved for clinical use as anticancer therapies (reviewed in (Scott *et al*, 2012)), antibodies provide exciting targeting moieties for the development of SPION-based targeted therapies for both imaging and treatment of cancers. Examples of FDA-approved antibodies used in targeting studies involving nanoparticles include: anti-epidermal growth factor receptor 2 (HER2) antibody (Trastuzumab, Herceptin®) (Chen *et al*, 2009; Cirstoiu-Hapca *et al*, 2007), anti-epidermal growth factor receptor 1 (EGFR) antibody (Cetuximab, Erbitux®) (Bouras *et al*, 2015; Kaluzova *et al*, 2015; Liu *et al*, 2011; Suwa *et al*, 1998) and anti-CD20 antibody (Rituximab, Mabthera®) (Cirstoiu-Hapca *et al*, 2007). Other studies have used antibodies developed for research against vascular endothelial growth factor (VEGF) (Abakumov *et al*, 2015; Hsieh *et al*, 2012), prostate-specific membrane antigen (PSMA) (Bates *et al*, 2014; Mukherjee *et al*, 2014; Tse *et al*, 2015), chemokine receptor 4 (CXCR4) (He *et al*, 2012), glypican-3 (GPC3) (Li *et al*, 2012) and mucin-1 (MUC1) (Shahbazi-Gahrouei & Abdolahi, 2013; Shanehsazzadeh *et al*, 2014).

Similar to whole antibodies a number of antibody fragments, specifically antigen binding fragments (Fab), have been FDA approved for use in the clinic (e.g. Cimzia®, ReoPro® and Lucentis®) (Herrington-Symes *et al*, 2013; Nelson, 2010).

Fab and single chain variable fragments (scFv) are the most commonly investigated fragments for the functionalisation and targeting of nanoparticles (Byrne *et al*, 2008). The small size of these fragments makes them more beneficial than whole antibody molecules as it allows the conjugation of multiple fragments per nanoparticle thus improving the multivalent targeting potential (Bazak *et al*, 2014). Examples of studies that used this approach include work by Huang *et al* using Docetaxel loaded iron oxide nanoparticles targeted with a scFv to Endoglin (Huang *et al*, 2014), while Vigor *et al* conjugated an anti-carcinoembryonic antigen (CEA) scFv to SPIONs and were able to achieve a specific MRI signal in CEA positive cancer cells (Vigor *et al*, 2010). Yang *et al* conjugated an anti-EGFR scFv to SPIONs and could show specific internalisation by EGFR expressing cells (Yang *et al*, 2009). SPIONs have also been functionalised by Fab fragments, for instance Ndong *et al* used Fab fragment derived from the anti-folate receptor alpha antibody Farletuzumab; their results showed specific uptake of the conjugate by receptor-positive cancer cells both *in vitro* and *in vivo* (Ndong *et al*, 2015). Similarly, Quatra *et al* targeted folate receptors by functionalising iron oxide nanocrystals with a Fab fragment derived from anti-folate receptor alpha antibody (MOV19) (Quarta *et al*, 2015). Some studies

also used the bivalent $F(ab')_2$ fragment to target iron oxide nanoparticles to E-selectin (Kang *et al*, 2002; Leung, 2004). Targeting with Fab fragments has also been employed with several liposomal preparations carrying chemotherapeutic cargos (Bazak *et al*, 2014).

1.9.4 Designed Ankyrin Repeat Proteins (DARPins)

The work presented in this thesis explores a novel targeting approach using Designed Ankyrin Repeat Proteins (DARPins). DARPins are small high affinity non-immunoglobulin protein scaffolds derived from naturally occurring ankyrin proteins, that can be readily generated to bind specific targets (Tamaskovic *et al*, 2012).

Ankyrin repeat (AR) proteins occur naturally in all species, including humans, and are implicated in a number of diverse biological processes. AR proteins are involved in many protein-protein interactions and were found intracellularly, extracellularly and even membrane bound. This versatility indicates that they can adapt to various environmental conditions (Binz *et al*, 2003). Furthermore more than 2000 AR proteins were identified highlighting their importance in nature (Letunic *et al*, 2002).

A typical AR consists of 33 amino acids that form a β-turn followed by two anti-parallel α-helices and a loop that reaches the β-turn of the next repeat (see Figure 2 in (Binz *et al*, 2003)). Usually four to six repeats constitutes an AR protein (Tamaskovic *et al*, 2012). An assembled AR protein was mimicked to a “cupped hand” where the fingers are the β-hairpins and α-helices represent the palm (see Figure 1 in (Sedgwick & Smerdon, 1999)). Interactions with targets occur via the protruding β-turns and the first α-helix (Binz *et al*, 2003; Sedgwick & Smerdon, 1999). The high versatility and modularity of the ankyrin repeat domains enable surface evolution by duplications, deletions or shuffling of the repeats (Kobe & Kajava, 2000). Hence, DARPins provide a versatile scaffold for the evolutionary generation of protein domains displaying specific binding surfaces.

DARPins have been generated from AR via consensus design approach (Binz *et al*, 2004), which has been applied for the design of other classes of repeat proteins (e.g. zinc finger peptides) (Kajander *et al*, 2006). Briefly, consensus design involves amino acid sequence alignments of many structurally related proteins to identify conserved residues. The hypothesis is that residues that occur with high frequency would maintain protein folding and stability while specific target interaction residues will not be conserved (Kajander *et al*, 2006). Using the consensus design strategy, a

library of designed AR proteins was generated with fixed framework residues and randomised potential interaction residues, then high affinity binders were selected against the specified target (Binz *et al*, 2004). DARPins are made up of a C-terminal and N-terminal capping repeats on either side of the protein enclosing a number of randomized designed ankyrin repeats module (Figure 1.8); they can be engineered to bind to specific targets with exceptionally high affinities (Binz *et al*, 2003; Stumpp *et al*, 2008) as well as being remarkably stable (Wetzel *et al*, 2010; Wetzel *et al*, 2008).

DARPins provide a wide range of possible applications; they can be used alone or genetically/chemically linked to other moieties (e.g. other DARPins, drugs, toxins, PEG (to increase their half-life), peptides, proteins or antibody Fc domains) (Stumpp *et al*, 2008).

DARPins are advantageous over antibodies in many aspects for instance (Binz *et al*, 2005; Stumpp *et al*, 2008): (a) their small size provides better tumour penetration; (b) antibodies are large and difficult to engineer site specific attachments to them; (c) DARPins are much more stable than antibodies and therefore will provide a better option for hyperthermia therapy when conjugated to SPIONs; (d) the production of whole antibodies is laborious and expensive.

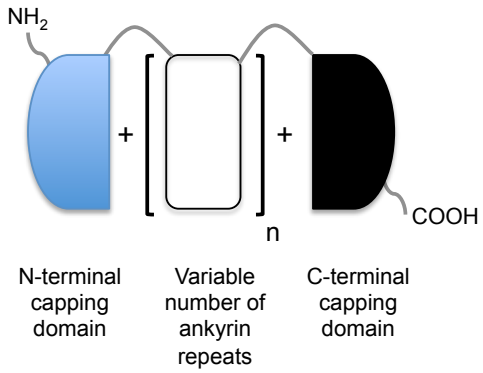

Figure 1.8: Basic structure of DARPins

A DARPin is made up of an N-terminal (blue) and a C-terminal (black) cap that encloses a variable number of ankyrin repeats.

1.10 Summary and research aims

SPIONs possess unique magnetic properties that could be exploited to develop effective anti-cancer therapies such as magnetic hyperthermia. Yet, many challenges lie ahead before this can be achieved. The aim of this project was to investigate means to address three major challenges encountered in the development of SPIONs for targeted cancer treatment (i) uptake by non-cancer cells, particularly the RES, leading to rapid clearance and potential for healthy tissue damage, (ii) lack of specificity for cancer cells and (iii) SPIONs heterogeneity. Resovist® (Ferucarbotran) was used as the major SPION for the study due to its clinical safety profile and heating potential.

First, the interaction of SPIONs with different cell types was characterised and the effects of scavenger receptor blockers measured (Chapter 3). It was hypothesised that SPIONs circulation time could be prolonged by blocking RES with polysaccharide derivatives. This hypothesis was tested in chapter 4.

Second, it was hypothesised that specific targeting of SPIONs could be achieved by functionalising with cancer-targeting proteins such as DARPins. This hypothesis was tested in Chapter 5.

Third, it was hypothesised that SPIONs heterogeneity could be addressed by physical separation to achieve more uniform preparations. This hypothesis was tested in Chapter 6.

Chapter 2

Materials and Methods

Maha Abdollah

2.1 Materials

All materials were purchased from Sigma Aldrich (Dorset, UK) unless otherwise specified.

2.1.1 General buffers

Table 2.1: Formulation of PBS buffers

Solution	Formula
Phosphate buffered Saline (PBS)	Dissolve 1 bottle (96 g) of Dulbecco's Phosphate Buffered Saline (Modified, without calcium chloride and magnesium chloride) in 10 L distilled water (dH_2O)
PBS/Tween (PBS/T)	Add 10 ml of Tween-20 to 10 L of PBS solution

2.1.2 Cell culture

Table 2.2: List of cell lines investigated

Cell line*	Cell type	Supplier
RAW 264.7	Murine monocytes/macrophages	American Type Culture Collection (ATCC®, TIB-71™)
U-87 MG	Human glioblastoma	ATCC®, HTB-14™
U-251 MG	Human glioblastoma	Health Protection Agency (HPA) Culture Collection
Neural stem cells (NSCs)	Murine NSCs	Dr Paolo Salomoni (UCL Cancer Institute)
A375	Human melanoma	Health Protection Agency (HPA) Culture Collection
LS174T	Human colorectal carcinoma	Health Protection Agency (HPA) Culture Collection
293T and 293T-EGFR	Human Embryonic Kidney (HEK) cells	Dr Martin Pule (UCL Cancer Institute)
SupT1, SupT1-EGFR and SupT1-EGFRvIII	Human lymphoblastic leukaemia	Dr Martin Pule (UCL Cancer Institute)

*All investigated cell lines were cultured as adherent cells except SupT1 cells were cultured as suspension cells.

Table 2.3: Cell culture media

Cell lines	Media Formula
RAW 264.7 and A375	Dulbecco's modified Eagle's medium (DMEM) (Gibco®, Thermo Fisher Scientific, Cheshire, UK) supplemented with 10% foetal bovine serum (FBS) (Gibco®), 100 U/ml of penicillin, 0.1 U/ml streptomycin and 1% L-glutamine
LS174T, U-87 MG and U-251 MG	DMEM supplemented with 10% FBS (Gibco®), 100 U/ml of penicillin, 0.1 U/ml streptomycin, 1% L-glutamine and 1% of non-essential amino acids (PAA Laboratories GmbH, Pasching, Austria)
293T	DMEM supplemented with 10% FBS (Gibco®) and 1% L-glutamine (PAA Laboratories GmbH, Pasching, Austria)
SupT1	RPMI-1640 supplied with L-glutamine and supplemented with 10% FBS (Gibco®)
Neural stem cells (undifferentiated)	NeuroCult™ Proliferation Kit (Mouse) (STEMCELL™ Technologies, Grenoble, France) media supplied with recombinant human epidermal growth factor (rh EGF), recombinant human basic fibroblast growth factor (rh bFGF) (STEMCELL™ Technologies) and 100 U/ml of penicillin and 0.1 U/ml streptomycin. 5 μl of 0.1 μg/μl of rh bFGF and 50 μl of 10 μg/ml rh EGF were added per 50 ml of the media

Table 2.4: Cell culture solutions

Solution	Formula
Trypsin	1x Trypsin (0.05%) with EDTA (PAA Laboratories GmbH, Pasching, Austria)
Accutase®	1x Accutase solution
Laminin	Prepare 10 μg/ml solution; dilute Laminin stock solution 1:100 in sterile PBS
PBS	1x Sterile PBS solution (Gibco®)
Freezing media for NSCs	Full media (as stated above in Table 2.3) supplied with 10% DMSO
Freezing media for SupT1	Cryoprotective Freezing Medium (Lonza, Basel, Switzerland)
Freezing media for all other cell lines	10% DMSO in FBS; 9 ml FBS + 1 ml DMSO

2.1.3 Iron quantification assays

Table 2.5: Solutions for ferrozine assay

Solution	Formula
50 mM NaOH	0.2 g of sodium hydroxide (NaOH) in 100 ml distilled water (dH_2O)
4 M HCl	250 ml of dH_2O + 125 ml 37% (12 M) hydrochloric acid (HCl) stock solution
Iron releasing buffer	0.45 g of potassium permanganate ($KMnO_4$) in 10 ml dH_2O + 3.5 ml 4 M HCl + 6.5 ml dH_2O
Iron detection buffer	In 5 ml dH2O dissolve 0.015 g neocuproine, 0.015 g ferrozine, 0.99 g ascorbic acid, 0.96 g ammonium acetate.

Table 2.6: Solutions for Prussian blue staining

Solution	Formula
Cell fixation solution	2% formalin and 2.5% glutaraldehyde in PBS
Staining solution	4 g potassium hexacyanoferrate (II) trihydrate dissolved in 20 ml dH_2O + 20 ml 2% HCl

2.1.4 Immunofluorescence staining

Table 2.7: Solutions for immunofluorescence staining

Solution	Formula
Fixation solution	4% formaldehyde (methanol-free ampoules) containing 20 mM HEPES buffer, pH 7.4
Permeabilisation solution	0.1% Triton-X in PBS
Blocking solution	5% goat serum in PBS/Tween (PBS/T)

2.1.5 Transmission Electron Microscopy (TEM)

Reagents kindly prepared by the Electron Microscopy Unit at UCL Medical School, Royal Free Campus.

Table 2.8: Solutions for TEM

Solution	Formula
Fixation solution	20 ml 20% paraformaldehyde (Analar BDH) + 16 ml 25% glutaraldehyde (TAAB) + 59 ml PBS (Oxoid)
Osmium tetroxide	1% osmium tetroxide (Analar BDH) + 1.5% potassium ferricyanide (BDH) in PBS (Oxoid)
Toluidine blue stain	1% Toluidine Blue (Raymond Lamb) with 0.2% Pyronin (Raymond Lamb) in 1% sodium tetraborate (Analar BDH)
Reynold's lead citrate	Dissolve 1.33 g lead nitrate (BDH) in 15 ml dH_2O and 1.76 g sodium citrate (BDH) in 15 ml dH_2O, mix solutions together (30 ml) and dissolve the resulting precipitate with 8 ml of 1 M NaOH (BDH), make up to final volume of 50 ml
Lemix epoxy resin (TAAB)	Lemix A (25 ml) + Lemix B (55 ml) + Lemix D (20ml). Pour into plastic resin bottle, mix and add 2 ml of benzyldimethylamin (BDMA), then mix well.

2.1.6 Superparamagnetic iron oxide nanoparticles (SPIONs)

Table 2.9: List of SPIONs investigated

SPIONs	Supplier	Size Range	Coating	Functional group	Iron concentration
Ferucarbotran **(FC)**	Meito Sangyo Co. LTD., Tokyo, Japan	45-65 nm	Carboxydextran	OH, COOH (Hydroxyl and carboxylic)	55.6-58.6 mgFe/ml
Nanomag®-D-spio-amine **(NM)**	Micromod Partikelte-chnologie GmbH, Germany	50-120 nm	Dextran	NH_2 (amine)	2.4 mgFe/ml

2.1.7 Chemical conjugation of Ferucarbotran

Table 2.10: Solutions used in SPIONs modification

Solution	Formula
50 mM borate buffer (pH=8.5)	Dissolve 4.77 g sodium tetraborate decahydrate in 250 ml dH2O; adjust to pH 8.5 with 4 M HCl
0.1 M MES buffer	Dissolve 1.95 g 2-(4-morpholino) ethanesulphonic HCl into 100 ml dH2O. Adjust to pH 6 with 5 M NaOH
230 mM sulfo-NHS	Add 40 μl of 0.1 M MES buffer to 1 vial of sulfo-NHS (N-hydroxysulfosuccinimide) (no weigh format, Thermo Fisher Scientific, Cheshire, UK)
EDC/NHS activation buffer	1.21 mg of EDC (1-Ethyl-3-[3-dimethylaminopropyl]carbodiimide-hydrochloride) and 8.8 μl of 230 mM sulfo-NHS (Thermo Fisher Scientific) in 200 μl of 0.1 M MES buffer (pH=6)
25 mM glycine	Dissolve 0.18 g glycine into 100 ml PBS
100 mM cysteine	Dissolve 1.2 g cysteine into 10 ml PBS

Table 2.11: List of near infrared (NIR) dyes used

Product	Supplier	Functional group	Reactivity
DyLight® 800 NHS ester	Thermo Scientific, Pierce Biotechnology	NHS ester (N-Hydroxysuccinimide)	Amine
IRDye® 800 CW azide	LI-COR Biosciences, Lincoln, Nebraska, USA	Azide	Copper free click reaction with dibenzocyclooctyne (DBCO)

2.1.8 RES blockers

Table 2.12: List of RES blockers investigated

Name	Product	Supplier	Average MW (Daltons)	Concentration for *in vitro* experiments	Doses for *in vivo* experiments
D-70	Dextran 70	Pharmacosmos ALS, Holbaek, Denmark	70,000 Da	32 mg/ml	Not tested
D-40	Dextran 40	Meito Sangyo Co. LTD.	40,000 Da	32 mg/ml	Not tested
DSO4 8	Dextran sulfate sodium salt 8	Sigma Aldrich	6,500-10,000 Da (Average ~8,000 Da)	1 mg/ml	Not tested
DSO4 500	Dextran sulfate sodium salt 500	Sigma Aldrich	500,000 Da	30 μg/ml	3, 7.5, 15 and 30 mg/kg
J-18	Dextran sulfate sodium sulphur 18 (for oral administration)	Meito Sangyo Co. LTD.	1600 Da	1 mg/ml	30 mg/kg
J-5	Dextran sulfate sodium sulphur 5 (for i.v. administration)	Meito Sangyo Co. LTD.	1600 Da	1 mg/ml	Not tested
Fucoidan	Fucoidan from *Fucus vesiculosus*	Sigma Aldrich	20000 - 200000 Da	30, 50 and100 μg/ml	15 mg/kg

MW: molecular weight, Da: Daltons

2.1.9 Reagents for protein characterisation

Table 2.13: Recipe for SDS-PAGE gels

Reagent	Formula
7.5% resolving gel	3.85 ml dH2O, 2 ml 30% Acrylamide (Protogel), 2 ml 1.5M Tris-HCl pH 8.8, 80 μl 10% sodium dodecyl sulfate (SDS), 80 μl 10% ammonium persulfate (APS), 8 μl tetramethylethylenediamine (TEMED)
10% resolving gel	3.2 ml dH2O, 2.67 ml 30% Acrylamide, 2 ml 1.5 M Tris-HCl pH 8.8, 80 μl 10% SDS, 80 μl 10% APS, 8 μl TEMED
16% resolving gel	1.6 ml dH2O, 4.27 ml 30% Acrylamide, 2 ml 1.5 M Tris-HCl pH 8.8, 80 μl 10% SDS, 80 μl 10% APS, 8 μl TEMED
4% stacking gel	3.6 ml dH2O; 0.67 ml 30% Acrylamide, 0.625 ml 1 M Tris-HCl pH 6.8, 50 μl 10% SDS, 50 μl 10% APS, 5 μl TEMED

Table 2.14 Reagents for protein analysis

Reagent	Formula
1x SDS-PAGE running buffer	25 mM Tris-HCl, 192 mM Glycine, 0.1% (w/v) SDS
4x Reducing buffer	1.25 mM Tris-HCl solution in dH2O (pH 6.8), 20% w/v glycerol, 4% w/v β-mercaptoethanol, 0.1% w/v bromophenol blue and 0.1% w/v SDS
4x Non-reducing buffer	1.25 mM Tris-HCl solution in dH2O (pH 6.8), 20% w/v glycerol, 0.1% w/v bromophenol blue and 0.1% w/v SDS
Coomassie gel staining solution	0.1 g Coomassie blue R-250 in 100 ml methanol, 20 ml glacial acetic acid and 80 ml dH2O
Coomassie gel de-staining solution	1.25 L methanol, 1 L dH2O and 250 ml glacial acetic acid

Table 2.15 Reagents for western blotting

Reagent	Formula
RadioImmunoPrecipitation Assay (RIPA) buffer	50 mM Tris HCl pH 8 + 150 mM NaCl + 1% Nonidet P-40 + 0.5% sodium deoxycholate + 0.1% SDS (solution was stored at 4^0C)
Cell lysis buffer	20 ml of RIPA buffer + 1 tablet of cOmplete ULTRA Tablets (protease inhibitors) (Roche). Aliquoted and stored at -20^0C
Transfer Buffer Stock (10x)	30 g Trizma® base, 144.2 g glycine and 10 g SDS in 1 L dH2O
Transfer Buffer (1x)	100 ml of 10x transfer buffer stock, 700 ml dH2O and 200 ml methanol
5% Milk	2.5 g semi-skimmed Marvel milk (Marvel, UK) in 50 ml PBS/T
1% Milk	0.5 g semi-skimmed Marvel milk in 50 ml PBS

2.1.10 Molecular weight markers

SeeBlue® Plus2 pre-stained protein standard was obtained from Invitrogen Ltd (Paisley, UK) and PageRuler™ Unstained Protein Ladder was obtained from Thermo Scientific.

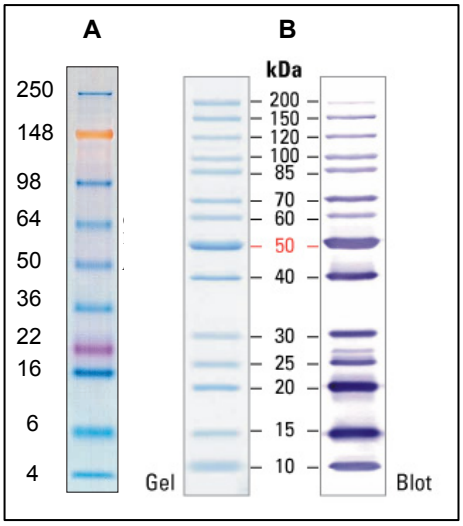

Figure 2.1: Pre-stained molecular weight markers used in SDS-PAGE

(A) SeeBlue® Plus2 and (B) PageRuler™ Unstained Protein Ladder (Pictures taken from Invitrogen Ltd and Thermo Scientific catalogues, respectively).

2.2 Methods

2.2.1 Cell culture

All cells were maintained in culture media previously stated in Table 2.3 at 37^0C in a humidified incubator containing 5% CO_2. All cell culture procedures were performed in a class II Hood and incubations were done inside the incubator at 37^0C (unless otherwise specified).

All cells were purchased as frozen aliquots and stored either in liquid nitrogen or in a -80^0C freezer. To bring cells into culture, cells were thawed in a water bath at 37^0C then resuspended in 6 ml of full media and centrifuged at 280 x g for 5 minutes. The supernatant was aspirated using vacuum pump and the pellet was resuspended in 10 ml media and transferred into T25 flasks (Corning®, Tewksbury, MA, USA).

For all adherent cell lines (except RAW 264.7 and NSCs) once they became confluent, the cells were washed once with 10 ml PBS and then detached from the flask by incubation with 7 ml Trypsin/EDTA (Table 2.4) for 5 minutes inside the incubator at 37^0C. Next the cells were neutralised with an equal volume of media

and then centrifuged at 280 x g for 5 minutes. Finally the media was aspirated using a vacuum pump and the cell pellets were resuspended in full media and split accordingly into a fresh flask containing full media.

For RAW 264.7 cells, once the cells became confluent they were washed once with 10 ml PBS and then 10 ml of fresh full media was added to the flask. Cells were then detached from the flask using Corning® cell scrapers and split accordingly into fresh flasks.

For suspension cell lines (SupT1), cells were maintained in 15 ml of full media in T125 flasks (Corning®) kept upright. Once the cells became confluent, 14 ml of media was aspirated using vacuum pump and replaced with 15 ml of fresh media.

For cryogenic storage, once cells were confluent they were detached from the flasks as explained above and centrifuged at 280 x g. The pellets were resuspended in 10 ml of freezing media (see Table 2.4) and then 1 ml were aliquoted into Nunc™ CryoTube® vials (Thermo Scientific) and stored at -80^{0}C in Mr. Frosty™ Freezing Container (Thermo Scientific) filled with isopropanol for at least 48 hours before being transferred to liquid nitrogen storage.

2.2.2 Cell uptake and blocking experiments

Generally cells were seeded at 2X10^5 cells/well in 24-well plates (Corning®) and left to attach overnight. Next day the cells were treated with Ferucarbotran at three different concentrations (0.1, 0.5, 1 mgFe/ml) for 4 hours. Cells were then washed 3 times with cold PBS to remove excess unbound SPIONs and treated according to one of the protocols described below.

In blocking experiments, cells were pre-treated with the blockers for 15 minutes before being challenged with Ferucarbotran. Dextran sulfates (DSO4 500 and DSO4 8) were tested at an initial concentration of 30 μg/ml, while fucoidan was tested at 30, 50 and 100 μg/ml. For low molecular weight dextran sulfates: DSO4 8, J-18 and J-5 dose escalation studies were done until a blocking effect was observed at 1 mg/ml. Unsulfated dextrans (D-70 and D-40) did not show any blocking effect even at concentrations as high as 32 mg/ml. Results shown in chapter 3 were performed at the concentrations stated in Table 2.12.

2.2.2.1 Ferrozine assay

After the cells were treated and washed as described in section 2.2.2, the number of cells in 3 control wells was counted and averaged to be used in Equation 2.1. Next, the cells were lysed with 200 μl of 50 mM NaOH and the intracellular iron content was determined using the colorimetric ferrozine assay developed by (Riemer *et al*, 2004) and then compared to a standard curve of Ferucarbotran samples of known iron concentrations. 100 μl of each cell lysate was aliquoted into an Eppendorf tube then 100 μl of dH_2O (solvent of Ferucarbotran) was added. 100 μl aliquots of serial dilutions of Ferucarbotran at 0.15, 0.3, 0.6, 1.25, 2.5, 5, 10, 15, 20, 25 and 50 μgFe/ml were prepared from the stock solution and then 100 μl of 50 mM NaOH was added to each tube. Next, to each tube of cell lysates and Ferucarbotran, 100 μl of iron releasing buffer (Table 2.5) was added and then the tubes were vortexed and incubated at 60^0C in a water bath for 2 hours. Next the tubes were left to cool down for 10 minutes before 30 μl of iron detection buffer (Table 2.5) was added to each tube. The tubes were then incubated for 30 minutes to allow for maximum colour development. 100 μl of each tube was then aliquoted into a 96-well plate (Corning®) and the absorbance was measured at 550 nm on Varioskan™ Flash Multimode reader (Thermo Scientific). The amount of iron per cell (pgFe/cell) was calculated as follows:

$$pgFe/cell = \frac{\text{Concentration } (\mu gFe/ml)}{\text{number of cells / ml}} X\,10^6 \qquad \text{Equation 2.1}$$

2.2.2.2 Perl's Prussian blue staining

Cells were treated in accordance to the protocol described above (section 2.2.2), washed thoroughly with cold PBS and then fixed using fixation solution (Table 2.6) for 10 minutes at room temperature (RT). Next, the cells were washed with PBS and stained with a freshly prepared Prussian blue staining solution (Table 2.6) for 10 minutes and counterstained with eosin, mounted with DPX and imaged with 100x oil immersion lens using Carl Zeiss Axioskop MOT 2 microscope (Carl Zeiss, Germany).

2.2.3 Confocal Laser Scanning Microscopy (CLSM)

$2X10^5$ cells/well were seeded on coverslips (VWR International, Leicestershire, UK) in 24-well plates then allowed to attach overnight. Next day, cells were incubated for

4 hours with 0.1 mgFe/ml Ferucarbotran labelled with Alexa Fluor® 633 hydrazide (Invitrogen) using the periodate oxidation chemistry as described in (Abdollah *et al*, 2014; Vigor *et al*, 2010). Afterwards, cells were washed with cold PBS then treated with CellMask™ Orange plasma membrane stain (2.5 μg/ml) (Invitrogen) for 5 minutes at 37^0C. After washing with PBS, cells were fixed with 4% formaldehyde/20 mM HEPES buffer pH 7.4 at 37^0C for 10 minutes. Finally, nuclei were counterstained with Hoeschst 33342 (Invitrogen) (1/5000) for 30 minutes at RT in the dark on a rocker before the coverslips were mounted with ProLong® gold antifade (Invitrogen) and imaged using a Zeiss LSM 510 meta confocal microscope (Carl Zeiss). Images were processed using Zeiss LSM Image Browser (Carl Zeiss) and Image J software (U.S. National Institutes of Health, Bethesda, Maryland, USA).

2.2.4 Transmission Electron Microscopy (TEM) and X-ray microanalysis

Cells were seeded at $2X10^5$ cells/well in 6-well plates (Corning®) and allowed to attach overnight. Next day the cells were treated with 0.5 mgFe/ml Ferucarbotran for 4 hours before being washed 3 times with cold PBS. Then the cells were fixed in 1.5% glutaraldehyde/1% paraformaldehyde/PBS pH 7.4, for a minimum of 2 hours, and stored at 4°C until processing for TEM.

TEM protocol (described below) was kindly provided and done by the Electron Microscopy Unit at UCL Medical School, Royal Free Campus.

Fixed cells were centrifuged to form a pellet in a 0.5 ml Eppendorf. The cells were then washed with two changes of phosphate buffer (Oxoid) and post-fixed with osmium tetroxide. The cells were resuspended during each change of solution and allowed to stand for 10 minutes, before removal of the supernatant and addition of the next processing solution. They were then washed using several changes of distilled water to remove the osmium tetroxide and dehydrated using increasing alcohol concentrations of 30%, 50%, 70%, 90% and 100%. The samples were left in 50% alcohol / 50% Lemix (TAAB) epoxy resin mixture on a mixer overnight to infiltrate with resin. They were then placed in 100% Lemix resin for a minimum of 4 hours, embedded in fresh Lemix Resin and polymerised at 70^0C overnight.

Semi-thin (1μm) sections were cut using glass knives on a Reichert-Jung Ultracut microtome, collected on glass microscope slides and stained using 1% Toluidine Blue. Ultrathin sections were cut using a diamond knife (Diatome) and collected on

300HS, 3.05 mm copper grids (Gilder). The ultrathin sections were stained using saturated alcoholic uranyl acetate (UA) (TAAB) for 5 minutes followed by Reynold's lead citrate, also for 5 minutes. Sections examined with EDAX were not stained with UA or Lead.

The sections were viewed and photographed using a Philips CM120 transmission electron microscope fitted with EDAX DX-4 microanalytical system for X-ray microanalysis of the samples.

2.2.5 Neuronal stem cells culture

Protocols for maintenance, differentiation and staining of mouse neuronal stem cells (NSCs) were kindly provided by Dr Paolo Salomoni (UCL Cancer Institute). Prior to culturing the cells, T25 flasks (Greiner), 24-well plates (Corning®) or cover slips (VWR) were coated with 10 μg/ml of laminin in sterile PBS for 2 hours at RT on a rocker. Then the laminin was aspirated and the cells were maintained in media described in Table 2.3.

2.2.5.1 Differentiation protocol

When cells reached 80-90% confluency, they were detached from the flasks using Accutase® then centrifuged at 240 x g before being resuspended in fresh media supplemented with rh bFGF and rh EGF, counted and seeded at 2 $X10^5$ cells/well in 24-well plates pre-coated with laminin. Next day the media was removed and the cells were washed with sterile PBS before adding media supplemented with rh bFGF only (i.e. rh EGF was removed). The cells were left for 3 days then on the fourth day the cells were again washed with sterile PBS and incubated with media containing no growth factors and then left for 5 days. At the end of the 8-day period the cells were differentiated into a mixed culture of neurons, oligodendrocytes and astrocytes before being treated with SPIONs.

2.2.5.2 Immunofluorescence staining for CLSM

Coverslips were placed in 24-well plates and coated with laminin for 2 hours. Then $2X10^5$ cells were seeded on each coverslip and allowed to attach overnight. Next day the cells were differentiated according to the protocol described above (section 2.2.5.1). Then cells were fixed using 4% formaldehyde/20 mM HEPES buffer pH 7.4 at 37^0C for 10 minutes. Cells were permeabilised using 0.1% triton in PBS for 5

minutes at RT before being incubated with a blocking solution of 5% goat serum in PBS/T for 1 hour at RT.

To confirm differentiation; undifferentiated and differentiated cells were prepared as described above then stained for the neuronal markers using a mouse anti-neuronal βIII tubulin (Promega, 1/2000) for neurons, rabbit anti-GFAP (Dako, 1/3000) for astrocytes and rabbit anti-OLIG2 (Millipore, 1/1000) for oligodendrocytes. Cells were incubated with the primary antibodies overnight at 4^0C. Next day, Alexa Fluor® 488 goat anti-mouse IgG (Life Technologies, 1/1000) and Alexa Fluor® 488 goat anti-rabbit IgG (Molecular Probes, 1/1000) prepared in 5% goat serum were added to the cells for 1 hour at RT in the dark. Nuclei were counterstained with Hoechst 33342 (Invitrogen, 1/5000) for 30 minutes at RT in the dark. Finally the cells were washed 3 times with PBS and the coverslips were mounted with ProLong® gold antifade (Invitrogen) and left overnight to dry at RT. Slides were imaged using a 63x oil immersion lens on Zeiss LSM 510 meta confocal microscope. Images were processed using Image J software and Zeiss LSM Image Browser (Carl Zeiss).

For uptake experiments, differentiated cells were incubated with 0.5 mgFe/ml Ferucarbotran for 4 hours before being washed 3 times with sterile cold PBS, fixed and treated as described above. Ferucarbotran was detected in the cells using mouse anti-dextran antibody (STEMCELL™, 1/100) followed by Alexa Fluor® 488 goat anti-mouse IgG (Life Technologies, 1/500). Neurons were detected with rabbit anti-neuronal βIII tubulin (Covance, 1/1000), while OLIG2 and GFAP were stained using the same primary antibodies as above then Alexa Fluor® 546 goat anti-rabbit IgG (Molecular Probes, 1/1000) was used to detect the neuronal markers.

2.2.5.3 Uptake and blocking experiments

$2X10^5$ cells/well of NSCs were seeded in 24-well plates or coverslips (for Prussian blue staining) pre-coated with laminin. Next the cells were differentiated following the protocol described above (section 2.2.5.1). After the differentiation cells were pre-treated with the blockers at the concentrations stated in Table 2.12 for 15 minutes before adding Ferucarbotran at concentrations of 0.1, 0.5 and 1 mgFe/ml for 4 hours. The cells were then either lysed with 50 mM NaOH and the intracellular iron content determined using the ferrozine assay (as described in 2.2.2.1) or stained with Prussian blue (as described in 2.2.2.2).

2.2.6 PrestoBlue™ cell viability assay

PrestoBlue™ (Invitrogen) is used to quantitatively measure the proliferation of cells by being reduced in viable cells to a highly florescent compound (Invitrogen product data sheet). Cells were seeded in 96-well plates at 20,000 cells/well then allowed to attach overnight. Next day they were incubated with 1:2 serial dilutions of Ferucarbotran (10 to 0.02 mgFe/ml), DSO4 500 (300 to 0.59 μg/ml) and J-18 (10 to 0.02 mg/ml) for 4 hours followed by incubation with PrestoBlue™ (10 μl/ml) for 1 hour. The fluorescence was measured at 560/600 nm and percentage cell viability was calculated in reference to untreated controls. Each concentration was performed in triplicate and the experiment was repeated 3 times. Percentage cell viability was calculated using the equation below:

$$\% \text{ Cell viability} = \frac{Rs-Rm}{Rc-Rm} \times 100 \qquad \text{Equation 2.2}$$

Where Rs = fluorescence reading of sample, Rm = fluorescence reading of media (without cells) and Rc = fluorescence reading of control (untreated control).

To ensure that the brown colour of Ferucarbotran did not interfere with the assay; fluorescence readings of wells containing Ferucarbotran only were compared to fluorescence reading of media (without cells). No difference was detected between the two readings.

2.2.7 Conjugation of Nanomag®-D-spio-NH_2 to DyLight® 800 NHS ester dye

The particles were purchased as a suspension in water, which is incompatible with the labelling protocol. Consequently, water was exchanged with 50 mM sodium borate buffer (pH 8.5) using a PD-10 desalting column (GE Healthcare, UK).

500 µl of 50 mM sodium borate buffer was added to 50 µg of the lyophilized dye. The resultant dye solution was subsequently added to 1 ml of SPIONs solution (2.4 mgFe). The reaction was allowed to proceed for 1 hour at RT on a roto-torque. The solution was purified by applying the sample on a PD-10 column equilibrated with PBS.

2.2.8 Conjugation of Ferucarbotran to IRdye® 800CW azide

Ferucarbotran (88.6 μl, 5 mg Fe) was buffer exchanged into 0.1 M MES buffer using a PD-10 column. Next the solution was incubated with 200 μl of EDC/sulfo-NHS activation buffer (Table 2.10). The reaction was allowed to proceed for 20 minutes at RT (on a rotator) and was terminated by application to a PD-10 column equilibrated with PBS (pH=7.4). Next, 200 μg of dibenzocyclooctyne-amine (DBCO-NH_2) linker in 1 ml PBS was sonicated to promote dissolution then added to the reaction mixture and incubated for 2 hours at RT followed by the addition of 100 μl/ml of 25 mM glycine for 30 minutes to block the remaining reactive sites. The sample (FC-NH-DBCO conjugate) was buffer exchanged using a PBS-equilibrated PD-10 column to remove excess unreacted linker. Finally, 2.5 μl of 20 mg/ml (~50 μg) of IRDye® 800 CW azide was incubated with the FC-NH-DBCO conjugate for 3 hours at 37^0C in a water bath. The resultant NIR-conjugated SPIONs were extensively purified by passing, at least thrice, through PD-10 columns equilibrated with PBS to remove any dye that was non-specifically attached to the dextran coat of Ferucarbotran.

Following all SPIONs conjugations, the integrated signal intensity of a serial dilution of known iron concentrations of the conjugates was measured at 800 nm on an Odyssey® infrared scanner (LI-COR Biosciences, Lincoln, Nebraska, USA) to plot a standard curve. Integrated signal intensity (also known as pixel volume) is defined by the Odyssey® infrared scanner software as the sum of the intensity values for all pixels enclosed by a shape, multiplied by the area of the shape (counts mm^2).

2.2.9 Characterisation of SPIONs following conjugation

2.2.9.1 Dynamic Light Scattering (DLS)

SPIONs were characterised before and after functionalisation using a Zetasizer Nano ZS90 (Malvern, Worcestershire, UK) to identify their hydrodynamic diameter and polydispersity index (PDI). SPIONs solutions were prepared in sterile-filtered 5 mM NaCl.

2.2.9.2 Transmission Electron Microscopy (TEM)

TEM characterisation of SPIONs was kindly done by Dr Joseph Bear. SPIONs samples were diluted in distilled water and visualised with a Jeol 2100 HRTEM with a LaB_6 source operating at an acceleration voltage of 200 kV with an Oxford

Instrument UTW EDX detector running AZTEC software. Micrographs were taken in a Gatan-Orius charge coupled device (CCD). Core sizes were measured from high-resolution TEM images using ImageJ software.

2.2.10 Uptake of FC-IRDye 800 on RAW 264.7 cells

$2X10^5$ cells/well were seeded in 24-well plates and allowed to attach overnight. Next day the cells were pre-treated with DSO4 500 or J-18 for 15 minutes before being incubated with 0.1 mgFe/ml of FC-IRDye 800 for 4 hours. The cells were then washed 3 times with cold PBS and the NIR signal measured on the Odyssey® infrared scanner (LI-COR). Finally the cells were lysed using 50 mM NaOH and the intracellular iron measured using ferrozine assay as described in section 2.2.2.1.

2.2.11 *In vivo* blocking of the uptake of SPIONs by the RES

All *in vivo* experiments were performed using mouse models in compliance with licenses issued under the U.K. Animals (Scientific Procedures) Act 1986 after local ethical committee review. All mice were 6-8 week old female BALB/c (Charles River Laboratories, UK). The mice had an average weight of 20 g at the start of the experiments. All NIR-labelled SPIONs were injected at a dose of 10 μmolFe/kg. SPIONs and blockers were prepared in PBS and sterile filtered (using 0.22 μm syringe filter) under a cell culture hood prior to injections to minimise bacterial contamination. All injections were administered intravenously through tail veins.

For Nanomag-D-spio-DyLight 800 (NM-DyLight 800), DSO4 500 was first tested (2 mice per group) at 4 different concentrations: 0 (unblocked), 3, 7.5, 15 and 30 mg/kg and then a period of 24 hours was given to allow for sufficient blocking of the liver then NM-DyLight 800 was injected.

For the remainder of the blocking experiments, DSO4 500 and J-18 were evaluated at 30 mg/kg while fucoidan was tested at 15 mg/kg.

In the next set of experiments DSO4 500 was tested in 4 independent experiments (n=8). 24 hours following the administration of DSO4 500, NM-DyLight 800 or FC-IRDye 800 were injected. Blocked mice were compared to unblocked control (n=8) injected with NM-DyLight 800 or FC-IRDye 800 only.

Next, DSO4 500 was further evaluated at 3 different blocking times: either DSO4 500 and FC-IRDye 800 were given simultaneously (0 hours, n=3), or the blocker was given either 2 hours (n=3) or 24 hours (n=3) before the administration of FC-IRDye 800. In the experiments testing J-18 as a blocker; it was injected 0, 30 and 120 minutes prior to the administration of FC-IRDye 800, each group had 2 mice similar to the unblocked control. Next, fucoidan (n=3) was evaluated in comparison with DSO4 500 (n=3); blockers were administered 24 hours prior to FC-IRDye 800 and compared to unblocked control (n=1). Finally fucoidan (n=2) and DSO4 500 (n=2) were tested when given directly before FC-IRDye 800 and evaluated against the unblocked control (n=2).

One hour following the injection of the NIR-labelled SPIONs, the mice were anaesthetized using a 1% isoflurane (Ivax Pharmaceuticals, UK) oxygen mixture. Blood was collected by cardiac puncture in EDTA-coated tubes (Teklab or BD Vacutainer®) and the mice were sacrificed by cervical dislocation. For SPIONs quantification, a 100 µl aliquot of each blood sample was transferred into a 96-well plate (Corning®) and then the integrated signal intensity was measured at 800 nm on an Odyssey® infrared scanner.

2.2.12 Radiolabelling of Ferucarbotran with Technetium-99m (^{99m}Tc) for SPECT/CT imaging

The work described below was done by Dr Rafael Torres Martin de Rosales (King's College London) as part of a collaboration with UCL. Radiolabelling and SPECT imaging were done at the Division of Imaging Sciences and Biomedical Engineering, King's College London, Lambeth Wing, St. Thomas' Hospital.

Technetium-99m-dipicolylamine-alendronate (^{99m}Tc-DPA-ale) linker was synthesized as previously described in (De Rosales *et al*, 2009; de Rosales *et al*, 2011). The linker was purified using a C18 Sep-Pak® light column, yielding 200 µl of 460 MBq of ^{99m}Tc-DPA-ale in dH_2O. Then 3 µl of pure Ferucarbotran (0.174 mgFe) was added and the mixture was incubated at 40^0C for 30 minutes while shaking. The vial was then cooled down to RT and the contents transferred to an Amicon® Ultra 0.5 ml centrifugal filter with a 10 KDa cut off that had been previously washed with 3 × 500 µl of dH_2O. The filter was centrifuged at 11000 x g for 3 minutes. The remaining retained solution contained 50 µl of radiolabelled nanoparticles to which 300 µl of saline was added and the mixture was sonicated for 1 minute and

centrifuged as described before. This process was repeated 5 times until no more unbound ^{99}Tc-DPA-ale was detected in the filtrates. The total radioactivity in the filtrates and SPIONs solution was measured to determine the radiolabelling yield (36%). The final ^{99}Tc-DPA-ale-Ferucarbotran conjugate was diluted to 500 μl using saline ready to be injected into mice (100 μl/mouse).

Prior to injections and imaging, female BALB/c mice (6-8 weeks) were anesthetized with isoflurane and oxygen mixture and kept under its influence for the duration of the experiment (maximum 4 hours) and culled by cervical dislocation at the end of the imaging session. All injections were done intravenously through the tail vein using 0.3 ml insulin syringes. Six mice were used in total (3 pre-treated with fucoidan and 3 unblocked). In the blocked group, mice were injected with 100 μl of fucoidan solution at a dose of 15 mg/kg followed by 100 μl of the ^{99}Tc-DPA-ale-Ferucarbotran conjugate (15-30 MBq of ^{99m}Tc) 2-10 minutes after the blocker. While the unblocked group was treated with 100 μl of radiolabelled Ferucarbotran only. Immediately after the injections the mice were imaged with SPECT/CT.

SPECT/CT images were obtained with a NanoSPECT/CT PLUS preclinical animal scanner (Mediso, Hungary) equipped with four heads, each with nine 1 mm pinhole collimators, in helical scanning mode in 20 projections over 20 minutes. The CT images were obtained with a 45 kV X-ray source, 1000 ms exposure time in 180 projections over 10 minutes. Images were reconstructed in a 256 × 256 matrix using the HiSPECT (Scivis GmbH) reconstruction software package, and fused using InVivoScope (IVS) software (Bioscan, France).

After the mice were culled, selected organs were harvested, washed and weighed. The retained radioactivity in each organ was measured with a CRC-25R dose calibrator (Capintec, USA) or a 1282 COMPUGAMMA gamma counter (LKB Wallac, Finland) and the percentage-injected dose per gram of tissue (%ID/g) was calculated.

2.2.13 Statistical analysis

2.2.13.1 In vitro cell experiments

All *in vitro* experiments were repeated at least 4 times with 3 triplicates per treatment. Representative data is shown unless otherwise specified, values

represent means and error bars are for standard deviations. p values were calculated using Student's unpaired 2 tailed t test.

2.2.13.2 In vivo experiments

Statistical analysis was kindly done by Mr Ankur Ravinarayana Chakravarthy, MSc (UCL Cancer Institute).

For NM-DyLight 800 and FC-IRDye 800 *in vivo* experiments, the effect of DSO4 500 blocking was assessed using a total of 8 mice per group in 4 independent experiments (2-mice/group for NM-DyLight 800 and 1-3 mice/group for FC-IRDye 800). An ANOVA test was used to assess variance associated with the different experiments, and statistical significance between groups (blocked versus unblocked) was assessed using a Tukey HSD test on the fitted model. For FC-IRDye 800 final experiment with DSO4 500 (Figure 4.15), Shapiro-Wilk test confirmed that the data was normally distributed, and therefore a Student's unpaired 2 tailed t test was used to assess statistical significance of the data. p values less than 0.05 were considered statistically significant.

2.2.14 Sodium dodecyl sulfate-polyacrylamide gel electrophoresis (SDS-PAGE)

Gel casting was done using Mini-PROTEAN® Tetra Handcast Systems (Bio-Rad, Hemel Hempstead, Hertfordshire, UK). Gels were prepared using the recipes mentioned in Table 2.13. The resolving gel was first prepared and then poured into the casting glass and allowed to dry before adding the 4% stacking gel and the comb. After gels were completely dried they were placed in the electrophoresis chamber containing 1x SDS-PAGE running buffer (Table 2.14) and the combs were removed before the samples were loaded. The electrophoresis chamber was then connected to PowerPac™ 3000 electrophoresis power supply set at 150 V and allowed to run for 60 minutes. The gels were either subjected to western blotting (section 2.2.15) or stained using Coomassie blue stain by incubating the gels with Coomassie blue staining solution (Table 2.14) for 30 minutes followed by de-staining solution (Table 2.14) for 1 hour.

2.2.15 Western blotting

Following gel electrophoresis (see section 2.2.14) proteins were transferred from SDS-PAGE gels into polyvinylidene difluoride (PVDF) membrane (Bio-Rad). The gel

was sandwiched between PVDF membrane (pre-activated in methanol for 5 minutes) and pre-wetted layers of chromatography filter paper (Whatmen, Maidstone, UK) and sponges, before being placed in the gel holding cassette (Bio-Rad). The cassette was then submerged in Mini Trans-Blot® electrophoretic transfer cell (Bio-Rad) containing 1x transfer buffer (Table 2.15). Finally the cell was connected to PowerPac™ 3000 power supply set at 100 V and allowed to run for 70 minutes.

Next the membrane was removed from the cassette and washed once with PBS before being blocked in 5% milk (Table 2.15) at 4^0C overnight on platform shaker. Next day, the membrane was incubated with the appropriate dilution of the primary antibody prepared in 1% milk for 1 hour at RT on platform shaker. The membrane was then washed in PBS/T for 30 minutes with 3 buffer changes while shaking. Next the membrane was incubated with the solution of horseradish peroxidase (HRP) conjugated secondary antibody prepared in 1% milk for 1 hour at RT on shaking platform before being washed in PBS/T for 30 minutes with 3 buffer changes (List of antibodies used is shown in Table 2.16). Finally the membrane was incubated with 1 ml of Luminata™ Classico Western HRP substrate (Merck Millipore Ltd., Cork, Ireland) for 2 minutes and the chemiluminescent signal was developed using Amersham Hyperfilm ECL (GE Healthcare, UK).

Table 2.16: Antibodies used in western blotting

Target protein	Primary antibody	Dilution	Secondary antibody	Dilution
EGFR 1	Rabbit Anti-EGFR 1 (Cell Signalling Technology, Inc.)	1:1000	Anti-Rabbit HRP	1:500
HER2	Rabbit Anti-HER2 (Cell Signalling Technology, Inc.)	1:2000	Anti-Rabbit HRP	1:2000
β-Tubulin	Mouse Anti β-Tubulin (Sigma)	1:20,000	Anti-mouse HRP	1:1000
E69	Polyclonal mice serum immunised with E69 (provided by Dr Berend Tolner, UCL Cancer Institute)	1:500	Anti-Mouse HRP	1:1000
G3	Polyclonal mice serum immunised with G3 (provided by Dr Berend Tolner)	1:500		

2.2.16 Conjugation of Ferucarbotran to DARPins

DARPins (anti-EGFR E69 and anti-HER2 G3) were kindly provided by Dr Berend Tolner (UCL Cancer Institute). DARPins were stored under reducing conditions in PBS/5 mM dithiothreitol (DTT) to keep the proteins as monomers. However, DTT interferes with the reaction; therefore it was removed immediately before use by a PD-10 column equilibrated with PBS and protein concentrations were determined spectrophotometrically at 280 nm using Equation 2.3.

$$A_{280} = \varepsilon_{280} \times C \times L \qquad \textbf{Equation 2.3}$$

Where A_{280} = absorbance at 280 nm, ε_{280} = molar extinction coefficient (0.1%, 280 nm, 1 cm path length), C= protein concentration (g/L) and L= path length of the cuvette (cm).

A_{280} was measured on NanoDrop® (ND-1000) spectrophotometer (Thermo Scientific). ε_{280} was calculated based on the protein primary amino acid sequence using ExPASy ProtParam tool (http://web.expasy.org/protparam/). Amino acid sequences of E69 and G3 were kindly provided by Dr Berend Tolner and are shown in Figure 2.2. For E69, ε_{280} = 0.859 and for G3, ε_{280} = 0.208.

E69 sequence:

```
         10         20         30         40         50         60
HEHEHEGSDL GKKLLEAARA GQDDEVRILL ANGADVNADD NAGRTPLHLA ANFGHLEIVE

         70         80         90        100        110        120
VLLKNGADVN AKGHHSNTPL HLAAWAGHLE IVEVLLKYGA DVNADDDEGY TPLHLAADID

        130        140        150        160        170        180
LEIVEVLLKY GADVNAWDMY GRTPLHLAAS AGHLEIVEVL LKYGADVNAQ DKFGKTAFDI

        190        200
SIDNGNEDLA EILQKLNGGC
```

G3 sequence:

```
         10         20         30         40         50         60
HEHEHEGSDL GKKLLEAARA GQDDEVRILM ANGADVNAKD EYGLTPLYLA TAHGHLEIVE

         70         80         90        100        110        120
VLLKNGADVN AVDAIGFTPL HLAAFIGHLE IAEVLLKHGA DVNAQDKFGK TAFDISIGNG

        130
NEDLAEILQK LNGGC
```

Figure 2.2: Amino acid sequence of E69 and G3 DARPins

Ferucarbotran is dissolved in water, which was exchanged with 0.1 M MES buffer (pH=6) by running 1.42 ml of Ferucarbotran stock solution (58.6 mgFe/ml) on a PD-10 column equilibrated with 0.1 M MES buffer. Next the samples were incubated with 1.6 ml of EDC/sulfo-NHS activation buffer (19.2 mg of EDC and 140.8 μl of 230 nM sulfo-NHS (Table 2.10)) for 20 minutes at RT (on a rotator). The reaction was terminated by application of the sample to a PD-10 column equilibrated with PBS (pH=7.4). Next, 71.2 mg of BMPH linker (N-beta-maleimidopropionic acid hydrazide-TFA, Thermo Scientific) in 1.6 ml PBS was added to the reaction mixture and incubated for 2 hours at RT followed by 100 μl/ml of 25 mM glycine for 30 minutes to block the remaining reactive sites. The sample (FC-NH-BMPH conjugate) was purified using a PBS-equilibrated PD-10 column to remove excess unreacted linker. Next, FC-NH-BMPH conjugate solution was divided into two equal volumes. To each tube either 2 mg of E69 or 1.2 mg of G3 (molar equivalent to E69) in PBS was added to the reaction mixture and incubated overnight at RT on the rotator. Next day, 100 μl/ml of 0.1 M cysteine was added for 30 minutes to block the unreacted active sites. The samples were then concentrated using Centriprep® centrifugal filters (cut off 30 KDa) (Merck Millipore) by spinning them for 10 minutes at 1500 x g. Finally the samples were purified using SEC on a column packed with Superdex 75. To detect proteins in the purified conjugates, 30 μl of selected fractions were mixed with 10 μl of 4x reducing buffer and boiled for 15 minutes at 99^0C. Samples were run on 16% SDS-PAGE gels then stained with Coomassie blue to visualise the proteins (as previously described in section 2.2.14).

2.2.17 Characterisation of Ferucarbotran-DARPins conjugates

Conjugates were characterised with DLS and western blotting. DLS and zeta potential measurements were performed on Zetasizer Nano ZS90 (Malvern) as previously described in section 2.2.9.1. For western blots, 30 μl of 300 μgFe/ml of Ferucarbotran (FC) or its conjugates (FC-E69 and FC-G3) were added to 10 μl of either 4x reducing or non-reducing buffers (Table 2.14). Control samples of the corresponding DARPin at 1 μg/ml and Ferucarbotran at 1 mgFe/ml were also prepared. Under reducing conditions the samples and controls were boiled for 15 minutes at 99^0C to ensure the dissociation of the bond between the linker and the DARPins. Next, 20 μl of each sample was loaded into a 16% SDS-PAGE gel and run as previously described in section 2.2.14 and 2.2.15. The membranes were then probed with either anti-E69 or anti-G3 polyclonal mouse sera before being incubated with anti-mouse HRP secondary antibody (as described in Table 2.16).

2.2.18 Testing binding of Ferucarbotran-E69 conjugates to EGFR using ELISA

Layouts of the ELISA plates and the raw experimental results are shown in Appendix 1.

2.2.18.1 Indirect ELISA

Nunc MaxiSorp 96-well plate (Thermo Scientific) was washed once with PBS and then either coated with PBS or 4.7 μg/ml of EGFR (Sino Biologicals Inc., Beijing, China) overnight at 4^0C. Next day the plate was washed 3 times with PBS/T and 3 times with PBS before adding 300 μl/ well of the blocking solution PBS/TB (PBS containing 0.1% Tween and 1% BSA). The plate was incubated for 1 hour at RT on a shaker. Next the wells were treated (according to the diagram in Appendix 1) with 80 μl (in PBS) of either 500 μgFe/ml of Ferucarbotran (FC) or its conjugates (FC-E69 and FC-G3); 1 μM of DARPins (E69 =21.6 μg/ml and G3=14.35 μg/ml); 5 μg/ml of Cetuximab or PBS. The samples were left on the plate for 1 hour at RT on the shaker before being washed with PBS/T (3x) and PBS (3x). 80 μl/well of the primary antibodies (prepared in PBS/TB) were then added: anti-E69 (1:500) in half of the plate and anti-dextran (1:100) in the other half for 1 hour at RT on the shaker. The plate was again washed in PBS/T (3x) and PBS (3x) before adding 80 μl/well of the secondary antibodies (prepared in PBS/TB) to the wells. Anti-mouse IRDye 800 CW (1:5000) was used to detect bound anti-E69 and anti-dextran while Cetuximab was detected with anti-human DyLight 649 (2 μg/ml). The plates were incubated for 1 hour at RT in the dark on the shaker and then washed as described above. The signal of the bound secondary antibodies was measured on Odyssey® infrared scanner at 800 nm and 700 nm for anti-mouse IRDye 800 CW and anti-human DyLight 649, respectively.

2.2.18.2 Immobilizer plates

Nunc™ Amino™ Immobilizer polysorp plates (Thermo Scientific) were used to covalently link EGFR via its sulfhydryl groups at pH 7.5 to the nucleophilic groups present on the surface of the plate. The plate was washed once with PBS before coating the wells with 4.7 μg/ml of EGFR in PBS (pH=7.5) for 1 hour at RT on the shaker. The plate was then washed 3 times with PBS/T and 3 times with PBS. An extra blocking step was employed to block the reactive sites on the plate using 300 μl/well of 10 mM cysteine. The plate was incubated for another hour before being treated with 300 μl/well of PBS/TB for 1 hour at RT on the shaker. Next the plate

was washed as explained previously and incubated with 80 μl (in PBS) of either 500 μgFe/ml of Ferucarbotran or its conjugates (FC-E69 and FC-G3); 1 μM of DARPins (E69 and G3); 5 μg/ml of Cetuximab or PBS (according to the diagram in Appendix 1). The samples were left on the plates for 1 hour at RT on the shaker before being washed with PBS/T (3x) and PBS (3x). 80 μl/well of the primary antibodies (prepared in PBS/TB) were then added to the corresponding wells: anti-E69 (1:500); anti-G3 (1:500) and anti-dextran (1:100) were added to E69, G3 and Ferucarbotran (or its conjugates) coated wells, respectively, and incubated for 1 hour at RT on the shaker. The plates were washed as described previously and then incubated with 80 μl/well of secondary antibodies prepared in PBS/TB. Anti-mouse IRDye 800 CW (1:5000) was used to detect bound anti-E69, anti-G3 and anti-dextran while Cetuximab was detected with anti-human DyLight 649 (2 μg/ml). The plates were incubated in the dark on the shaker for 1 hour and then washed as described above. The signal of the bound secondary antibodies was measured on Odyssey® infrared scanner at 800 nm and 700 nm for anti-mouse IRDye 800 CW and anti-human DyLight 649, respectively.

2.2.18.3 Sandwich ELISA

Nunc MaxiSorp 96-well plate (Thermo Scientific) was washed once with PBS and then coated with 80 μl (in PBS) of either 500 μgFe/ml of Ferucarbotran or its conjugates (FC-E69 and FC-G3); 1 μM of DARPins (E69 and G3); or PBS (according to the diagram in Appendix 1) for 1 hour at RT on the shaker. The wells were then blocked with 300 μl/well of PBS/TB for 1 hour on the shaker before being washed 3 times with PBS/T and 3 times with PBS. The wells were then incubated with 80 μl/well of 4.7 μg/ml of EGFR in PBS for another hour on the shaker and then washed as described previously. Bound EGFR was detected by adding 80 μl/well of 5 μg/ml Cetuximab solution in PBS and incubated for an hour on the shaker. Finally the plates were washed and incubated with anti-human DyLight 649 (2 μg/ml) for 1 hour on the shaker in the dark and then washed. The signal of the bound secondary antibodies was measured on Odyssey® infrared scanner at 700 nm.

2.2.19 Detecting EGFR and HER2 expression on cells using western blotting

$2X10^6$ cells were centrifuged at 280 x g and washed once with cold PBS and re-pelleted. The cell pellet was resuspended in 100 μl cell lysis buffer (Table 2.15) and incubated on ice for 30 minutes. Next the samples were centrifuged at 280 x g for

10 minutes at 4^0C and the supernatants were transferred to fresh tubes and placed on ice. Total protein concentration was measured using Bio-Rad protein assay (Bradford assay) and compared to 1:2 serial dilutions of bovine serum albumin (BSA) starting from 5 mg/ml. 5 μl of each sample was placed in a 96-well plate then 25 μl of Bio-Rad reagent A and 200 μl of Bio-Rad reagent B were added to each well and incubated for 15 minutes. The absorbance was measured at 630 nm on Varioskan™ Flash Multimode reader (Thermo Scientific) and the total protein concentrations of each cell lysate was calculated from the standard curve. Next, each cell lysate was prepared in 4x reducing buffer (Table 2.14) and dH2O to a final total protein concentration of 1 μg/ml. The samples were then denatured at 99^0C for 5 minutes then stored at -20^0C until processing.

Gels were prepared as described in section 2.2.14 then 20 μl of each sample was loaded into the gels and run as described in section 2.2.15. The membranes were then probed with either anti-EGFR, anti-HER2 or anti β-Tubulin before being incubated with the corresponding HRP conjugated secondary antibodies (as described in Table 2.16).

2.2.20 Testing binding of E69 DARPin on EGFR expressing cell lines using flow cytometry

In these experiments all incubations, washings and centrifugations were done on ice or at 4^0C to minimise internalisation. All data analysis was done using FlowJo software (Treestar Inc., San Carlos, CA, USA).

2.2.20.1 U-251 glioma cell line

When cells reached 70-80% confluency, they were detached from the flasks using trypsin. The cells were centrifuged and the pellet was washed with cold PBS before being centrifuged again and resuspended in cold PBS at the concentration of 10^6 cells/ml. 500 μl of the cell suspension was placed into each FACS tube (BD Falcon™, Beford, USA). Cells were then treated according to Table 2.17. Cells were incubated with the samples for 1 hour then centrifuged at 280 x g for 5 minutes and the pellet was resuspended in cold PBS supplemented with 0.5% bovine serum albumin (BSA) (PBS/BSA) and gently vortexed. The primary antibodies were added and further incubated for 1 hour. The washing step was repeated before the secondary antibodies were added for 20 minutes in the dark. After the final washing step, the cells were resuspended in 300 μl of cold PBS/BSA and kept on ice until

analysed using BD LSRFortessa™ X-20 cell analyser (BD Biosciences, San Jose, California, USA). Cells treated with anti-DARPins and secondary antibodies (anti-DARPins control) were used as negative control.

Table 2.17: Treatments added for Flow cytometry analysis on U251 MG cells.

Name	Sample added	Primary antibody	Secondary antibody
Untreated	n/a	n/a	n/a
Cetuximab	100 nM Cetuximab (15 μg/ml)	n/a	Anti-human DyLight 647 (1:2000, Thermo Scientific)
Herceptin	100 nM Herceptin (15 μg/ml)	n/a	Anti-human DyLight 647 (1:2000)
E69	100 nM E69 (2.16 μg/ml)	Polyclonal anti-E69 mouse serum (1:1000)	Anti-mouse DyLight 647 (1:2000, Thermo Scientific)
G3	100 nM G3 (1.435 μg/ml)	Polyclonal anti-G3 mouse serum (1:1000)	Anti-mouse DyLight 647 (1:2000)
Anti-DARPins control	n/a	Polyclonal anti-E69 or anti-G3 mouse serum (1:1000)	Anti-mouse DyLight 647 (1:2000)

n/a: not applicable

2.2.20.2 293T cells

Once confluent, the media was aspirated and the cells were washed with cold PBS. Cells were detached from the flask with 0.1% EDTA in PBS, centrifuged and resuspended in cold PBS before being counted and resuspended at a concentration of 10^6 cells/ml. 0.5 ml of the cell suspension was placed into each FACS tube. The cell suspensions were then ready to be treated according to Table 2.18. Cells were incubated with the samples for 1 hour then centrifuged at 300 x g for 5 minutes and the supernatant decanted, the pellet was resuspended in cold PBS, gently vortexed and centrifuged again before being resuspended in 500 μl of cold PBS and the primary antibodies were added and further incubated for 1 hour. The washing step was repeated before the secondary antibodies were added for another hour in the dark. After the final washing step, the cells were resuspended in 500 μl of cold PBS and kept on ice until analysed using CyAn™ ADP Flow Cytometer (Beckman Coulter) to detect fluorescence in the Alexa Fluor 488 channel. Untreated cells and cells treated with secondary antibodies only were used as negative controls.

Table 2.18: Treatments added for Flow cytometry analysis of E69 binding to 293T cells.

Name	Sample added	Primary antibody	Secondary antibody
Untreated	n/a	n/a	n/a
Cetuximab	100 nM Cetuximab (15 μg/ml)	n/a	Anti-human Alexa Fluor 488 (1:1000, Molecular probes)
E69	100 nM E69 (2.16 μg/ml)	Polyclonal anti-E69 mouse serum (1:500)	Anti-mouse Alexa Fluor 488 (1:1000, Molecular probes)
G3	100 nM G3 (1.435 μg/ml)	Polyclonal anti-G3 mouse serum (1:500)	Anti-mouse Alexa Fluor 488 (1:1000, Molecular probes)

n/a: not applicable

2.2.20.3 SupT1 cells

Three types of SupT1 cells were used: SupT1-NT, SupT1-EGFR and SupT1-EGFRvIII, all were treated in a similar manner as will be described below. Cells were centrifuged at 280 x g and then the media was removed before the cells were washed with cold PBS once and resuspended in PBS. Cells were counted and resuspended at a concentration of 10^6 cells/ml. 1 ml of the cell suspension was placed into each FACS tube. The cell suspensions were then ready to be treated with samples, primary and secondary antibodies according to Table 2.19 and in a similar fashion to 293T cells (see 2.2.20.2).

To investigate whether foetal bovine serum (FBS) present in the full cell culture media affects the binding of E69 to EGFR, cells were resuspended in cell culture media (RPMI) containing 0, 0.1%, 1%, 5% and 10% FBS instead of cold PBS and treated similar to above.

Cells were analysed using BD Accuri™ C6 flow cytometer (BD Biosciences). Untreated cells and cells treated with secondary antibodies only were used as negative controls.

Table 2.19: Treatments added for Flow cytometry analysis of E69 binding to SupT1 cells.

Name	Sample added	Primary antibody	Secondary antibody
Untreated	n/a	n/a	n/a
Cetuximab	100 nM Cetuximab (15 μg/ml)	n/a	Anti-human DyLight 649 (2 μg/ml, Thermo Scientific)
MR 1.1	MR 1.1 2 μg/ml	n/a	Anti-human DyLight 649 (2 μg/ml, Thermo Scientific)
E69	100 nM E69 (2.16 μg/ml)	Polyclonal anti-E69 mouse serum (1:500)	Anti-mouse APC (1:1000, Molecular probes)
G3	100 nM G3 (1.435 μg/ml)	Polyclonal anti-G3 mouse serum (1:500)	

n/a: not applicable

2.2.21 Testing binding of Ferucarbotran-DARPins conjugates on EGFR expressing cell lines

2.2.21.1 Gliomas

U-251 MG cells were seeded at $2X10^5$ cells/well in 24-well plates (Corning®) and left to attach overnight. Next day they were pre-treated with 30 μg/ml of DSO4 500 for 15 minutes followed by challenging the cells with Ferucarbotran, FC-E69 or FC-G3 at 0.5 mgFe/ml for 4 hours. Cells were then washed 3 times with PBS to remove excess unbound SPIONs and intracellular iron content determined using ferrozine assay (see section 2.2.2.1).

2.2.21.2 SupT1

$3X10^5$ cells/well were added to a V-bottom sterile 96-well plates (Corning®). Cells were pre-treated with 30 μg/ml of DSO4 500 for 15 minutes before adding Ferucarbotran, FC-E69 or FC-G3 at 0.3 mgFe/ml for 4 hours. The plates were then centrifuged at 300 x g and the supernatant was decanted. 200 μl of cold PBS was added per well then the cells were centrifuged again. The washing was repeated for 3 times to remove excess unbound SPIONs. Finally the cells were centrifuged and the pellet resuspended in 200 μl 50 mM NaOH and the intracellular iron content determined using ferrozine assay (see section 2.2.2.1).

2.2.22 Magnetic separation of Ferucarbotran using MACS® LS column

MACS® LS columns (Miltenyi Biotec GmbH, Germany) were inserted into a QuadroMACS™ Separator (Miltenyi Biotec GmbH) then they were rinsed with 3 ml of degassed and sterile filtered buffer (PBS, 0.5% BSA and 2 mM EDTA). Ferucarbotran solutions were prepared in 500 μl of the same buffer to the final amount of either 50 μg or 20 μg iron. Ferucarbotran solutions were applied to the column and the flow through was collected. The column was washed 3 times using 3 ml of buffer each time. The eluents were collected and denoted (wash 1, 2 or 3). The LS column was then removed from the separator and placed on a new collection tube. Finally 5 ml of buffer was applied into the LS column and the magnetic fraction was immediately eluted by firmly applying the plunger supplied. The iron content of the collected samples was measured using ferrozine assay (see section 2.2.2.1).

2.2.23 Column packing for Size Exclusion Chromatography (SEC)

All solutions were sterile filtered and degassed using 0.22 μm Corning® bottle top vacuum filters prior to use. ÄKTA prime plus FPLC system (Amersham Biosciences) was used for all size exclusion chromatography studies. All SEC media were purchased from GE-Healthcare (Amersham, UK). All columns appeared to be uniformly packed and elution profiles of the gel filtration standard (Bio-Rad) are shown in Appendix 2.

2.2.23.1 Sephadex G-100

This media is made up of soft beads that require swelling prior to packing the column. 17.33 g of dry Sephadex G-100 coarse was incubated in 260 ml of PBS for at least 72 hours at RT. After incubation, the slurry was poured slowly and in one portion into an XK16/100 column fitted with a packaging reservoir and held at an angle to avoid the formation of air bubbles. The column was connected to the FPLC system and run at 0.5 ml/min with maximum pressure of 0.05 MPa.

To check the packing efficiency, a gel filtration standard (Bio-Rad) was applied on the column. The lyophilised powder was dissolved in 0.5 ml PBS and injected into the column. The sample was run at flow rates between 0.2 and 0.4 ml/min with maximum pressure of 0.05 MPa, which was eventually increased to 0.2 MPa.

2.2.23.2 Superdex 75 Prep Grade

This media is made up of hard beads that do not require swelling; it is supplied by the manufacturer as a solution in 20% ethanol. To remove the storage solution, the media was left at RT until all the media settled then the upper solution was decanted and the media re-suspended in dH_2O. This was repeated at least 2 times to remove all traces of ethanol.

The slurry was then poured into an XK16/60 column fitted with a packing reservoir. The column was packed in 3 steps according to the manufacturer's instructions: step 1 at flow rate of 3 ml/min and maximum pressure of 0.45 MPa for 90 minutes. Step 2: at 2.5 ml/min and maximum pressure of 0.45 MPa for 30 minutes. Step 3: the packing reservoir was removed and the top adapter of the column attached and the packing process was continued at 3 ml/min for another 20 minutes. After all the media settled the top adapter was adjusted and the column was ready for use.

To check the packing efficiency, 300 μl of gel filtration standard was injected into the column and run at 1 ml/min with maximum pressure of 0.45 MPa.

2.2.23.3 Superdex 200

This column was purchased as a pre-packed XK 16/60 column.

2.2.23.4 Superose 6 and 12 Prep Grade

This media is made up of hard beads similar to Superdex 75. The slurry preparation was similar to that explained for Superdex 75 (see section 2.2.23.2).

The slurry was then poured into an XK16/60 column fitted with a packing reservoir. The column was packed following the manufacturer's protocol at a flow rate of 2 ml/min until all media had settled. Then it was increased to 3 ml/min and 4 ml/min for Superose 6 and 12 respectively, for 60 minutes. The packing reservoir was disconnected and replaced with the top adapter that was adjusted to the top of the media bed. Then the flow rate was increased to reach maximum pressure of 0.4 MPa and 0.5 MPa for Superose 6 and 12, respectively, for another 5-6 minutes. Finally the top adapter was re-adjusted on top of the media bed and the column was ready for use.

To check the packing efficiency, 500 μl of gel filtration standard was injected into the columns and run at 1 ml/min with maximum pressure of 0.3 MPa and 0.5 MPa for Superose 6 and 12, respectively.

2.2.24 Fractionation of Ferucarbotran with SEC

All fractionation experiments were done on columns equilibrated with PBS. 80 μl of Ferucarbotran stock solution (56.3 mgFe/ml) was diluted in 1 ml PBS and injected into the columns. The samples were run at 1 ml/min except on Sephadex G-100 where the samples were run at 0.1-0.5 ml/min.

2.2.25 Measuring the heating ability of fractionated Ferucarbotran

Magnetic hyperthermia experiments were kindly done by Dr Paul Southern at the UCL Healthcare and Biomagnetics Laboratory, The Royal Institution of Great Britain. Magnetic hyperthermia heating ability was characterised by the intrinsic loss parameter (ILP) using the Magnetic Alternating Current Hyperthermia (MACH) system using a 6 turn coil, inner diameter 20 mm and length 35 mm with an AC field of 13500 A/m at a frequency of 905 kHz. The temperature was measured using fluoroptic temperature probes to minimize non-specific radiofrequency heating of the probes. The temperature profile was fitted using the corrected slope analysis as described by Wildeboer *et al* to determine the ILP (Wildeboer *et al*, 2014).

Chapter 3
Cellular Interactions of Ferucarbotran

Maha Abdollah

3.1 Introduction

The aim of the work presented in chapter 3 is to investigate means to address the rapid clearance of SPIONs by the RES. This is an important challenge in the development of SPIONs because a short circulatory half-life severely limits availability and potential for non-RES targeted applications. The SPION investigated in this chapter is Ferucarbotran, which in its pharmaceutical formulation (Resovist®) was clinically developed as an MRI contrast agent targeting the RES (Reimer & Balzer, 2003).

The uptake of Ferucarbotran is mediated by macrophages as described in many published reports, which have concluded that this internalisation is mediated by scavenger receptor class A (SR A) (see introduction section 1.6.3) (Chao *et al*, 2012a; Chao *et al*, 2012b; Lunov *et al*, 2010b; Raynal *et al*, 2004; Yang *et al*, 2011). Ferucarbotran is coated with dextran (Reimer & Balzer, 2003); a branched polysaccharides derived from a bacterium called *Leuconostoc mesenteroides* (Jeanes *et al*, 1954; Pleuvry, 2004; Quon, 1988). Dextran is made up of repeated units of D-glucose linked mainly by alpha glycosidic 1,6 linkages with occasional alpha 1,3 branching (Figure 3.1, left) (Jeanes *et al*, 1954; Quon, 1988). Since some of the ligands of SR A are sulfated polysaccharides (e.g. dextran sulfate and fucoidan) (Chao *et al*, 2012b; Segers *et al*, 2013; Sonia *et al*, 2009); it was hypothesised that the RES uptake of SPIONs could be competitively blocked using polysaccharide derivatives. To test this hypothesis a range of polysaccharides were evaluated for their ability to block Ferucarbotran uptake at a cellular level.

3.1.1 Polysaccharides investigated as RES blockers

Seven different polysaccharides were chosen for investigation in this study. The polysaccharides investigated are listed in Table 3.1, along with their clinical applications. Their characteristics are described below. The RES blockers were divided into blockers of scavenger receptors and pharmaceutical agents.

3.1.1.1 Scavenger receptor blockers

Dextran sulfate 500 (DSO4 500): is a synthetic dextran derivative prepared by the esterification of bacterially derived dextran with sulphuric acid to replace some of the hydroxyl (OH) groups with sulfate (SO_4) groups (Figure 3.1, right) (Ricketts, 1952). The DSO4 500 chosen for investigation in this thesis contained 17% sulfur content, which corresponds to approximately 2.3 sulfate groups per glucosyl residue (Sigma

product information sheet). DSO4 500 is a known inhibitor of scavenger receptors *in vitro* especially on macrophages and has been used before in many inhibitory studies (Sonia *et al*, 2009). DSO4 500 is also known to block liver Kupffer cells and has been studied extensively *in vivo* (Bradfield *et al*, 1974; Das *et al*, 1987; Fujiwara *et al*, 1996; Illum *et al*, 1986; Jansen *et al*, 1991; Liu *et al*, 1992; Patel *et al*, 1983; Sands & Jones, 1987; Yoshinobu *et al*, 1994).

Fucoidan: Another known ligand of scavenger receptor A is fucoidan (Thelen *et al*, 2010), which has also been used in some inhibitory studies on macrophages (Segers *et al*, 2013). Fucoidan is a polysaccharide mainly made up of fucose and sulfate ester groups (Cumashi *et al*, 2007; Li *et al*, 2008) (see Figure 3.1, right). Fucoidan is extracted from different species of brown seaweed (e.g. *Fucus vesiculosus, Undaria pinnatifida and Macrocystis pyrifera*) and some marine invertebrates (e.g. sea urchins and sea cucumbers) (Li *et al*, 2008). It is commercially available in many food supplements (Fitton, 2011) and has been subjected to intense research for the past decade due to its versatile biological applications (Cumashi *et al*, 2007; Li *et al*, 2008). These biological functions include antioxidant, antiviral, anticoagulant, anti-inflammatory and reduction of blood lipids among other applications (Cumashi *et al*, 2007; Li *et al*, 2008; Lira *et al*, 2011). Fucoidan has also been reported to have an anti-cancer effect (Kwak, 2014) and has been investigated in osteoarthritis, stem cell modulation, kidney disease and liver disease (Fitton, 2011).

3.1.1.2 Pharmaceutical agents

Pharmaceutical agents might have potential as RES blockers and could provide a safer and clinically approved alternative to DSO4 500.

A number of dextrans are available as pharmaceutical products and were shown to be safe and well tolerated by patients. For instance dextran 40 and 70 have been mainly used as plasma expanders in patients suffering from trauma, burns, hypovolemia and hypotension (Wade *et al*, 1997).

Two low molecular weight dextran sulfates were provided by Meito Sangyo Co. Japan. Dextran sulfate sodium salt sulfur 18 (J-18) (also known as MDS KOWA) (RAD-AR Council, 2015) is approved in Japan as an anti-hyperlipidemic and anti-arteriosclerotic agent (Fujishima *et al*, 1986); it has also been tested for the

treatment of diabetic retinopathy (Mimura *et al*, 1983) and acute cerebral thrombotic infarction (Fujishima *et al*, 1986).

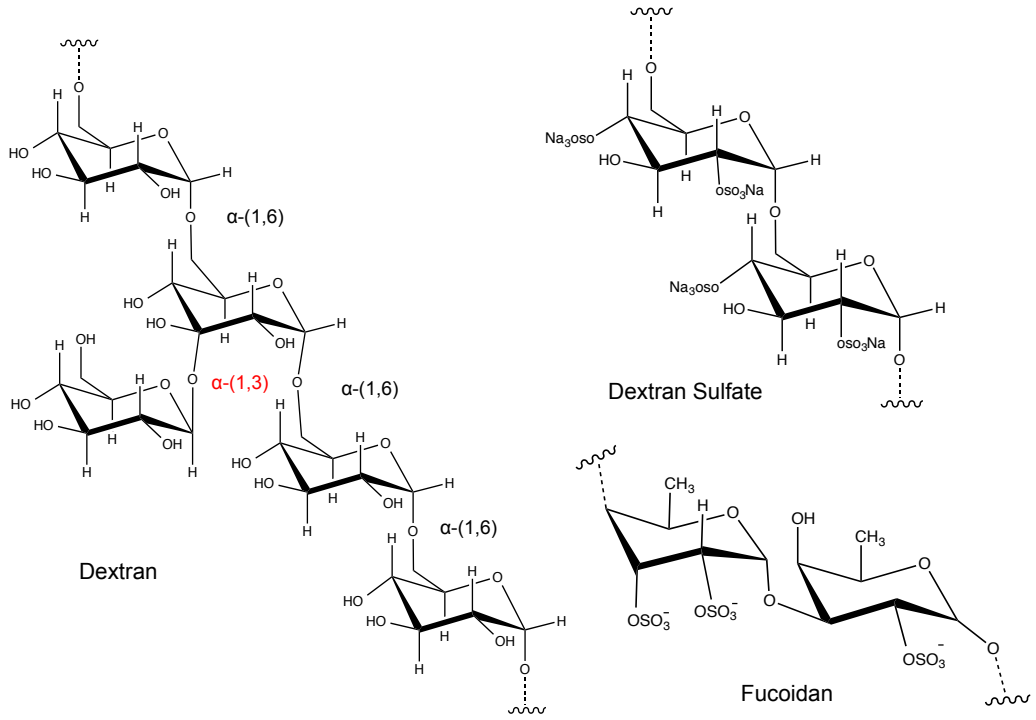

Figure 3.1: Chemical structure of polysaccharides investigated

Dextran is made up of repeated glucose units linked together with α-(1,6) linkages with few α-(1,3) branchings. In dextran sulfate, some of the hydroxyl groups are replaced with sulfate groups. While fucoidan is a fucose rich sulfated polysaccharide derived from seaweed.

Table 3.1: Clinical applications of the blockers used

Name	Product	Clinical application	References
D-70	Dextran 70	Plasma expander	(Wade *et al*, 1997).
D-40	Dextran 40	Plasma expander	
DSO4 8	Dextran sulfate sodium salt 8	Dextran sulfates were tested as anti-coagulants and anti-HIV but not used clinically	(Flexner *et al*, 1991)
DSO4 500	Dextran sulfate sodium salt 500		
J-18	Dextran sulfate sodium sulphur 18 (for oral administration)	Oral anti-hyperlipidemic	(RAD-AR Council, 2015).
J-5	Dextran sulfate sodium sulphur 5 (for I.V administration)	Parenteral anti-hyperlipidemic	
Fucoidan	Fucoidan extracted from brown seaweed *Fucus vesiculosus*	Food supplement	(Fitton, 2011).

n/a: not available

3.1.2 Experimental approach

The effect of the polysaccharides investigated was first evaluated on a murine monocyte/macrophage cell line; RAW 264.7 originally developed by Raschke *et al* (Raschke *et al*, 1978). This cell line has been used extensively in the study of the interactions of nanoparticles, and specifically SPIONs, with macrophages (Chao *et al*, 2012a; Lunov *et al*, 2010a; Lunov *et al*, 2010b; Yang *et al*, 2011). Once the experimental conditions were established on macrophages, the research was further expanded to include tumour cell lines.

Having established the effect of the blockers on macrophages and tumour cell lines, the next step was to investigate the same blockers on other cell types that would occur within the tumour microenvironment (see introduction section 1.8). For this, with a focus on glioblastoma, differentiated neural stem cells (NSCs) were used.

Neural stem cells (NSCs) provide a good model for investigating the uptake of Ferucarbotran by normal brain cells. In adult human brains, NSCs were isolated from various regions (e.g. the subventricular zone (SVZ), the dentate gyrus, the lining of the lateral ventricles, the hippocampus and the subcortical white matter) (Sanai *et al*, 2005). NSCs are multipotent and self-renewing cells that can give rise to the neuronal and glial progenitors cells. Neuronal progenitor cells then differentiate into neurons while glial progenitor cells can give rise to astrocytes and oligodendrocytes (Sanai *et al*, 2005). Neurons are responsible for conducting the electrical signals throughout the nervous system while astrocytes and oligodendrocytes provide insulation, structural support and nutrition for the neurons (Rinholm & Bergersen, 2012; Sanai *et al*, 2005). *In vitro* isolated murine neural stem cells could be stimulated to differentiate into neurons, astrocytes and oligodendrocytes (Regad *et al*, 2009). Studying the interaction with these cells could elucidate the non-target specific uptake of Ferucarbotran by cells within the tumour microenvironment and will not only detract the SPIONs from reaching the desired target but it might induce toxic side effects if taken up by normal cells.

3.1.3 Research Aims and Objectives

Aim: To develop a system to investigate the effect of polysaccharide derivatives on the cellular interactions of Ferucarbotran with different types of cells.

Objectives:

- Establish assays to evaluate the uptake, internalisation and blocking of Ferucarbotran by RAW 264.7 macrophage cell line via quantitative and qualitative iron assays that can be applicable to other cells.
- Test the effect of seven different polysaccharides as potential RES blockers on macrophages.
- Investigate the cellular interactions of Ferucarbotran and polysaccharide blockers with different tumour cell lines. These include gliomas (U-87 MG and U-251 MG), melanoma (A375) and colorectal carcinoma (LS174T) cell lines.
- Evaluate the uptake of Ferucarbotran by components of glioblastoma microenvironment using differentiated neural stem cells as a model for normal brain cells.

3.2 Results

3.2.1 Uptake of Ferucarbotran by macrophages

Two different methods were established to measure internalisation of Ferucarbotran: (1) A quantitative colorimetric iron assay (ferrozine assay) originally developed by Riemer *et al* to measure intracellular iron (Riemer *et al*, 2004) and (2) Prussian blue staining to visualise Ferucarbotran inside the cells. The latter method gives visually striking dense blue aggregates due to the reaction of the reagent with the iron, it has been used extensively to stain SPIONs in cells and tissues (Branca *et al*, 2010; Kalber *et al*, 2005; Lee *et al*, 2009; Schöpf *et al*, 2005; Smith *et al*, 2007). The assays were developed on RAW 264.7 cells, a murine monocyte/macrophage cell line (Campa *et al*, 2005).

First, serial dilutions of known iron concentrations of Ferucarbotran were used to establish the linear range of the ferrozine assay and create a standard curve (Figure 3.2).

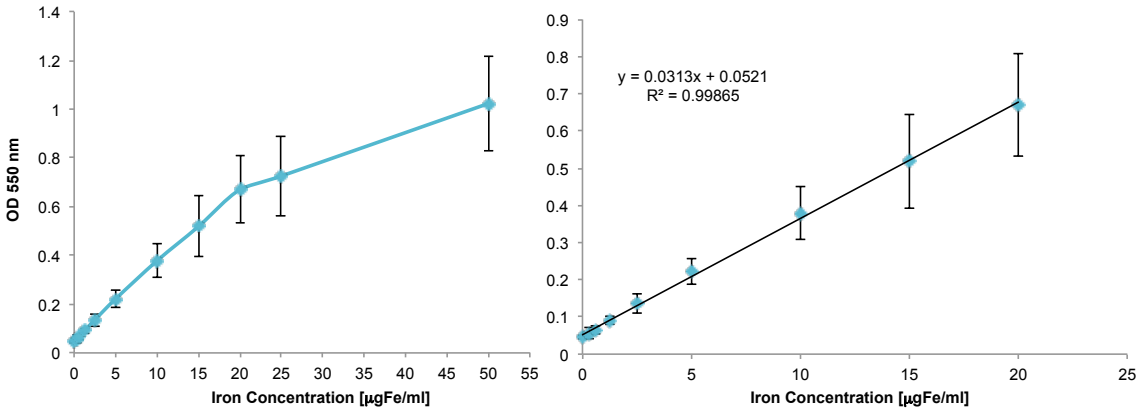

Figure 3.2: Standard curve of serial dilution of Ferucarbotran measured with ferrozine assay.

Left: Iron concentrations above 20 µgFe/ml were in the non-linear range of the assay. **Right:** A linear increase (R^2 = 0.996) was observed in the absorbance of Ferucarbotran samples with concentrations between 0.3 - 20 µgFe/ml.

The ferrozine assay was then applied to measure iron levels in lysates from cells that had been incubated with different concentrations of Ferucarbotran. Absorbance values of the different samples were extrapolated from the standard curve to measure the iron concentrations, which were then converted to pgFe/cell values according to Equation 2.1 as described in materials and methods section 2.2.2.1.

Results (Figure 3.3 A) showed that the intracellular iron levels of macrophages increased, in a dose dependent manner, as the concentration of Ferucarbotran applied on cells increased.

Prussian blue staining showed the presence of blue aggregates, apparently inside the cells treated with Ferucarbotran, indicating that Ferucarbotran had been internalised (Figure 3.3 B).

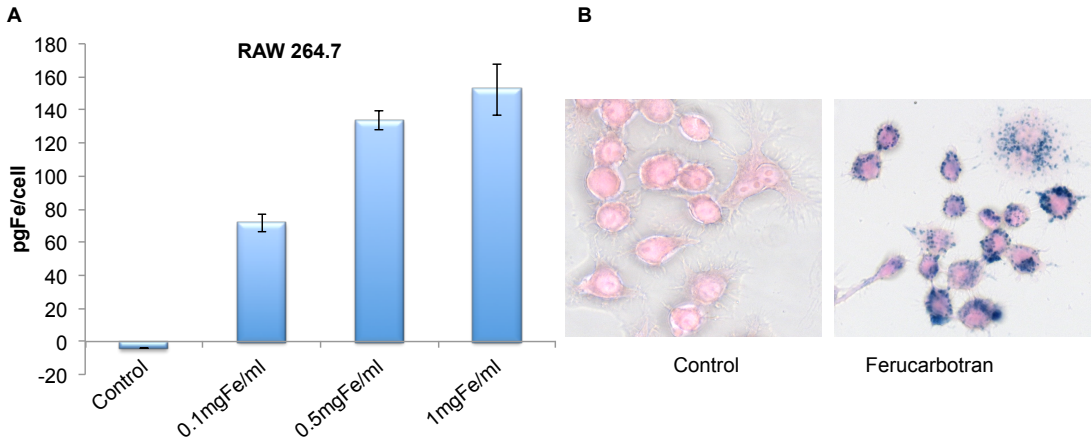

Figure 3.3: Uptake of Ferucarbotran by RAW 264.7 cells

A: Ferrozine assay was used to measure the uptake of Ferucarbotran by macrophages. Cells were treated with 3 different concentrations of Ferucarbotran 0.1, 0.5 and 1 mgFe/ml as the concentration of Ferucarbotran increased the intracellular iron increased while the untreated control showed no detectable iron levels. **B:** Prussian blue staining showed the presence of Ferucarbotran as blue aggregates inside the cells compared to none visible in the untreated control. Bars represent the average of readings of 3 wells/treatment and error bars are for standard deviations.

3.2.2 Internalisation of Ferucarbotran by macrophages

Further studies using TEM and CLSM were used to confirm that Ferucarbotran is being internalised by the cells rather than adhering extracellularly.

For CLSM, Ferucarbotran was chemically conjugated to Alexa Fluor® 633-hydrazide dye (shown in green) in order to visualize it inside the cells; the cell membrane was labelled using CellMask® orange (red) to define the cell boundaries. The nuclei were counterstained with Hoechst 33342 (blue). CLSM images of RAW 264.7 cells (Figure 3.4) showed the presence of aggregates of Ferucarbotran in the cytoplasm of the cells with none localising in the nucleus. CellMask® orange is slowly internalised by the cells (Invitrogen product data sheet) and showed some cytoplasmic staining in addition to membrane staining; nevertheless it clearly showed the cell boundaries. Z–series stacks were performed to confirm the presence of Ferucarbotran within the cells (Figure 3.5).

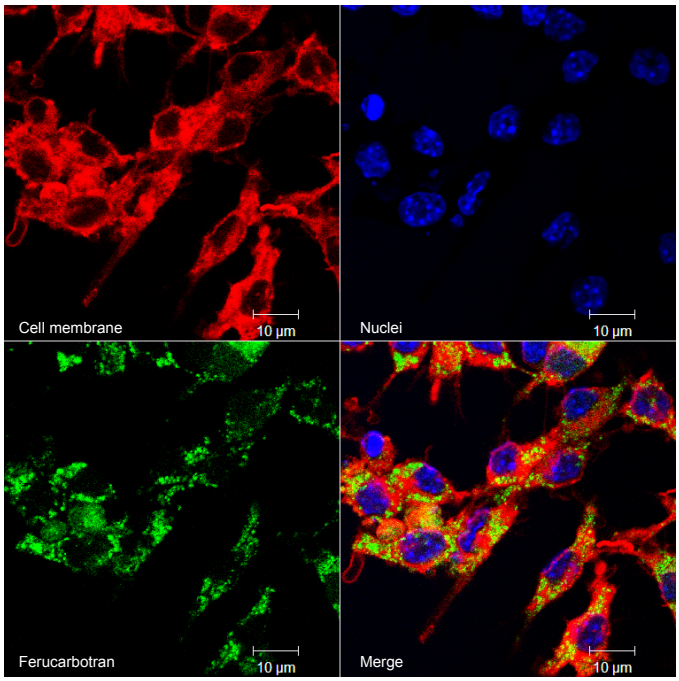

Figure 3.4: Internalisation of Ferucarbotran as seen with CLSM

RAW 264.7 cells were incubated with Ferucarbotran fluorescently labelled with Alexa Fluor® 633-hydrazide (shown in green) for 4 hour. The cell membrane was then stained with CellMask® orange (red) before the cells were fixed and the nuclei counterstained with Hoechst 33342 (blue). CLSM showed internalisation of Ferucarbotran by the macrophages. No unspecific background signal was detected in control cells treated with secondary antibodies only (not shown).

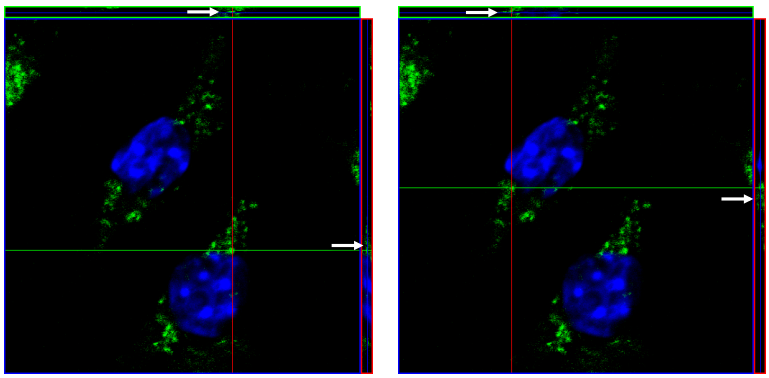

Figure 3.5: Orthogonal views of a Z-series confocal micrograph of RAW 264.7 cells treated with Ferucarbotran.

Ferucarbotran (green) appears to be internalised by the cells (white arrows) as shown in two orthogonal views across the Z-series. Nuclei were counterstained with Hoechst 33342 (blue).

Internalisation of Ferucarbotran was further studied using TEM; this method is well suited to SPIONs analysis as the electron dense iron content of SPIONs facilitates the visualisation of their cores (Figure 3.6). Furthermore X-ray microanalysis on TEM sections can confirm the elemental content of the electron dense aggregates seen inside the cells (Figure 3.8).

TEM showed that Ferucarbotran was indeed internalised by macrophages and appeared as aggregates rather than as single entities. All intracellular nanoparticles detected were in cytoplasmic vesicles and none seen in the nucleus. Low magnification TEM images of macrophages (Figure 3.7) showed nanoparticles in the process of being phagocytosed; invagination of the cell membrane was seen as the cells were engulfing Ferucarbotran aggregates. Some particles were also seen attaching to the extracellular membrane. X-ray microanalysis of unstained TEM slides (Figure 3.8) confirmed the presence of iron in the electron dense aggregates detected inside the macrophages and also differentiated the SPIONs from other electron dense structures seen inside the cells.

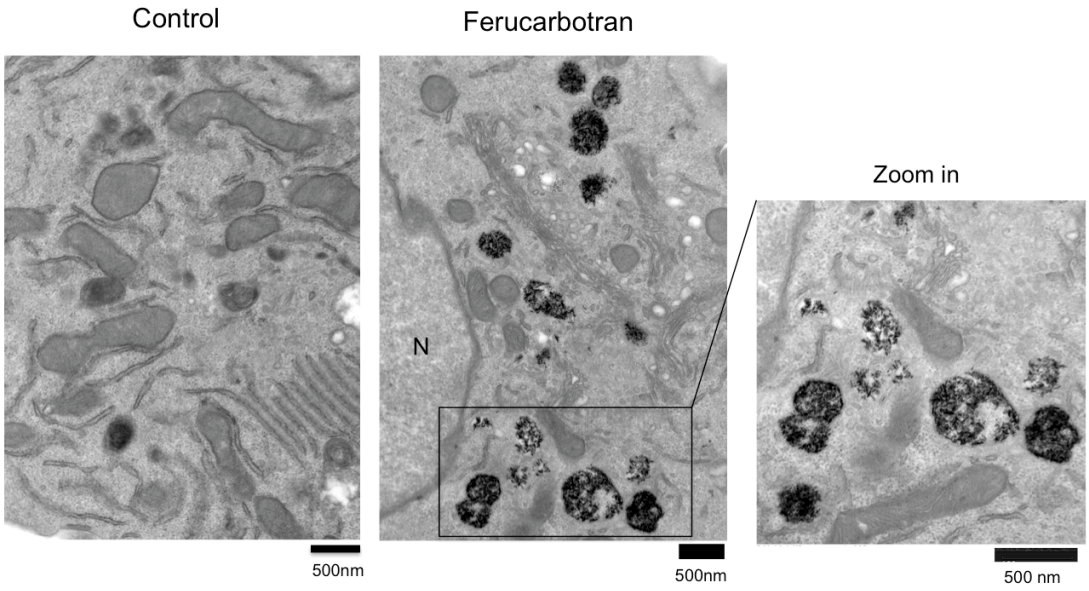

Figure 3.6: TEM images of macrophages (RAW 264.7)

Ferucarbotran was seen inside macrophages as electron dense vesicles in the cytoplasm. No particles were detected in the nucleus (N) or the untreated control.

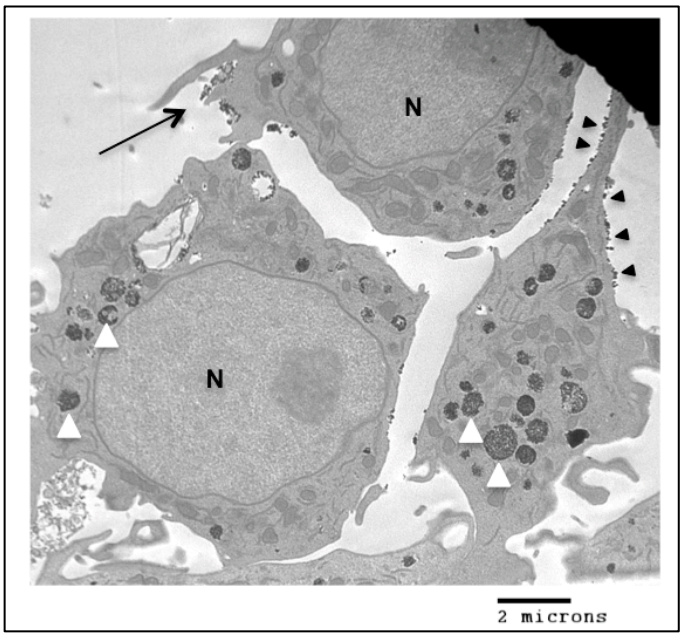

Figure 3.7: TEM micrograph of RAW 264.7 showing phagocytosis

Low magnification TEM image (6000x) showed some nanoparticles being phagocytosed by macrophages (black arrow) while other particles appear on the surface of the cells attached to the outer membrane (black arrow heads). Other particles were internalised and appeared as clusters inside the cells (white arrow heads). Vesicles containing Ferucarbotran were mainly seen in the cytoplasm with none detected in the nucleus (N).

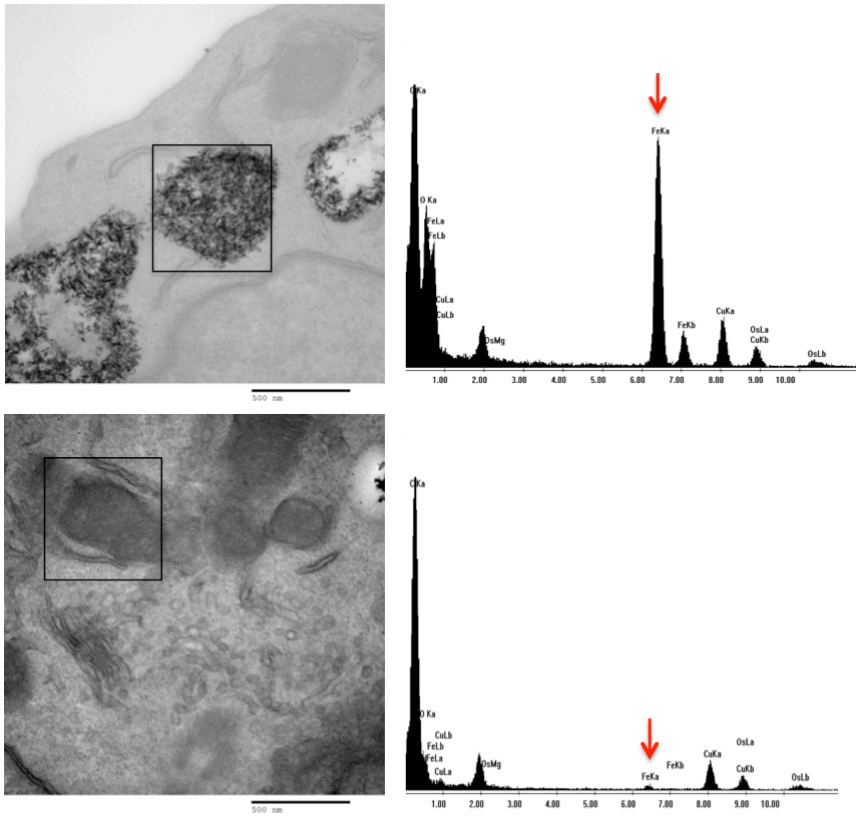

Figure 3.8: X-ray microanalysis on TEM sections of RAW 264.7 cells

To confirm the presence of iron in the aggregates observed inside the macrophages; X-ray microanalysis was used. An iron peak (red arrow, up) was observed in the vesicles containing the rod shaped aggregates compared to no iron peak (red arrow, down) in the other uniformly shaped electron dense vesicles inside the cells that are suspected to be glycogen or lipid storage.

3.2.3 Blocking the uptake of Ferucarbotran by macrophages

Having established the quantitative and qualitative iron assays for SPIONs internalisation, the next step was to investigate the effect of different polysaccharides as potential blockers of Ferucarbotran uptake by cells.

As shown in Figure 3.9, compared to unblocked cells, DSO4 500 followed by DSO4 8 showed the most efficient blocking ability causing 94% (±15) and 89% (±2.55) reduction in the uptake of Ferucarbotran, respectively. J-18 showed a moderate blocking ability with 56% (± 13.2) reduction and finally J-5 caused a slight reduction of 20% (± 12.7) in the iron uptake of cells. On contrast both unsulfated dextrans, D-40 and D-70, surprisingly showed an increase in the uptake of Ferucarbotran by cells.

Results obtained with Prussian blue staining were consistent with the quantitative findings of the ferrozine assay. Ferucarbotran appeared as blue aggregates inside the unblocked cells but no staining was visible in the DSO4 500 treated cells. DSO4 8 and J-18 showed a reduction in the blue aggregates while D-70 appeared similar to the unblocked cells (Figure 3.10).

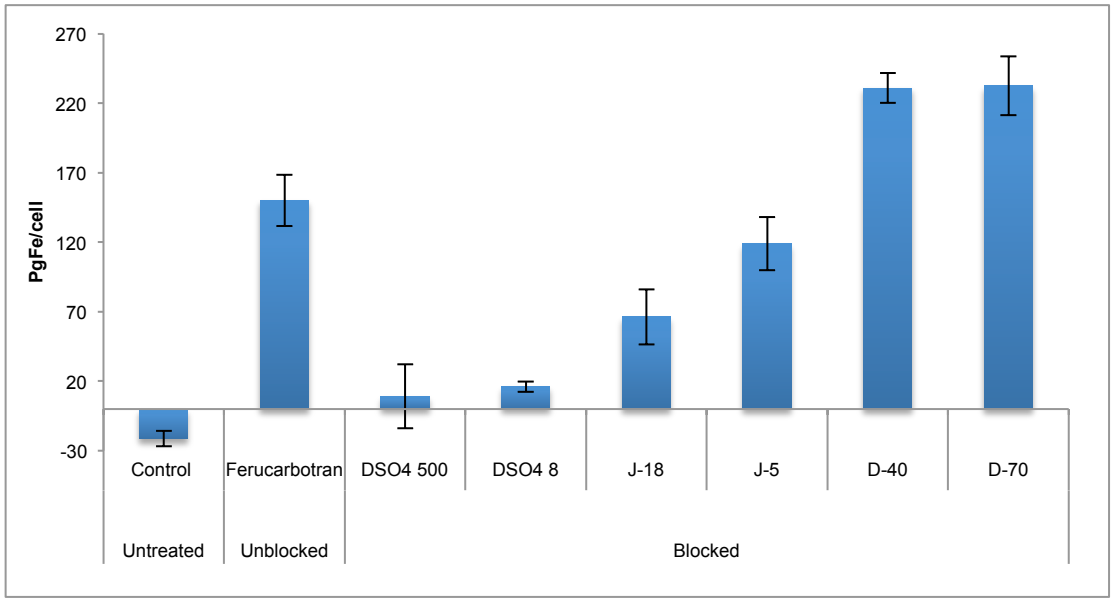

Figure 3.9: Blocking the uptake of Ferucarbotran by RAW 264.7 cells as measured with ferrozine assay

Cells pre-treated with DSO4 500 showed the lowest iron uptake followed by DSO4 8. Both J-18 and J-5 showed small but significant decrease in the uptake of Ferucarbotran by cells. Unsulfated dextrans (D-40 and D-70) caused an unexpected increase in Ferucarbotran uptake. Bars represent the average of readings of 4 wells/treatment and error bars are for standard deviations. All results of blocked compared to unblocked cells were statistically significant ($p<0.05$) as measured by Student's two-tailed unpaired t test.

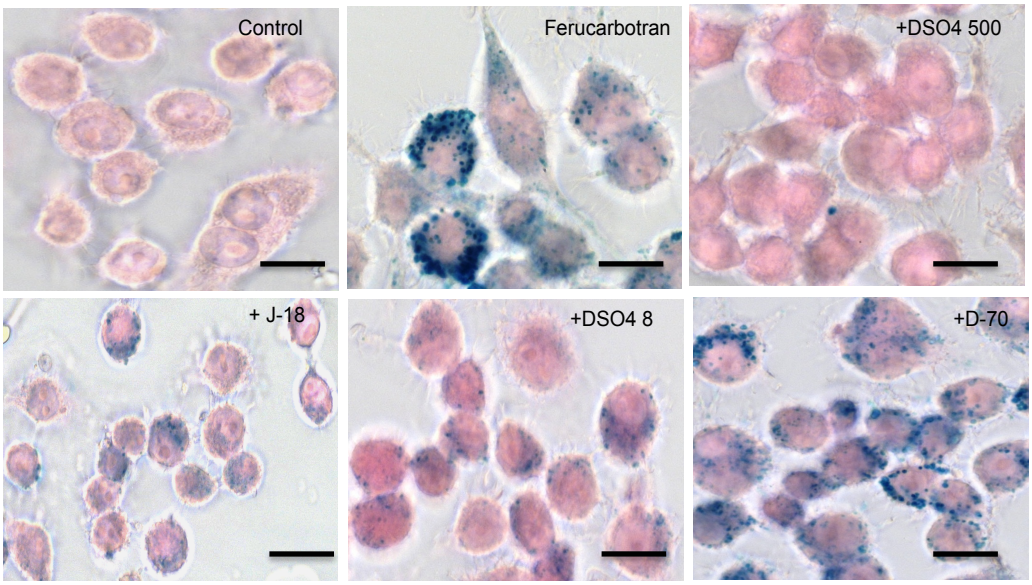

Figure 3.10: Prussian blue staining of RAW 264.7 cell

DSO4 500 caused a marked reduction in the uptake of Ferucarbotran (blue aggregates) by macrophages (top right) while the lower molecular weight dextran sulfates were less effective (bottom left and bottom middle). D-70 (bottom right) did not show any blocking ability, as the uptake of Ferucarbotran was similar to unblocked cells (top middle). Cells were imaged using a 100x oil immersion lens, scale bar=20 μm.

DSO4 500 and J-18 were further investigated at different iron concentrations (Figure 3.11). Macrophages were pre-treated with the blockers before being challenged with 3 different concentrations of Ferucarbotran. Results showed that DSO4 500 caused a dramatic decrease in the uptake of Ferucarbotran by cells at all the tested iron concentrations. While J-18 blocked the uptake to a much lesser extent with the most efficient blocking seen at Ferucarbotran concentration of 0.1 mgFe/ml as a 43.6 % (± 1.7) reduction was observed at this iron concentration compared to 38.6% (±1.3) and 30.2% (±3.7) reduction at 0.5 and 1 mgFe/ml respectively.

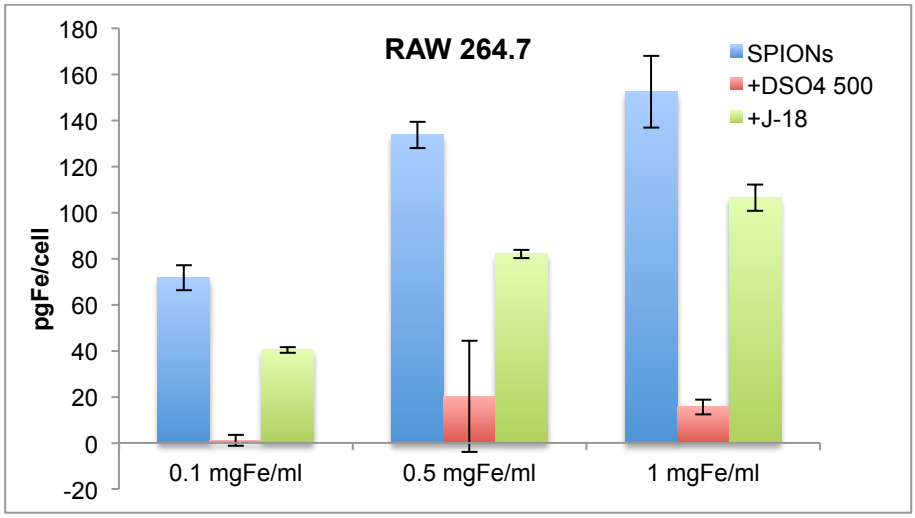

Figure 3.11: Uptake and blocking of 3 different concentrations of Ferucarbotran with DSO4 500 and J-18 on RAW 264.7 cells.

Blue bars represent unblocked cells treated with 3 different concentrations of Ferucarbotran: 0.1, 0.5 and 1 mgFe/ml. An increase in the intracellular iron was observed as the concentration of Ferucarbotran increased as measured with ferrozine assay. On the contrary cells pre-treated with DSO4 500 (red bars) and J-18 (green bars) showed a marked reduction in Ferucarbotran uptake (at all tested concentrations) with DSO4 500 being a more efficient blocker. Bars represent the means of readings of 3 wells/treatment and error bars are for standard deviations. $p<0.001$ of blocked cells compared to unblocked controls.

3.2.4 Uptake of Ferucarbotran by tumour cell lines

Next the interaction of Ferucarbotran with four different tumour cell lines was investigated on: two glioma cell lines (U-87 MG and U-251 MG), a melanoma (A375) and a colorectal carcinoma (LS174T) cell lines.

Following the initial experiments performed on macrophages, DSO4 500 and J-18 were selected to be tested on tumour cell lines because DSO4 500 showed the strongest blocking ability while J-18 represent a clinically approved alternative to DSO4 500. Cells were pre-treated with the blockers before being challenged with three different concentrations of Ferucarbotran.

On all the tested cell lines, there was an increase in the intracellular iron content as the concentration of Ferucarbotran applied on cells increased. Interestingly, DSO4 500 and J-18 were able to block the uptake of Ferucarbotran by cells at all the tested concentrations of Ferucarbotran (see Figure 3.12).

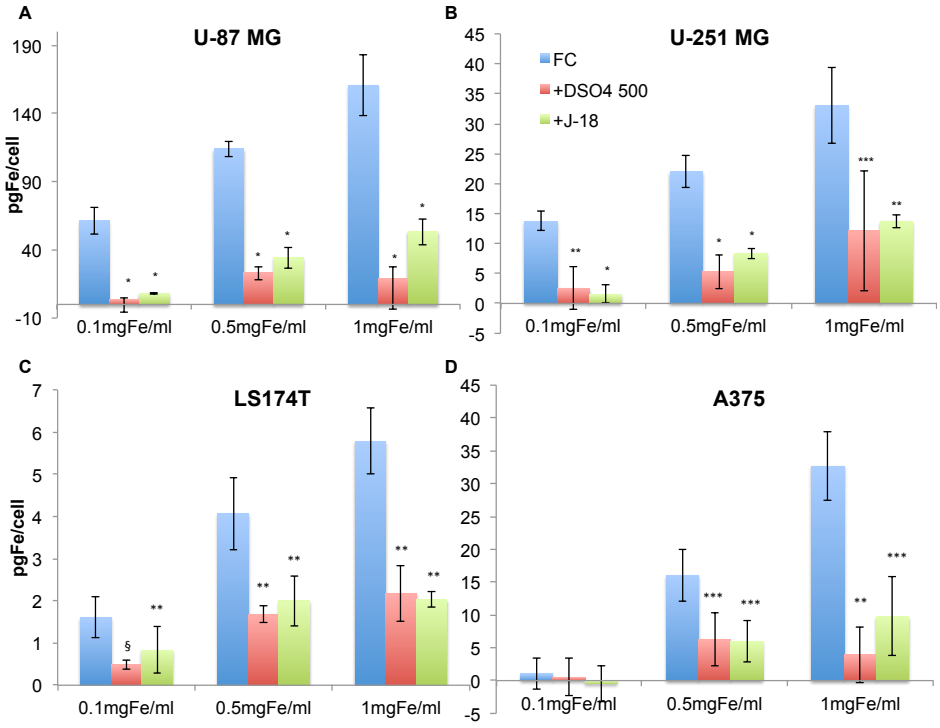

Figure 3.12 Uptake and blocking of Ferucarbotran by different tumour cell lines

All tested cell lines showed an increase in the uptake of Ferucarbotran by cells as the concentration of Ferucarbotran increased (blue bars). While both blockers tested: DSO4 500 (red bars) and J-18 (green bars) decreased the amount of intracellular iron when cells were pre-treated with them. Bars represent the means of readings of 3 wells/treatment and error bars are for standard deviations. Due to the difference in the cell uptake the column graphs have different scaling on the y-axis. *p< 0.0001, **p<0.001, ***p≤0.01 and §p=0.07 as measured with Student's unpaired t test compared to unblocked control.

3.2.5 Internalisation studies on glioma cell lines

One of the most developed areas for the use of SPIONs in hyperthermia therapy has been for glioblastoma (see introduction section 1.8). Therefore, the internalisation of Ferucarbotran by the glioma cell lines was further investigated using CLSM and TEM.

Similar to macrophages, confocal images of glioma cells showed the presence of Ferucarbotran aggregates in the cytoplasm with no nanoparticles detected in the nucleus (Figure 3.13). The images showed that U-87 MG cells tend to accumulate more Ferucarbotran compared to U-251 MG cells; these findings are consistent with the data obtained from the ferrozine assay. Orthogonal views of the confocal images showed the presence of Ferucarbotran inside the cells, nevertheless in U-87 MG some Ferucarbotran appeared to be around the cells either attached to cell debris or the glass slide (Figure 3.13 top right).

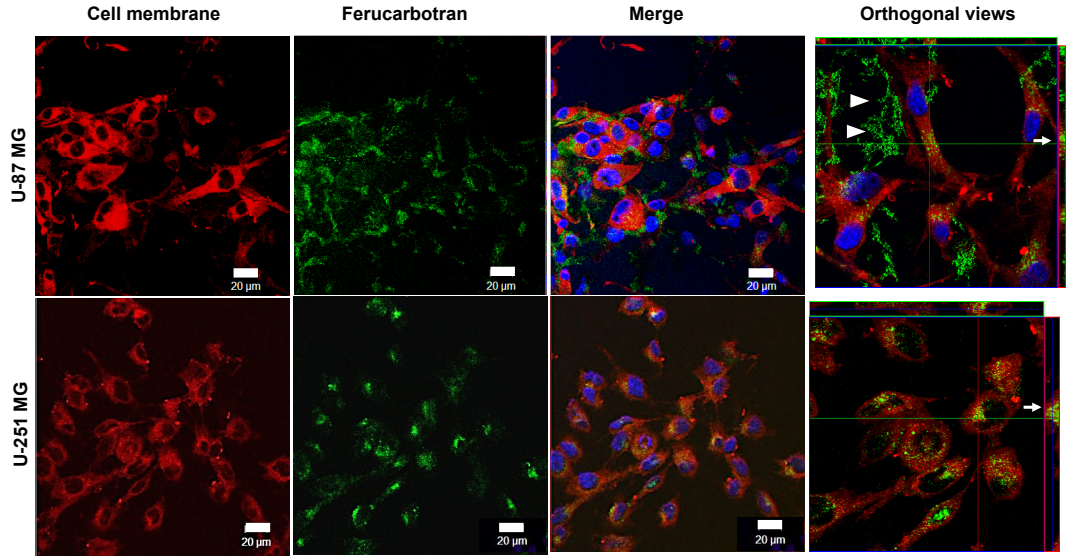

Figure 3.13: CLSM of glioma cell lines

U-87 MG and U-251 MG cells were incubated with Ferucarbotran chemically labelled with Alexa Fluor® 633-hydrazide (shown in green) for 4 hours. The cell membrane was then stained with CellMask® Orange (red) before the cells were fixed and the nuclei counterstained with Hoechst 33342 (blue). CLSM showed internalisation of Ferucarbotran by both cell lines with U-87 MG cells having more Ferucarbotran than U-251 MG. Scale bar =20μm. Orthogonal views (far right) of the Z-stacks showed the presence of Ferucarbotran inside the cells (white arrows) with some particles appearing outside the cells (arrow heads, U-87 MG). No unspecific background signal was detected in control cells treated with secondary antibodies only (not shown).

To further confirm the internalisation of Ferucarbotran by cells, TEM was used to visualise the electron dense nanoparticles inside the gliomas cells. Similar to CLSM, Ferucarbotran was internalised by both glioma cell lines (Figure 3.14 and Figure 3.15). Ferucarbotran appeared as electron dense aggregates seen inside vesicles in the cytoplasm and not in the nucleus. These vesicles containing the aggregates were positive for iron when analysed with X-ray microanalysis, unlike other electron dense structures seen inside the cells.

In summary, ferrozine assay, CLSM and TEM data all confirmed the uptake of Ferucarbotran by the glioma cells lines.

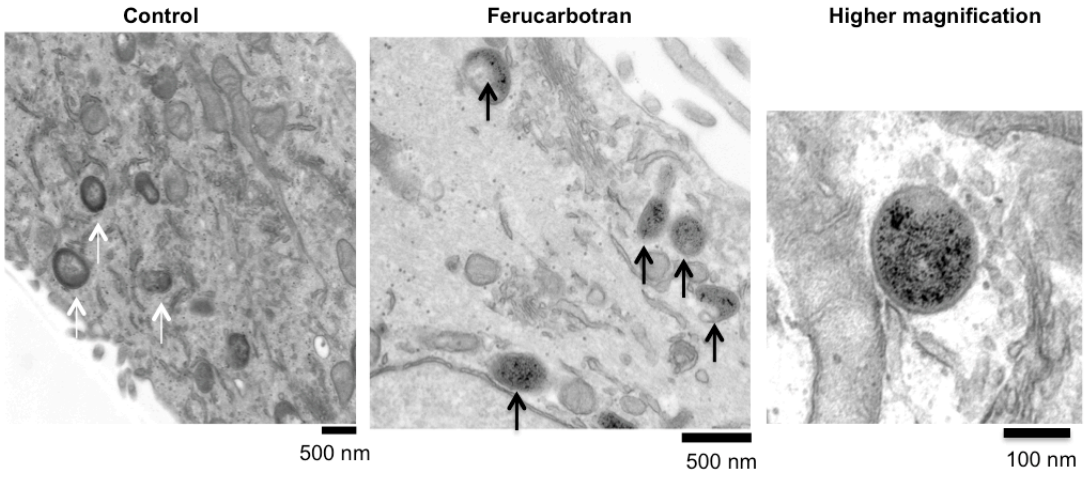

Figure 3.14: TEM micrographs of U-251 MG cells

U-251 MG cells treated with Ferucarbotran showed small black aggregates (black arrows and higher magnification (far right)) of particles inside the cells compared to untreated controls showing morphologically different electron dense vesicles (white arrows) which might be lipid or glycogen vesicles.

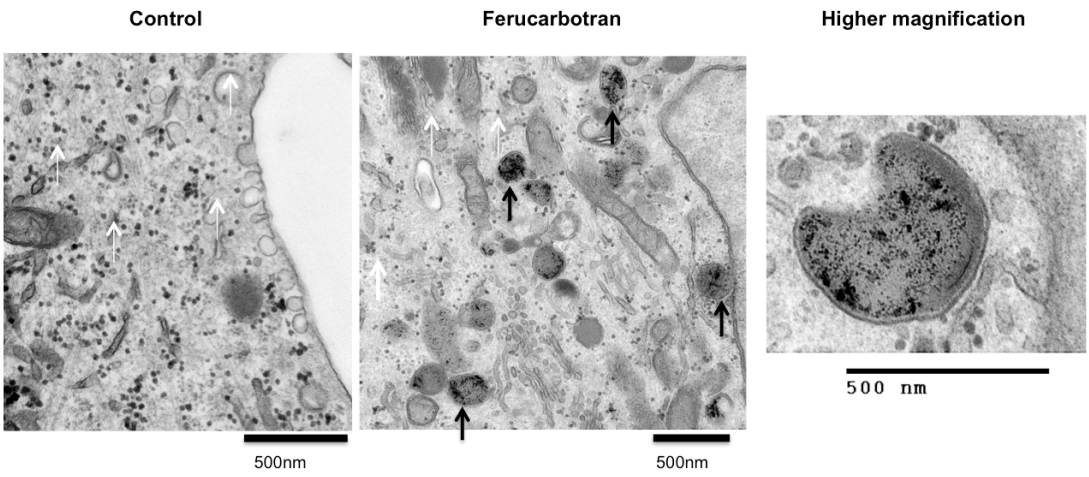

Figure 3.15: TEM micrographs of U-87 MG cells

U-87 MG cells showed a similar pattern to U-251 MG cells; however, Ferucarbotran uptake (black arrows) appears to be more in U-87 MG cells. In the untreated controls and Ferucarbotran treated cells electron dense structures were seen in the cytoplasm (white arrows), which might be ribosomes.

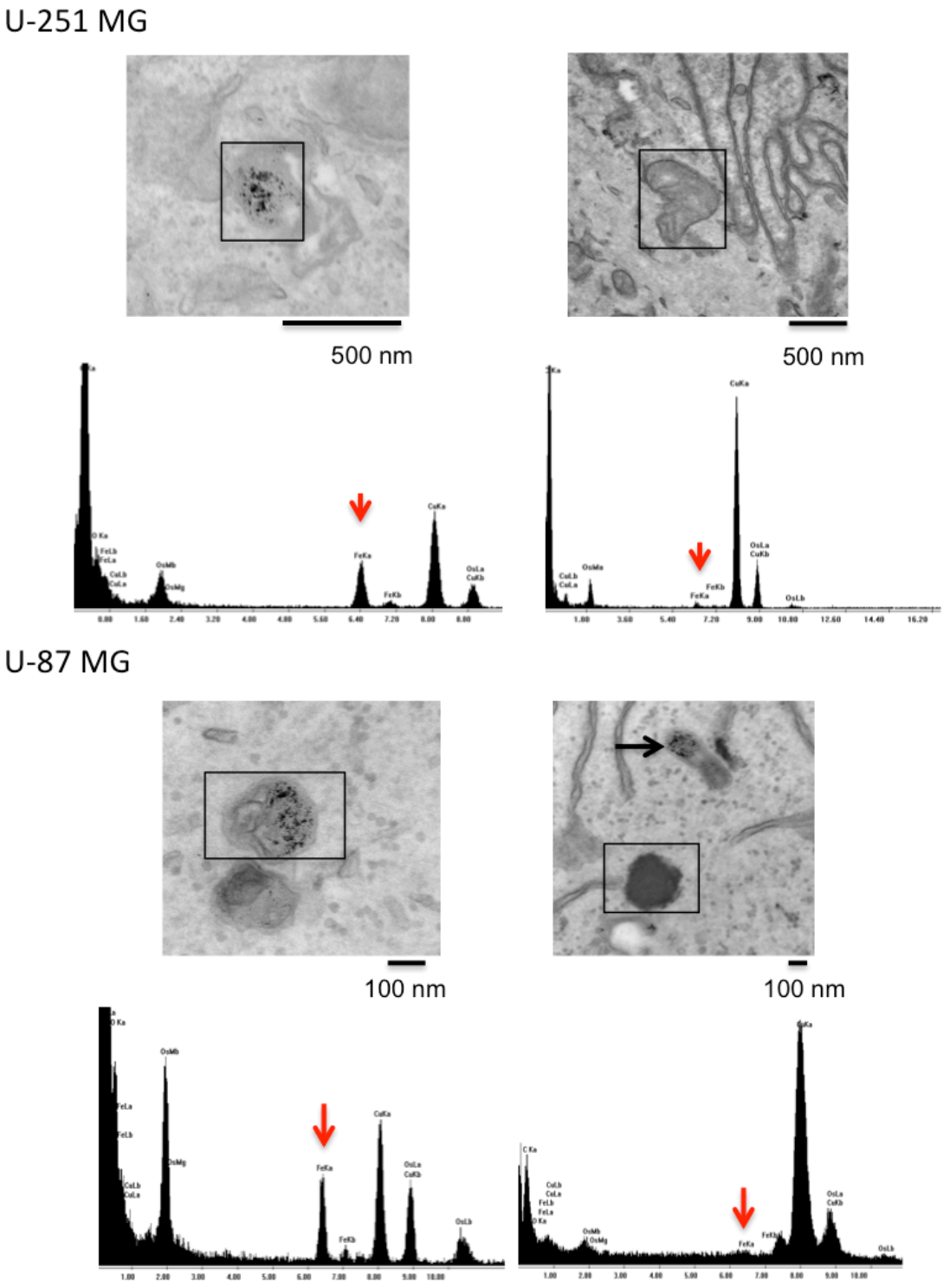

Figure 3.16: X-ray microanalysis of TEM sections of U-87 MG and U-251 MG cells

Both glioma cell lines were tested for the elemental content of the electron dense aggregates, thought to be Ferucarbotran using X-ray microanalysis. The results shown (left) confirm the presence of iron (red arrows) in these aggregates (squares) indicating that these are indeed nanoparticles. Other electron dense areas in the TEM sections were also tested and are shown to be devoid of iron (squared regions right). These areas appear morphologically different from Ferucarbotran vesicles.

3.2.6 Neural stem cells (NSCs)

After investigating the uptake and internalisation of Ferucarbotran by glioma cell lines, the uptake was further evaluated by other cells that might be present within proximity of the glioblastoma microenvironment; of great importance are the normal brain cells. A model that could mimic normal brain cells was achieved by using neural stem cells (NSCs) isolated from mouse brains (Regad *et al*, 2009) (discussed in more details in section 3.1.2). NSCs were differentiated following the protocol described in materials and methods section 2.2.5.1. Briefly, NSCs maintain their stemness and self-renewal properties when cultured in the presence of growth factors (EGF and FGF). To promote differentiation the cells were deprived of these growth factors leading to their transformation into neurons and glial cells. Glial cells then continue differentiation into astrocytes and oligodendrocytes (see Figure 3.17).

To investigate the success of the differentiation protocol, the cells were investigated using CLSM and phase contrast microscopy. Once NSCs start to differentiate into a mixed culture of 3 cell types (neurons, astrocytes and oligodendrocytes); a clear change in their morphology was observed (Figure 3.18). The undifferentiated stem cells appear to have elongated and flattened cell bodies while differentiated cells have smaller nuclei and star-shaped ramifications. Each cell type was detected by immunofluorescence staining for differentiation markers (Olynik & Rastegar, 2012): neuronal βIII tubulin for early neurons; OLIG2 for cells derived from oligodendrocytes lineage and GFAP for astrocytes. As seen in Figure 3.18, both GFAP and neuronal βIII tubulin are structural cytoskeleton protein while OLIG2 is a nuclear protein. Undifferentiated stem cells tested negative for GFAP and βIII tubulin, which were then positive following differentiation to astrocytes and neurons, respectively. The undifferentiated stem cells tested positive for OLIG2 appearing in the elongated nuclei of all the stem cells while following differentiation, a clear change in the morphology of the cells' nuclei could be seen (as they become rounder) with much fewer cells testing positive for the marker.

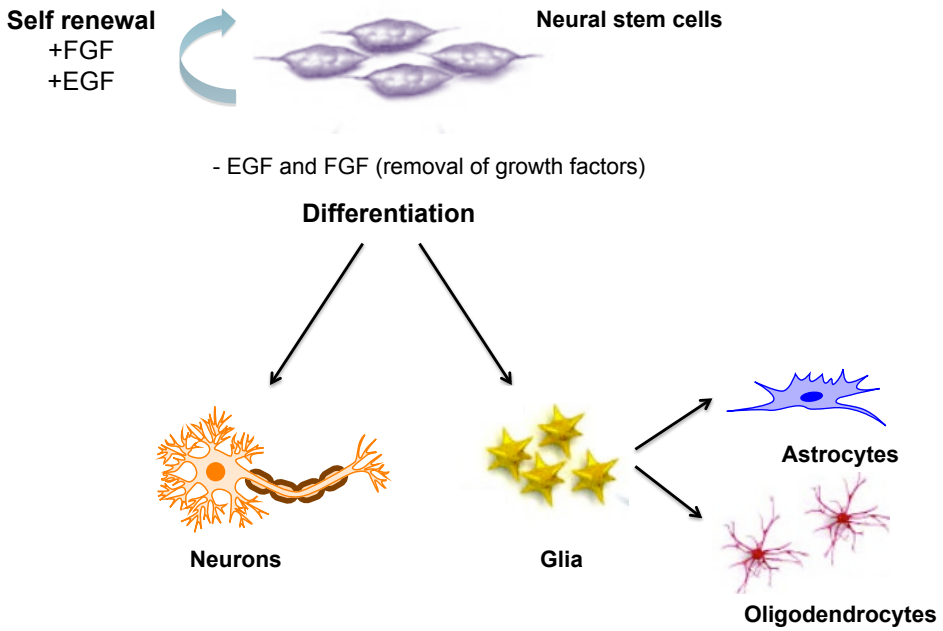

Figure 3.17: Differentiation protocol of NSCs

NSCs maintain their stemness in culture media supplied with growth factors (EGF and FGF), once removed the cells differentiate into neurons, astrocytes and oligodendrocytes.

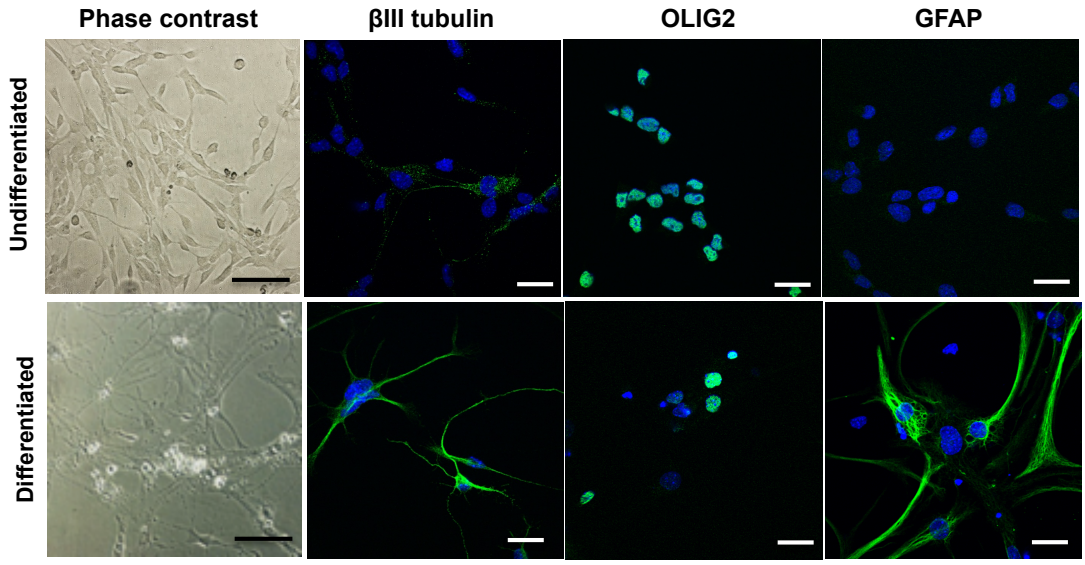

Figure 3.18: Differentiation of Neural Stem cells (NSCs)

After the differentiation protocol a change in the morphology of the cells was observed as seen from the phase contrast images on the far left. Cells were stained for different markers both before and after the differentiation protocol. Undifferentiated cells are positive for OLIG2 only, which is positive in all the cells in the culture before differentiation. While the stem cells are negative for neural βIII tubulin and GFAP, unlike differentiated neuron and astrocytes respectively. Following differentiation, OLIG2 can only be seen in cells derived from the oligodendrocytes lineage. In phase contrast images the scale bar=100 μm, while CLSM images the scale bar=20 μm. In cells treated with secondary antibodies only, no unspecific background signal was detected (not shown).

Following the confirmation of differentiation, differentiated cells were treated with increasing concentrations of Ferucarbotran. Results of these experiments revealed that the differentiated NSCs had a similar pattern of uptake as previously tested cells (macrophages and tumour cell lines). As before there was an increase in the accumulation of intracellular iron as the concentration of Ferucarbotran increased (Figure 3.19 A). Prussian blue staining revealed the presence of blue aggregates inside the cells treated with Ferucarbotran (Figure 3.19 B).

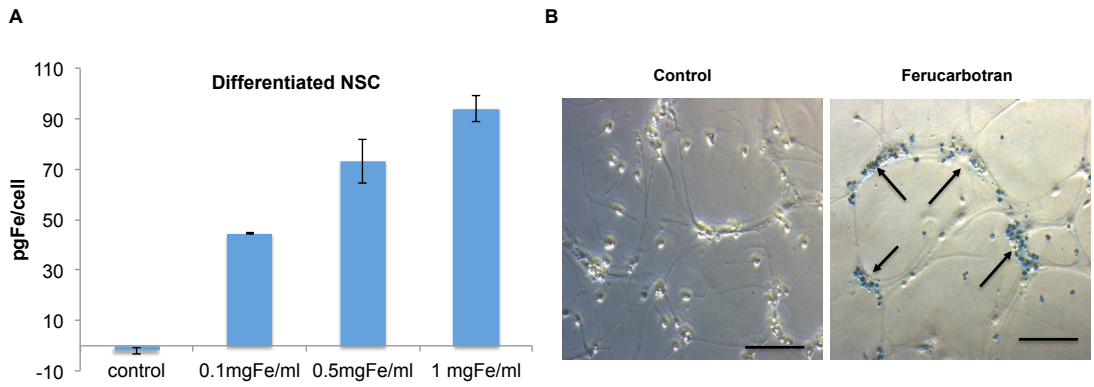

Figure 3.19: Uptake of Ferucarbotran by differentiated Neural Stem cells (NSCs)

A: Ferrozine assay showed an increase in the intracellular iron content as the concentration of Ferucarbotran applied increased ($p<0.0001$ compared to untreated control). **B:** Prussian blue staining of differentiated NSCs. Cells treated with Ferucarbotran at 0.5 mgFe/ml showed the presence of blue aggregates compared to untreated controls. Scale bar=100 μm.

To confirm the internalisation of Ferucarbotran by all the differentiated cells in the mixed culture, immunofluorescence staining was used. Cells were co-stained for Ferucarbotran using anti-dextran antibody and the 3 different neuronal markers (neuronal βIII tubulin, OLIG2 and GFAP). Results shown in Figure 3.20 revealed that Ferucarbotran was internalised by all the cells in the mixed culture (neurons, astrocytes and oligodendrocytes).

It has been observed that once the cells starts differentiation some cell death occur and since the differentiation protocol entails maintaining the cells in the same culture media for 5 days; a lot of cell debris were seen. Extensive washing with PBS did not eliminate the debris suggesting that they either attach to the plastic plates or to live cells. In the CLSM images a lot of cell debris could be observed with Ferucarbotran attaching unspecifically to them (see arrow heads in Figure 3.20).

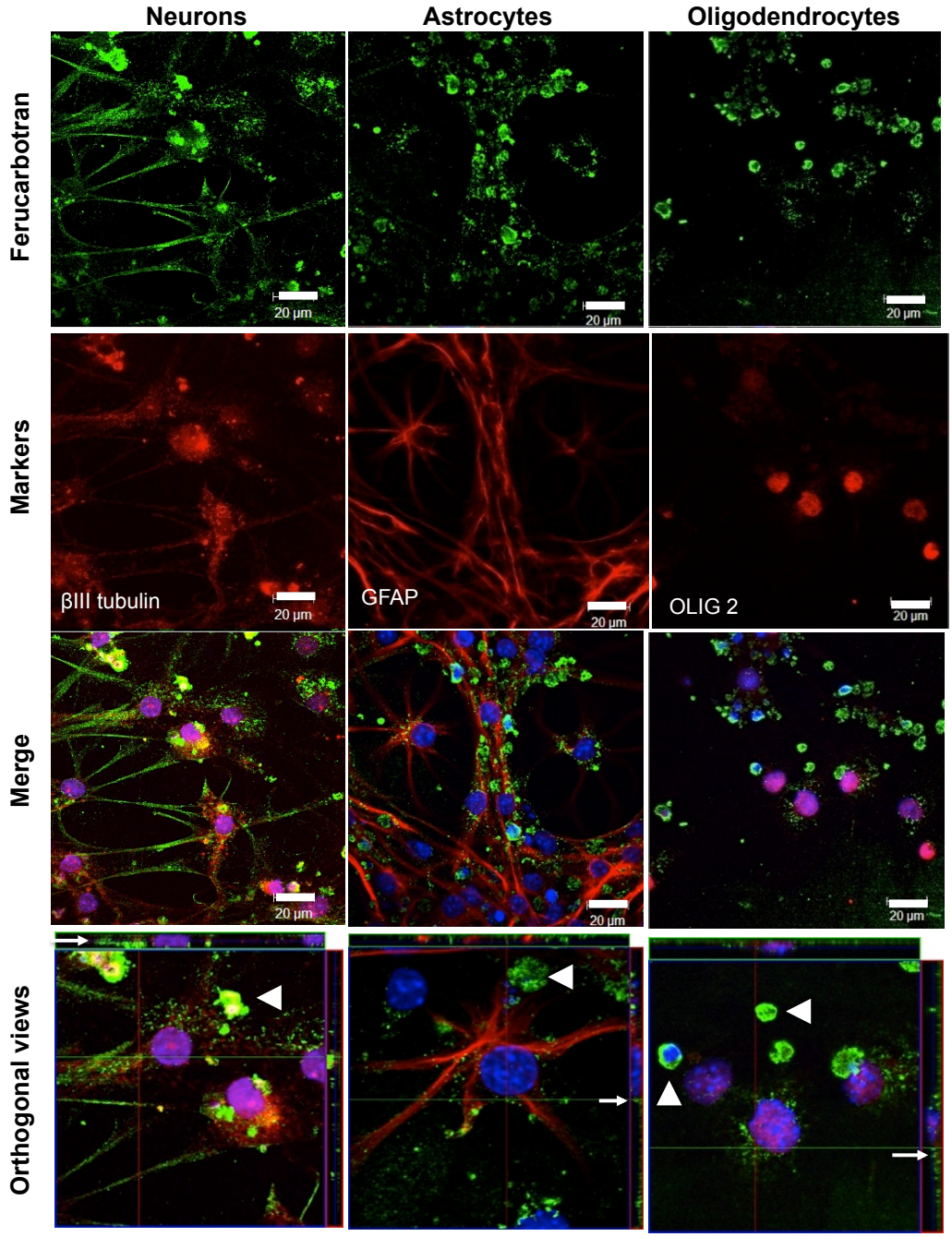

Figure 3.20: CLSM of differentiated NSCs treated with Ferucarbotran

Cells were stained for Ferucarbotran (green) and different neural markers (red): anti-βIII tubulin for neurons, anti-GFAP for astrocytes and anti-OLIG2 for oligodendrocytes. Nuclei were counterstained with Hoechst 33342 (blue). All the neural cells in the mixed culture have internalised Ferucarbotran as shown from the orthogonal views of the Z-series stacks (white arrows). Ferucarbotran appear to attach unspecifically to cell debris as well (arrow heads). Scale bar=20 µm, no unspecific background signal was detected in control cells treated with secondary antibodies only (not shown).

Next, blockers tested on macrophages were also investigated for their ability to reduce the uptake of Ferucarbotran by NSCs. As shown in Figure 3.21, both DSO4 500 and J-18 significantly reduced the intracellular iron levels of Ferucarbotran at all the tested concentrations as investigated with ferrozine assay and Prussian blue staining.

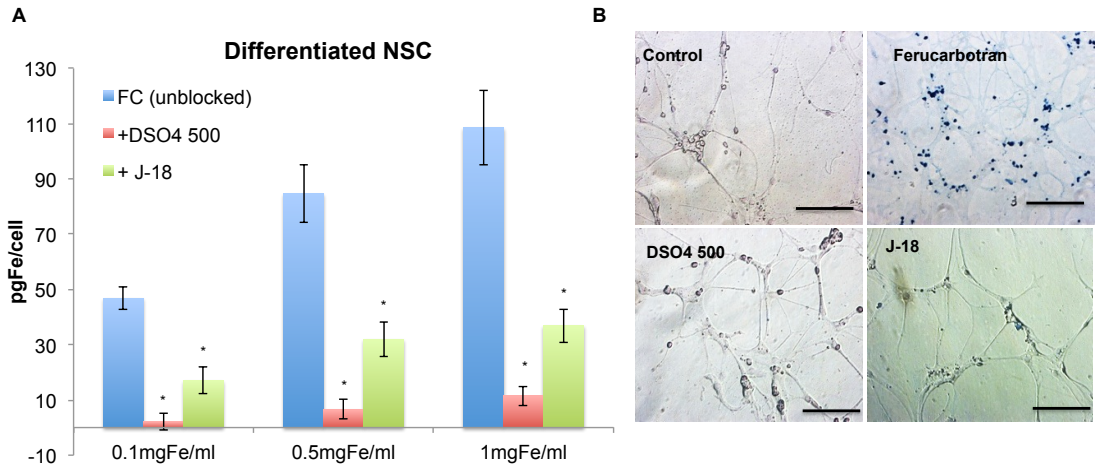

Figure 3.21: Blocking the uptake of Ferucarbotran (FC) by differentiated NSCs

Intracellular iron was detected with ferrozine assay **(A)** and Prussian blue staining **(B)**. Blue bars represent unblocked cells, which show an increase in the intracellular iron as the concentration of Ferucarbotran increased. On the contrary cells pre-treated with DSO4 500 (red bars) and J-18 (green bars) showed a marked reduction in Ferucarbotran uptake (at all tested concentrations) with DSO4 500 being a more efficient blocker. Bars represent the means of readings of 3 wells/treatment for 3 independent experiments and error bars are for standard deviations, *p<0.0001 compared to unblocked cells. **B:** Prussian blue staining showed similar findings with a marked reduction in the blue aggregates (Ferucarbotran) in the cells pre-treated with DSO4 500 and J-18. Cells were imaged with 20x phase contrast lens, scale bar=100 μm.

3.2.7 PrestoBlue™ cell viability assay

To investigate whether Ferucarbotran or the blockers (DSO4 500 and J-18) might induce cell death, PrestoBlue™ cell viability assay was used. Three cell lines (RAW 264.7, U-87 MG and U-251 MG cells) were used as a preliminary platform to develop the assay.

The assay was done to ensure that the concentrations of both Ferucarbotran and the blockers used were not toxic to cells. Concentrations tested started at 10 times higher than the ones used in the blocking experiments: Ferucarbotran (0.02 mgFe/ml to 10 mgFe/ml), DSO4 500 (0.59 to 300 μg/ml) and J-18 (0.02 mg/ml to 10 mg/ml). Incubations were done for four hours to mimic the uptake and blocking experiments.

Both DSO4 500 and J-18 did not affect the cell viability of the investigated cell lines at any of the concentrations tested when compared to PBS treated cells. Similarly Ferucarbotran treated tumour cells (U-251 MG and U-87 MG) showed no reduction in cell viability except with U-251 MG cells where a 20% reduction was observed at the highest tested Ferucarbotran concentration (10 mgFe/ml). RAW 264.7 cells also showed a 30% reduction in cell viability at Ferucarbotran concentrations of 5 and 10 mgFe/ml.

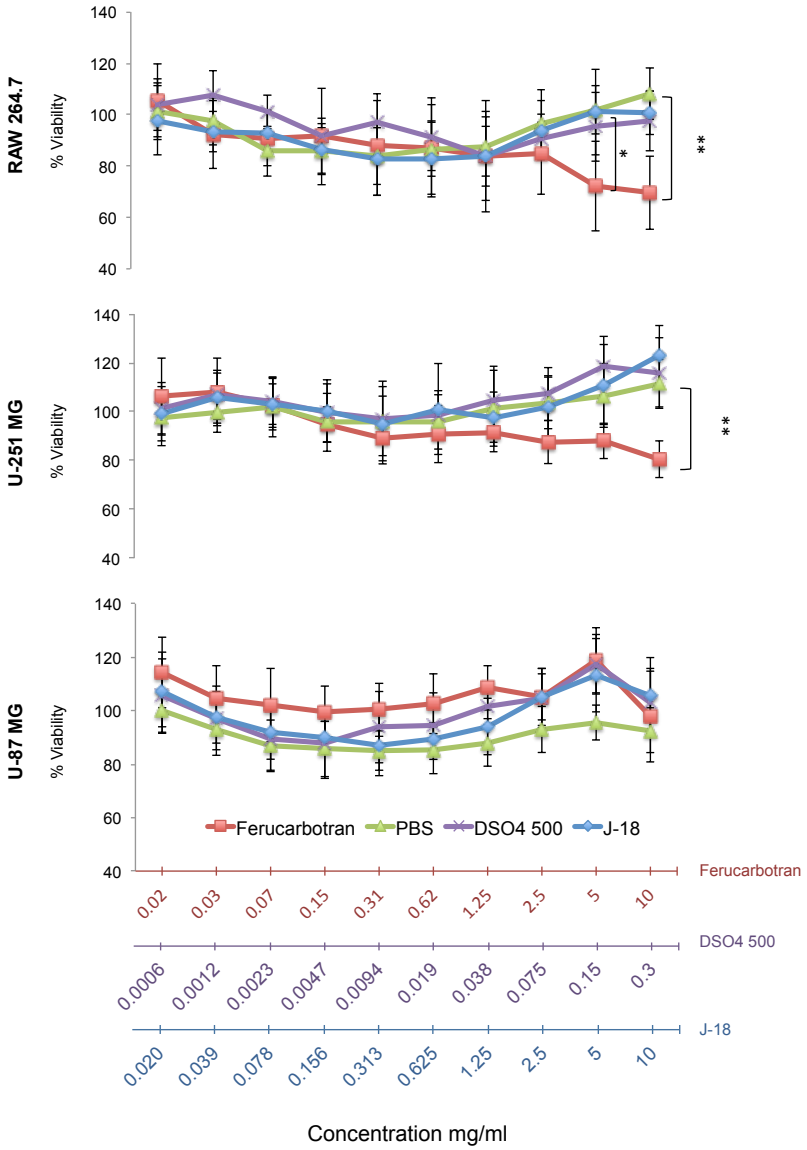

Figure 3.22: PrestoBlue™ cell viability assay

Three cell lines (RAW 264.7, U-251 MG and U-87 MG cells) were incubated with Ferucarbotran (0.02 mgFe/ml to 10 mgFe/ml, red scale), DSO4 500 (0.59 to 300 μg/ml, purple scale) and J-18 (0.02 to 10 mg/m, blue scale) for 4 hours. No clear effect on the percentage cell viability was observed under the tested condition except with RAW 264.7 cells (top) where a reduction of ~30% in cell viability was observed at 5 and 10 mgFe/ml. U-251 MG cells also showed a reduction of ~20% in cell viability at 10 mgFe/ml. *p= 0.0005 and **p < 0.000007. Each point represents the means of readings of 3 wells/treatment for 3 independent experiments and error bars are for standard deviations.

3.2.8 Fucoidan as a blocker

Although DSO4 500 was shown to be a very efficient blocker, it has not been used clinically. Consequently a known ligand for scavenger receptors A and a food supplement, namely fucoidan, was introduced in the project. Fucoidan was investigated in preliminary proof-of-concept experiments on macrophages and a glioma cell line (U-251 MG).

RAW 264.7 murine macrophages were pre-treated with fucoidan at 3 different concentrations: 30, 50 and 100 µg/ml followed by Ferucarbotran at 0.1, 0.5 and 1 mgFe/ml. Cells pre-treated with fucoidan showed significant reduction in the uptake of Ferucarbotran at all tested conditions (Figure 3.23 Top). Furthermore, when fucoidan was compared to a similar concentration of DSO4 500 (30 µg/ml), fucoidan appears to have slightly less blocking ability; nevertheless, the uptake of Ferucarbotran by macrophages is significantly reduced with both blockers (Figure 3.23 Bottom).

Next, fucoidan was tested for its ability to block the unspecific uptake of Ferucarbotran by a glioma cell line (U-251 MG). Similar to the results discussed above; fucoidan decreased the uptake of Ferucarbotran by U-251 MG cells but to a lesser extent than DSO4 500 (Figure 3.24).

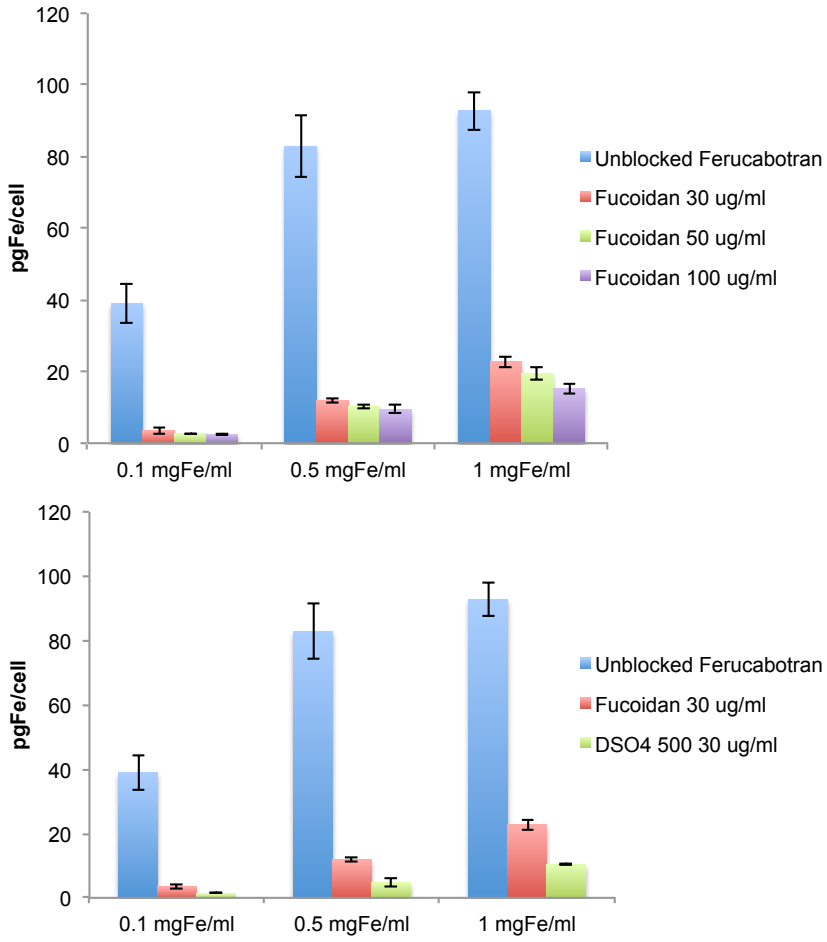

Figure 3.23: Blocking the uptake of Ferucarbotran by RAW 264.7 using fucoidan

Top: Macrophages were pre-treated with three different concentrations of both fucoidan and Ferucarbotran and the intracellular iron was detected using ferrozine assay. Macrophages pre-treated with fucoidan showed a significantly ($p<0.001$ for all blocked compared to unblocked) lower uptake of Ferucarbotran at all the tested concentrations of the blocker and with different concentrations of Ferucarbotran. **Bottom:** Fucoidan and DSO4 500 were tested at equal concentrations of 30 μg/ml before the cells were challenged with 3 different concentrations of Ferucarbotran. Both blockers caused significant reduction in the uptake of Ferucarbotran by cells with DSO4 500 showing a slightly better blocking ability. Bars represent the means of readings of 3 wells/treatment and error bars are for standard deviations.

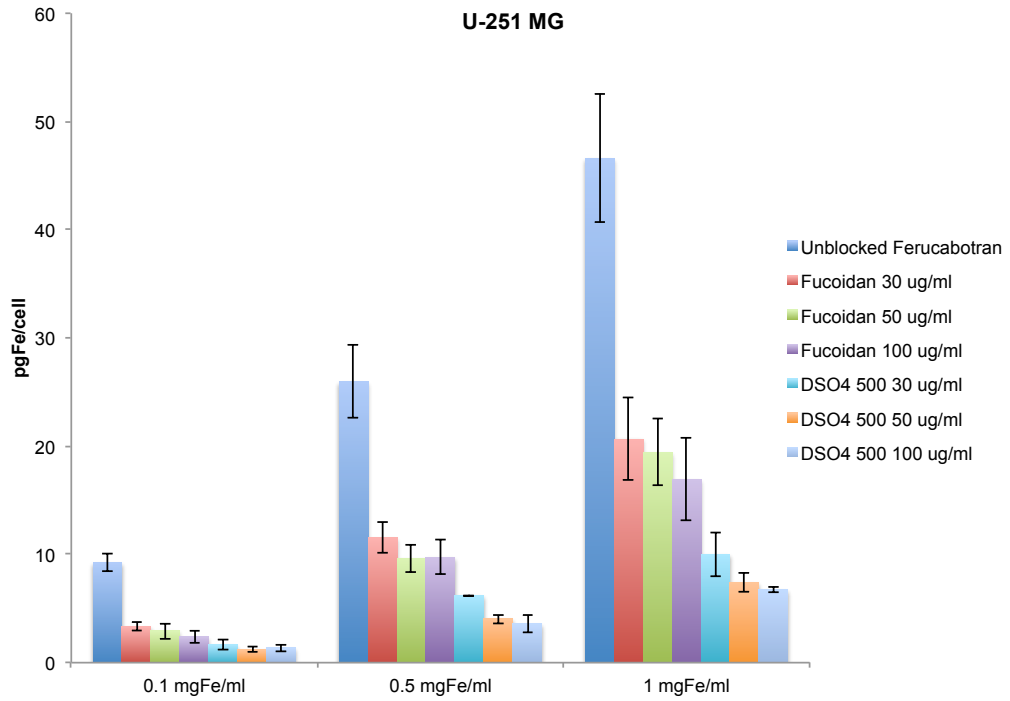

Figure 3.24: Effect of fucoidan on the uptake of Ferucarbotran by U-251 MG cells

Cells were pre-treated with 3 different concentrations of Fucoidan and DSO4 500. Both blockers reduced the unspecific uptake of Ferucarbotran by cells at all tested concentrations of Ferucarbotran and the blockers. DSO4 500 appears to be more efficient than fucoidan. $p<0.003$ for all blocked compared to unblocked control. Bars represent the means of readings of 3 wells/treatment and error bars are for standard deviations.

3.3 Discussion

The work presented in this chapter investigated one of the central hypotheses of this thesis: the rapid clearance of SPIONs by the RES could be blocked using polysaccharide derivatives.

RAW 264.7 murine macrophages were studied first and consistent with previous published reports (Hsiao *et al*, 2008; Yang *et al*, 2011), these cells showed concentration dependent uptake of Ferucarbotran. Internalisation was confirmed with TEM and CLSM where Ferucarbotran was observed in cytoplasmic endocytic vesicles with no localisation in the nucleus. In addition to published reports the work presented here utilised X-ray microanalysis to confirm that the observed electron dense aggregates in macrophages treated with Ferucarbotran were indeed iron oxide nanoparticles.

Macrophages pre-treated with scavenger receptor A blockers, DSO4 500 and fucoidan, showed a significant decrease in the uptake of Ferucarbotran unlike the results observed with unsulfated dextrans (D-40 and D-70). These results are consistent with published literature reporting the blocking effect of DSO4 500 (Sonia *et al*, 2009) and fucoidan (Segers *et al*, 2013) and the lack of an inhibitory effect by unsulfated dextrans (Chao *et al*, 2012a) on the uptake of SPIONs by macrophages.

Other investigated blockers in chapter 3 were low molecular weight dextran sulfates (DSO4 8, J-5 and J-18); these agents were not reported as RES blockers before. Results showed that DSO4 8 and J-18 blocked the uptake of Ferucarbotran by macrophages with J-5 showing a small blocking effect. Although the blocking effect was not as effective as DSO4 500 suggesting that the molecular weight affects the blocking ability of dextran sulfates.

Tumour cell lines tested also showed an increase in the accumulation of Ferucarbotran proportional to the concentration applied in a similar pattern to that observed with macrophages and also consistent with published reports (Mailänder *et al*, 2008; Sun *et al*, 2005). Further internalisation studies using TEM and CLSM were performed on glioma cells confirming the presence of iron oxide vesicles in the cytoplasm. Furthermore, the effect of the polysaccharide blockers was evaluated on tumour cells. Despite the absence of reports recording the expression of scavenger receptor A on tumour cells, the blockers significantly reduced the uptake of

Ferucarbotran by cells. This effect has not been reported before which represents an interesting novel finding.

The uptake of SPIONs by non-RES cells has been previously investigated in various cell tracking and homing studies. SPIONs can be used to magnetically label cells either *in vitro* or *in vivo* owing to their unique magnetic properties (Mailänder *et al*, 2008; Wilhelm *et al*, 2003). MRI can then be used to image and track the homing of labelled cells *in vivo* (Mailänder *et al*, 2008). However, most of these studies utilised transfection agents and/or targeting agents or small peptides (e.g. protamine, PLL (poly-L-lysine) or HIV-Tat peptide) to increase the uptake of SPIONs by cells (Golovko *et al*, 2010; Lewin *et al*, 2000; Mailänder *et al*, 2008; Wilhelm *et al*, 2003). Nonetheless, these transfection agents are not suitable for use in humans and might have toxic effects on cells (Mailänder *et al*, 2008). The use of targeting strategies might also affect the biological function of cells (Sun *et al*, 2005) as well as affect the stability and overall charge of SPIONs altering their properties and behaviour. Therefore studying the uptake of unmodified SPIONs by non-RES cells becomes crucial, as it is a poorly investigated area.

Similar to the findings presented in this chapter, Mailänder *et al* found that the uptake of formulated Ferucarbotran (Resovist®) is possible by cells without the need for a transfection agent. They investigated the uptake of Resovist® and Feridex® in mesenchymal stem cells (MSCs) and HeLa cells and found that Ferucarbotran was being readily taken up by both cell lines in a significantly higher dose dependent manner compared to Feridex® (Mailänder *et al*, 2008). They accounted the difference in uptake to the negatively charged carboxydextran coat of Resovist® unlike the neutral dextran coat of Feridex®. Similar findings were also reported by Sun *et al,* their work compared the uptake of SPIONs (Resovist®) to USPIO (SHU 555C) by human fibroblasts, immortalized rat progenitor cells and HEP-G2 hepatocellular carcinoma cells. They found that the cell lines tested had a higher capacity to accumulate SPIONs (Resovist®) more efficiently than USPIOs (Sun *et al*, 2005). However, in both mentioned studies, they investigated the commercially formulated product (Resovist®) rather than the active ingredient (Ferucarbotran), the presence of excipients in Resovist® formulation (e.g. mannitol, lactic acid and sodium hydroxide (Schering, 2002)) might affect the way the cells interact with the nanoparticles, therefore, their data should be interpreted cautiously.

Similar to Resovist®, unformulated Ferucarbotran (studied in this chapter) is coated with carboxydextran; the presence of carboxylic groups on the surface of the particles renders them negatively charged (-25.7 mV) at physiological pH (Abdollah *et al*, 2014; Mailänder *et al*, 2008). The surface charge of SPIONs determines their behaviour and the way they interact with cells as previously discussed in the introduction section 1.4.1.2. The uptake of Ferucarbotran by tumour cell lines can therefore be accounted to its overall negative charge. It has been shown before that anionic SPIONs interact with the positively charged regions on the cell membrane and become internalised by fluid-phase endocytosis (Vigor *et al*, 2010; Wilhelm *et al*, 2003). Nevertheless, very little is understood regarding these processes (Jordan *et al*, 1999). In addition the blocking effects observed in this chapter with negatively charged sulfated polysaccharides (DSO4 500, J-18 and fucoidan) has not been reported before and could be due to the competition of the blockers with Ferucarbotran at the sites of internalisation leading to a decrease in the unspecific uptake of Ferucarbotran by cells.

Next, the uptake of Ferucarbotran was evaluated on neurons, astrocytes and oligodendrocytes derived from differentiated NSCs. Ferrozine assay, Prussian blue staining and CLSM showed that Ferucarbotran is taken up and internalised by the differentiated neural cells, furthermore this was blocked using DSO4 500 and J-18. The cell uptake findings are similar to the work of Politi *et al* where Resovist® has been used to label neural stem/precursor cells (NPCs) in order to track their homing *in vivo* in mice using MRI (Politi *et al*, 2007); NPCs were labelled *ex vivo* with Endorem® (Feridex®) and Resovist®. Similar to finding by Mailänder *et al* discussed previously (Mailänder *et al*, 2008), Resovist® was able to label the cells without the need for a transfection agent while Endorem® conjugated to PLL showed a significantly higher uptake by cells (Politi *et al*, 2007). Nevertheless, the uptake of Ferucarbotran by the differentiated cells (neurons, astrocytes and oligodendrocytes) was not reported before.

The expression of scavenger receptors in neural glial cells has been studied extensively due to their role in inflammatory responses associated with neurodegenerative diseases (e.g. Alzheimer's disease) (Alarcón *et al*, 2005). Some reports have mentioned that scavenger receptor A is mainly expressed in microglial cells (brain macrophages) with astrocytes mainly expressing scavenger receptor class B (Alarcón *et al*, 2005). However, more recent studies have reported the expression of scavenger receptor A in astrocytes extracted from rat brains and are

believed to play a critical role during neuroinflammatory processes (Godoy *et al*, 2012; Murgas *et al*, 2014). Therefore the uptake of Ferucarbotran by astrocytes might be mediated via these receptors. Furthermore, the blocking effect observed with DSO4 500 and J-18 could be accounted to competitive blockage of scavenger receptors on astrocytes. In contrasts, no data is available on the expression of scavenger receptor A on neurons and oligodendrocytes. Thus the uptake of Ferucarbotran might be accounted to unspecific uptake mechanisms similar to the results observed with tumour cells.

3.4 Summary and conclusions

The work presented in this chapter was investigating the hypothesis that polysaccharide derivatives could block the unwanted uptake of Ferucarbotran by cells. Four main research aims were proposed all of which were fulfilled: (i) quantitative and qualitative iron assays were developed to assess the intracellular iron uptake of Ferucarbotran; (ii) a number of cell lines were investigated (macrophages, tumour and non-tumour cell lines) for their ability to take up and internalise Ferucarbotran; (iii) seven different polysaccharides were investigated for their ability to block the uptake of Ferucarbotran by macrophages and finally (iv) a model mimicking normal brain cells was developed to investigate the interaction of Ferucarbotran with non-tumour cells. All tested cell lines have successfully taken up Ferucarbotran and interestingly sulfated polysaccharides (e.g. DSO4 500, J-18 and fucoidan) were able to reduce the cellular internalisation of SPIONs regardless of the cell type, proving the hypothesis.

In conclusion, the work presented here showed some novel and crucial findings regarding the cellular interactions of Ferucarbotran with macrophages and components of the tumour microenvironment. The use of pharmaceutical agents as blockers, if proved successful *in vivo*, will provide a safe approach to evade the RES and consequently a better prospective for clinical development. The anti-hyperlipidemic drug (J-18), that has not been investigated before as a potential RES blocker, and the food supplement (fucoidan) showed a promising blocking effect *in vitro*. Furthermore the effect of the blockers on the uptake of SPIONs by tumour cells and NSCs have not been previously reported which might be a crucial finding that will affect the use of Ferucarbotran together with the blockers.

Chapter 4
Prolonging the Circulatory Retention of SPIONs

Maha Abdollah

4.1 Introduction

The work presented in chapter 3 with the RAW 264.7 cell model established that it is possible to reduce the uptake of Ferucarbotran by macrophages *in vitro* using polysaccharide derivatives. Work in the current chapter was designed to investigate if the blockers would perform to block Ferucarbotran uptake by the RES in the more complex *in vivo* environment. SPIONs are usually rapidly cleared by the RES leading to very short half-lives (see Figure 4.1 and sections 1.3.1.2 and 1.6.3). Therefore, a successful outcome of RES blocking would be to prolong the circulatory retention of SPIONs.

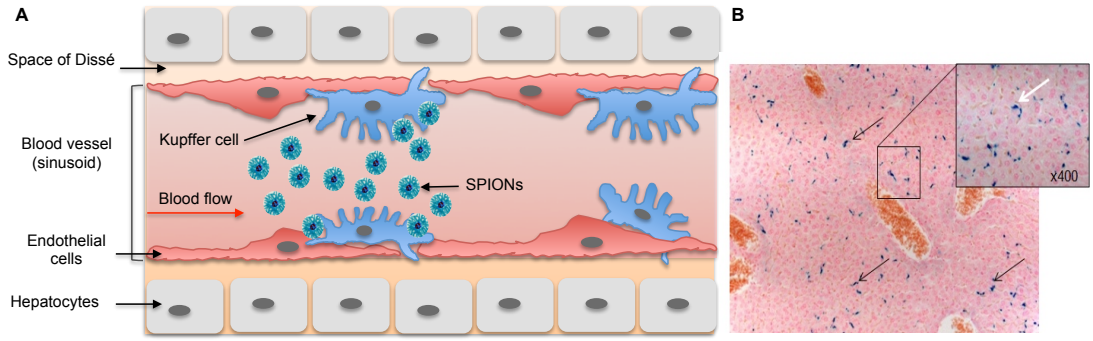

Figure 4.1: Uptake of SPIONs by liver Kupffer cells

A: Kupffer cells are specialised phagocytic cells lining the endothelium of liver sinusoids that have the ability to rapidly internalise SPIONs as they pass through the liver blood vessels. **B:** Prussian blue staining of a liver histology section of a mouse treated with 100 μmolFe/kg showing Ferucarbotran (blue aggregates, black arrows) internalised by Kupffer cells (white arrow).

4.1.1 Experimental approach

Approaches developed to measure circulatory retention of SPIONs are outlined below: first, methods were established to conjugate SPIONs to NIR dyes. Second, an experimental BALB/c mouse model (Figure 4.2) was developed for quantitative measurement of the SPIONs blood levels. Results from these experiments were used to select the lead *in vivo* blocker. Finally, for more comprehensive evaluation of the lead blocker, the SPIONs' core was radiolabelled (De Rosales *et al*, 2009; de Rosales *et al*, 2011) allowing SPECT/CT imaging to measure the biodistribution of Ferucarbotran in different organs.

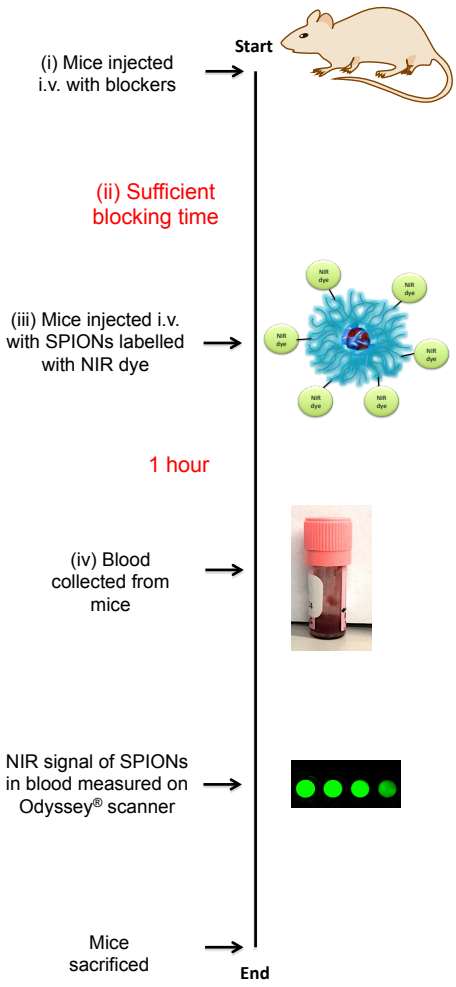

Figure 4.2: Experimental design of the *in vivo* blocking experiments

(i) A blocker was injected intravenously. (ii) A blocking period was allowed ranging from 0 to 24 hours depending on the blocker investigated. (iii) NIR dye-labelled SPIONs were injected intravenously. (iv) One hour following SPIONs injection, blood was collected from mice and measured on Odyssey® scanner.

4.1.2 Research Aims and Objectives

Aim: To develop a system to increase the circulatory retention of Ferucarbotran.

Objectives:

- To develop chemical conjugation strategies to link SPIONs to near infrared (NIR) dyes.
- Evaluate the colloidal stability and characterize NIR-labelled SPIONs using visual inspection, DLS and TEM measurements.
- Investigate the blocking effect of different polysaccharide derivatives *in vivo* as potential RES blockers.
- Use SPECT/CT imaging to measure the effect of the lead RES blocker on the biodistribution of Ferucarbotran *in vivo*.

4.2 Results

4.2.1 Conjugation of Nanomag-D-spio-NH_2 (NM) to DyLight® 800

First, a commercially available SPION was investigated. Nanomag®-D-spio-NH_2 (NM) are dextran coated amine functionalised SPIONs with hydrodynamic diameter in the range of 50-120 nm (Table 2.9). NIR labelled NM was used to establish the *in vivo* experimental conditions for SPIONs measurement in blood because the surface amine (NH_2) groups are available for conjugation to NHS ester dyes (DyLight® 800 NHS ester) in a simple and efficient reaction (Figure 4.3).

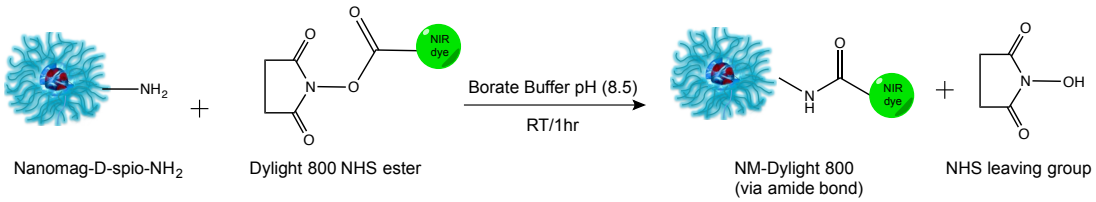

Figure 4.3: Schematic presentation of the chemical reaction between Nanomag-D-spio-NH2 (NM) and DyLight® 800 NHS ester NIR dye.

The NHS ester group available on the NIR dye attacks the amine groups on the dextran coat of NM. The reaction proceeded for 1 hour at RT in 50 mM sodium borate buffer.

Following the conjugation reaction, serial dilutions of the conjugates were measured on the Odyssey® NIR scanner to check the success of the labelling. A linear increase in the signal intensity was observed as the iron concentration increased (Figure 4.4). Results showed that a high fluorescence signal could be detected for concentrations as low as 0.11 μgFe/ml indicating a very efficient conjugation reaction.

The colloidal stability of the dye labelled SPIONs was investigated. Visual inspection revealed no apparent precipitations or changes in the physical appearance. DLS measurements were performed to further confirm the stability. Only minor changes in the Z-average hydrodynamic diameter and the polydispersity index (PDI) were observed before and after conjugation (Table 4.1). TEM was used to examine the iron oxide cores of SPIONs; no apparent changes were observed following the conjugation (Figure 4.5). NM SPIONs appeared highly crystalline with average core size of 6.019 (±1.82) nm in diameter ((Abdollah *et al*, 2014), Appendix 5).

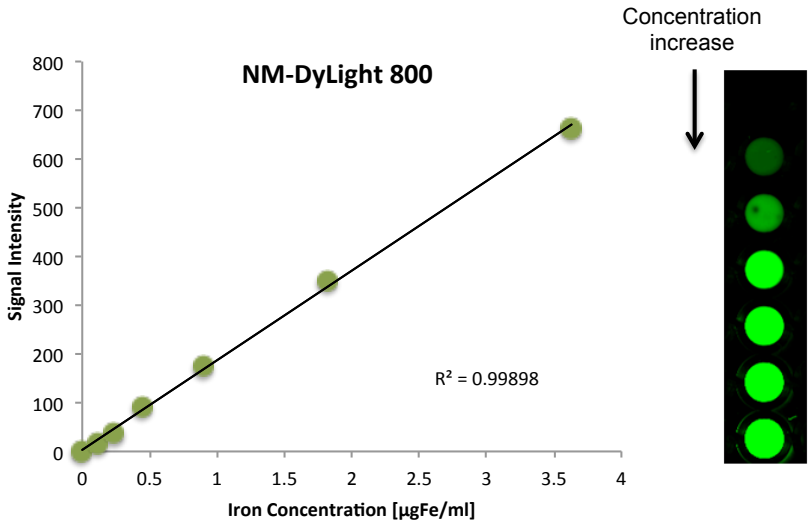

Figure 4.4: Signal intensity of Nanomag-D-spio-NH2 labelled with DyLight 800 NIR dye

A linear increase (R^2=0.998) in the signal intensity of dye labelled Nanomag-D-spio-NH_2 (NM-DyLight 800) was observed as the iron concentration increased. Images of individual wells illustrating fluorescence intensity are shown on the right.

Table 4.1: Characterisation data of Nanomag-D-spio (NM)

Sample	Hydrodynamic diameter	
	Z-Average (nm)	PDI
NM	75.4	0.187
NM-DyLight 800	74.3	0.208

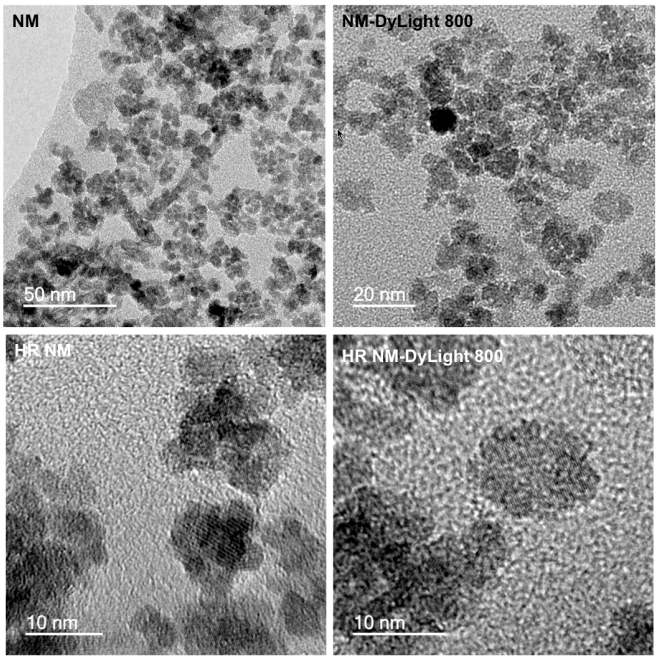

Figure 4.5: TEM micrograph of NIR labelled Nanomag-D-spio

No clear changes were observed in the cores of the SPIONs following conjugation. High-resolution TEM (HRTEM) images (lower panel) show lattice planes of iron oxide cores measuring 6.019 (±1.82) nm in diameter.

Next, NM-DyLight 800 was tested *in vivo* with DSO4 500, an established RES blocker. Four DSO4 500 doses were tested: 3, 7.5, 15 and 30 mg/kg injected 24 hours prior to NM-DyLight 800. Results showed that the NIR signal intensity of NM-DyLight 800 was strongly enhanced in a dose dependent manner (Figure 4.6) (Abdollah *et al*, 2014). An improvement in the blood signal was seen even at the lowest tested concentration of DSO4 500 with approximately a 2-fold improvement observed as the doses doubled.

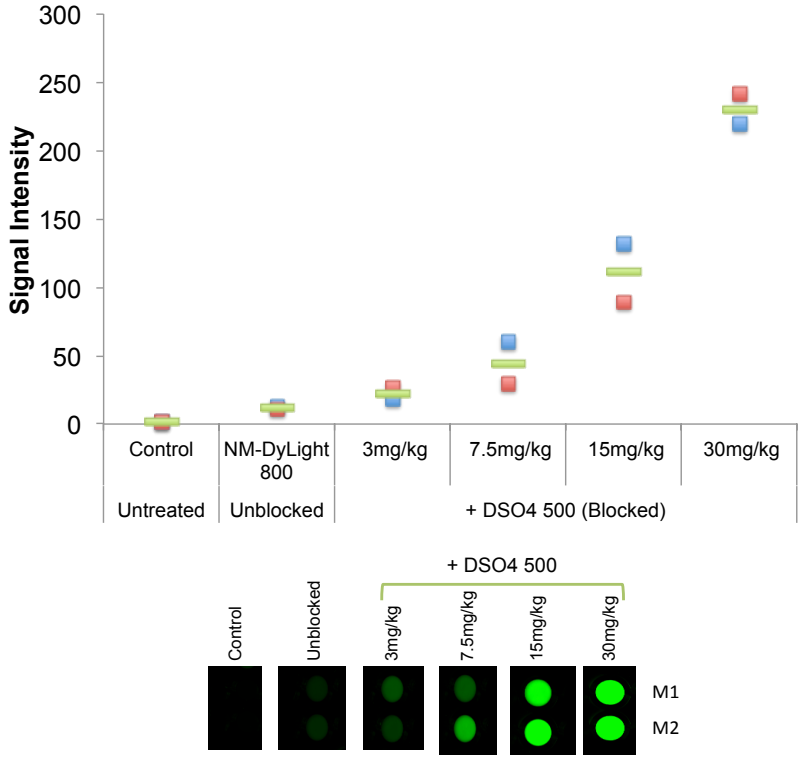

Figure 4.6: Dot plot of mean signal intensity of mice treated with NM-DyLight 800

The mean signal intensity (bar) (n=2) for mice treated with NM-DyLight 800 with and without 24-hour pre-treatment with different doses of DSO4 500. A dose-dependent increase in the signal intensity was observed as the dose of DSO4 500 increased. Each mouse is represented by a square. Bottom: Images of individual wells illustrating fluorescence intensity are shown. M1= mouse 1, M2 = mouse 2.

DSO4 500 was further tested at 30 mg/kg in four independent experiments (2-mice/group each) with different batches of NM-DyLight 800. Mice pre-treated with the blockers showed a significant 15.6-fold improvement (p=0.0016, Tukey HSD test) in the median signal intensity compared to unblocked controls. The median signal intensity of the blocked group was 112 compared to 7.17 for unblocked mice (Figure 4.7) (Abdollah *et al*, 2014).

These results showed that DSO4 500 is an efficient RES blocker *in vivo* and that the developed animal model is suitable for tracing the blood levels of SPIONs. Next, Ferucarbotran was investigated.

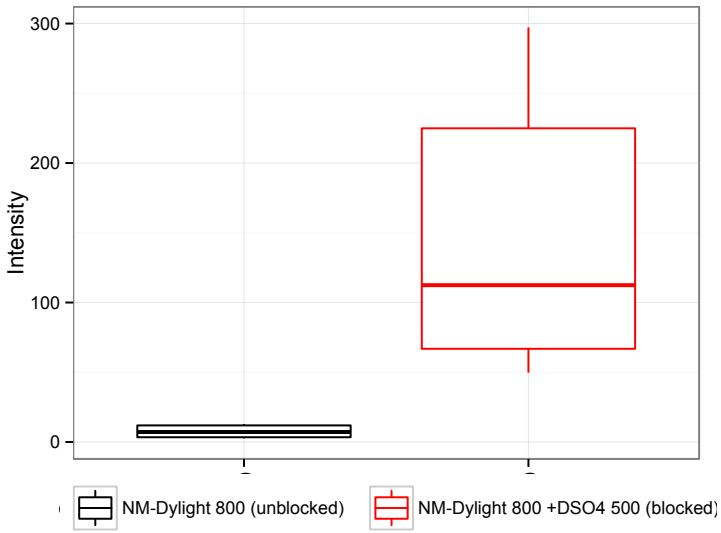

Figure 4.7: Box plot of compiled NM-DyLight 800 and DSO4 500 combined experiments

Box plot of all NM-DyLight 800 experiments showing a statistically significant difference between the signal intensity of NM-DyLight 800 in mice pre-treated with DSO4 500 for 24 hours prior to the administration of NM-DyLight 800 compared to unblocked control. Median signal intensity of blocked group was 112 compared to 7.17 for unblocked mice (p=0.016).

4.2.2 Conjugation of Ferucarbotran to NIR dyes

Having established the *in vivo* experimental conditions with NM-DyLight 800 and the known RES blocker DSO4 500, the next challenge was to develop a strategy to label Ferucarbotran.

Ferucarbotran is coated with carboxydextran and therefore hydroxyl or carboxylic groups are available for conjugation (Figure 4.8). Three different strategies were investigated to functionalise these groups; two strategies utilised the hydroxyl groups while the third targeted carboxylic groups. Whilst conjugations to the hydroxyl groups tended to cause destabilisation of the SPIONs and/or a low labelling efficiency (Abdollah *et al*, 2014), conjugation to carboxylic groups proved successful as detailed below.

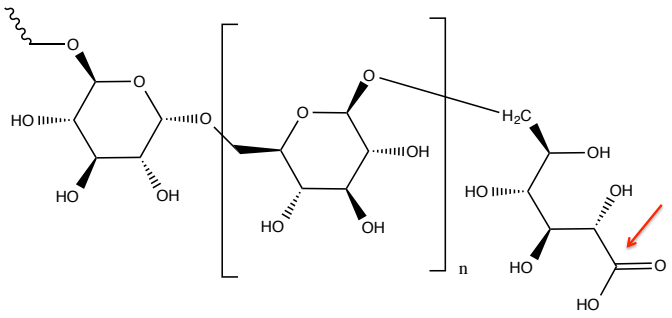

Figure 4.8: Structure of carboxydextran

Ferucarbotran is coated with carboxydextran, which is a glucose polymer with a terminal carboxylic group. There are two functional groups available on its surface: hydroxyl (OH) and carboxylic groups (COOH) (red arrow).

4.2.2.1 Conjugation of Ferucarbotran to IRDye 800 CW azide via carboxylic groups

A 2-step approach was developed to conjugate a NIR dye to the carboxylic groups of Ferucarbotran using a bifunctional linker (dibenzocyclooctyne (DBCO)-amine). First, carboxylic groups were reacted with the amine moieties of the linker via the standard EDC/NHS chemistry. Second, the Ferucarbotran-DBCO was "clicked" with an IRDye® 800CW azide dye (Figure 4.9) (Abdollah *et al*, 2014).

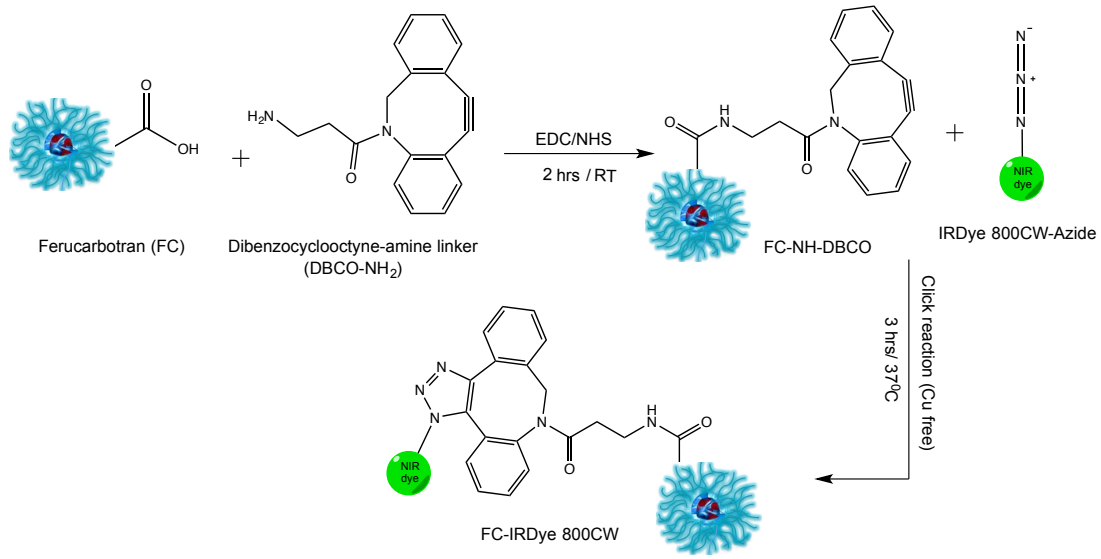

Figure 4.9: Schematic presentation of the 2-step reaction between Ferucarbotran and IRDye 800CW-Azide.

This method combines the activation of the COOH groups present on the carboxydextran coat of Ferucarbotran using EDC/NHS to react with a DBCO-amine linker. The conjugate is then "clicked" with azide functionalised NIR dye (IRDye® 800CW-Azide).

Following the reaction, visual inspection of Ferucarbotran solution revealed no apparent changes (Figure 4.10). DLS measurements showed a 5.83 nm increase in the hydrodynamic diameter of FC-IRDye 800, which could be accounted to the presence of the dye. While PDI measurements confirmed the stability of the conjugates as only a slight difference was detected after conjugation (Table 4.2). To ensure the success of the conjugation, a serial dilution of the conjugate (FC-IRDye 800) was measured on the Odyssey® NIR scanner. A linear increase in the fluorescence signal was observed as the iron concentration increased (Figure 4.11) (Abdollah *et al*, 2014). Similar to NM-DyLight 800, no changes were detected in the iron oxide cores following the conjugation as seen with TEM (Figure 4.12).

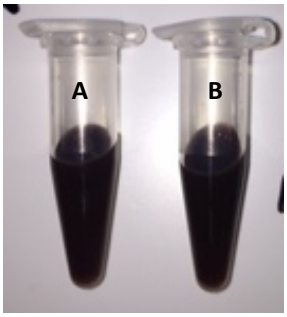

Figure 4.10: Picture of Ferucarbotran solution before and after conjugation to IRDye 800

Visual inspection revealed no apparent difference between unconjugated Ferucarbotran **(A)** and FC-IRDye 800 **(B)**.

Table 4.2: Characterisation data of FC-IRDye 800

Sample	Hydrodynamic diameter	
	Z-Average (nm)	PDI
FC	59	0.223
FC-IRDye 800	64.83	0.237

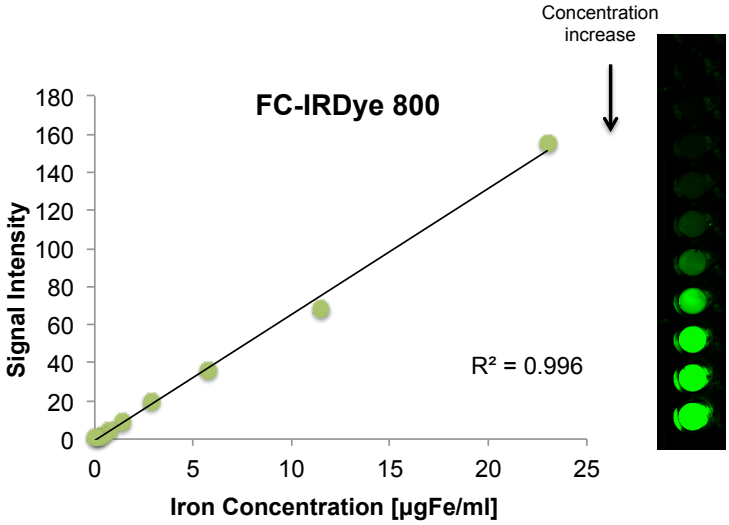

Figure 4.11: Signal Intensity of FC-IRDye 800

A linear relationship (R^2=0.99) was observed between the iron concentration of FC-IRDye 800 and the signal intensity as measured on Odyssey® scanner. Right: Images of individual wells illustrating fluorescence intensity are shown.

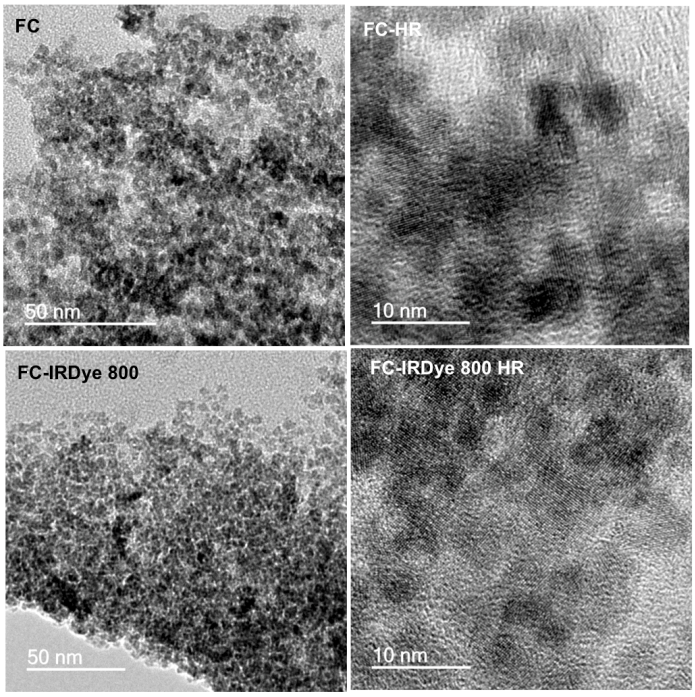

Figure 4.12: TEM micrograph of FC and FC-IRDye 800

No clear changes were observed in the iron oxide cores following conjugation. HRTEM showed core sizes of 3.75 (±0.834) nm.

4.2.2.2 Testing the labelled Ferucarbotran on RAW 264.7 cells

FC-IRDye 800 was next evaluated for *in vitro* interactions with RES using the RAW 264.7 cell line. The quantification by the NIR signal was compared to the quantification of iron using the ferrozine assay. Results (Figure 4.13) showed that both measurements revealed similar pattern of uptake and blocking where DSO4 500 showed the highest reduction in the uptake of FC-IRDye 800 by cells while J-18 led to ~ 2 fold reduction.

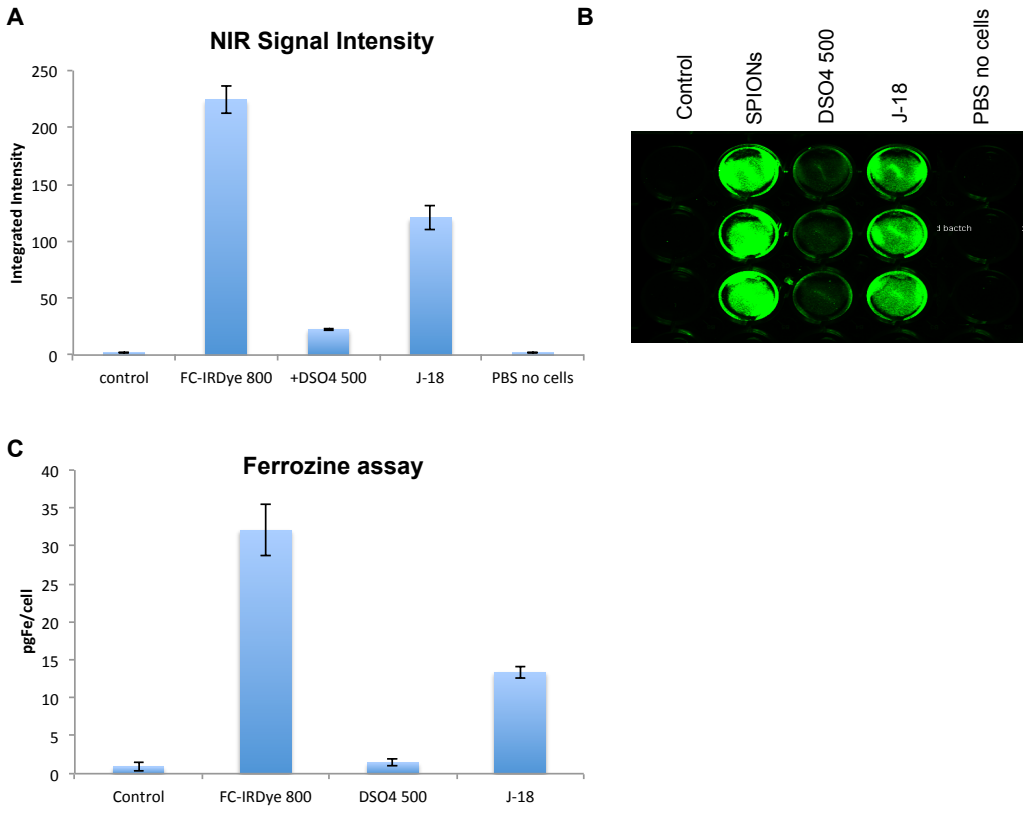

Figure 4.13: Blocking the uptake of FC-IRDye 800 on RAW 264.7 cells

Macrophages were pre-treated with DSO4 500 or J-18 before adding FC-IRDye 800. Cells were incubated for 4 hours and then washed and the NIR signal **(A and B)** measured then the cells were lysed and the intracellular iron detected with ferrozine assay **(C).** Both methods showed that DSO4 500 caused a significant reduction in FC-IRDye 800 uptake while J-18 showed a small blocking effect. $p<0.001$ of all blocked groups compared to unblocked control in both assays as measured with Student's unpaired t test. Values represent the means and error bars are for standard deviation for 3 measurements per treatment.

4.2.2.3 Testing FC-IRDye 800 in vivo with RES blockers

FC-IRDye 800 was taken forward for *in vivo* testing, first with the established blocker DSO4 500 and subsequently with more translational polysaccharides: (i) the pharmaceutical agent J-18 and (ii) the food supplement fucoidan.

DSO4 500 was investigated with four different batches of FC-IRDye 800; results were combined in a box plot shown in Figure 4.14. Mice were pre-treated with DSO4 500 24 hours before the administration of FC-IRDye 800. Results showed that a 5-fold improvement ($p=0.0039$, Tukey HSD test) in the blood signal was observed in mice pre-treated with the blocker compared to unblocked control. Median signal intensity of the blocked group was 14.13 compared to 2.76 in the unblocked control (Figure 4.14) (Abdollah *et al*, 2014).

The *in vivo* blocking results presented so far have evaluated DSO4 500 when administered 24 hours before NIR labelled SPIONs. Next, the blocking effect of DSO4 500 was investigated when injected 0, 2 or 24 hours before FC-IRDye 800. DSO4 500 increased the blood levels at all the tested conditions with 24-hour blocking giving the highest blood signal of FC-IRDye 800 (Figure 4.15) (Abdollah *et al*, 2014).

The results observed with DSO4 500 and FC-IRDye 800 confirmed the success of the conjugation reaction *in vivo*, and revealed similar trend of blocking to the one experienced with NM-DyLight 800. After establishing the system with colloidally stable dye labelled Ferucarbotran, J-18 and fucoidan were investigated *in vivo*.

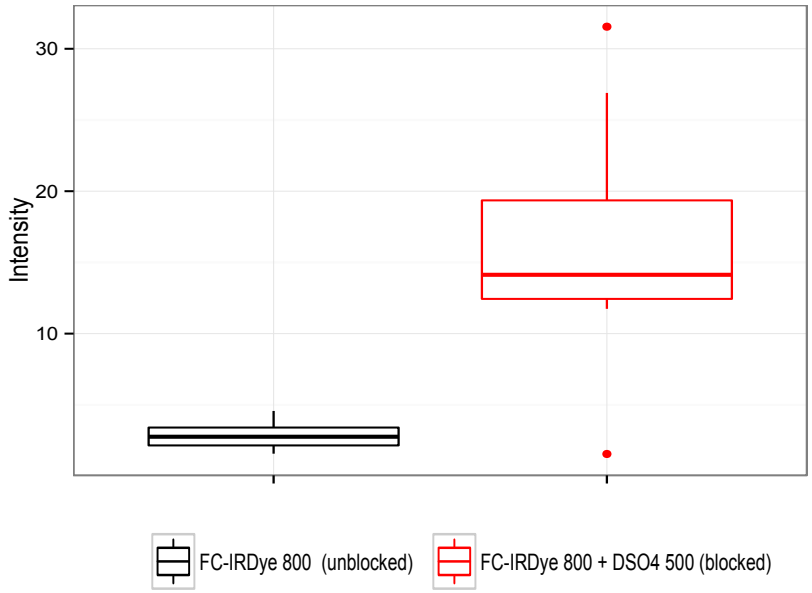

Figure 4.14: Box plot of signal intensities of mice treated with FC-IRDye 800 with and without blocking

Box plot of FC-IRDye 800 treated mice with and without 24-hour blocking with DSO4 500 showing a significant increase in the signal of FC-IRDye 800 in the blood of blocked mice compared to unblocked control (p=0.0039). Median signal intensity of blocked group is 14.13 compared to 2.76 in unblocked control.

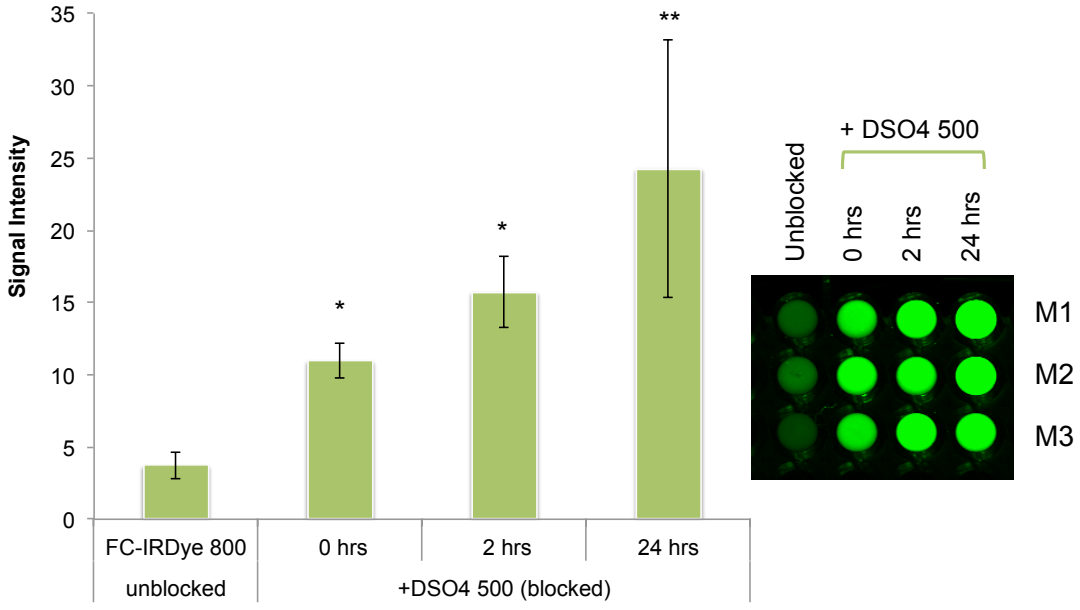

Figure 4.15: Signal of FC-IRDye 800 remaining in the blood of mice pre-treated with DSO4 500 at different blocking times

Twelve mice were tested in total (3 mice per group). All blocking times tested (0, 2 and 24 hours) showed an improvement in the blood concentration of FC-IRDye 800 with the highest observed with 24 hour blocking. *p=0.001 **p=0.01 compared to unblocked control, bars represent mean values (n=3) and error bars are for standard deviation. **Right:** Images of individual wells illustrating fluorescence intensity are shown. M1, M2 and M3 stand for mouse number.

The blocking effect of J-18 was tested in a small (2 mice/group) pilot experiment at 3 different blocking times: 0, 30 and 120 minutes before administration of FC-IRDye 800. A small improvement was observed in all the tested groups and more specifically when J-18 was given 30 minutes prior to Ferucarbotran injection (Figure 4.16). Nonetheless, the blocking effect of J-18 was not as effective as DSO4 500.

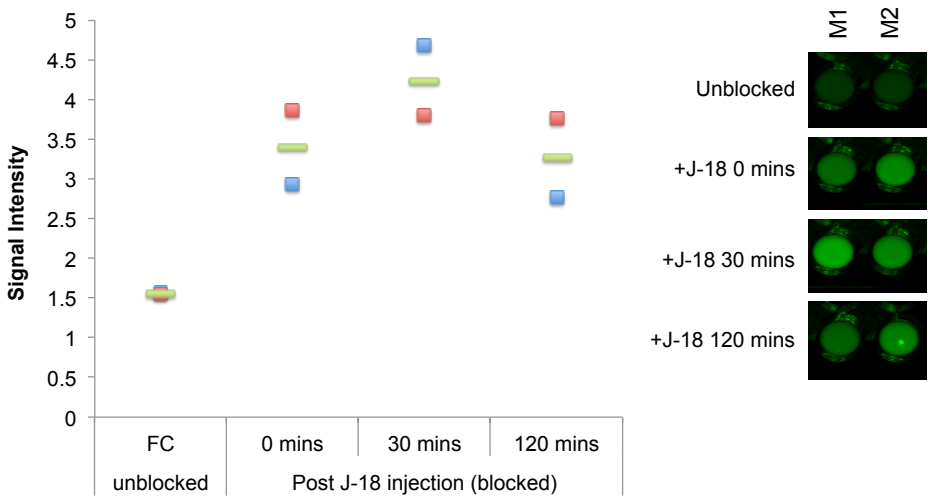

Figure 4.16: Signal of FC-IRDye 800 remaining in the blood of mice pre-treated with J-18 at different blocking times

Mice pre-treated with J-18 showed a small improvement in their blood signal compared to the unblocked group. The highest effect (2.7 times improvement) was seen in mice pre-treated with J-18 for 30 minutes before FC-IRDye 800 injection. Each mouse is represented with a square and average with a bar. Fluorescence intensity of the blood samples are illustrated on the right, M1 = Mouse 1, M2 = Mouse 2.

The final blocker tested was fucoidan when administered 24 hours prior to FC-IRDye 800; conditions already developed for DSO4 500. Results (Figure 4.17) showed no increase in the blood levels of Ferucarbotran in the fucoidan-treated group, unlike mice pre-treated with DSO4 500. When the experiment was repeated with the blockers administered directly before Ferucarbotran, results (Figure 4.18) revealed that mice pre-treated with fucoidan showed a 5.8 improvement in the blood signal of Ferucarbotran compared to 2.5 fold improvement seen with DSO4 500.

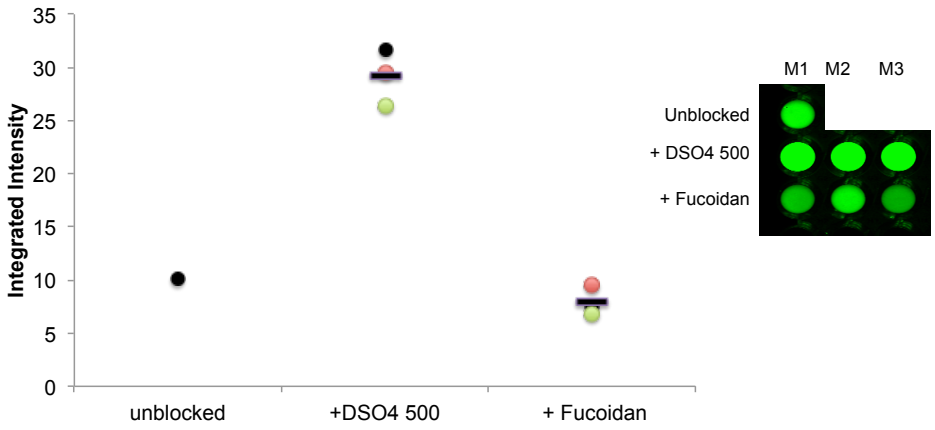

Figure 4.17: Testing blocking effect of fucoidan when administered 24 hours prior to FC-IRDye 800

Blockers were injected 24 hours prior to NIR labelled Ferucarbotran, mice pre-treated with DSO4 500 (n=3) showed an increase in the blood signal of Ferucarbotran compared to fucoidan blocked mice (n=3) and unblocked control (n=1). Each mouse is represented with a circle and average with a bar. On the right fluorescence intensity of the blood samples are illustrated. M1 = Mouse 1, M2 = Mouse 2, M3 = Mouse 3.

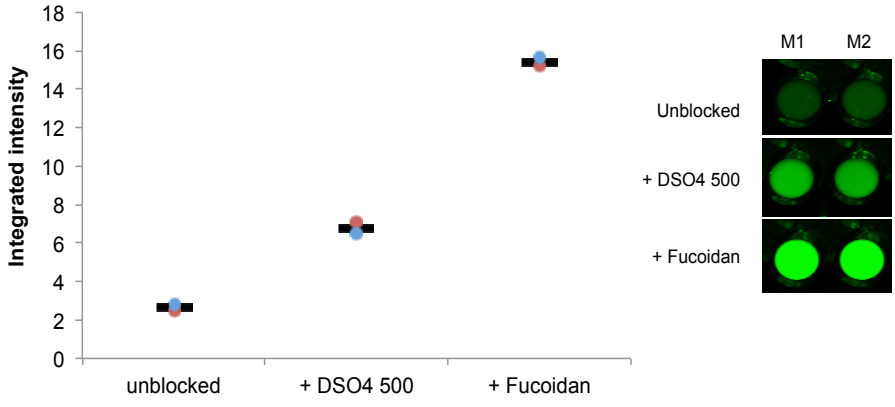

Figure 4.18: Fucoidan and DSO4 500 blockers tested when administered directly before FC-IRDye 800

Fucoidan caused an increase in the signal of Ferucarbotran detected in the blood indicating effective blocking of RES. Under the tested conditions, fucoidan appears to be more efficient than DSO4 500. Each mouse is represented with a circle and average with a bar. Fluorescence intensity of the blood samples are illustrated on the right, M1 = Mouse 1 and M2 = Mouse 2.

4.2.3 Testing the blocking effect of fucoidan using SPECT/CT imaging

Since Fucoidan was shown to be an efficient RES blocker as well as being readily available as a food supplement, it was tested with another system using radiolabelled Ferucarbotran. Ferucarbotran was labelled with Technetium-99m (^{99m}Tc) in order to trace its biodistribution with SPECT/CT imaging. Fucoidan was injected directly before ^{99m}Tc–Ferucarbotran then mice were scanned for 90 minutes (3 X 30 minutes slots) before being sacrificed and the organs harvested.

A clear change in the pharmacokinetic behaviour of Ferucarbotran was observed in the fucoidan-blocked mice compared to unblocked control. As seen in Figure 4.19, in the fucoidan treated mice, more ^{99m}Tc–Ferucarbotran was detected in the circulation (heart) up to 90 minutes post injection. Furthermore, in the blocked mice a higher signal was detected in the spleen and the kidneys versus an almost exclusive signal in the liver of the unblocked mice. Biodistribution data revealed similar findings to the images as shown in Figure 4.20. The most striking difference is in the liver uptake as in unblocked mice the liver to blood ratio was 8.5 compared to only 0.5 in the blocked counterpart. While all other tissues showed similar tissue to blood ratios.

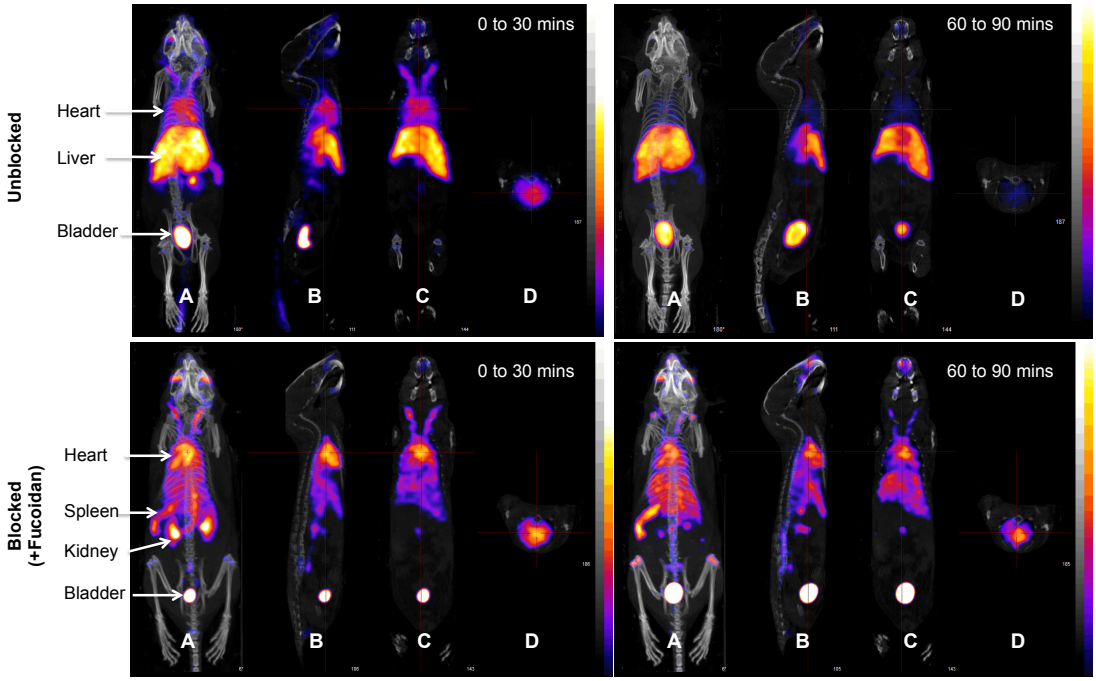

Figure 4.19: SPECT/CT images taken at 30 and 90 minutes post treatment of mice with ^{99m}Tc-Ferucarbotran

(A) Maximum intensity projection (MIP) SPECT/CT images after i.v. injection of radiolabelled ^{99m}Tc-Ferucarbotran, **(B)** sagittal slice and **(C)** coronal slices of the MIP centered at the heart and **(D)** transverse slice also centered at the heart. Mice pre-treated with fucoidan (bottom panel) showed a clear change in the pharmacokinetics of Ferucarbotran. In the blocked mice a higher signal was detected in the heart (blood pool) even after 90 minutes following the injection, with more SPIONs detected in the spleen. While in the unblocked mice (top panel) the highest signal was detected in the liver and bladder with some still visible in the heart in the first 30 minutes, however by the end of the scan almost an exclusive signal is seen in the liver and the bladder. The bladder signal corresponds to the excreted metabolised radioisotope.

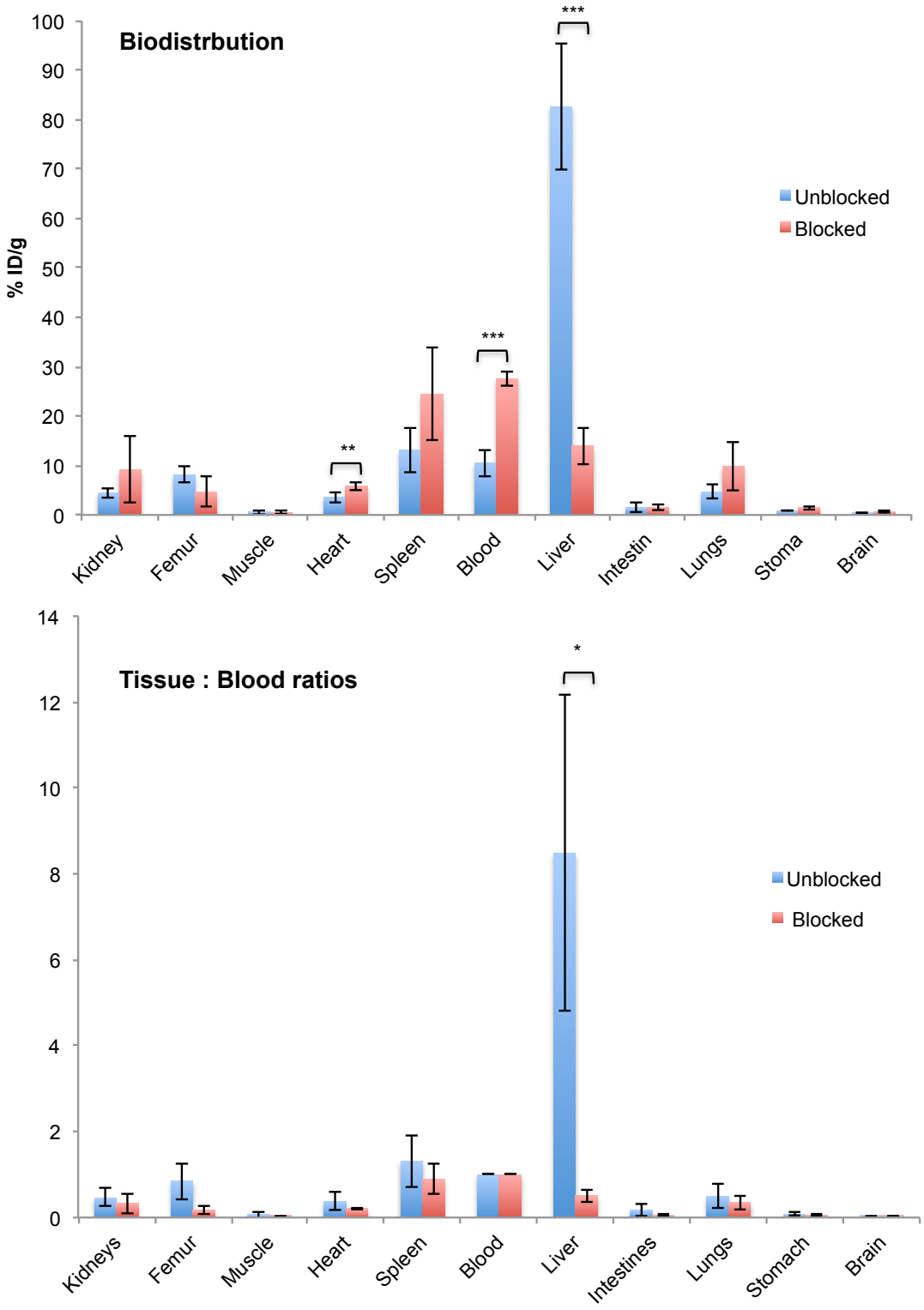

Figure 4.20: Biodistribution of ^{99m}Tc-Ferucarbotran in different tissues

Top: Unblocked mice (blue bars) showed almost exclusive uptake of Ferucarbotran by the liver, while in blocked mice (red bars) SPIONs could be detected mainly in the blood and the spleen. In the tissue to blood ratios (bottom), the most striking difference was observed in the liver while the rest of the organs showed similar ratios between the two tested groups. ***p<0.01, **p=0.05, *p=0.063 as tested with t test.

4.3 Discussion

The work presented in this chapter supported the hypothesis that polysaccharide derivatives would prolong the circulatory retention of SPIONs. To test the hypothesis *in vivo*, two SPIONs (Ferucarbotran and Nanomag-D-spio-NH_2) were conjugated to NIR dyes to measure their blood levels following administration of polysaccharide derivatives (DSO4 500, J-18 and fucoidan). Some of these new findings were published in ((Abdollah *et al*, 2014), Appendix 5) and are novel in two aspects: (i) methods for conjugation of NIR dyes to Ferucarbotran and (ii) the investigation of DSO4 500 and pharmaceutical agents (J-18 and fucoidan) as blockers of the uptake of SPIONs by the RES.

Tracing SPIONs in blood is confounded by the presence of haemoglobin, rendering iron quantification assays very difficult. Alternative methods have been used, for instance radioactive iron isotopes (e.g. ^{59}Fe) were incorporated during the synthesis process (Majumdar *et al*, 1990), however this could be difficult for commercially available SPIONs. Other approaches used magnetic susceptibility measurements (MSM) via a magneto-susceptometer (Maurizi *et al*, 2014). The approach used in chapter 4 utilised NIR imaging which has been used extensively *in vivo* (Kondepati *et al*, 2008). Haemoglobin, oxyheamoglobin and water show low background interference as they exhibit low molar extinction coefficients at NIR wavelengths (Kim *et al*, 2005), this will facilitate measurement of NIR labelled SPIONs in whole blood. Whilst, labelling iron oxide nanoparticles with NIR dyes has been reported before (Hou *et al*, 2010; Tang *et al*, 2014); the mentioned studies fabricated their own nanoparticles and added the NIR labelling step during the manufacturing process. Meanwhile the work in chapter 4 labelled commercially available SPIONs.

The initial *in vivo* experiments were performed with Nanomag-D-spio-NH_2 labelled with an NHS ester dye. The conjugation reaction was gentle and maintained SPIONs colloidal stability. DSO4 500 was tested with NM-DyLight 800; different doses of the blocker were evaluated and 30 mg/kg appeared to show the highest blocking effect. DSO4 500 injected at doses as high as 50 mg/kg were reported to be tolerated by mice without significant lethality (Patel *et al*, 1983), however a safer 30 mg/kg was chosen to minimize the side effects which might be induced by the toxic nature of DSO4 500. This dose was further evaluated in repeated experiments and results revealed a significant 15.6-fold improvement in the blood retention of

SPIONs in blocked mice. These results were very promising as well as consistent with previous findings *in vitro* (see chapter 3) and with DSO4 500 published data.

Next, the main SPION of interest in this thesis was investigated. A conjugation strategy to label Ferucarbotran with NIR dyes was developed. The dextran coat maintains the stability of the nanoparticles in solution and solubilizes the cores (Shubayev *et al*, 2009), therefore, the coat is crucial in maintaining the colloidal stability of Ferucarbotran rendering functionalisation challenging. Most commercially available NIR dyes are usually functionalised with maleimide or NHS ester functional moieties to react with amines and sulfhydryl groups, respectively. These groups are readily available on biomolecules (e.g. proteins) but not on the carboxydextran coat of Ferucarbotran which contain either hydroxyl or carboxylic moieties.

The most efficient labelling strategy was achieved via the carboxylic groups on Ferucarbotran carboxydextran coat by using a commercially available heterobifunctional linker (DBCO-amine). This employed using a combination of EDC/NHS and click chemistries under mild reaction conditions without breaking the hexose rings of dextran, thus maintaining the colloidal stability of Ferucarbotran. Visual inspection of Ferucarbotran solution following the reaction revealed no precipitations and only minor changes were recorded with DLS.

Following the establishment of a conjugation strategy for Ferucarbotran, FC-IRDye 800 was tested *in vitro* and *in vivo. In vitro* results were consistent with those observed with RAW 264.7 cell lines in chapter 3, DSO4 500 blocked the uptake of FC-IRDye 800 by cells more efficiently than J-18. *In vivo,* mice pretreated with DSO4 500 showed a significant 5-fold increase in the blood levels of Ferucarbotran. It appeared that DSO4 500 was more efficient in modifying the rapid clearance of NM-DyLight 800 than FC-IRDye 800, as a 15-fold improvement was observed with the former.

In an attempt to optimise DSO4 500 blocking, the blocker was tested at different blocking times. Although a blocking effect was observed at all the tested conditions, the highest blood levels of Ferucarbotran was observed with 24 hours blocking consistent with the work done by Patel *et al*., which examined the effect of DSO4 500 on the pharmacokinetic profile of liposomes. Similar to SPIONs, liposomes are also rapidly cleared from the circulation by liver Kupffer cells. Patel *et al* found that

liver blocking started as early as 2 hours post injection of DSO4 500 and peaked at 12 hours. 70% of liver uptake of liposomes was blocked by 24 hours and recovery occurred 48 hours later with liver uptake resuming to normal (Patel *et al*, 1983).

However a major drawback of using dextran sulfates is their potential toxicity. Dextran sulfate has been tested before as an anti-viral in HIV-1 positive patients and was poorly tolerated (Flexner *et al*, 1991). Although it should be taken into account that in this study dextran sulfate was used over a period of 2 weeks as a continuous i.v. infusion, which is different than if given as a single dose.

Next, J-18 was tested with FC-IRDye 800; J-18 has smaller molecular weight than DSO4 500 (see Table 2.12) and therefore was tested with shorter blocking periods. A small improvement was seen with 30 minutes blocking. These results suggest that J-18 might need multiple i.v. dosing and/or intraperitoneal administration to achieve sustained release of the drug into the blood stream. This might enhance the small blocking effect seen in the preliminary experiments presented herein.

Following the very promising results observed with fucoidan *in vitro* (see chapter 3), the blocker was investigated *in vivo*. Fucoidan was administered 24 hours prior to FC-IRDye 800, no enhancement in the signal was observed compared to DSO4 500. Similar to J-18, this might be explained by the short half-life of fucoidan and its heterogeneity leading to its rapid clearance. Fucoidan tested in this thesis was obtained from Sigma Aldrich; it is a crude extract from *Fucus vesiculosus with* a wide size distribution (molecular weight between 20,000 – 200,000 Da (Sigma product information sheet)). This might affect its pharmacokinetic behaviour when given *in vivo* making it difficult to control. Nonetheless, when fucoidan was injected directly before FC-IRDye 800, a 5.8-fold improvement in the blood signal was observed compared to 2.4-fold improvement seen with DSO4 500 tested under the same conditions.

To further evaluate the changes that occur in the biodistribution of Ferucarbotran following blocking with fucoidan, a new labelling strategy was applied. Ferucarbotran was radiolabelled with the gamma-emitting radioisotope ^{99m}Tc to trace its biodistribution using SPECT/CT imaging. The conjugation utilized the high affinity of a bifunctional bisphosphonate linker to the metal oxide core of Ferucarbotran; a technique developed by De Rosales *et al* (De Rosales *et al*, 2009) and have been used for SPECT detection of USPIO by Sandiford *et al* (Sandiford *et*

al, 2012). As expected, Ferucarbotran was mainly detected in the liver of the unblocked mice. On the contrary, pre-treatment with fucoidan dramatically changed the biodistribution of Ferucarbotran as more SPIONs were detected in the circulation, indicating efficient blocking of the liver. These findings are very exciting, as fucoidan might provide a safer alternative to DSO4 500 with fewer, if any, toxicities. Studies done with fucoidan has so far reported no toxic side effects both *in vitro* and *in vivo* (Kwak, 2014).

There have been a number of approaches developed for evading the RES uptake of SPIONs. These include: (a) reducing their hydrodynamic diameter (i.e. using USPIO) to escape recognition by the RES and (b) modifying SPIONs coat with hydrophilic polymers (e.g. PEG, PVP, poloxamines and poloxamers) to reduce opsonisation (see introduction section 1.4.1.4).

Many studies utilised the first approach; ultra-small long-circulating dextran coated iron oxide nanoparticles (LCDIO) of an average hydrodynamic diameter of 20 nm were developed (Moore *et al*, 2000; Shen *et al*, 1993). The long half-life of LCDIO extended their application beyond RES imaging, for instance they were used in vascular imaging (Frank *et al*, 1994), detection of lymph node metastasis (Weissleder *et al*, 1990) and labelling glioma tumours by passing the hyperpermeable tumour-brain interface (Moore *et al*, 2000; Zimmer *et al*, 1997).

Apart from USPIO, PEGylation is still the main method used to create stealth nanoparticles (Fan *et al*, 2011; Gaur *et al*, 2000; Gupta & Gupta, 2005; Sandiford *et al*, 2012; Shubayev *et al*, 2009). However, some studies suggest that PEGylation might hinder the extravasation of nanoparticles to tumour cells (Li & Huang, 2010). Furthermore, the prolonged half-life caused by PEGylation might introduce unexpected toxicity or immunogenic responses. For instance stealth modified Doxil® significantly reduced the cardiotoxicity of doxorubicin but the prolonged half-life led to the emergence of new side effects (e.g. mucositis and hand-foot syndrome) (Li & Huang, 2010; Lyass *et al*, 2000). In addition, the repeated administration of Doxil® in mice have resulted in the generation of anti-PEG IgM antibodies causing "accelerated blood clearance (ABC) phenomenon". Binding of anti-PEG antibodies to the PEGylated liposomes led to their rapid clearance by the liver and spleen upon second administration (Li & Huang, 2010; Tagami *et al*, 2010).

Some studies combined both approaches of using USPIO and stealth coating. For instance Fan *et al* have coated their nanoparticles with o-carboxymethyl chitosans (OCMCS) and folic acid to evade the RES and target tumours expressing folate receptors, respectively. Their targeted/stealth nanoparticles were around 40 nm in diameter. In this study, the researchers concluded that the presence of OCMCS increased the hydrophilicity of SPIONs compared to uncoated ones; this enhanced their stability and reduced their recognition by macrophages. They also observed a 27% reduction in the MRI signal intensity in mice bearing folate receptor positive tumours and receiving the targeted/stealth SPIONs (Fan *et al*, 2011).

However, all the approaches discussed above would require manipulation of nanoparticles during the synthesis process, which is not possible for commercially available products with well-studied safety profiles (e.g. Ferucarbotran and Endorem®). Therefore, the work presented in this chapter provides a new perspective to prolong the half-life of SPIONs without the need to change their physicochemical characteristics.

4.4 Summary and conclusions

The work presented in this chapter tested one of the central hypotheses of this thesis: RES uptake of SPIONs could be blocked using polysaccharide derivatives. Results were consistent with the proposed hypothesis; DSO4 500 and fucoidan were shown to have the strongest effect on increasing the circulatory retention of SPIONs. To prove the hypothesis, a method to trace the blood levels of SPIONs was designed by chemically conjugating them to NIR dyes. Nanomag-D-spio-NH_2 was easily functionalised while Ferucarbotran proved to be very challenging. Nonetheless, both SPIONs were successfully labelled with NIR dyes while maintaining their colloidal stability as confirmed with visual inspection and DLS. Furthermore a new method to trace Ferucarbotran *in vivo* using SPECT/CT imaging was introduced.

In conclusion, dye-labelled and radiolabelled SPIONs were readily traced *in vivo* and a method to modify their poor pharmacokinetics was established. The work presented in this chapter provides a step towards the clinical development of SPIONs by overcoming their rapid RES clearance.

Chapter 5
Functionalisation of Ferucarbotran with Cancer-Targeting DARPins

Maha Abdollah

5.1 Introduction

The aim of the work described in this chapter was to address one of the main challenges of cancer nanomedicine: the need for functionalisation of nanoparticles with cancer targeting moieties. DARPins, small antibody-like proteins described in section 1.9.4, were chosen for use as targeting agents because they are small and stable proteins that are readily engineered to have a unique cysteine tag for site-specific attachment to SPIONs.

E69 (Boersma *et al*, 2011), a DARPin reactive with the epidermal growth factor receptor 1 (EGFR/HER1/ErbB1) tyrosine kinase transmembrane receptor was chosen as an exemplar DARPin for attachment. EGFR is overexpressed in many tumours for example glioblastoma (Chong & Jänne, 2013; Sanai *et al*, 2005), head and neck cancers, gastric, breast, cervical and non-small cell lung cancers (Mendelsohn & Baselga, 2006; Nicholson *et al*, 2001) and lined to poor prognosis (Boersma *et al*, 2011).

The EGFR family comprises of four structurally related members: ErbB1 (EGFR/HER1), ErbB2 (HER2/*neu*), ErbB3 (HER3) and ErbB4 (HER4) (Goffin & Zbuk, 2013; Mendelsohn & Baselga, 2006; Sheng & Liu, 2011). They consist of extracellular, transmembrane and cytoplasmic regions. Eleven ligands (e.g. EGF, TGF-α and neuregulin 1-4) are known to bind to these receptors, which result in their homodimerisation or heterodimerisation and subsequent conformational changes (with the exception of HER2, which can form stable dimers without ligand binding). Autophosphorylation of the cytoplasmic domain then occur triggering numerous downstream signalling pathways (Goffin & Zbuk, 2013; Sheng & Liu, 2011).

EGFR receptors play a critical role in normal tissue as well as in cancer. The deregulation of this family has been linked to malignant transformation and prognosis (Mendelsohn & Baselga, 2006). Several mechanisms were linked to abnormal receptor activation (e.g. gene amplification, overexpression of the receptors or their ligands, activating mutations and/or loss of negative regulatory mechanisms) (Mendelsohn & Baselga, 2006). The EGFR family has therefore been of great therapeutic interest especially in cancer and several therapies are being developed to target these receptors (Chong & Jänne, 2013; Mendelsohn & Baselga, 2006).

Targeting SPIONs with E69 is advantageous because E69 is biologically inert (Boersma *et al*, 2011). The extracellular region of EGFR consists of four domains (I-IV); EGF binds simultaneously to two sites on domain I and III leading to receptor dimerization and activation (Li *et al*, 2005). The antagonistic therapeutic antibody Cetuximab binds exclusively to domain III; the variable heavy chain (V_H) of the bound antibody sterically inhibits the dimerization of the receptor and consequently the downstream signalling pathways (Bangham, 2005; Li *et al*, 2005). On the contrary to these biologically active binders, E69 binds to domain I away from the binding sites of both EGF and Cetuximab.

Functionalised SPIONs able to specifically target the EGFR receptor could potentially facilitate the use of targeted magnetic hyperthermia therapy for cancers overexpressing this receptor (e.g. gliomas, colorectal carcinomas and lung cancers).

5.1.1 Experimental approach

Ferucarbotran was site-specifically conjugated to E69 and a control DARPin G3, reactive with HER2 (Goldstein *et al*, 2014; Zahnd *et al*, 2007).

Assays were developed to investigate the presence of DARPins on the surface of SPIONs following the conjugation reaction; these include: western blots and DLS measurements. However, the presence of E69 on the coat of Ferucarbotran does not necessarily ensure that targeting could be achieved. Therefore, a series of immuno- and cellular assays were used to examine the specificity of Ferucarbotran-E69 (FC-E69) conjugates to the target protein, EGFR.

Immunoassays included the development of a suitable ELISA assay to examine the specificity of FC-E69. In order to develop cellular assays; EGFR expression on different cell lines was examined with western blotting and flow cytometry. Next, ferrozine assay was used to test the uptake of conjugates on the different cell models including cells expressing endogenous EGFR (e.g. U-251 MG cells) as well as cells retrovirally transduced with EGFR (SupT1 cells).

5.1.2 Research Aims and Objectives

Aims: To develop a system to functionalise Ferucarbotran with cancer targeting agents.

Objectives:

- Conjugate Ferucarbotran to DARPins via site-specific attachment.
- Evaluate the success of the conjugation chemistry via western blotting and DLS.
- Develop various ELISA assays to evaluate the binding of FC-E69 to EGFR.
- Establish suitable cell assays for the investigation of the specificity of the conjugates.

5.2 Results

5.2.1 Conjugation of Ferucarbotran to DARPins

A 2-step approach was used to link the carboxylic groups present on the carboxydextran coat of Ferucarbotran to the cysteine tag of the DARPins. First, a standard EDC/NHS chemical conjugation was employed to link Ferucarbotran to the amine moiety of a bifunctional linker; BMPH. Second, the maleimide moieties of the linker, now attached to the nanoparticles, were reacted with the thiol groups present on the cysteine tags of the DARPins (Figure 5.1).

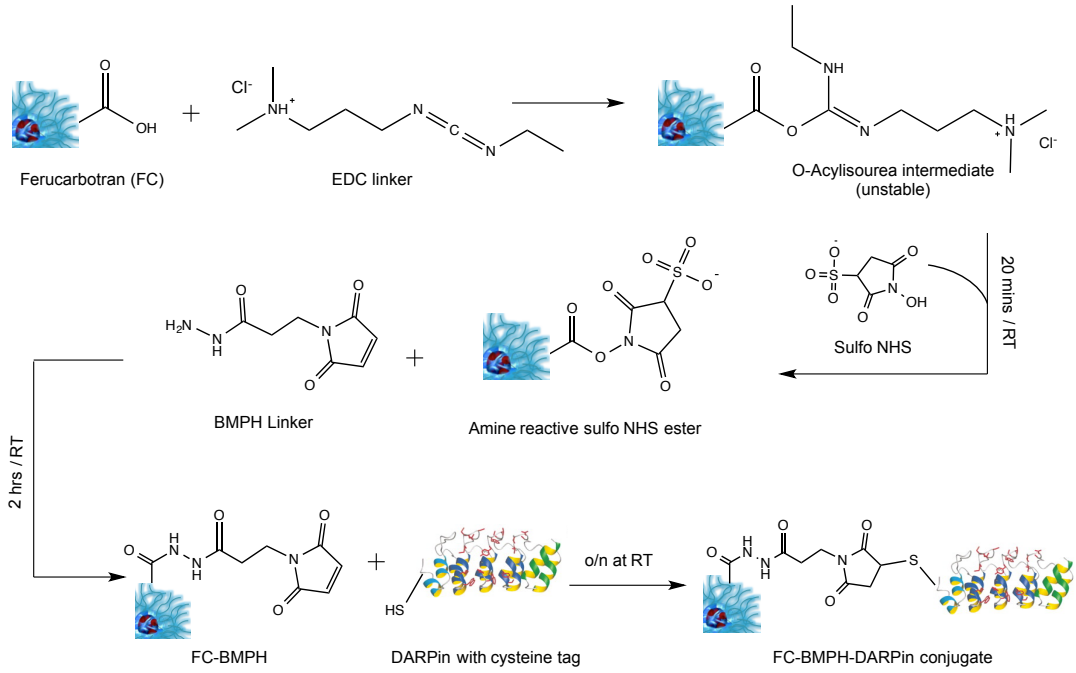

Figure 5.1: Schematic presentation of the conjugation strategy between Ferucarbotran and DARPins (E69 and G3).

A two-step approach was employed by using a bifunctional linker: BMPH. The amine part of the linker was first conjugated to the carboxylic groups available on the carboxydextran coat of Ferucarbotran followed by the reaction of the maleimide moieties of the linker to the cysteine tags of the DARPins.

5.2.2 Purification of Ferucarbotran-DARPins conjugates using Superdex 75

Following the reactions, Ferucarbotran-DARPin conjugates were purified with size exclusion chromatography (SEC) on Superdex 75. First, a sample of E69 tested on Superdex 75 was eluted as a single peak and was shown on a Coomassie stained SDS-PAGE to have the right molecular weight (21.4 KDa) (Figure 5.2).

Ferucarbotran conjugated to E69 (FC-E69) was eluted first in a single peak followed by a small peak of free E69 at the tail of the conjugate peak. Fractions 4 to 15 were pooled together and named “peak 1”, which corresponds to the conjugate FC-E69. Coomassie stained reducing gel confirmed the presence of E69 in peak 1 and fraction 24 (small peak for free E69). The presence of free E69 in peak 1 is due to the reducing conditions used in preparing the samples which leads to the dissociation of the bond between Ferucarbotran and E69 (Figure 5.3 top).

The control anti-HER2 DARPin (G3) was conjugated to Ferucarbotran and then purified in a similar manner to FC-E69. Ferucarbotran-G3 (FC-G3) conjugate was eluted first followed by a smaller peak for G3. Fractions 5 to 17 were pooled together and named ‘peak 1’, which corresponds to the conjugate FC-G3. Coomassie stained gel confirmed the presence of G3 in fractions 40 and 47, which corresponds to free G3. While a faint band was seen in peak 1 due to the reducing conditions (Figure 5.3 bottom).

The eluted samples were further tested with:

- Western blotting: using polyclonal anti-DARPin mouse sera to detect the presence of DARPins on the conjugates.
- Dynamic light scattering (DLS): to measure the change in the nanoparticle size following conjugation.

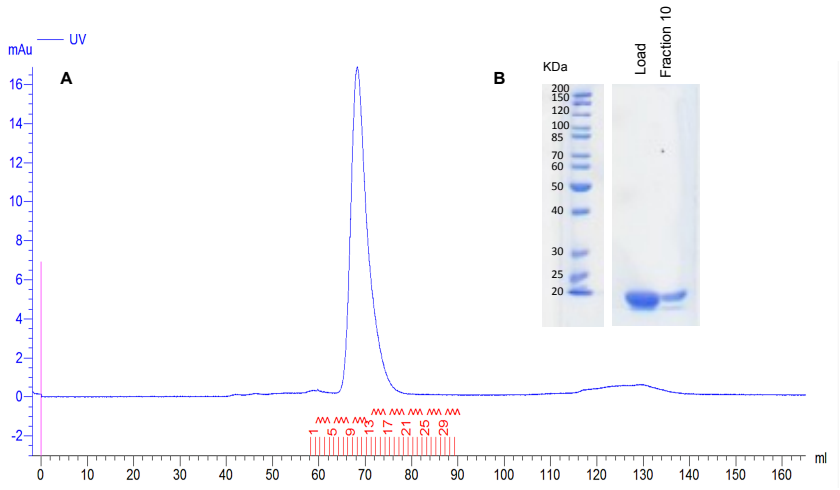

Figure 5.2: Elution of E69 on Superdex 75 packed column.

(A) Chromatogram showing the elution of E69 as a single peak. **(B)** Coomassie stained gel showing fraction 10 (peak) to contain ~20 KDa protein consistent with E69 molecular weight.

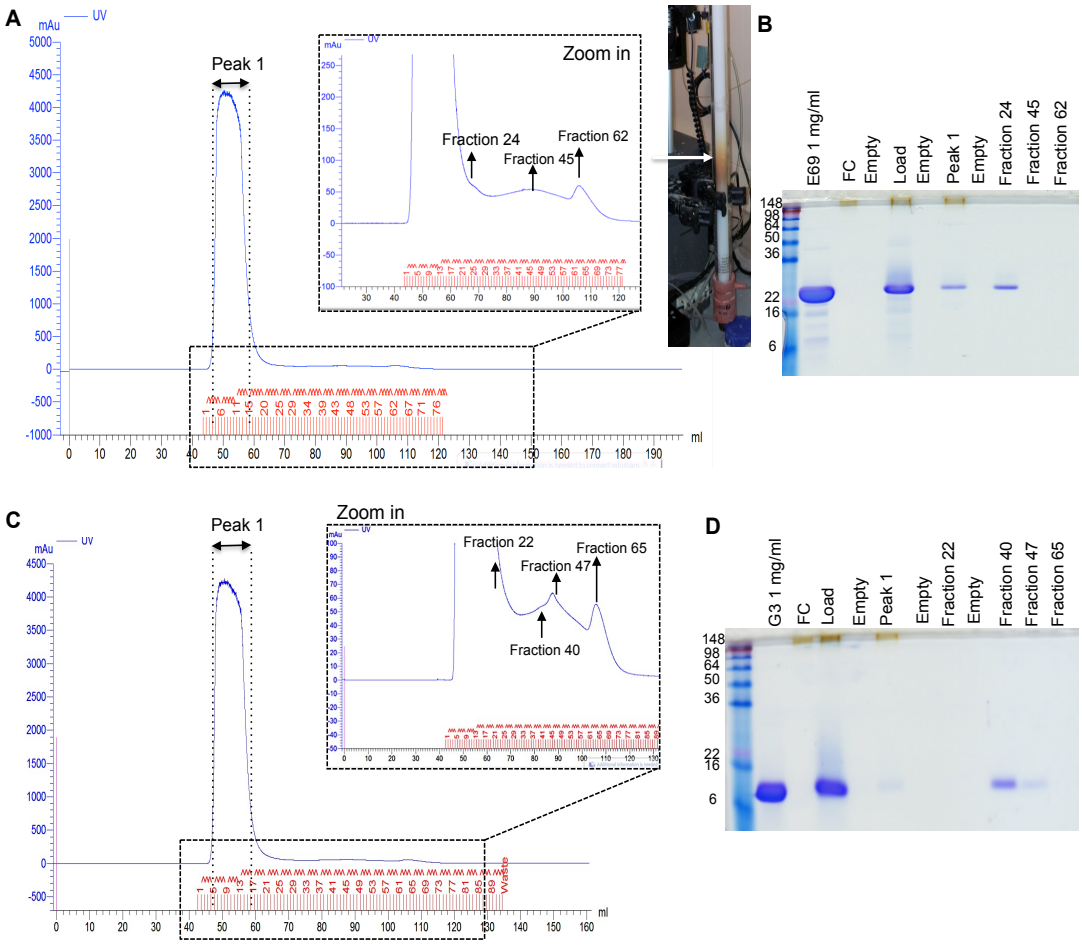

Figure 5.3: Purification of FC-E69 (Top) and FC-G3 (bottom) conjugates on Superdex 75 column.

A, C: Chromatogram showing the elution of FC-E69 or FC-G3 first as a single peak followed by the free E69 or G3, respectively. A picture of the column showing FC-E69 (brown) moving along the column as a single peak (top middle). **B, D:** Coomassie stained 16% gel confirming the presence of free E69 in fraction 24 and free G3 in fractions 40 and 47.

5.2.3 Characterisation of the conjugates

5.2.3.1 Western blotting

Western blotting was used for sensitive detection of DARPins on the conjugates. Samples were prepared either in reducing or non-reducing loading buffer. As shown from Figure 5.4 A, for FC-E69: peak 1 and fraction 24 tested positive for E69. Under non-reducing conditions, E69 could be detected at the top of the gel, as Ferucarbotran is too big to move through the gel, nevertheless some free E69 (at ~22 KDa) was detected. Fraction 24, corresponding to excess unreacted E69, also tested positive. Under reducing conditions, no E69 was detected at the top of the gel due to the reduction of the bond. Two more peaks (fractions 45 and 62) were seen in the chromatogram, both tested negative for E69 and were not further analysed.

As shown from Figure 5.4 B, similar findings were observed with FC-G3. The conjugate (FC-G3) was eluted first in a single peak named 'peak 1'. Peak 1 was investigated at 150 and 300 μgFe/ml; both tested positive for G3 at the top of the gel (under non-reducing conditions). Fractions 40 and 47, corresponding to free G3, also tested positive. Fraction 65 appeared to be negative for G3 and was not further analysed. Under reducing conditions, G3 could be detected at ~ 14 KDa corresponding to monomer G3.

5.2.3.2 DLS

The conjugates were characterised using DLS to monitor the changes in their hydrodynamic diameter and PDI. A summary of the DLS characterisations is shown in Table 5.1. A 22.6 nm and 24.48 nm increase in the Z-average hydrodynamic diameter of FC-E69 and FC-G3, respectively, was observed with small changes in the PDI of the measured samples. DLS have also shown that the conjugate samples were uniform with no signs of destabilisation of the nanoparticles. Zeta potential measurement revealed a -4.6 mV and -2.7 mV increase in the charge of FC-E69 and FC-G3, respectively, compared to unconjugated Ferucarbotran. The increased negative charge might be accounted to the negative charge of the DARPins on the surface of SPIONs.

As shown in Figure 5.5, when size-distribution by intensity histograms were overlaid, a clear shift in the size distributions of both conjugates (FC-E69 and FC-G3) was observed in comparison to unconjugated Ferucarbotran. These results are

consistent with the presence of proteins on the surface of Ferucarbotran leading to an increase in the hydrodynamic diameter.

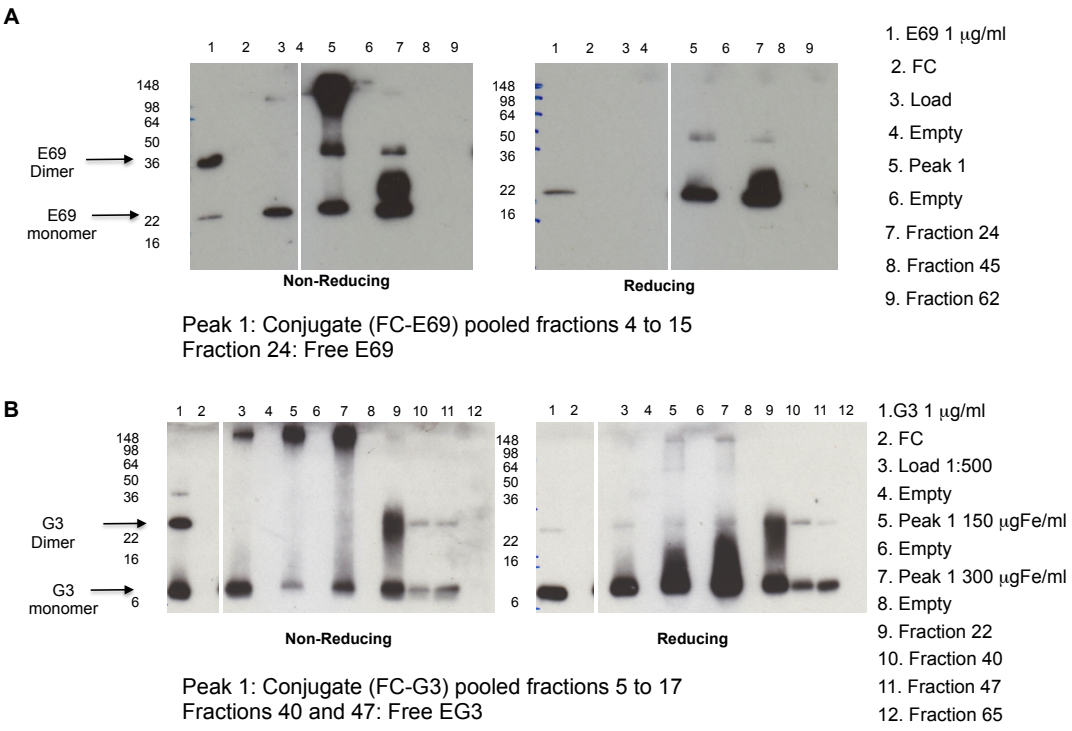

Figure 5.4: Detection of DARPins on the conjugates with western blotting

Samples were run on 16 % SDS-PAGE gel and DARPins detected with anti-E69 (A) or anti-G3 (B) polyclonal mouse sera followed by anti-mouse HRP secondary antibody. **A:** Western blots to detect E69. Under non-reducing conditions; for FC-E69 the majority of E69 could be detected at the top of the gel where FC is expected to be found while under reducing conditions all E69 is found at ~ 22 KDa. **B:** Western blots to detect G3. Under non-reducing conditions the majority of G3 on FC-G3 could be detected at the top of the gel while under reducing conditions all G3 is found at ~ 14 KDa. Load samples are the unpurified conjugates prepared at either 1:1000 for FC-E69 or 1:500 for FC-G3. Control FC samples were prepared at 1 mgFe/ml.

Table 5.1: Characterisation of Ferucarbotran-DARPins conjugates

Sample	Hydrodynamic diameter		Zeta Potential (mV)	
	Z-Average (nm)	PDI	Mean (mV)	Zeta Deviation (mV)
FC	51.51	0.198	-28.3	17.2
FC-E69	74.11	0.230	-32.9	13.7
FC-G3	75.99	0.238	-31.0	8.32

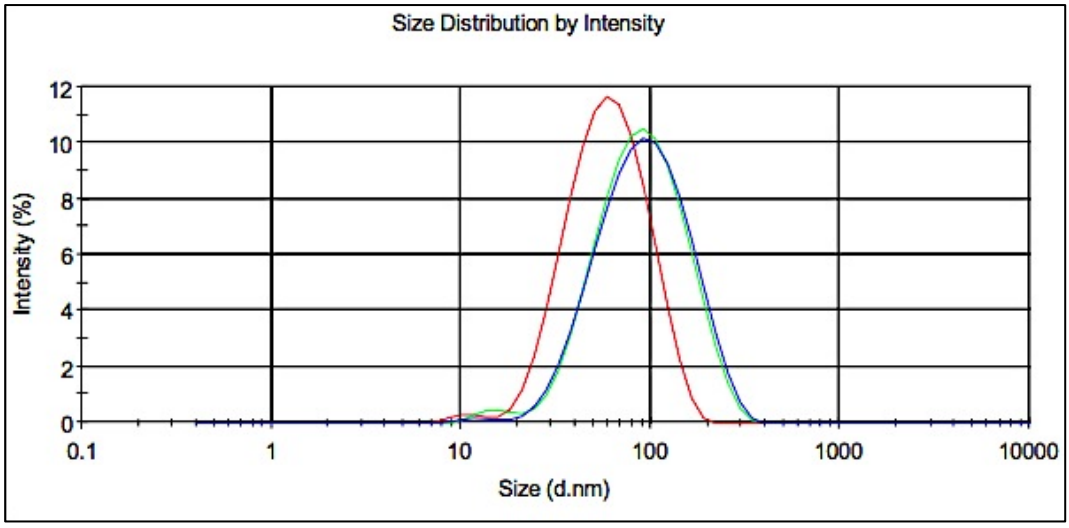

Figure 5.5: Size distribution by intensity of Ferucarbotran conjugates.

DLS measurements showing the size distribution of unconjugated Ferucarbotran (red), FC-E69 (green) and FC-G3 (blue). A clear shift in the size distribution could be seen following the conjugation due to the presence of proteins on the surface of the nanoparticles.

5.2.4 Development of ELISA assays

The ELISA assays were developed with a fluorescently labelled secondary antibody rather than the more commonly used horseradish peroxidase (HRP) 3,3'-diaminobenzidine (DAB) because the brown colour of Ferucarbotran interferes with the DAB signal giving a high background.

5.2.4.1 Indirect ELISA

A schematic presentation of the ELISA layout is shown in Figure 5.6; first the plate was coated with the target protein then the samples were added. Suitable primary and secondary antibodies were then applied to detect the specific binding. Two primary antibodies were used: anti-E69 to detect the DARPins present on Ferucarbotran and anti-dextran to detect Ferucarbotran itself, an anti-mouse-IRDye 800 CW was employed as a secondary antibody, except for Cetuximab treated wells which were detected with an anti-human DyLight 649 antibody and no primary antibody. The signal of the fluorophore labelled secondary antibodies was measured on Odyssey NIR scanner at 700 and 800 nm.

Results are shown in Figure 5.7. In the anti-E69 treated samples, a positive signal was observed with FC-E69 and with the positive controls: E69 and Cetuximab. G3 treated wells showed a small positive signal, this can be due to the cross reaction of anti-E69 with G3 DARPins. However, in the anti-dextran treated wells, all wells treated with Ferucarbotran (regardless of its functionalisation) gave a positive signal. This can be accounted to the unspecific binding of Ferucarbotran samples to the ELISA plate giving false positive results.

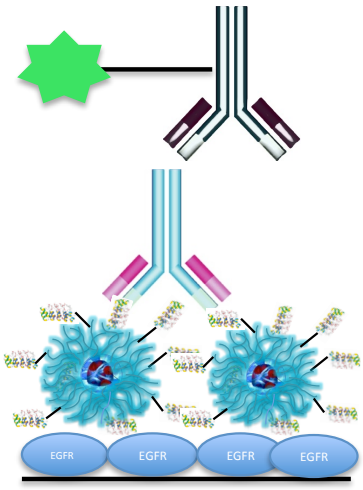

*For Cetuximab: detect with anti-human DyLight 649

Figure 5.6: Indirect EGFR ELISA layout

ELISA plates were coated with EGFR followed by blocking then the addition of samples, primary antibodies and finally the fluorophore labelled secondary antibodies.

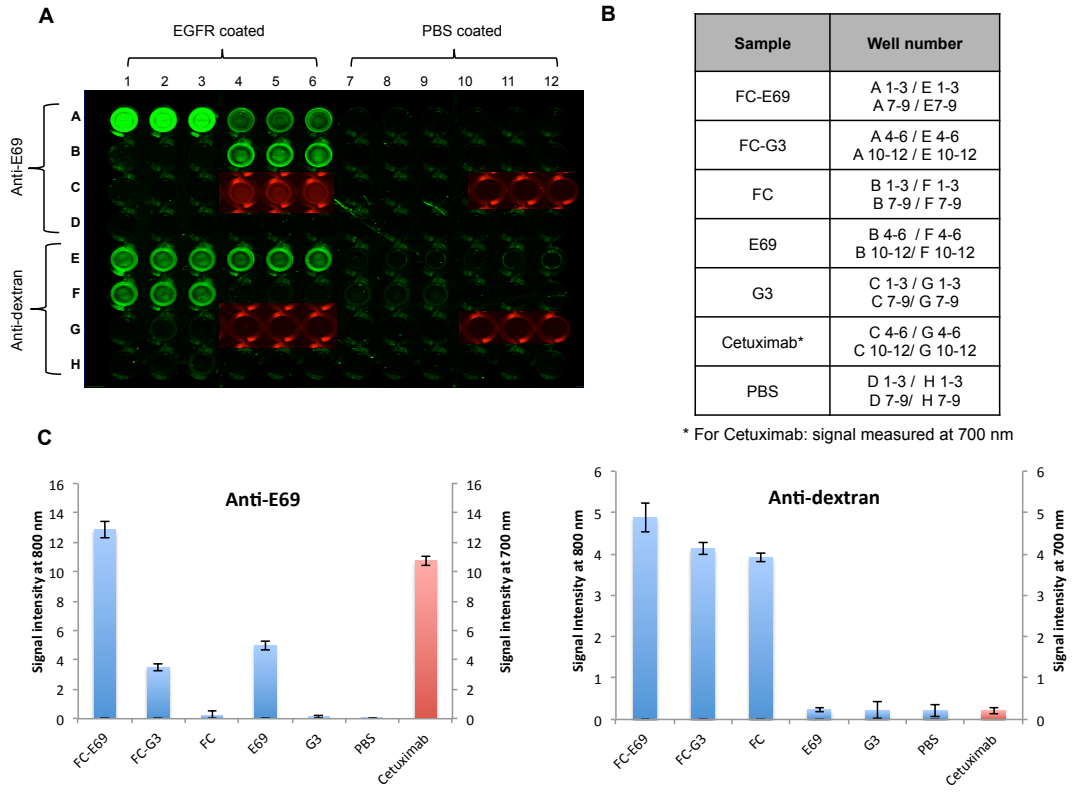

Figure 5.7: Indirect EGFR ELISA results

A: picture of the fluorescence signal obtained from the ELISA plate when measured at 800 nm (green wells) and at 700 nm (for Cetuximab, red wells). **B:** table showing the samples corresponding to each well. **C:** column chart representing the average signal intensity of each sample and error bars are for the standard deviation. In the anti-E69 treated wells: FC-E69, E69 and Cetuximab gave a positive signal. In the anti-dextran treated wells, it became apparent that Ferucarbotran was binding unspecifically to the ELISA plate regardless of the functionalisation. Signals of the PBS coated corresponding controls is subtracted from the signals intensities.

5.2.4.2 Immobilizer plates ELISA

The low hydrophilicity of Nunc™ Amino™ Immobilizer hydrophobic polysorp plates was thought to reduce the unspecific adsorption of the nanoparticles to the surface of the plate. Binding of biomolecules to the Immobilizer plate occurs via covalent linkage of amino or sulfhydryl groups (depending on pH) available on the biomolecules to reactive electrophilic groups tethered on a spacer arm on the surface of the plate (Thermo Fisher Scientific Inc., 2011). EGFR was immobilized on the surface of these plates via sulfhydryl (SH) groups then the samples were added, followed by anti-dextran to detect Ferucarbotran, anti-E69 or anti-G3 to detect E69 and G3 treated wells, respectively. Then the binding was detected using an anti-mouse IRDye 800 CW. For Cetuximab treated wells, an anti-human DyLight 649 was used to detect the binding (Figure 5.8).

Results shown in Figure 5.9 revealed that Ferucarbotran bound non-specifically to the plate regardless of its functionalisation. Furthermore, although Cetuximab showed a positive signal, confirming the presence of EGFR on the plate, the signal observed for E69 was very low. One explanation could be accounted to the random covalent linkage between the plate and EGFR which might have affected the availability of E69 binding sites on EGFR's domain I causing the low positive signal observed, but not the epitope of Cetuximab on domain III of EGFR's extracellular region.

Due to the difficulties in preventing Ferucarbotran from sticking unspecifically to the plastic microtiter plate, a different approach was investigated using sandwich ELISA.

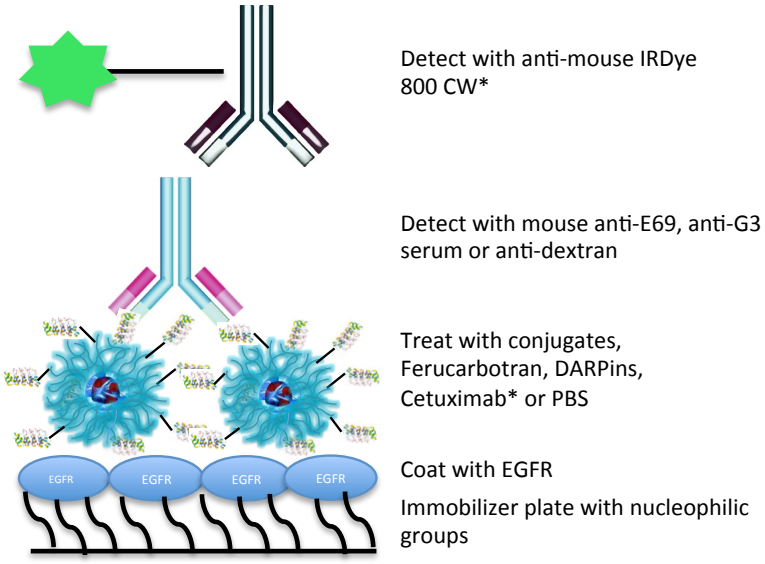

Figure 5.8: EGFR ELISA layout using Nunc™ Amino™ Immobilizer plates

The plates have low hydrophilicity and are designed to have nucleophilic groups on a tethered arm attached to the plastic plate. At pH 7.5 these active sites react with the sulfhydryl groups present on EGFR to covalently link it to the plate. The samples are then added followed by primary and secondary antibodies.

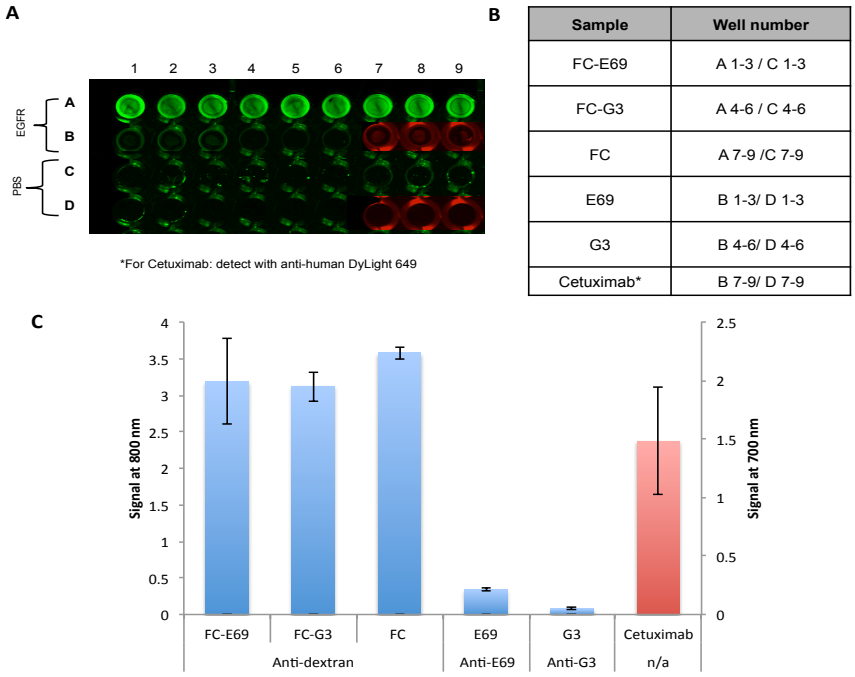

Figure 5.9: EGFR ELISA results using Nunc™ Amino™ Immobilizer plates

Ferucarbotran (FC) bound unspecifically to the plate regardless of conjugation. Cetuximab was able to bind to EGFR while E69 gave a small positive signal. Anti-dextran was used to detect FC and its conjugates, anti-E69 and anti-G3 used to detect E69 and G3. Anti-mouse IRDye 800 CW was used to detect them while Cetuximab was detected with anti-human DyLight 649. **A:** picture of the fluorescence signal obtained from the ELISA plate when measured at 800 nm (green wells) and at 700 nm (for Cetuximab, red wells). **B:** table showing the samples corresponding to each well. **C:** column chart representing the average signal intensity of each sample and error bars for the standard deviation. Signals of the PBS coated corresponding controls are subtracted from the signals intensities.

5.2.4.3 Sandwich ELISA

In this approach the target protein is "sandwiched" between the ligand and the detection antibodies as shown in Figure 5.10. It was hypothesised that this layout would provide a means to overcome non-specific binding of Ferucarbotran to plastic plates. It was made possible because E69 and Cetuximab bind to different epitopes on the EGFR receptor (Boersma *et al*, 2011). Thus the ELISA plate was coated with FC, FC-E69, FC-G3, E69, G3 or PBS. The samples were subsequently incubated with EGFR, which was detected with Cetuximab followed by anti-human DyLight 649. The signal was measured at 700 nm on Odyssey NIR scanner.

Results of the sandwich ELISA, shown in Figure 5.11, demonstrated that this approach is feasible and that E69 is in indeed successfully conjugated to Ferucarbotran in functional form; a positive signal was observed in FC-E69 and E69 treated wells, as they were able to capture EGFR, unlike the rest of the samples. This layout might also give freedom to the EGFR protein to conformationally

orientate itself to bind to E69 immobilized on the surface of Ferucarbotran or on the plate.

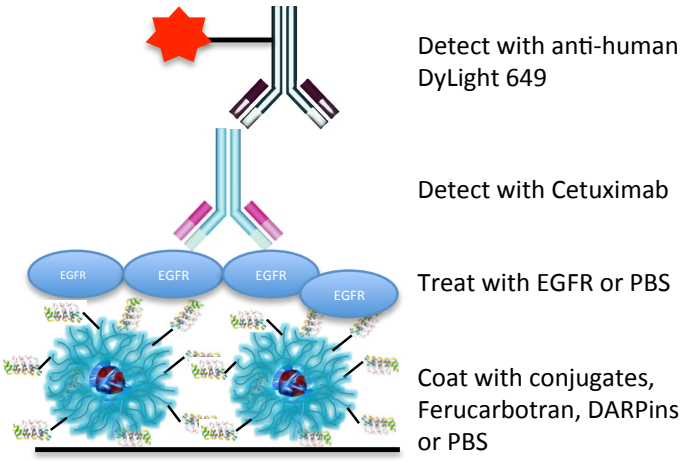

Figure 5.10: Sandwich EGFR ELISA layout

ELISA plate was coated with the samples then the target protein (EGFR) was "sandwiched" between them and Cetuximab. Finally fluorophore labelled anti-human antibody was used to detect the specific binding.

A

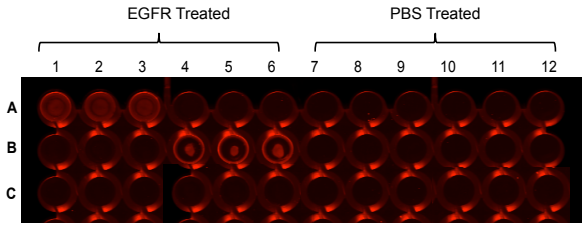

B

Sample	Well number
FC-E69	A 1-3/ 7-9
FC-G3	A 4-6/ 10-12
FC	B 1-3/ 7-9
E69	B 4-6 / 10-12
G3	C 1-3 / 7-9
PBS	C 4-6 / 10-12

C

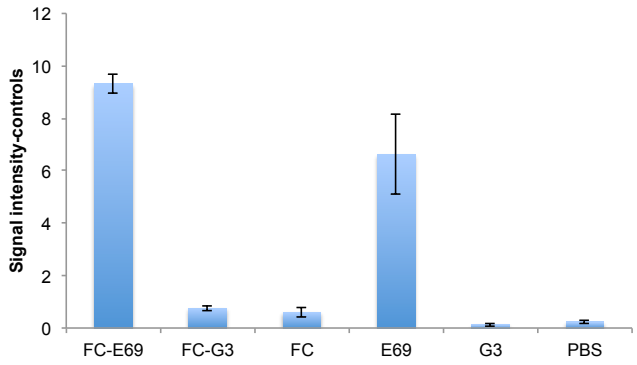

Figure 5.11: Sandwich EGFR ELISA results

Both FC-E69 and E69 showed their ability to capture EGFR and tested positive, unlike the rest of the controls. Signal intensity was measured at 700 nm. **A:** picture of the fluorescence signal obtained from the ELISA plate when measured at 700 nm **B:** table showing the samples corresponding to each well. **C:** column chart representing the average signal intensity of each sample and error bars for the standard deviation. Signals of the PBS coated corresponding controls are subtracted from the signals intensities.

5.2.5 EGFR expression on U-251 MG cells

Having established the binding of FC-E69 to EGFR in ELISA, the conjugates were then evaluated on cells.

U-251 MG, human glioma cell line, was first investigated with the conjugates. U-251 MG cells were previously reported to express intermediate levels of endogenous EGFR (Kang *et al*, 2006; Stea *et al*, 2003; Zhang *et al*, 2005). To further confirm EGFR expression on these cells, western blotting and flow cytometry were employed.

Western blot (Figure 5.12) revealed that U-251 MG cells express moderate levels of endogenous EGFR similar to positive control cells (Hela53). Next, Binding of E69 to U-251 MG cells was confirmed with flow cytometry. Positive controls used were commercially available therapeutic antibodies: Cetuximab (anti-EGFR antibody) and Herceptin (anti-HER2). As shown in Figure 5.13, E69 and Cetuximab tested positive on the U-251 MG cells indicating the expression of EGFR on the cells while both anti-HER2 G3 and Herceptin tested negative.

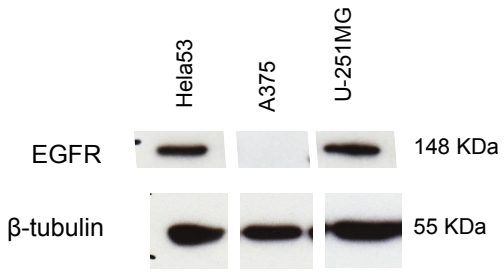

Figure 5.12: Western blot showing EGFR expression on U-251 MG cells

Cell lysates were loaded into a 10% SDS-PAGE gel and EGFR expression was detected with a rabbit anti-EGFR antibody followed by an anti-rabbit HRP antibody. A mouse anti-β tubulin was used as a loading control followed by an anti-mouse HRP secondary antibody. U-251 MG glioma cells tested positive for EGFR similar to positive control (Hela53 cells) while A375 cells were negative for EGFR.

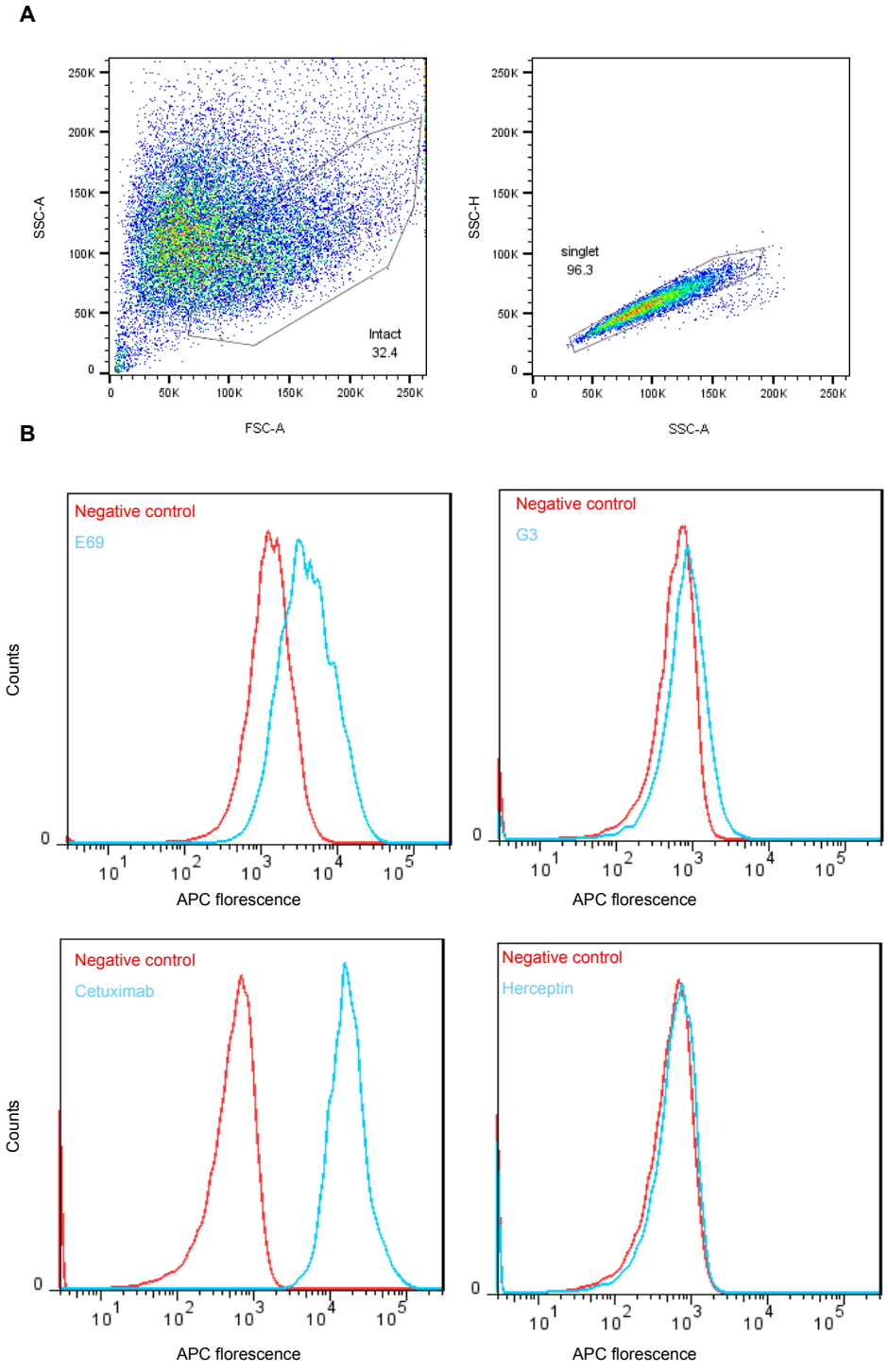

Figure 5.13: Flow cytometry analysis of EGFR expression on U-251 MG cells

A: Gating was done using forward scatter area (FSC-A) and side scatters area (SSC-A) plots to identify intact cell population. Further gating was done to select for the singlet cell population using SSC area versus SSC height. **B:** Cells were treated with DARPins (E69 and G3) and control antibodies (Cetuximab (anti-EGFR) and Herceptin (anti-HER2)) followed by Allophycocyanin (APC) labelled secondary antibodies. For DARPins: the detection antibody (anti-E69 or anti-G3) followed by anti-mouse-APC antibody was used as a negative control, while cells treated with anti-human APC antibody were used as negative control for Cetuximab and Herceptin. E69 and the positive control Cetuximab bound specifically to EGFR (left) with no detected binding for G3 or Herceptin on the cells. APC fluorescence signal is plotted on X-axis versus cell counts.

5.2.6 Uptake of conjugates on U-251 MG cells

Next, the conjugates were tested on the glioma cells and iron content was measured with the ferrozine assay. As seen in Figure 5.14, there was a substantial increase in the uptake of FC-E69 by the cells compared to FC alone. However, the additional control of FC-G3 showed similar uptake to FC-E69, indicating that the apparent specific uptake of FC-E69 is due to an increase in non-antigen specific uptake of the nanoparticles following conjugation. Pre-treatment with DSO4 500 led to a decrease in the unspecific uptake, nonetheless, no increase in the uptake of FC-E69 was seen compared to FC-G3.

The lack of specific binding might have been accounted to the presence of serum proteins in the cell culture media. Serum proteins could be adsorbed on the surface of Ferucarbotran forming a protein corona and masking E69 binding to EGFR. For this reason the binding was tested in the absence of serum. Results (Figure 5.14) revealed a generalised increase in the uptake of FC and its conjugates in the absence of serum. However, no clear difference was observed in the uptake of FC-E69 compared to FC-G3. Blocking this unspecific uptake was achieved by pre-treatment with DSO4 500, but similar to pervious results, no specific uptake of FC-E69 was observed.

Next, the conjugates were investigated on paired EGFR +/- isogenic cell lines for more rigorous studies of non-antigen specific background cell uptake.

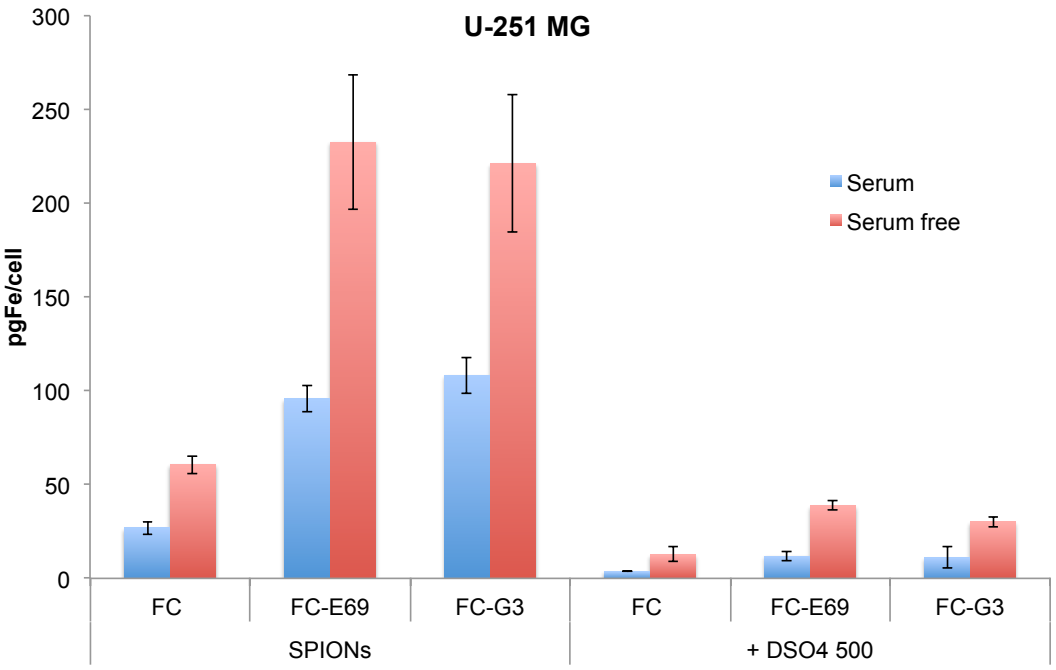

Figure 5.14: Uptake of Ferucarbotran-DARPins conjugates on U-251 MG cells detected with ferrozine assay

Uptake of Ferucarbotran conjugates was investigated on U-251 MG cells in the presence (blue bars) and absence (red bars) of serum. Cells showed an increase in the uptake of FC-E69 and FC-G3 compared to non-functionalised Ferucarbotran, which was further enhanced in the absence of serum. Cells pre-treated with DSO4 500 showed a reduction in the unspecific uptake of Ferucarbotran by the cells; nonetheless, no specific uptake was detected with FC-E69. Bars represent the means of readings of 3 wells/treatment and error bars are for standard deviations.

5.2.7 Selection of isogenic cell models

Retrovirally-transduced EGFR +/- cell lines (293T and SupT1 cells) were kindly provided by Dr Martin Pule's lab (UCL Cancer Institute) and used to develop appropriate cell models to test the FC-E69 conjugates. EGFR and HER2 expression on these cell lines was investigated using western blotting while E69 binding was evaluated with flow cytometry.

5.2.7.1 Western blotting

Results showed that SupT1 and 293T cells tested negative for EGFR but their transduced counterparts were positive (Figure 5.15 A and B). SupT1 cells transduced with EGFR variant III (vIII), were also generated as a negative control because E69 does not bind to this variant. EGFR vIII had a lower molecular weight due to the truncation of part of domain I of the extracellular region of the receptor

(Klausz *et al*, 2011) (Figure 5.15 B). Hela53 cells were used as positive controls while RAW 264.7 and A375 cells were negative controls.

HER2 expression results are shown in Figure 5.15 C. 293T cells expressed HER2 similar to the positive controls (BT 474 cells), while SupT1 cells tested negative for the receptor similar to the negative control cells; MDA-MD 468.

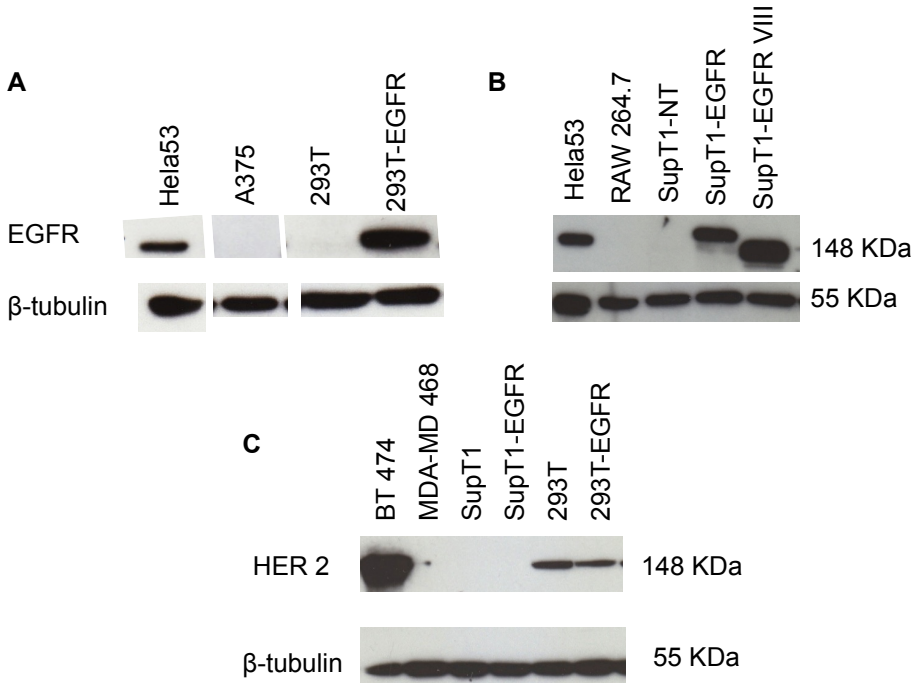

Figure 5.15: Western blots showing EGFR and HER2 expression in different cell lines

Cell lysates were loaded into 7.5% SDS-PAGE gel. Blots were incubated with rabbit anti-EGFR (A and B) or anti-HER2 antibody (C) or mouse anti-β tubulin antibody, as a loading control, before being treated with the corresponding HRP conjugated secondary antibodies. **(A) and (B):** non-transduced 293T and SupT1 cells tested negative for EGFR similar to negative controls (RAW 264.7 and A375 cells). EGFR transduced SupT1 and 293T cells tested positive similar to positive control cells (Hela53). Anti-EGFR antibody reacts with the truncated receptor EGFRvIII as shown in SupT1-EGFRvIII (B), which ran lower than EGFR. **(C)** 293T cells tested positive for HER2 similar to positive control BT 474, while SupT1 cells are negative for HER2.

5.2.7.2 Flow cytometry

Binding of E69 to EGFR was investigated on the isogenic cell lines. The non-transduced cells were used as a negative control to account for cells autofluorescence and detect any unspecific binding.

E69 binding on 293T cells

Cells were gated as shown in Figure 5.16. The gating was done on non-transduced and unstained 293T cells. Cells treated with secondary antibodies only showed no background above the unstained cells (Figure 5.17).

Results showed that whilst both E69 and Cetuximab (positive control) bound strongly to EGFR-transduced 293T cells, both proteins also appeared to bind to non-transduced 293T cells (Figure 5.18), despite the lack of EGFR on these cells (as tested with western blotting, Figure 5.15). This could be due to the very low levels of endogenous EGFR present on 293T cells (Pao *et al*, 2004; Pennock & Wang, 2008). Therefore, although the binding appeared to be stronger in EGFR transduced cells than their non-transduced counterparts (Figure 5.18), the 293T model was considered unsuitable for specific testing of FC-E69 conjugates. Furthermore, 293T cells express HER2 rendering them unsuitable model for testing G3 conjugates (used as control).

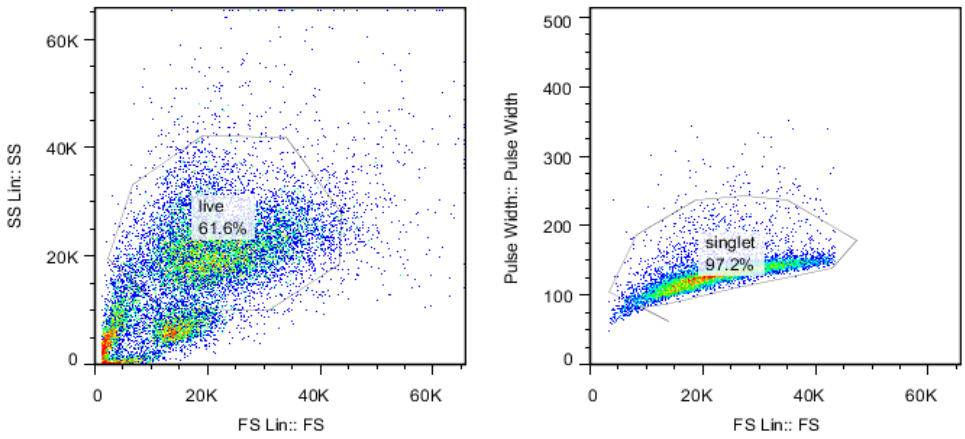

Figure 5.16: Gating for intact singlet cells using unstained and non-transduced 293T cell lines.

Forward (FS) and side scatters (SS) were used to identify intact live cell population in the flow cytometry samples of 293T cells. Further gating was done to select for the singlet cell population using FS versus pulse width plots.

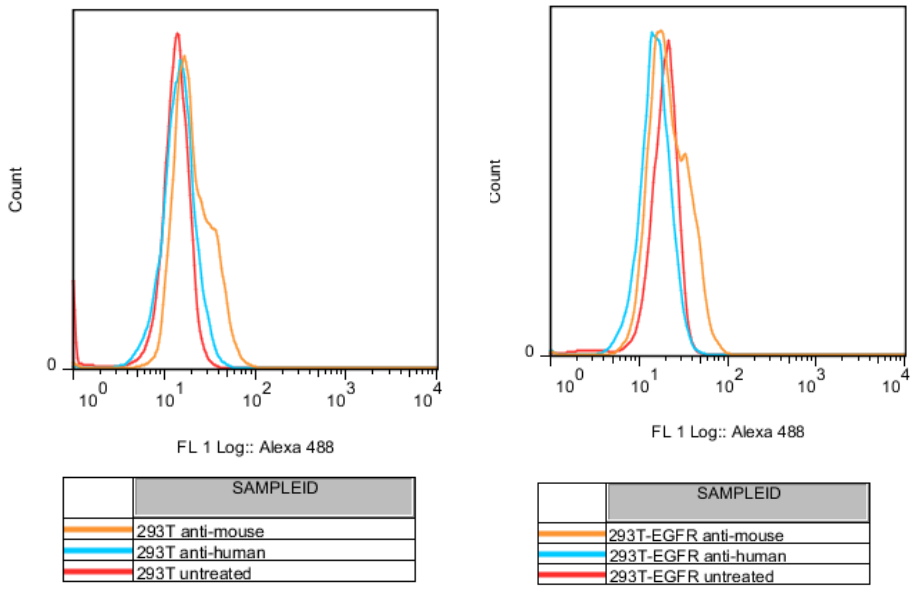

Figure 5.17: Histograms of 293T and 293T-EGFR cells treated with secondary antibodies only

No background was detected when cells were treated with secondary antibodies only (anti-mouse Alexa 488 and anti-human Alexa 488) compared to unstained cells.

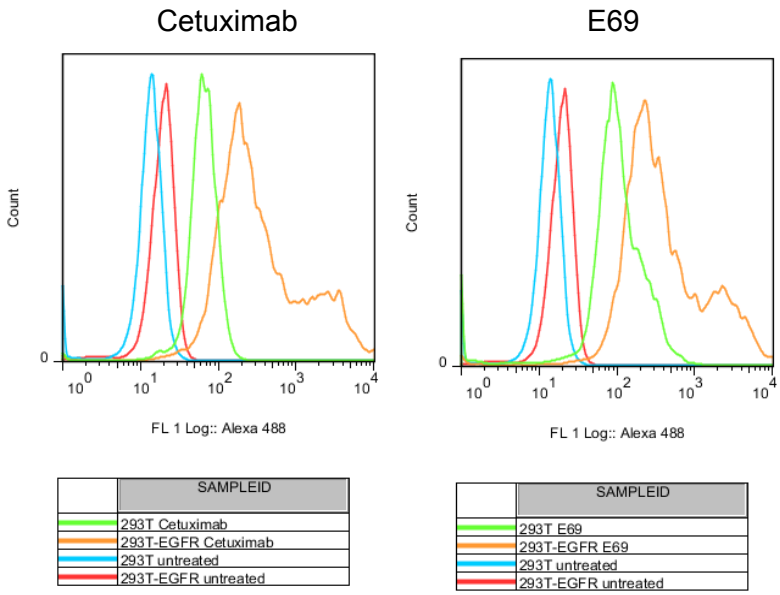

Figure 5.18: Overlay of Cetuximab and E69 binding on EGFR transduced and non-transduced 293T cells.

Cells were treated with E69 and Cetuximab followed by Alexa Fluor 488 labelled secondary antibodies. Compared to untreated controls of both cell lines (blue: 293T and red: 293T-EGFR), a shift in the fluorescence intensity can be seen in both cell lines when treated with Cetuximab and E69. However, a greater shift in the fluorescence can be seen in the EGFR transduced cell lines (orange) compared to non-transduced cells (green). Alex Fluor 488 fluorescence is plotted on X-axis versus cell counts.

E69 binding on SupT1 cells

Three different types of SupT1 cells were tested: the non-transduced cell line (SupT1-NT) was used as negative control; cells transduced with EGFR (SupT1-EGFR) and control cells transduced with EGFRvIII (SupT1-EGFRvIII). Cetuximab and MR1.1 (anti-EGFR and anti-EGFRvIII antibodies, respectively (Klausz *et al*, 2011)) were used as positive controls.

Gating for intact cells in the samples was performed on the unstained SupT1-NT by plotting forward (FS) versus side scatters (SS) (Figure 5.19).

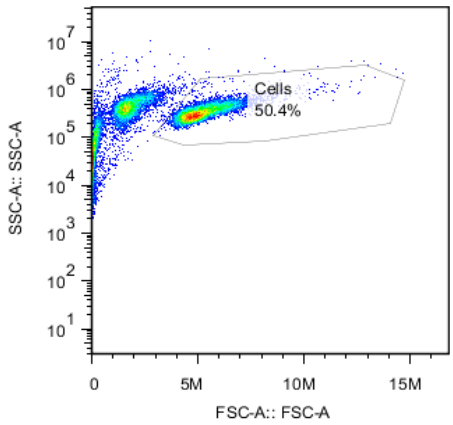

Figure 5.19: Gating applied to select intact SupT1 cells

Forward (FS) and side scatters (SS) were used to identify intact cell population using unstained and non-transduced SupT1 cells as a control.

Results (Figure 5.20) showed that none of the tested proteins bound to SupT1-NT cells. While Figure 5.21 demonstrated that E69 bound specifically to SupT1-EGFR but not to SupT1-EGFRvIII. In contrast, Cetuximab, which is known to cross-react with EGFRvIII, bound to both cell types. G3 (anti-HER2) tested negative on all cell lines.

The possibility that the serum proteins present in the cell culture media might interfere with E69 binding to EGFR was evaluated by flow cytometry. Binding was tested on SupT1-EGFR cells in the presence of different concentrations of foetal bovine serum (FBS) ranging from 0.1 up to 10% in cell culture media (RPMI). No reduction in the binding ability of E69 was detected in the presence of serum as shown in Figure 5.22.

In summary results have shown that SupT1 cells do not express any endogenous EGFR or HER2 rendering them a potentially more suitable model than 293T for testing specific EGFR binding of the FC-E69 conjugates.

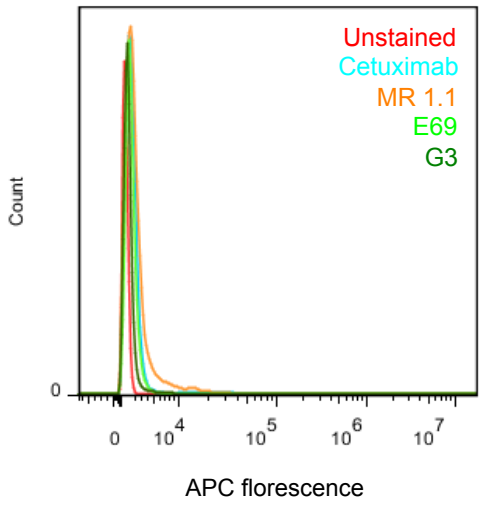

Figure 5.20: Binding of DARPins and control antibodies to SupT1-NT cells

None of the tested antibodies or DARPins bound to the control non-transduced cell line (SupT1-NT). APC fluorescence signal is plotted on X-axis versus cell counts.

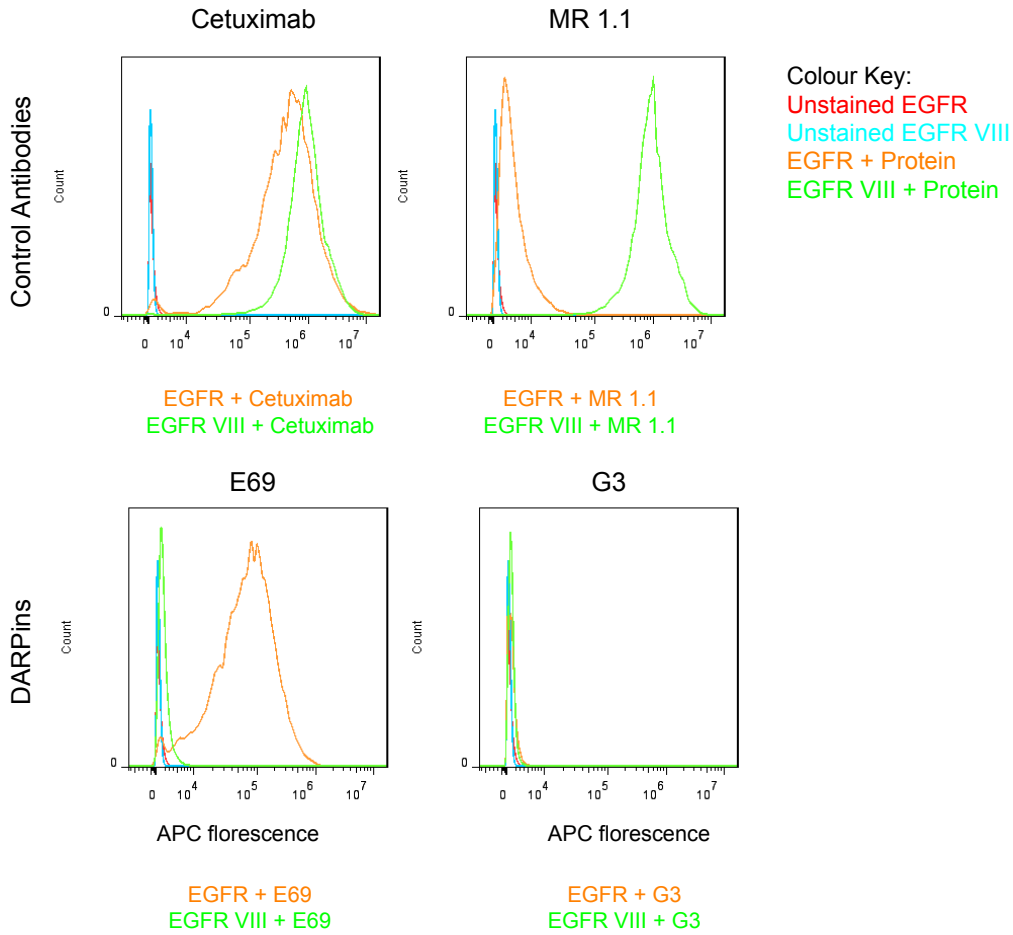

Figure 5.21: Binding of E69 to transduced SupT1 cells (SupT1-EGFR and SupT1-EGFRvIII) using flow cytometry.

Cells were treated with DARPins (E69 and G3) and positive controls (Cetuximab and MR 1.1) followed by APC labelled secondary antibodies. Only E69 bound specifically to EGFR (bottom left) with no detected binding on EGFRvIII cells. Cetuximab (top left) and MR 1.1 (top right) cross-reacted with EGFRvIII and EGFR, respectively. Control anti-HER2 DARPin (G3, bottom right) did not bind to any of the tested cell lines. APC fluorescence signal is plotted on X-axis versus cell counts.

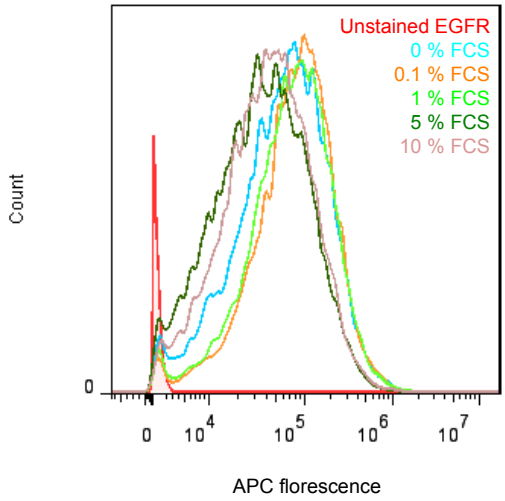

Figure 5.22: E69 binding to SupT1-EGFR cells in the presence of serum

E69 binding to EGFR was challenged in the presence of FBS (0 to 10%) using flow cytometry. No effect on the binding was observed. APC fluorescence signal is plotted on X-axis versus cell counts.

5.2.8 Uptake of conjugates by SupT1 cells

Ferucarbotran and its conjugates were incubated with the different SupT1 cell lines and the intracellular iron uptake was evaluated by ferrozine assay. Results showed that, in standard cell culture conditions, the uptake of FC conjugates was higher than non-functionalised FC, but no EGFR specificity was detected (Figure 5.23 A). This pattern was consistent with results observed with the previously investigated glioma cell line (U-251 MG) (Figure 5.14).

The possibility that serum proteins formed a corona around Ferucarbotran, shielding the DARPins on its surface, was addressed by repeating the experiment in serum free media. Here, a similar pattern of uptake was observed (Figure 5.23 B) but with less differential uptake between the FC conjugates and the non-functionalised FC; in general higher pgFe/cell levels were observed in the absence of serum especially with SupT1-EGFRvIII cells (Figure 5.23 B Vs. Figure 5.23 A). Pre-treatment with DSO4 500 showed a decrease in the unspecific uptake, nevertheless, no increase in the uptake of FC-E69 was seen compared to FC-G3 in SupT1-EGFR cells. Interestingly, it appears that DSO4 500 was less efficient in the presence of serum.

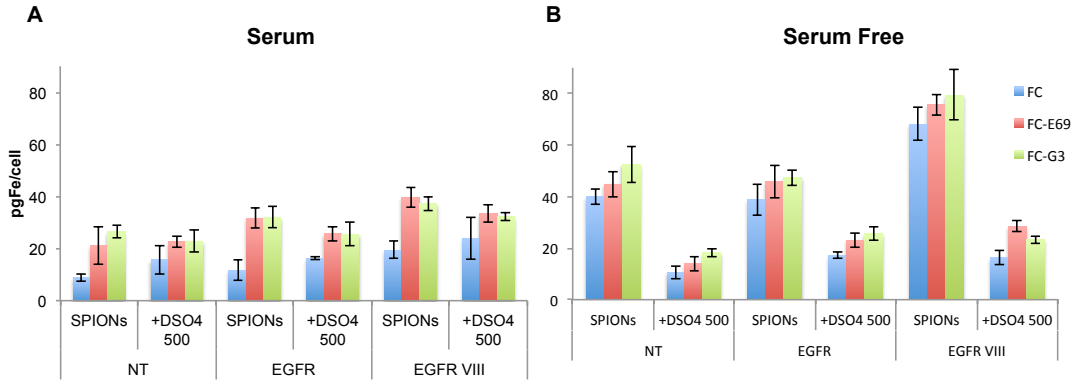

Figure 5.23: Uptake of FC and its conjugates by SupT1 cells

SupT1 cells (NT, EGFR and EGFRvIII) were incubated with SPIONs (FC, FC-E69 or FC-G3) for 4 hours in cell culture media, **(A)** containing serum or **(B)** serum free, with or without pre-treatment with DSO4 500, before being washed, lysed and the iron content measured by the ferrozine assay. No evidence of specific uptake of FC-E69 by SupT1-EGFR cells was detected under the tested conditions. It also appears that DSO4 500 is less efficient in blocking SPIONs uptake by cells in the presence of serum. Results represent average of 3 wells/treatment and error bars are for standard deviation.

5.3 Discussion

The work presented in this chapter describes the development of methods for site-specific attachment of anti-EGFR DARPin to Ferucarbotran and the evaluation of the cancer targeting potential of the conjugates.

Many studies have functionalised SPIONs with proteins (Bouras *et al*, 2015; Kaluzova *et al*, 2015) and most functionalisation strategies utilise random associations to functional groups present on the surface of the targeting protein to link it to the nanoparticles. This is usually achieved via the amino, sulfhydryl or carboxylic groups present on lysine, cysteine or glutamic acid residues, respectively, of the proteins. Nevertheless, the random associations to these amino acids might interfere with the protein's binding site to the target ligand. To overcome this problem, the work presented in this thesis employed a site-specific conjugation strategy to link DARPins to Ferucarbotran. The conjugation was achieved via heterobifunctional linker (BMPH) to a unique C-terminal cysteine tag on the DARPins away from its binding domains, thus maintaining DARPin functionality. The results were particularly encouraging as all other Ferucarbotran conjugation methods investigated in this project were not successful. Furthermore, there is very little published data on Ferucarbotran labelling techniques. Aurich et *al* reported covalently labelling Ferucarbotran with fluorescent markers via reductive amination of the hydroxyl groups (Aurich *et al*, 2012). While another study by Jeon *et al* conjugated Ferucarbotran to doxorubicin via ionic rather than covalent linkage; the positively charged chemotherapeutic drug was loaded on the negatively charged carboxydextran coat of Ferucarbotran (Jeon *et al*, 2014). However, to the best of my knowledge, there have been no published reports on successful attachments of proteins to Ferucarbotran.

Following the conjugation reaction, methods were established to: (i) purify the conjugates and (ii) confirm the success of the conjugation reaction by developing assays to test the presence of DARPins on the surface of the SPIONs. For this purpose Superdex 75, a SEC matrix, was used for purification, furthermore, western blotting and DLS measurements showed the presence of DARPins on the surface of the conjugates. After this analysis, the conjugates were tested for their ability to bind to the target antigen. Developing ELISA assays to confirm the specificity of FC-E69 to EGFR proved to be difficult. Two different microtiter plates were investigated, the hydrophilic Nunc™ MaxiSorp and the hydrophobic Nunc™ Amino™ Immobilizer

plates, where Ferucarbotran bound unspecifically to both plates causing high background signal. To overcome these difficulties, a sandwich ELISA assay was developed in which the strong interaction between Ferucarbotran and the microtiter plate was exploited. Both E69 and FC-E69 tested positive while Ferucarbotran controls (FC and FC-G3) tested negative suggesting specific binding of EGFR to FC-E69.

Despite the promising ELISA results, the specificity of FC-E69 conjugate was lost on cells. These findings direct us back to the challenging cellular interactions of SPIONs, which are still to be fully understood. Prior to functionalisation, the uptake of Ferucarbotran by a wide range of tumour and non-tumour cell lines was investigated in chapter 3. The negatively charged Ferucarbotran was unspecifically internalised by all the tested cells (macrophages, tumour cell lines and NSCs). Thus, it was expected that the same pattern would persist upon functionalisation with DARPins since the conjugates exhibit higher negative charge and bigger hydrodynamic diameters when compared to Ferucarbotran (Table 5.1). However, the conjugates were internalised by the cells more efficiently than the non-functionalised Ferucarbotran. Furthermore, pre-treatment with the blocker DSO4 500, which was previously shown to reduce the unspecific uptake of Ferucarbotran by cells, further highlighted that the increased uptake was not mediated via EGFR as both FC-E69 and FC-G3 uptake by cells was reduced.

The formed protein coronas around nanoparticles upon exposure to serum were reported to occur rapidly and were shown to be extremely complex (Tenzer *et al*, 2013). For instance the study done by Tenzer *et al,* on silica and polystyrene nanoparticles with various sizes and surface charges, revealed a corona of about 300 different proteins formed within seconds of exposure of nanoparticles to human plasma (Tenzer *et al*, 2013). Furthermore, it has been reported that the formed corona around targeted protein-functionalised nanoparticles could shield the binding sites of the protein leading to loss of target specificity (Salvati *et al*, 2013). Therefore, the cell uptake experiments in chapter 5 were repeated in serum free media. Results of these experiments revealed a generalised increase in the uptake of Ferucarbotran by cells regardless of the functionalisation. This increase might be explained by the effect of cell starvation. Smith *et al* have reported a 20-fold increase in the uptake of carboxylated polystyrene nanoparticles by HeLa cells in the absence of serum (Smith *et al*, 2012). Similar findings were also postulated by

Lesniak *et al* in studies done on silica nanoparticles; a higher internalisation efficiency was reported in serum-free media (Lesniak *et al*, 2012).

The concept of targeting nanoparticles to cancer cells has been widely exploited (see introduction sections 1.3 and 1.9). In general the size, charge and surface coatings of the targeted nanoparticles greatly affected their interactions with target cells (Albanese *et al*, 2012; Sun *et al*, 2005; Thorek & Tsourkas, 2008; Vigor *et al*, 2010). Several attempts to target nanoparticles to cancer cells via the EGFR receptor have been reported, either for therapeutic or diagnostic applications (Bazak *et al*, 2014). Targeting nanoparticles to EGFR has been achieved by functionalising them with whole monoclonal antibodies (e.g. Cetuximab) (Bouras *et al*, 2015; Kaluzova *et al*, 2015; Liu *et al*, 2011; Suwa *et al*, 1998), small antibody fragments (e.g. anti-EGFR scFv) (Yang *et al*, 2009) or EGFR ligands (e.g. EGF) (Shevtsov *et al*, 2014). These studies all appeared to show EGFR-specific cellular uptake of nanoparticles, although none of them employed Ferucarbotran, which might explain the discrepancy with the work presented in this thesis. Some postulated reasons for the lack of FC-E69 specificity on cells are:

Firstly, the anionic surface charge of Ferucarbotran greatly affects its interaction with cells as demonstrated here and in chapter 3, leading to high background signal. This property was further enhanced when functionalised with proteins. Successful targeting examples found in literature utilised SPIONs coated with neutral dextran (Shevtsov *et al*, 2014; Vigor *et al*, 2010), which exhibit low background uptake in cells. For instance, the study done by Shevtsov *et al*, 33 nm dextran coated SPIONs were functionalised with EGF and showed specific uptake by EGFR expressing C6 glioma cell line (Shevtsov *et al*, 2014).

Secondly, direct comparison between EGFR targeted Ferucarbotran and published material is difficult, because cellular interactions of nanoparticles are governed by their individual physicochemical properties (Albanese *et al*, 2012; Sun *et al*, 2005; Thorek & Tsourkas, 2008; Vigor *et al*, 2010). For instance, in the study done by Kaluzova *et al* and Bouras *et al*, PEG (MW 2000) coated iron oxide nanoparticles (IONPs) were functionalised with Cetuximab, an anti-EGFRvIII antibody and a control human IgG antibody. The negatively charged nanoparticles were internalised by the cells before functionalisation, similar to the findings presented here. Nevertheless, the study reported that specific uptake of Cetuximab-IONPs could be detected above the background signal of IONPs in EGFR expressing cell lines

leading to enhanced cytotoxicity (Bouras *et al*, 2015; Kaluzova *et al*, 2015). When compared to Ferucarbotran, the investigated PEG nanoparticles were relatively small (11 and 20 nm for IONPs and IONPs-Cetuximab, respectively), which are around 4 to 5 times smaller than Ferucarbotran (51 nm) and its DARPins conjugates (~75 nm), making direct comparison difficult. In contrast with their findings, specificity of anti-CEA scFv functionalised SPIONs to CEA was lost when charged PEGylated-dextran coated SPIONs were used compared to neutral dextran coated ones (Vigor *et al*, 2010). These contradicting findings emphasize that a case-by-case examination of targeted nanoparticles is crucial.

Thirdly, DARPins are inherently different in structure and size compared to whole antibody (Cetuximab) investigated in most studies (e.g. (Bouras *et al*, 2015; Kaluzova *et al*, 2015)); E69 is 21 KDa compared to 150 KDa for whole antibody. Although both E69 and Cetuximab, when compared in the same experiment, showed high affinity and specificity to EGFR, the presence of the protein on the surface of the nanoparticles makes the interaction more complex. The DARPins might be buried within the dextran coat of Ferucarbotran making them less available for binding.

Finally, a critical look at some published studies has revealed some concerns in cell assays studying targeting SPIONs to cancer cells. Most studies investigate the uptake of functionalised SPIONs in two different types of cancer cells lines: one expressing the target protein and the other showing no detected expression (e.g. (Fan *et al*, 2011; Vigor *et al*, 2010)). The work presented in chapter 3 has revealed that this could be problematic; as it appears that cancer cells internalise SPIONs with different capacities, with some able to accumulate high pgFe/cell concentrations, while in others barely detectable levels were observed. Therefore the use of isogenic +/- cell lines might provide a better-controlled system. Furthermore, some studies compare the functionalised SPIONs to the non-functionalised counterparts (e.g. (Fan *et al*, 2011; Shevtsov *et al*, 2014)), flagging another concern. If FC-E69 was compared to Ferucarbotran only, one might have concluded specific false positive results if the control FC-G3 was not added. Therefore, to better interpret experimental results, SPIONs should be functionalised with a null-binder targeting moiety with similar size and/or structure to the targeting protein. The lack of binding of FC-E69 conjugates in the established well-controlled cellular models has highlighted these concerns.

5.4 Summary and conclusions

A method to site specifically conjugate Ferucarbotran to a cancer-targeting agent was developed. Conjugates were purified using SEC and the success of the conjugation was confirmed with western blotting and DLS measurements. The specific uptake of FC-E69 conjugates by EGFR was evaluated with ELISA and cellular assays. FC-E69 specifically bound to EGFR in ELISA, nevertheless, no specific binding was detected on cells.

In conclusion, the work presented here has revealed crucial findings; Ferucarbotran can be functionalised with cancer-targeting agents but this does not necessarily lead to cell-specific uptake. SPIONs interact differently with cells when functionalised with a protein on their surface. This altered behaviour might be mistaken as false positive results and therefore it is of utmost importance to add the relevant experimental controls to correctly interpret the results.

Chapter 6
Fractionation of Ferucarbotran using Size Exclusion Chromatography

Maha Abdollah

6.1 Introduction

Ferucarbotran has been shown to have good heating potential both *in vitro* and *in vivo* (see section 1.7). This, together with the established safety profile of Resovist® makes it an excellent candidate to develop for localised hyperthermia in the clinic. However, Ferucarbotran is composed of a mixture of SPIONs with different hydrodynamic diameters ranging from 45-65 nm (product information sheet). This heterogeneity is a draw back for hyperthermia applications because the SPION size is related to its heating potential at a given frequency (Gonzales-Weimuller *et al*, 2009). Such heterogeneity can result in an ill-defined mixture of therapeutic agents, with possibly some particles being ineffective. Therefore, it becomes crucial to optimise nanoparticle preparations to reduce polydispersity (Kowalczyk *et al*, 2011) and achieve improved magnetic heating characteristics (Jordan *et al*, 2003). It was hypothesised that this could be achieved by fractionating SPIONs and selecting fractions with the best magnetic heating properties. It is proposed that more defined Ferucarbotran, with greater heating potential, would have new application in the emerging field of magnetic hyperthermia as anti-cancer treatment (see sections 1.6.4, 1.7 and 1.8).

Fractionation of nanoparticles has been achieved via centrifugation, filtration or chromatographic techniques which are dependent on the particle size and shape (Kowalczyk *et al*, 2011). For magnetic nanoparticles the two main methods used are: SEC (Nunes & Yu, 1989; Rheinländer *et al*, 2000a; Rheinländer *et al*, 2000b) and magnetic separation (Ishihara *et al*, 2013; Jordan *et al*, 2003; Rheinländer *et al*, 2000a).

Magnetic separation separates nanoparticles based on their magnetic moments as they pass through a column packed with magnetic spheres in the presence of magnetic field gradients. Magnetic size separation has been correlated with the nanoparticles core diameter which affects their magnetic moments (Aurich *et al*, 2012; Rheinländer *et al*, 2000b).

SEC is the separation of molecules based on their sizes as they pass through a column packed with a gel filtration matrix (Barth *et al*, 1996; GE-Healthcare, 2014; Rheinländer *et al*, 2000b). The matrix consists of porous beads; as the sample passes through the matrix, large molecules are eluted first while smaller ones get trapped in the matrix pores and thus are eluted later (GE-Healthcare, 2014) (see

Figure 6.1). As shown in the theoretical chromatogram in Figure 6.1 C, high molecular weight components are eluted first either in the column void volume or as the first peaks depending on the column's cut off, followed by the intermediate then the small molecular weight components. Therefore SEC relies on the hydrodynamic diameter of nanoparticles, which include both the nanoparticles' core and coat. Nevertheless, Rheinländer *et al* showed that the core diameter usually correlates with the overall hydrodynamic diameter of the nanoparticles (Rheinländer *et al*, 2000a). Therefore one can conclude that although the two separation methods rely on completely two different characteristics of magnetic nanoparticle they render similar results (Rheinländer *et al*, 2000a).

6.1.1 Experimental approach

The work presented in chapter 6 investigated both methods of fractionation with a special emphasis on SEC, a much gentler method usually employed for separation of proteins (Barth *et al*, 1996). Three different SEC matrices were investigated for their ability to fractionate Ferucarbotran: Sephadex G-100, Superdex Prep Grade (75 and 200) and Superose Prep Grade (6 and 12). The properties of the different media investigated are shown in Table 6.1.

Fractionated Ferucarbotran was characterised with DLS and tested for heating potential. The most commonly used measurements for magnetic heating ability of SPIONs are either the specific absorption rate (SAR) or the intrinsic loss power (ILP) (Wildeboer *et al*, 2014). SAR is an extrinsic parameter defined as the heating power generated per unit mass of magnetic nanoparticles (Wildeboer *et al*, 2014) and is represented in Equation 6.1. While, the intrinsic loss power is an intrinsic system independent parameter, which relies on the heating capacity of the magnetic nanoparticle (Kallumadil *et al*, 2009; Wildeboer *et al*, 2014) and is represented in Equation 6.2. ILP is generally considered more reliable and therefore was used in this chapter as a measure of the heating ability of fractionated Ferucarbotran.

$$SAR = \frac{\Delta T}{\Delta t}\frac{C}{mFe}$$ **Equation 6.1**

$$ILP = \frac{SAR}{\mathrm{H}^2 f}$$ **Equation 6.2**

Where SAR (Wg^{-1}) is specific absorption rate; ΔT is the change in temperature; Δt change of time; C (Jg^{-1} K^{-1}) is the heat capacity per unit mass of fluid; mFe (g) is the iron mass in the fluid per unit mass of fluid, ILP ($Hm^2 g^{-1}$) is the intrinsic loss power, H is the strength of the alternating magnetic field (AMF) and f (Hz) is the frequency of AMF.

6.1.2 Research Aims and Objectives

Aim: To fractionate Ferucarbotran into more uniform solution with improved heating potential.

Objectives:

- Evaluate different SEC matrices for their ability to fractionate Ferucarbotran into different sizes.
- Analyse Ferucarbotran fractions with DLS and magnetic hyperthermia heating ability.

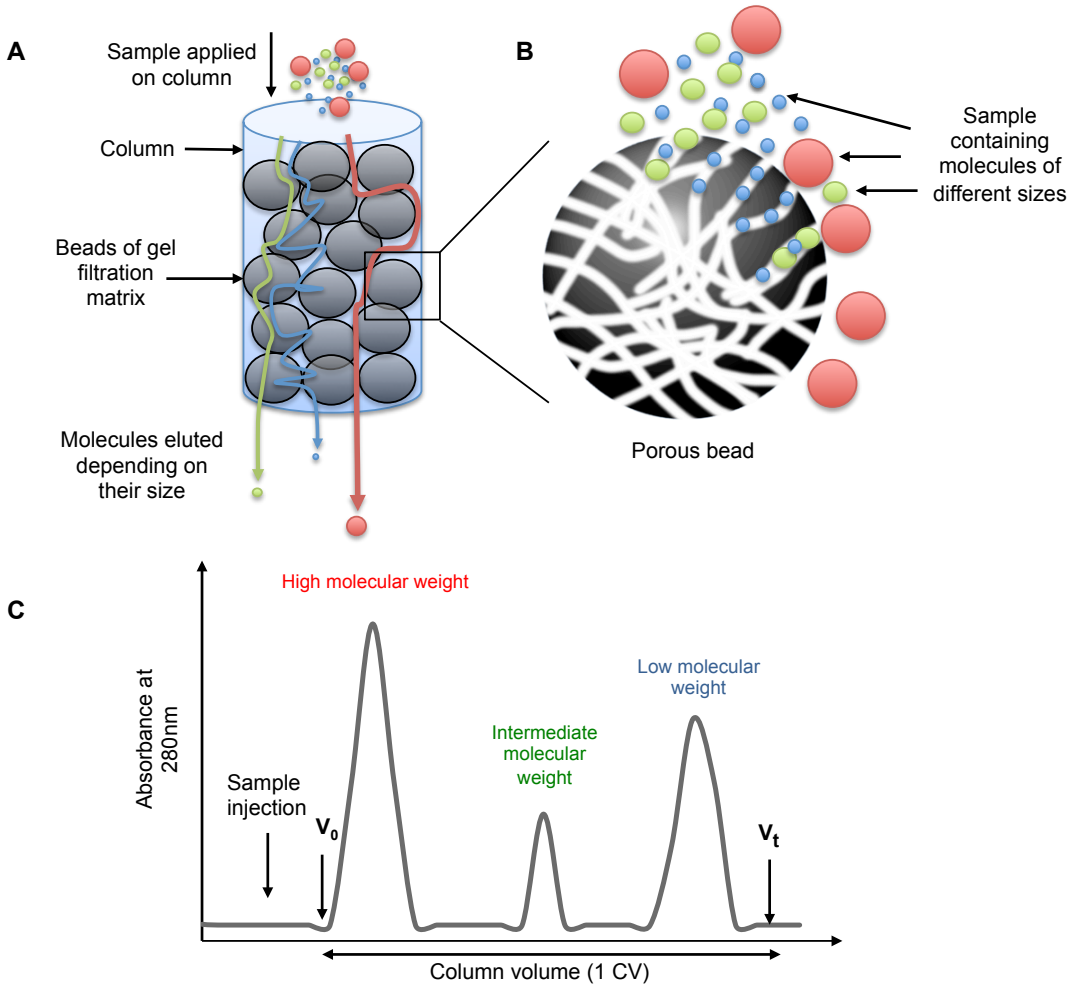

Figure 6.1: Principles of size exclusion chromatography

A: Schematic presentation of a SEC column packed with gel filtration matrix as a sample containing molecules of different sizes pass through it. **B:** Zoomed in schematic presentation of a single bead. A gel filtration matrix is made of porous beads with different pore sizes; large molecular weight molecules (red circles, B) are the quickest to pass through the column (red arrow, A), as they are not trapped within the pores and therefore are eluted first, unlike intermediate (green) and small (blue) molecules that are eluted in later fractions. **C:** Theoretical chromatogram of a typical elution profile. Void volume (V_0): the volume equivalent to ~30% of total column volume and is the volume external to the column pores. Large molecules are expected to elute in or just after the void volume depending on the column cut off. Total volume (V_t): is the total volume of the column from sample injection to the last eluted peak. Column volume (CV) is the volume between V_0 and V_t.

Table 6.1: General properties of gel filtration media investigated in this chapter

Information from (GE-Healthcare, 2014).

Medium	Bead size (µm)	Compositions	Fractionation range for dextran	Fractionation range for globular proteins
Sephadex G-100	100-310 (wet)	Cross-linked dextran	1-100 KDa	4-150 KDa
Superdex 75 Prep grade	24-44	Composite of cross-linked agarose and dextran	0.5-30 KDa	3-70 KDa
Superdex 200 Prep grade	24-44		1-100 KDa	10-600 KDa
Superose 6 Prep grade	30-40	Highly cross-linked agarose	n/a	5-5000 KDa
Superose 12 Prep grade	30-40		n/a	1-300 KDa

KDa: Kilo Daltons, n/a: not available

6.2 Results

6.2.1 Magnetic separation of Ferucarbotran using MACS® LS column

Magnetic separation of Ferucarbotran was performed on commercially available MACS LS columns used with QuadroMACS™ Separator.

Magnetic separation protocol was adapted from the guidelines provided by the manufacturer. Initially 50 μg of Ferucarbotran was applied on the column and the amount of iron recovered at each stage was calculated; 21.34% of the sample was lost in the first wash while only 35.6% was eluted from the column and 34.8% appears to have irreversibly bound to the column. This was considered as poor recovery of the sample and might be due to insufficient binding of Ferucarbotran to the magnetic column. Therefore a lower amount of 20 μg iron was tested in an attempt to improve recovery. A small improvement was observed as 40.1% of the sample was successfully eluted from the column while 23.4% was irreversibly bound to the column. These results were disappointing and this method was thought not to be suitable for the separation of Ferucarbotran.

Table 6.2: Results of purification of Ferucarbotran using MACS columns

	50 μgFe loaded		**20 μgFe loaded**	
	μg of iron	% of sample	μg of iron	% of sample
Flow through	1.17	2.34	0.67	3.36
Wash 1	10.67	21.34	4.66	23.30
Wash 2	1.49	2.97	1.09	5.47
Wash 3	1.44	2.87	0.88	4.39
Eluted	17.81	35.62	8.02	40.10
Total		**65.13%**		**76.6%**
Irreversibly bound		**34.8%**		**23.4%**

6.2.2 Size exclusion chromatography (SEC)

Next, a number of SEC media were investigated for their ability to fractionate Ferucarbotran. Despite the information available by GE-Healthcare (SEC media manufacturer) regarding the fractionation range of each SEC media (see Table 5.1), the interaction of Ferucarbotran with SEC beads is unpredictable. Furthermore, the exact molecular weight of Ferucarbotran is unknown and therefore 5 different media were investigated.

6.2.2.1 Sephadex G-100 and Superdex 75 Prep Grade

Sephadex G-100

The first matrix investigated was Sephadex, a media prepared by cross-linking dextran with epichlorohydrin. Sephadex G-25 (MW cut off = 5 KDa) had been previously used to purify Ferucarbotran from NIR dyes (used in chapter 4). Encouragingly, these experiments showed that Ferucarbotran did not bind irreversibly to Sephadex. However, Ferucarbotran was eluted unfractionated in the void volume i.e. too large to enter the column matrix, indicating that Sephadex with higher MW fractionation range would be more suitable leading to the investigation of Sephadex G-100. However, results for Sephadex G-100 showed that Ferucarbotran still eluted in a single peak in the column's void volume (Figure 6.2), making the matrix unsuitable for size fractionation of Ferucarbotran. In addition, due to the compressible nature of the matrix it was necessary to perform the purification process at very low flow rates, rendering the process time consuming. Therefore a number of other non-compressible hard matrices were evaluated for applicability (e.g. Superdex). Superdex matrix provides a combination of the high-resolution capacity of cross-linked dextran (e.g. Sephadex) as well as the rigidity and the stability of highly cross-linked agarose (e.g. Superose) (GE-Healthcare, 2014).

Superdex 75

As previously shown in chapter 5, Superdex 75 eluted Ferucarbotran-DARPins conjugates unfractionated in the column's void volume (Figure 5.3). Nonetheless, the conjugates were shown to be 22-24 nm bigger in size when compared to unconjugated Ferucarbotran (see Table 5.1). In addition, the presence of a protein on the surface of the SPIONs might interfere with their interaction with the chromatography media. Therefore a sample of unconjugated Ferucarbotran was loaded into the column and as previously described was eluted as a single peak in

the column's void volume (Figure 6.2). This indicates that Superdex 75, as with Sephadex G-100, is unsuitable for size fractionation of Ferucarbotran.

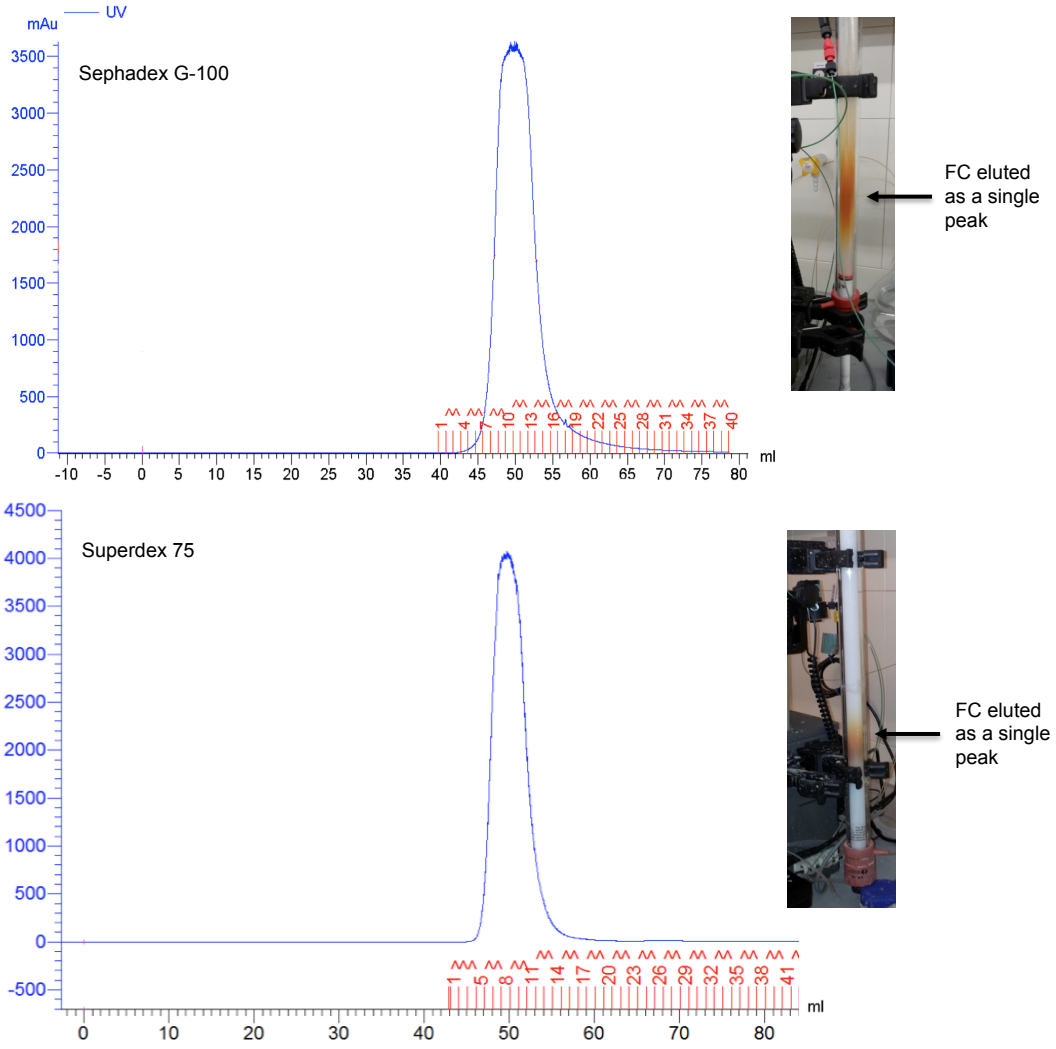

Figure 6.2: Chromatogram of Ferucarbotran elution on Sephadex G-100 and Superdex 75 packed columns

Ferucarbotran (brown) is eluted as a single peak in the column void volume as shown in both the chromatograms and the pictures.

6.2.2.2 Superdex 200

SEC matrices with higher fractionation ranges were explored. First Superdex 200 was investigated. It has a wide fractionation range and was found to fractionate Ferucarbotran into 2 distinct peaks (Figure 6.3). The 2 peaks of Ferucarbotran were investigated with DLS and results revealed that peak 1 (fractions 2-12) had a Z-average hydrodynamic diameter of 70.88 nm while peak 2 (fractions 14-41) was 27.2 nm in diameter. The heating potential of both peaks was subsequently

evaluated by measuring the temperature profile of the fractionated samples during exposure to the alternating magnetic field. Results revealed that the larger nanoparticles were effective generators of heat with an intrinsic loss of power (ILP) of 3.65 versus 1.07 for the smaller ones (Figure 6.4).

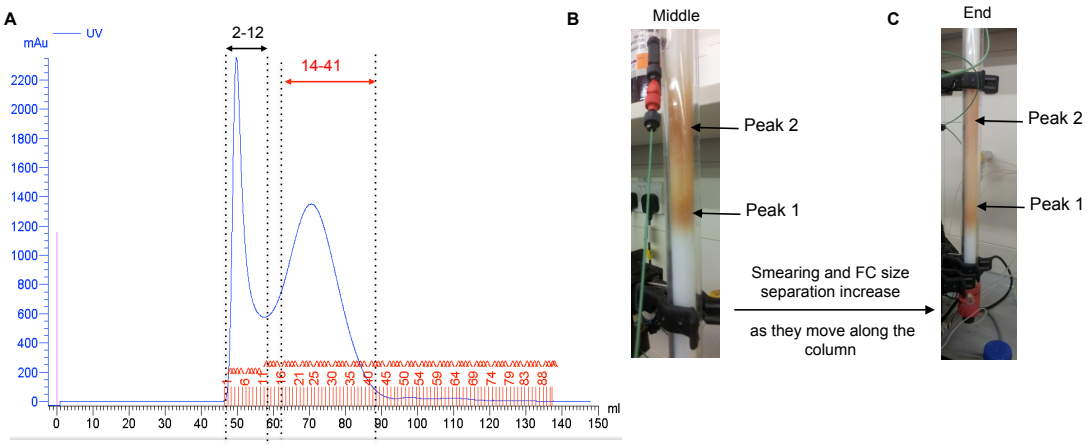

Figure 6.3: Elution profile of Ferucarbotran on Superdex 200

A: Chromatogram of Ferucarbotran loaded on a column packed with Superdex 200, Ferucarbotran was eluted in 2 peaks, peak 1: fractions 2-12 and peak 2: fractions 14-41. **B and C:** pictures of the column showing the 2 peaks of Ferucarbotran (brown).

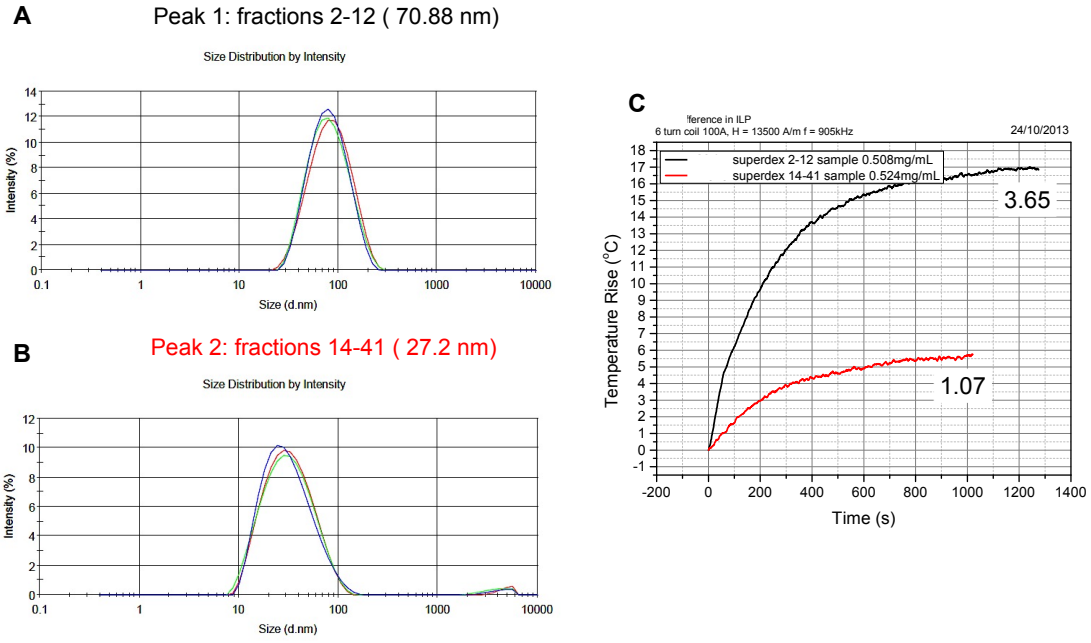

Figure 6.4: Characterisation results of fractionated Ferucarbotran on Superdex 200

Ferucarbotran peaks were pooled into fractions 2-12 which when measured on DLS had a Z-average hydrodynamic diameter of 70.88 nm and ILP of 3.65 (black curve, C) while fractions 14-41 were 27.2 nm in diameter with an ILP of 1.07 (red curve, C).

6.2.2.3 Superose

Superose 6 and Superose 12 were also investigated for their ability to fractionate Ferucarbotran. Superose medium is composed of highly cross-linked porous agarose particles with broad fractionation range.

Superose 12 Prep Grade

Results showed that, on the Superose 12 packed column, Ferucarbotran was separated in a single peak with a shoulder indicating poor and incomplete separation of the different sized particles (Figure 6.5). Superose 12 Ferucarbotran fractions 3-10 were pooled as peak 1 and the shoulder fractions (11-24) were pooled and named “shoulder”. DLS revealed that peak 1 had a uniform size distribution with a Z-average hydrodynamic diameter of 59.88 nm and a PDI of 0.203. The shoulder had a Z-average hydrodynamic diameter of 36.30 nm and PDI of 0.680 (Figure 6.6). The ILP of both peaks was measured revealing that peak 1 had a higher heating potential with an ILP of 2.59 while the shoulder has a very low ILP of 0.59 (as shown in Figure 6.7).

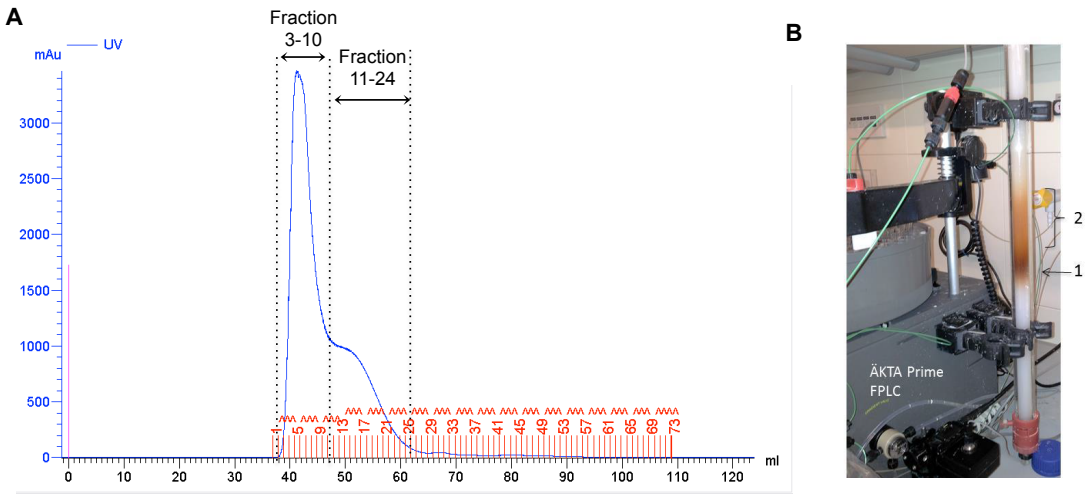

Figure 6.5: Separation of Ferucarbotran on Superose 12 packed column.

A: Ferucarbotran was eluted from the column in a peak (1) and a small shoulder (2), as also seen in the image of the column.

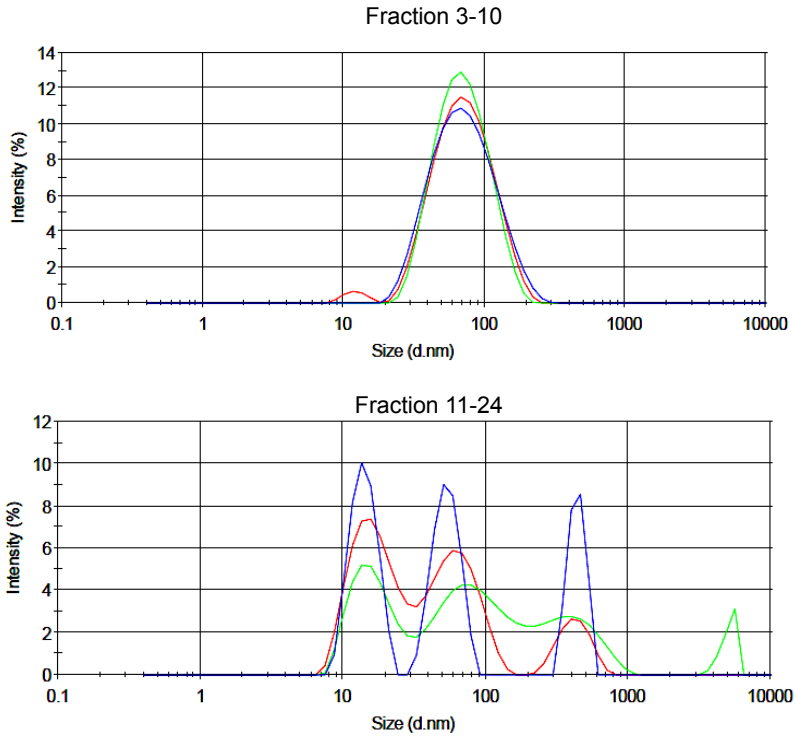

Figure 6.6: Characterisation of the different peaks of Ferucarbotran eluted on Superose 12 packed column using DLS.

Peak 1 (fractions 3-10) appears to have a uniform size distribution with a Z-average hydrodynamic diameter of 59.88 nm compared to the shoulder (fractions 11-24), which appear to be non-uniform.

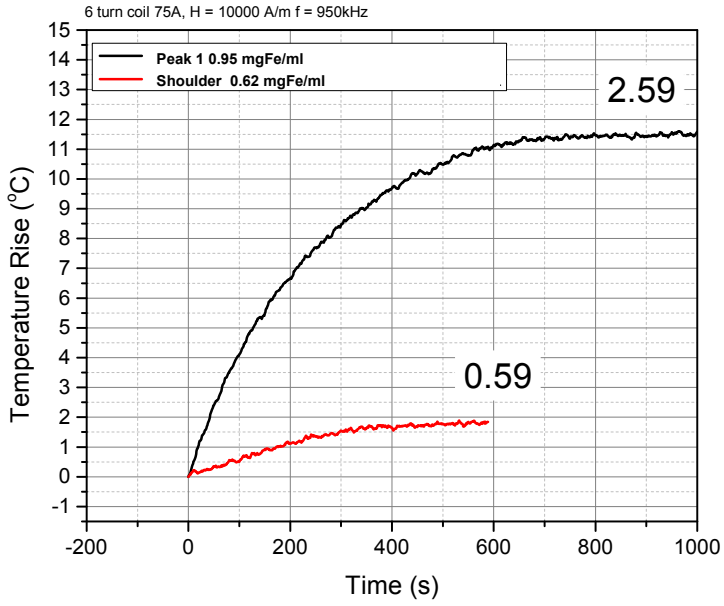

Figure 6.7: Heating profile of fractionated Ferucarbotran

Peak 1 (black) appears to have superior heating properties when compared to the shoulder (red). Although the samples were tested at different concentrations, the ILP is a concentration-independent value. Peak 1 had an ILP of 2.59 compared to 0.59 for the shoulder fraction.

Superose 6 Prep Grade

Ferucarbotran was also tested on Superose 6; this media has the widest fractionation range (Table 6.1). On this matrix, Ferucarbotran was separated into 3 pools of fractionated samples (Figure 6.8). Fractions 4-10 contained a distinct peak (peak 1), fractions 11-27 formed an indistinct peak where the trace did not return to baseline and fractions 28-47 formed a second distinct peak (peak 3). DLS measurements revealed that the peaks had a Z-average hydrodynamic diameter of 79.34 nm, 42.06 nm and 24.25 nm for peak 1, 2 and 3 respectively (Figure 6.9). ILP measurements of the 3 peaks revealed that peak 1 had the best heating potential (ILP=3.8), being superior to the other 2 peaks and the unfractionated starting material (ILP=1.4) (Figure 6.10).

Visual inspection of the fractions running through the Superose 6 packed column (Figure 6.8) revealed that most of the SPIONs within Ferucarbotran are eluted in the later fraction (peak 3) meaning that they are the small nanoparticles with poor heating properties (ILP= 0.04).

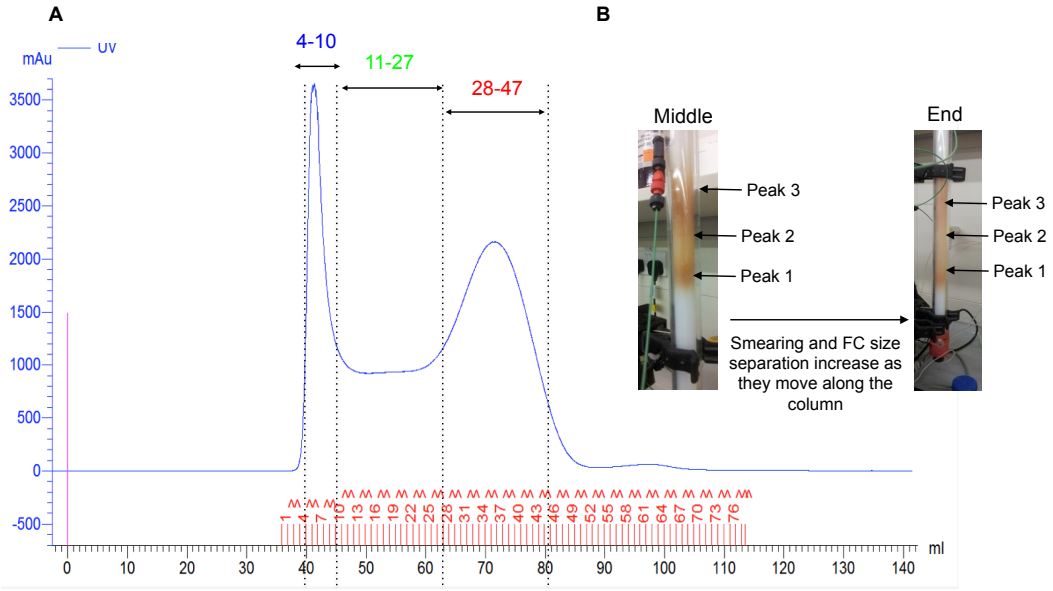

Figure 6.8: Chromatogram of fractionation of Ferucarbotran on Superose 6

(A) Chromatogram showing Ferucarbotran separated into 2 distinct peaks that did not return to baseline and were subsequently shown to be 3 overlapping peaks. **(B)** Picture of the column showing the three distinct populations of Ferucarbotran (brown).

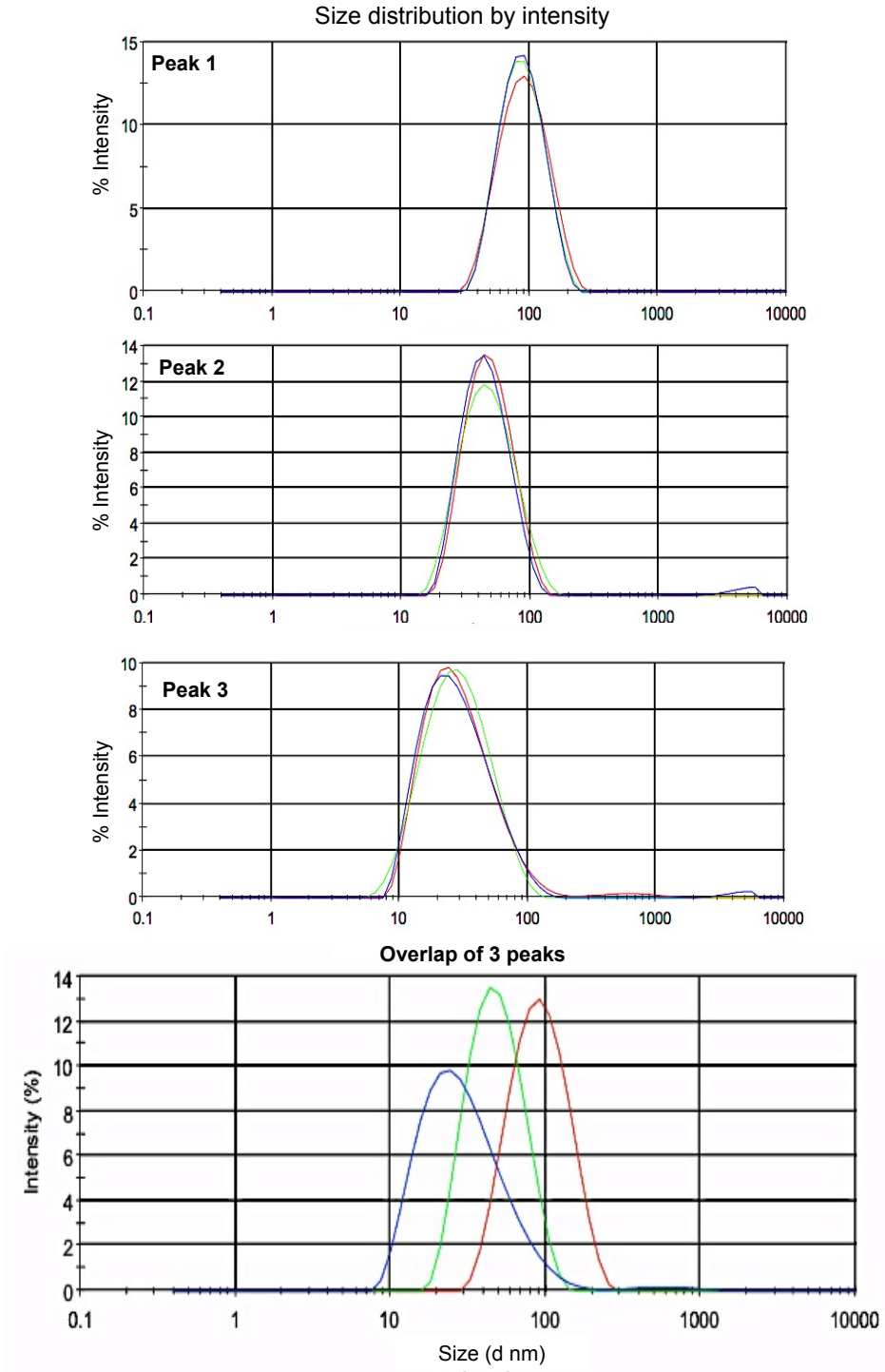

Peak1: Fractions 4-10: 79.34 nm Peak 2: Fractions 11-27: 42.06 nm
Peak 3: Fractions 28-47: 24.25 nm

Figure 6.9: Characterisation of the eluted fractions of Ferucarbotran on Superose 6 using DLS

The 3 fractions appear to have a uniform size distribution with peak 1 having a Z-average hydrodynamic diameter of 79.34 nm while peak 2 and peak 3 were 42.06 nm and 24.25 nm, respectively.

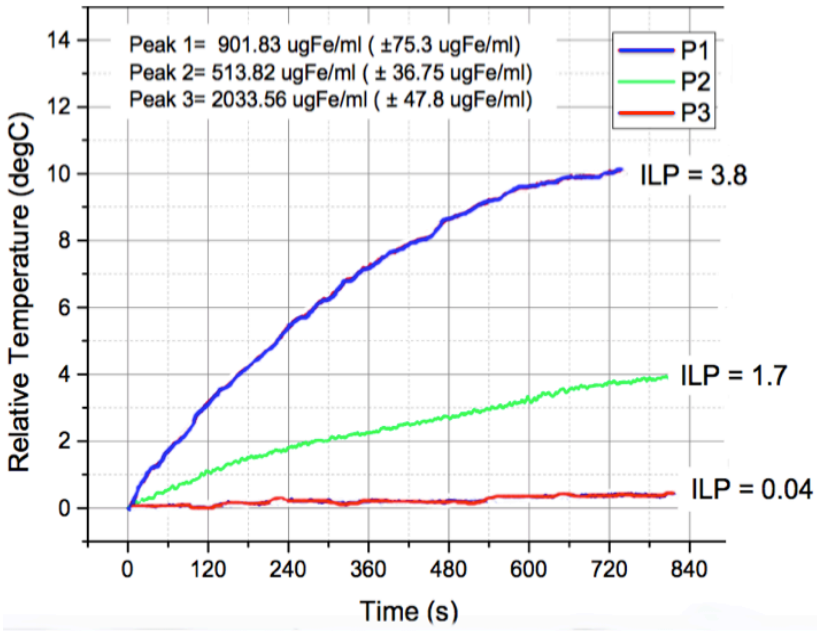

Figure 6.10: Heating profile of fractionated Ferucarbotran on Superose 6

Peak 1 (blue) had the highest ILP, showing superior heating potential. While peak 2 (green curve) and peak 3 (red curve) had ILP values of 1.7 and 0.04, respectively. The unfractionated Ferucarbotran had an ILP of 1.4, which shows the improved heating potential of fractionated Ferucarbotran. Despite the samples being prepared at different concentrations, the ILP is a concentration-independent value.

6.3 Discussion

The work presented in this chapter investigates the third central hypothesis of this thesis: Ferucarbotran heterogeneity could be overcome by physical separation using SEC.

The results of this chapter revealed that fractionation of Ferucarbotran could be successfully achieved by SEC. Three different types of matrices were investigated for their ability to fractionate Ferucarbotran. Only Superdex 200, Superose 6 and Superose 12 were able to fractionate Ferucarbotran due to their large fractionation ranges. The most efficient separation was achieved with Superose 6, a finding that has not been previously reported. Fractionated Ferucarbotran on Superose 6 contained different sizes of nanoparticles with the majority of SPIONs exhibiting small diameters. These results are consistent with published data by others that suggests that Ferucarbotran (Resovist®) exhibits bimodal size distribution; mainly consisting of small nanoparticles which can form stable multi-core aggregates with better magnetic properties (Eberbeck *et al*, 2011; Löwa *et al*, 2014; Thünemann *et al*, 2008). Those larger particles (core size ~25 nm) were estimated to constitute only 3% of Resovist® solution and were accounted for the superior magnetic particle imaging (MPI) potential of the SPIONs (Eberbeck *et al*, 2011).

Similar to other SPIONs, fractionation of Ferucarbotran has been investigated before, with most published reports utilising magnetic fractionation (Aurich *et al*, 2012; Ishihara *et al*, 2013; Nohara *et al*, 2013; Romanus *et al*, 2007; Yoshida *et al*, 2013) and no available published studies reporting the use of SEC. Generally, SEC is considered easier than magnetic fractionation because the latter usually includes bespoke manufacture of electromagnets with high magnetic field gradients. These magnets are usually manufactured by the researchers themselves (Löwa *et al*, 2014; Rheinländer *et al*, 2000a; Yoshida *et al*, 2013) or extensive tuning of commercially available electromagnets is required (Aurich *et al*, 2012; Löwa *et al*, 2014). This renders magnetic fractionation unstandardised, difficult to replicate and scale up to a bigger production environment required for the clinical development of SPIONs and their transition to the clinic. Therefore, the results discussed in this chapter propose a new technique to fractionate Ferucarbotran to optimise its magnetic properties using a simple and a reproducible method.

Examples of studies attempting the magnetic fractionation of Ferucarbotran are discussed below. For example Nohara *et al* used magnetic fractionation methods to separate Ferucarbotran in to 3 different fractions of 57 nm, 59 nm and 60 nm in diameter and exhibiting different T2 relaxivities (Nohara *et al*, 2013). While Ishihara *et al* explored centrifugal separation, gel filtration and magnetic separation to prepare Ferucarbotran samples with improved magnetizing properties and improved imaging capabilities (Ishihara *et al*, 2013). Nonetheless, efforts presented in this chapter using commercially available MACS LS magnetic columns with the QuadroMACS™ separator were not optimal and resulted in poor recovery of Ferucarbotran. This suggests that for effective magnetic separation of Ferucarbotran, strong electromagnetic field gradients are required. This conclusion was also confirmed by the work of Aurich *et al*. In their study magnetic fractionation of Ferucarbotran was done using MACS LS columns placed in a tuneable electromagnetic field. Fractions of mean hydrodynamic diameters of 92.3 nm, 64.7 nm, 45.5 nm and 26.9 nm were obtained (Aurich *et al*, 2012). Löwa *et al* have also used the MACS LS columns with a different electromagnet and were able to fractionate Ferucarbotran into 10 nm and 64 nm fractions (Löwa *et al*, 2014). The study by Löwa *et al* also used another technique called asymmetric flow field-flow fractionation, similar to SEC, separates particles based on their hydrodynamic diameter (Löwa *et al*, 2014). Asymmetric flow field-flow fractionation resulted in 8 fractions between 12 and 83 nm (Löwa *et al*, 2014). Romanus *et al* fractionated Ferucarbotran using MACS XS columns with an electromagnet that can be tuned with variable magnetic field strengths, this method yielded fractions with core sizes varying between 21 and 5.2 nm (Romanus *et al*, 2007). Since Ferucarbotran was mainly developed as an MRI contrast agent, most of the mentioned studies tested the magnetic particle imaging (MPI) potential of the fractions (Aurich *et al*, 2012; Ishihara *et al*, 2013; Löwa *et al*, 2014; Nohara *et al*, 2013; Yoshida *et al*, 2013). Meanwhile, the work presented in this chapter evaluated the heating profile of the fractions, which is an important parameter for the clinical development of Ferucarbotran for magnetic hyperthermia therapy of cancer.

6.4 Summary and conclusions

Ferucarbotran has been successfully fractionated to obtain a more homogeneous sub-population. This was done using SEC, which is an easy, fast and a reproducible method that could be scaled up. Furthermore the fractionation of Ferucarbotran

using SEC has not been reported before which highlights the importance of the work presented here.

In conclusion, the fractionated Ferucarbotran obtained here exhibited superior heating capabilities that might improve Ferucarbotran's prospective as an anti-cancer hyperthermia therapy.

Chapter 7
Conclusions and Future Directions

Maha Abdollah

The work presented in this thesis combined nanotechnology, cell biology, chromatography and chemistry techniques to provide some advances towards the development of SPIONs as cancer nanomedicines.

The site-specific delivery of therapies has been a difficult to achieve aim for the treatment of most illness and most specifically cancer. Due to the toxic nature of anti-cancer therapies, the need for targeted therapeutic effect is more urgent. In order for nanomedicines to fulfil their theranostic potential and achieve this goal, a number of biological barriers have to be overcome (Blanco *et al*, 2015). These barriers include: opsonisation and removal by the RES; nonspecific biodistribution; cellular internalisation; degradation by endosomal and lysosomal compartments and drug efflux pumps (Blanco *et al*, 2015; Ferrari, 2010).

The first and main culprit in the lack of efficacy of nanomedicines is the RES, which sequesters nanoparticles away from the intended site of delivery into the liver and spleen. Approaches developed for RES avoidance has been long sought after; of these PEGylation is the most widely used. Nonetheless newer approaches include developing bio-nano hybrid systems by using biomimetic coatings, coating with self peptide or loading into mesenchymal stem cells (Blanco *et al*, 2015; Gao *et al*, 2013). Nanoparticles have been functionalised with CD47, a “marker of self” peptide that gives a “don’t eat me” signal to macrophages leading to longer circulation times and better tumour localisation (Rodriguez *et al*, 2013). While the work of Parodi *et al* camouflaged silicon nanoparticles with leukocyte membrane (Parodi *et al*, 2013) and that of Hu *et al* clocked nanoparticles by coating them with the cell membrane of platelets (Hu *et al*, 2015) or red blood cells (RBCs) (Hu *et al*, 2011). In general, biomimetic coating of nanoparticles have led to prolong circulation times and/or localisation to the intended therapeutic sites (Blanco *et al*, 2015). Other approaches used cell carriers, specifically mesenchymal stem cells (MSCs). MSCs are therapeutically advantageous as vehicles for drug delivery owing to their low immunogenic properties and thus tend to “hide” nanoparticles from clearance by the host immune system (Auffinger *et al*, 2013; Gao *et al*, 2013). Furthermore, MSCs possess the ability to home to tumours and distant metastases (Hall *et al*, 2007; Kidd *et al*, 2009; Loebinger *et al*, 2009a; Loebinger *et al*, 2009c; Nakamizo *et al*, 2005; Studeny *et al*, 2004). For instance Loebinger *et al* showed that intravenously injected MSCs loaded with SPIONs were detectable with MRI in lung metastases (Loebinger *et al*, 2009c) while Riegler *et al* delivered SPIONs-loaded MSCs to the intended therapeutic region via magnetic targeting (Riegler *et al*, 2013).

The work presented in this thesis used a different stagey by using RES blockers, these blockers were able to not only block the liver uptake of SPIONs but also prolong their circulatory retention. Furthermore, the investigated polysaccharides proved effective *in vitro*, *in vivo* and with 2 different types of SPIONs. Although Nanomag-D-spio-NH2 has different surface chemistry, charge and size from Ferucarbotran, it appears that both SPIONs exhibited similar pharmacokinetic profile of rapid liver elimination and had prolonged circulatory retention in mice pre-treated with the blockers. These observations could potentially extend the work presented in this thesis to other SPIONs or indeed other classes of nanoparticles that might differ from Ferucarbotran yet are rapidly eliminated by the liver. The use of clinically safe RES blockers, particularly fucoidan, is advantageous as it might accelerate its progression to the clinic as a combination therapy with SPIONs.

Specific internalisation of nanoparticles by cancer cells is another barrier that needs to be addressed. The seminal review by Hanahan and Weinberg discussing the hallmarks of cancer in 2000, with an updated review published in 2011, revealed the unique properties of cancer cells that differentiate them from normal cells (Hanahan & Weinberg, 2000; Hanahan & Weinberg, 2011). These properties were greatly exploited to design targeted therapies; nanomedicines particularly exploited angiogenesis via the EPR effect (see section 1.3.1.1). The other hallmark widely used for targeting is the autonomy of cancer cells for growth factors, for this purpose the deregulation of cell surface receptors that convey growth-stimulatory signals are most commonly overexpressed in cancer cells (Hanahan & Weinberg, 2000), making them of particular interest for cancer-selective drug delivery. Examples of receptors targeted by nanomedicines include: the EGFR family, transferrin, folate, integrin and G protein-coupled receptors, among others (full list reviewed in (Akhtar *et al*, 2014)).

In this thesis EGFR, a known overexpressed receptor in a wide range of cancers (Mendelsohn & Baselga, 2006; Nicholson *et al*, 2001), was chosen for targeting using unique antibody-like proteins (DARPins). The use of DARPins to target nanoparticles to cancer cells has not been reported before, thus the findings presented herein are novel. Although EGFR targeting could not be achieved under the tested conditions, the complexity of the intertwined physicochemical properties of Ferucarbotran and the biological barriers of cancer cells was highlighted in my work. Therefore a number of critical insights were presented: (a) whilst Ferucarbotran internalisation by tumour cells could be beneficial for cancer cell

labelling, its internalisation by normal brain cells (as discussed in chapter 3) could lead to morbid side effects; (b) the presence of a protein on the surface of SPIONs changes their cellular interactions and should be carefully accounted for in experimental design and finally (c) although this was not shown in the work presented here, combining blocking of the unspecific uptake of SPIONs by cells with targeting might achieve the desired specificity of functionalised SPIONs by cancer cells.

Finally, the well-studied safety profile of MRI contrast SPIONs (e.g. Resovist® and Feridex®) in patients (Etheridge *et al*, 2013) should have facilitated their transition from diagnostic to therapeutic cancer nanomedicines. Nonetheless, the redirection of SPIONs from imaging agents to hyperthermia therapy requires reinvestigating their physicochemical properties, addressing the challenges that arise and thinking of novel approaches to optimise them for the new intended use. The work in this thesis showed that Ferucarbotran could have improved heating properties using a simple, fast and reproducible SEC-based fractionation method. Due to the ease of this process and its suitability for good manufacturing practice (GMP) standards, the inclusion of a final SEC fractionation step could be added during the manufacturing process of SPIONs to render a more homogenous population with improved heating properties. Furthermore, long-term stability studies and quality control checks done by the manufacturer on the fractionated samples could be employed; the presence of large nanoparticles in close proximity might lead to flocculation or irreversible aggregations.

Future directions

The work presented in this thesis has opened a wide range of exciting avenues on the path to develop SPIONs as cancer nanomedicines. Future work could be directed towards better understanding the mechanism of cellular interactions of SPIONs especially by non-RES cell lines. Fractionated Ferucarbotran by SEC could interact differently with cells, therefore, uptake experiments using the different fractions on different cell lines would provide useful insights on the effect of size on the cellular interactions of SPIONs.

The established chemical conjugation strategies to link SPIONs to NIR dyes (Abdollah *et al*, 2014) could be used to the trace their biodistribution *in vivo*. A mouse pod attached to the LI-COR Odyssey scanner can be used to trace and

quantify dye labelled conjugates *in vivo* (Kovar *et al*, 2007a; Kovar *et al*, 2009; Kovar *et al*, 2007b; Sampath *et al*, 2007). The NIR imaging system could also help characterise the change in SPIONs PK when blockers are administered via different routes. Future studies done to improve the PK behaviour of SPIONs could also exploit the preliminary results discussed with ^{99m}Tc-Ferucarbotran SPECT imaging system which showed the feasibility of this technique to trace the biodistribution of SPIONs *in vivo*. The live imaging of mice via SPECT at different time points following the administration of the blockers was beneficial but could be extended to include more time points or multiple injections of the blockers to completely block the RES.

Future work could include the optimisation of the RES blocking effect of the investigated polysaccharide derivatives. For instance fucoidan, a food supplement, could be administered orally or via intraperitoneal injection to enhance its blocking effect. Fucoidan has been extracted from different species of seaweed (Li *et al*, 2008); studying the blocking behaviour of the different fucoidans is another possibility. Fucoidan examined here, extracted from *Fucus vesiculosus,* exhibited wide size distribution and therefore its fractionation with SEC could provide a more uniform product with improved/prolonged RES blocking effect.

The lack of binding observed with FC-E69 to EGFR on cells might be accounted to the burial of E69 within the dextran coat of Ferucarbotran. Therefore, the use of variable length PEG linkers might solve this problem. In the study done by Salvati *et al*, they concluded that a certain length of PEG is required to achieve the targeting of their nanoparticles to transferrin receptor (Salvati *et al*, 2013); suggesting that a specific PEG length would achieve the desired exposure of the targeting moiety to the receptors present on the surface of the cancer cell. To take this work forward, intense characterisation of the Ferucarbotran-DARPin conjugates should be performed, this include the calculations of the number of DARPin moieties per nanoparticle and whether the achieved ratio is enough to enhance specific binding of the SPIONs to cancer cells. The use of G3 DARPin as a control is not optimal as it is smaller than E69, 14 KDa versus 21 KDa. Therefore, the use of a null binder DARPin with similar molecular weight to E69 would provide a better control. Finally, to achieve efficient targeting, another approach would be to conjugate neutral SPIONs to DARPins as this might overcome the unspecific uptake of negatively charged Ferucarbotran by cells. Once specificity is confirmed *in vitro*, *in vivo* studies using tumour xenografts could be done. The RES blocking, already established

(Abdollah *et al*, 2014), could help the targeted SPIONs localise better to the tumour xenografts and aid in the development of a targeted hyperthermia therapy for cancer.

In conclusion, my work showed that unwanted cellular uptake of SPIONs could be blocked with polysaccharide derivatives. The improved circulatory retention of SPIONs by RES blocking is achievable and obtaining more uniform SPIONs with improved magnetic properties is possible. The project also highlighted the complexity of the SPIONs' cellular interactions as well as the difficulties lying ahead. Despite the similarities between the size, charge, coating and core of a certain class of nanoparticles, each appear to behave in a unique way when in contact with biological systems like cells, blood, or organs. This complexity is further enhanced when they are coated with proteins. Therefore, the individuality of SPIONs makes their clinical development more difficult, but as our understanding increase this will help us develop more efficient, safer and targeted cancer nanomedicines.

Appendix 1

ELISA Experimental Results

Maha Abdollah

Indirect ELISA

2ry	1ry			1	2	3	4	5	6	7	8	9	10	11	12
+Anti-mouse IRDye 800	+ Anti-E69	+ Sample	**A**	FC-E69	FC-E69	FC-E69	FC-G3	FC-G3	FC-G3	FC-E69	FC-E69	FC-E69	FC-G3	FC-G3	FC-G3
			B	FC	FC	FC	E69	E69	E69	FC	FC	FC	E69	E69	E69
			C	G3	G3	G3	Cetuximab	Cetuximab	Cetuximab	G3	G3	G3	Cetuximab	Cetuximab	Cetuximab
			D	PBS	PBS	PBS				PBS	PBS	PBS			
	+ Anti-Dextran	+ Sample	**E**	FC-E69	FC-E69	FC-E69	FC-G3	FC-G3	FC-G3	FC-E69	FC-E69	FC-E69	FC-G3	FC-G3	FC-G3
			F	FC	FC	FC	E69	E69	E69	FC	FC	FC	E69	E69	E69
			G	G3	G3	G3	Cetuximab	Cetuximab	Cetuximab	G3	G3	G3	Cetuximab	Cetuximab	Cetuximab
			H	PBS	PBS	PBS				PBS	PBS	PBS			

White: EGFR coated **grey:** PBS coated **red:** measured at 700 nm channel

	1	2	3	4	5	6	7	8	9	10	11	12
A	13.69	13.4	12.59	3.72	3.68	4.13	0.34	0.35	0.35	0.32	0.3	0.37
B	0.9	0.53	0.51	5	5.64	5.28	0.3	0.3	0.29	0.34	0.28	0.3
C	0.57	0.4	0.37	16.38	16.42	15.84	0.37	0.32	0.3	5.45	5.43	5.56
D	0.43	0.39	0.33	0.28	0.33	0.33	0.55	0.29	0.3	0.3	0.3	0.28
E	6.02	5.53	5.32	4.78	5	5.04	0.65	0.73	0.86	0.59	0.79	1.05
F	4.95	4.81	5	0.64	0.7	0.59	1.02	0.95	1.05	0.35	0.36	0.49
G	0.39	0.77	0.48	5.36	5.35	5.23	0.32	0.35	0.29	5.02	5.13	5.16
H	0.43	0.49	0.71	0.32	0.29	0.34	0.34	0.31	0.32	0.31	0.3	0.39

Immobilizer ELISA

2ry	1ry			1	2	3	4	5	6	7	8	9	10	11	12
+Anti-mouse IRDye 800 or Anti-human DyLight 649	+ Anti-E69, anti-G3 or anti-Dextran	+ Sample	**A**	FC-E69	FC-E69	FC-E69	FC-G3	FC-G3	FC-G3	FC	FC	FC	PBS	PBS	PBS
			B	E69	E69	E69	PBS	PBS	PBS	G3	G3	G3	PBS	PBS	PBS
			C	Cetuximab	Cetuximab	Cetuximab	PBS	PBS	PBS						
		+ Sample	**D**	FC-E69	FC-E69	FC-E69	FC-G3	FC-G3	FC-G3	FC	FC	FC	PBS	PBS	PBS
			E	E69	E69	E69	PBS	PBS	PBS	G3	G3	G3	PBS	PBS	PBS
			G	Cetuximab	Cetuximab	Cetuximab	PBS	PBS	PBS						

White: EGFR coated; **Grey:** PBS coated; **Primary antibodies** were added according to colour code (e.g. FC-E69 was detected with anti-dextran). Underlined wells were treated with sample and then anti-human DyLight 649 (i.e. no 1ry antibody).

	1	**2**	**3**	**4**	**5**	**6**	**7**	**8**	**9**	**10**	**11**	**12**
A	4.23	3.12	3.36	3.28	3.67	3.57	4.01	4.04	3.88	0.59	0.26	0.26
B	0.59	0.6	0.63	0.25	0.24	0.24	0.32	0.33	0.35	0.26	0.26	0.25
C	7.97	8.2	7.32	5.47	5.58	5.57	0.24	0.24	0.25	0.24	0.25	0.25
D	0.23	0.23	0.25	0.24	0.25	0.24	0.22	0.26	0.28	0.27	0.28	0.27
E	0.29	0.46	0.39	0.58	0.28	0.3	0.38	0.39	0.42	0.24	0.24	0.25
F	0.26	0.27	0.26	0.23	0.24	0.24	0.25	0.25	0.25	0.23	0.24	0.25
G	6.19	6.73	6.12	6.34	6.54	6.39	0.26	0.24	0.23	0.23	0.26	0.25

Sandwich ELISA

2ry	1ry			1	2	3	4	5	6	7	8	9	10	11	12
+Anti-human DyLight 649	+ Cetuximab	+ EGFR or PBS	**A**	FC-E69	FC-E69	FC-E69	FC-G3	FC-G3	FC-G3	FC-E69	FC-E69	FC-E69	FC-G3	FC-G3	FC-G3
			B	FC	FC	FC	E69	E69	E69	FC	FC	FC	E69	E69	E69
			C	G3	G3	G3	PBS	PBS	PBS	G3	G3	G3	PBS	PBS	PBS

White: EGFR treated **Grey:** PBS treated

	1	2	3	4	5	6	7	8	9	10	11	12
A	14.83	14.13	14.53	5.93	5.82	5.99	5.15	5.18	5.22	5.01	5.17	5.31
B	5.88	5.75	5.52	10.76	10.89	13.48	5.01	5.18	5.15	4.96	5.1	5.21
C	5.26	5.29	5.17	5.57	5.48	5.46	5.11	5.11	5.1	5.22	5.3	5.29

Appendix 2

SEC Results

Maha Abdollah

Elution profile of gel filtration standard on SEC columns

Components of the gel filtration standard obtained from Bio-Rad.

Component	Molecular Weight (KDa)
Thyroglobulin (bovine)	670
γ-Globulin (bovine)	158
Ovalbumin (Chicken)	44
Myoglobin (horse)	17
Vitamin B12	1.35

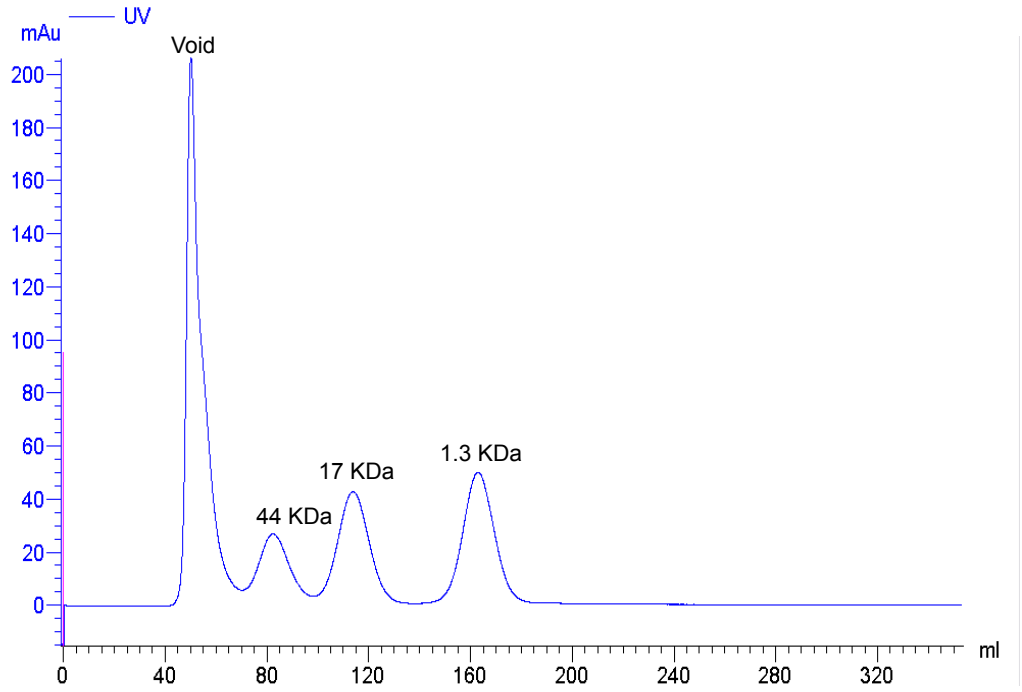

Chromatogram of gel filtration standard run on Sephadex G-100 packed column: Proteins that are larger than the cut off (150 KDa), i.e. thyroglobin and γ-globulin, came out in the column's void volume followed by 3 peaks representing ovalbumin, myoglobin and vitamin B12 with molecular weights of 44,17 and 1.3 KDa respectively.

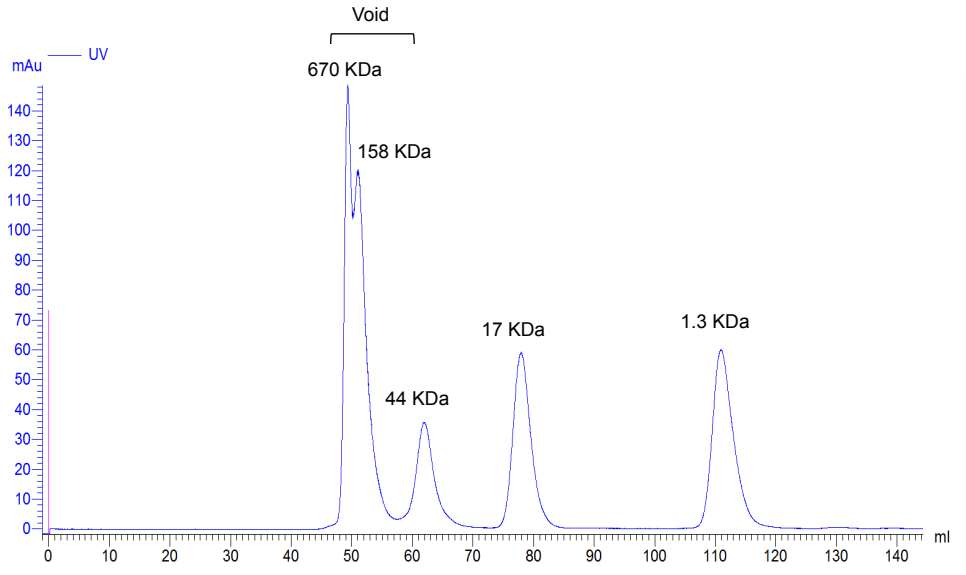

Elution profile of the gel filtration marker run through an XK 16/50 column packed with Superdex 75: Both high molecular weight proteins (thyroglobin 670 KDa and γ-globulin 158 KDa) were eluted as a double-headed peak in the column's void volume followed by the lower molecular weight proteins.

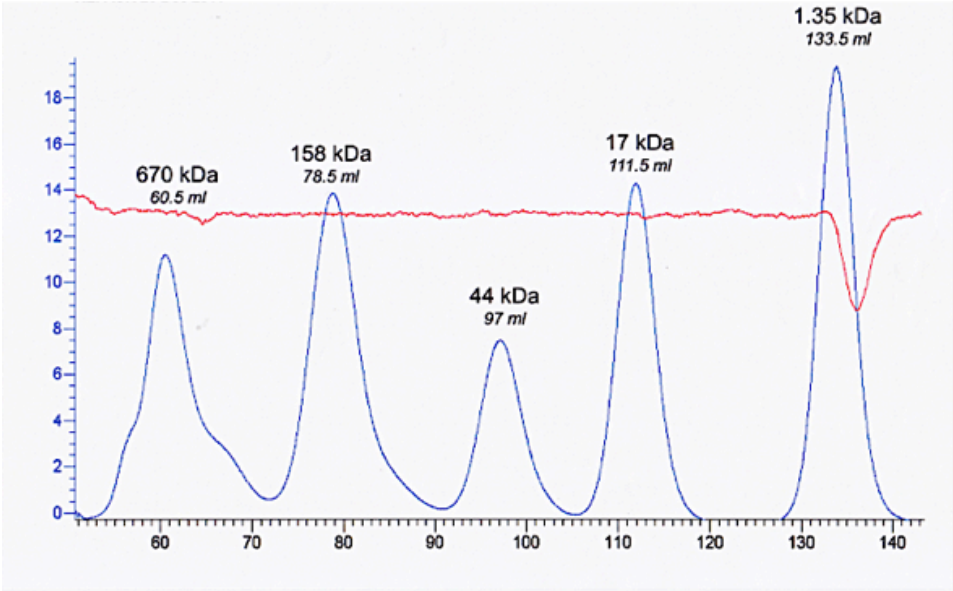

Elution profile of gel filtration standard on Superdex 200 packed column: All proteins in the molecular weight marker were separated into 5 distinct peaks conductivity trace is shown in red.

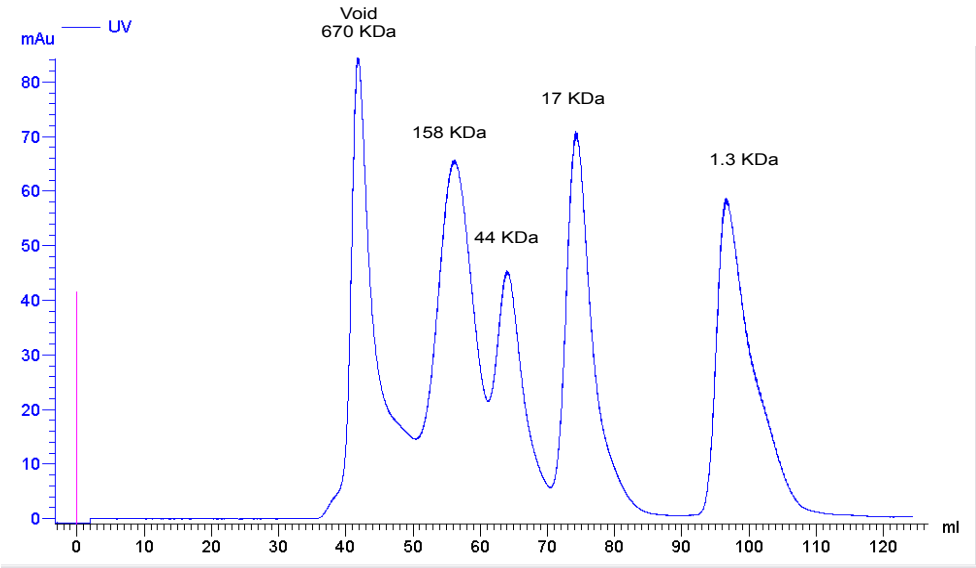

Elution profile of the gel filtration standard run on a column packed with Superose 12: Superose 12 has a fractionation range of 1-300 KDa so the biggest protein (thyroglobulin, 670 KDa) was eluted first in the column void volume followed by 4 different peaks of the other proteins.

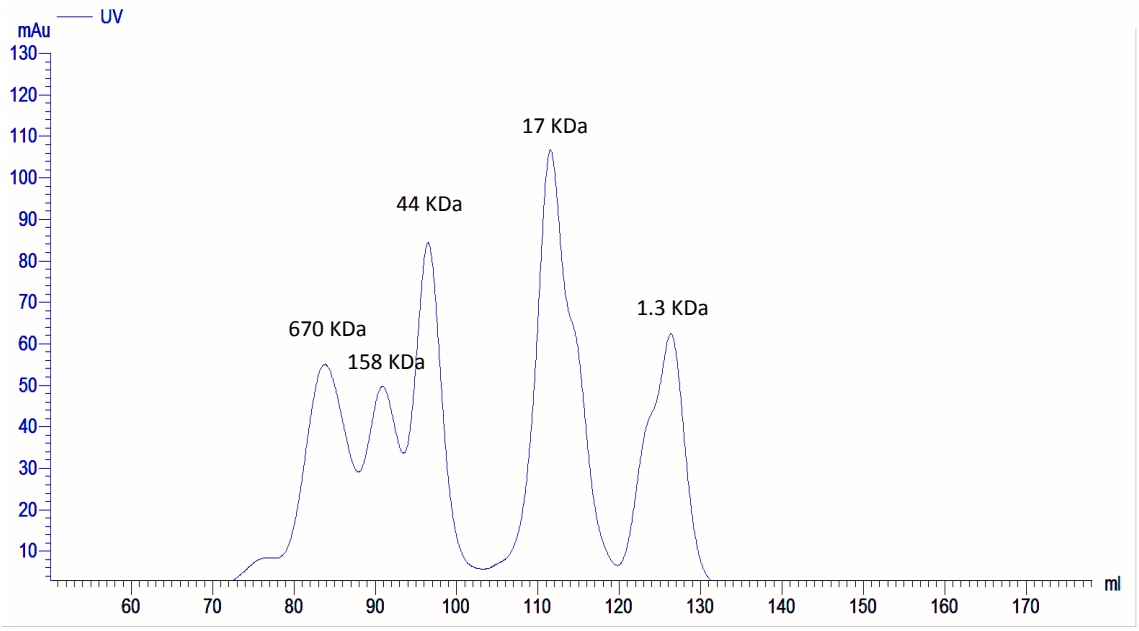

Elution profile of gel filtration standard run on column packed with Superose 6: All proteins in the molecular weight marker were separated into 5 distinct peaks as shown in the chromatogram. Nevertheless the fractionation efficiency appears to be less for the higher molecular weight proteins as the peaks overlap.

Appendix 3

Publications and Presentations

Maha Abdollah

Publications:

Prolonging the circulatory retention of SPIONs using dextran sulfate: *in vivo* tracking achieved by functionalisation with near-infrared dyes. Maha R. A. Abdollah, Tammy Kalber, Berend Tolner, Paul Southern, Joseph C. Bear, Mathew Robson, R. Barbara Pedley, Ivan P. Parkin, Quentin A. Pankhurst, Paul Mulholland and Kerry Chester (2014). **Faraday Discussions 175** (0): 41-58, http://dx.doi.org/10.1039/c4fd00114a.

Presentations:

Evaluating the Effectiveness of RES Uptake Blockers using Radiolabeled Nanoparticles and SPECT Imaging. Maha R.A Abdollah, Julia Bagunya-Torres, Rafael T. M. de Rosales and Kerry Chester (2015). Presentation and Poster presented in the **Preclinical Nuclear Imaging (PNI) Symposium**, London, UK, November 2015.

Developing Superparamagnetic Iron Oxide Nanoparticles (SPIONs) as Cancer Nanomedicines. Maha Abdollah, Tammy Kalber, Berend Tolner, Sara Galavotti, Paolo Salomoni, Mathew Robson, Barbara Pedley, Shane Minogue, Quentin Pankhurst, Paul Mulholland, Kerry Chester. **UCL Cancer Institute** poster competition 2015.

Developing superparamagnetic iron oxide nanoparticles (SPIONs) as cancer nanomedicines. Maha Abdollah, Tammy Kalber, Berend Tolner, Sara Galavotti, Paolo Salomoni, Shane Minogue, Paul Mulholland, Quentin Pankhurst, and Kerry Chester. **NCRI conference** poster presentation, Liverpool, UK 2013. http://conference.ncri.org.uk/abstracts/2013/abstracts/B66.htm

Appendix 4

Bibliography

Maha Abdollah

Abakumov MA, Nukolova NV, Sokolsky-Papkov M, Shein SA, Sandalova TO, Vishwasrao HM, Grinenko NF, Gubsky IL, Abakumov AM, Kabanov AV (2015) VEGF-targeted magnetic nanoparticles for MRI visualization of brain tumor. *Nanomedicine: Nanotechnology, Biology and Medicine* **11**(4)**:** 825-833

Abdollah MRA, Kalber T, Tolner B, Southern P, Bear JC, Robson M, Pedley RB, Parkin IP, Pankhurst QA, Mulholland P, Chester K (2014) Prolonging the circulatory retention of SPIONs using dextran sulfate: in vivo tracking achieved by functionalisation with near-infrared dyes. *Faraday Discussions* **175**(0)**:** 41-58

Akhtar MJ, Ahamed M, Alhadlaq HA, Alrokayan SA, Kumar S (2014) Targeted anticancer therapy: Overexpressed receptors and nanotechnology. *Clinica Chimica Acta* **436:** 78-92

Akinc A, Battaglia G (2013) Exploiting endocytosis for nanomedicines. *Cold Spring Harbor perspectives in biology* **5**(11)**:** a016980

Alarcón R, Fuenzalida C, Santibáñez M, von Bernhardi R (2005) Expression of scavenger receptors in glial cells. Comparing the adhesion of astrocytes and microglia from neonatal rats to surface-bound beta-amyloid. *Journal of Biological Chemistry* **280**(34)**:** 30406-30415

Albanese A, Tang PS, Chan WCW (2012) The Effect of Nanoparticle Size, Shape, and Surface Chemistry on Biological Systems. *Annual Review of Biomedical Engineering* **14**(1)**:** 1-16

Alcantar NA, Aydil ES, Israelachvili JN (2000) Polyethylene glycol-coated biocompatible surfaces. *Journal of biomedical materials research* **51**(3)**:** 343-351

Allen TM, Martin FJ (2004) Advantages of liposomal delivery systems for anthracyclines. *Seminars in oncology* **31:** 5-15

American Cancer Society A (2013) Cancer Facts & Figures 2013 Vol. 2014.

Arruebo M, Valladares M, González-Fernández Á (2009) Antibody-conjugated nanoparticles for biomedical applications. *Journal of Nanomaterials* **2009:** 37

Auffinger B, Morshed R, Tobias A, Cheng Y, Ahmed AU, Lesniak MS (2013) Drug-loaded nanoparticle systems and adult stem cells: a potential marriage for the treatment of malignant glioma? *Oncotarget* **4**(3)**:** 378

Aurich K, Spoerl M-C, Fürll B, Sietmann R, Greinacher A, Hosten N, Weitschies W (2012) Development of a method for magnetic labeling of platelets. *Nanomedicine: Nanotechnology, Biology and Medicine* **8**(5)**:** 537-544

Balzer T CE, Shamsi K, Niendorf HP (1996) Results of a multicenter phase II clinical trial with a susceptibility contrast medium for magnetic resonance imaging of the liver. *Academic radiology* **3 suppl 2:1996 Aug pg S417-9**

Bamrungsap S, Chen T, Shukoor MI, Chen Z, Sefah K, Chen Y, Tan W (2012) Pattern recognition of cancer cells using aptamer-conjugated magnetic nanoparticles. *ACS nano* **6**(5)**:** 3974-3981

Bangham J (2005) Cetuximab constricts conformational contortionist. *Nature Reviews Cancer* **5**(6)**:** 421-421

Barenholz YC (2012) Doxil®—the first FDA-approved nano-drug: lessons learned. *Journal of Controlled Release* **160**(2)**:** 117-134

Barrett D, Hartshorne M, Hussain M, Shaw P, Davies M (2001) Resistance to nonspecific protein adsorption by poly (vinyl alcohol) thin films adsorbed to a poly (styrene) support matrix studied using surface plasmon resonance. *Analytical chemistry* **73**(21)**:** 5232-5239

Barth HG, Boyes BE, Jackson C (1996) Size exclusion chromatography. *Analytical Chemistry* **68**(12)**:** 445-466

Barua S, Yoo J-W, Kolhar P, Wakankar A, Gokarn YR, Mitragotri S (2013) Particle shape enhances specificity of antibody-displaying nanoparticles. *Proceedings of the National Academy of Sciences* **110**(9)**:** 3270-3275

Bates D, Abraham S, Campbell M, Zehbe I, Curiel L (2014) Development and characterization of an antibody-labeled super-paramagnetic iron oxide contrast agent targeting prostate cancer cells for magnetic resonance imaging.

Bazak R, Houri M, El Achy S, Kamel S, Refaat T (2014) Cancer active targeting by nanoparticles: a comprehensive review of literature. *Journal of cancer research and clinical oncology***:** 1-16

Bilzer M, Roggel F, Gerbes AL (2006) Role of Kupffer cells in host defense and liver disease. *Liver International* **26**(10)**:** 1175-1186

Binz HK, Amstutz P, Kohl A, Stumpp MT, Briand C, Forrer P, Grütter MG, Plückthun A (2004) High-affinity binders selected from designed ankyrin repeat protein libraries. *Nature biotechnology* **22**(5)**:** 575-582

Binz HK, Amstutz P, Plückthun A (2005) Engineering novel binding proteins from nonimmunoglobulin domains. *Nature biotechnology* **23**(10)**:** 1257-1268

Binz HK, Stumpp MT, Forrer P, Amstutz P, Plückthun A (2003) Designing repeat proteins: well-expressed, soluble and stable proteins from combinatorial libraries of consensus ankyrin repeat proteins. *Journal of molecular biology* **332**(2)**:** 489-503

Blanco E, Shen H, Ferrari M (2015) Principles of nanoparticle design for overcoming biological barriers to drug delivery. *Nature biotechnology* **33**(9)**:** 941-951

Bleeker EA, de Jong WH, Geertsma RE, Groenewold M, Heugens EH, Koers-Jacquemijns M, van de Meent D, Popma JR, Rietveld AG, Wijnhoven SW (2013) Considerations on the EU definition of a nanomaterial: science to support policy making. *Regulatory toxicology and pharmacology* **65**(1)**:** 119-125

Boersma YL, Chao G, Steiner D, Wittrup KD, Plückthun A (2011) Bispecific designed ankyrin repeat proteins (DARPins) targeting epidermal growth factor receptor inhibit A431 cell proliferation and receptor recycling. *Journal of Biological Chemistry* **286**(48)**:** 41273-41285

Bonnemain B (1998a) Superparamagnetic Agents in magnetic resonance imaging: physicochemical characteristics and clinical applications a review. *Journal of drug targeting* **6**(3)**:** 167-174

Bonnemain B (1998b) Superparamagnetic agents in magnetic resonance imaging: physicochemical characteristics and clinical applications. A review. *J Drug Target* **6**(3)**:** 167-74

Bouras A, Kaluzova M, Hadjipanayis CG (2015) Radiosensitivity enhancement of radioresistant glioblastoma by epidermal growth factor receptor antibody-conjugated iron-oxide nanoparticles. *Journal of neuro-oncology***:** 1-10

Bradfield JW, Souhami RL, Addison IE (1974) The mechanism of the adjuvant effect of dextran sulphate. *Immunology* **26**(2)**:** 383-92

Brahmachari B, Hazra A, Majumdar A (2011) Adverse drug reaction profile of nanoparticle versus conventional formulation of paclitaxel: An observational study. *Indian journal of pharmacology* **43**(2)**:** 126

Branca RT, Cleveland ZI, Fubara B, Kumar CSSR, Maronpot RR, Leuschner C, Warren WS, Driehuys B (2010) Molecular MRI for sensitive and specific detection of lung metastases. *Proceedings of the National Academy of Sciences* **107**(8)**:** 3693

Brown MS, Goldstein JL (1979) Receptor-mediated endocytosis: insights from the lipoprotein receptor system. *Proceedings of the National Academy of Sciences* **76**(7)**:** 3330-3337

Byrne JD, Betancourt T, Brannon-Peppas L (2008) Active targeting schemes for nanoparticle systems in cancer therapeutics. *Advanced drug delivery reviews* **60**(15)**:** 1615-1626

Campa V, Iglesias J, Carcedo M, Rodriguez R, Riera J, Ramos S, Lazo P (2005) Polyinosinic acid induces TNF and NO production as well as NF-κB and AP-1 transcriptional activation in the monocytemacrophage cell line RAW 264.7. *Inflammation Research* **54**(8)**:** 328-337

Cancer Research UK A (2012) Cancer mortality statistics Vol. 2014.

Canton J, Neculai D, Grinstein S (2013) Scavenger receptors in homeostasis and immunity. *Nat Rev Immunol* **13**(9)**:** 621-634

Chachuat A, Bonnemain B (1995) European clinical experience with Endorem. A new contrast agent for liver MRI in 1000 patients. *Der Radiologe* **35**(11 Suppl 2)**:** S274

Chao Y, Karmali PP, Simberg D (2012a) Role of Carbohydrate Receptors in the Macrophage Uptake of Dextran-Coated Iron Oxide Nanoparticles. *Nano-Biotechnology for Biomedical and Diagnostic Research***:** 115-123

Chao Y, Makale M, Karmali PP, Sharikov Y, Tsigelny I, Merkulov S, Kesari S, Wrasidlo W, Ruoslahti E, Simberg D (2012b) Recognition of Dextran–Superparamagnetic Iron Oxide Nanoparticle Conjugates (Feridex) via Macrophage Scavenger Receptor Charged Domains. *Bioconjugate chemistry* **23**(5)**:** 1003-1009

Charles NA, Holland EC, Gilbertson R, Glass R, Kettenmann H (2011) The brain tumor microenvironment. *Glia* **59**(8)**:** 1169-1180

Chauhan VP, Jain RK (2013) Strategies for advancing cancer nanomedicine. *Nat Mater* **12**(11)**:** 958-962

Chen C, Ke J, Zhou XE, Yi W, Brunzelle JS, Li J, Yong E-L, Xu HE, Melcher K (2013) Structural basis for molecular recognition of folic acid by folate receptors. *Nature* **500**(7463)**:** 486-489

Chen T-J, Cheng T-H, Chen C-Y, Hsu SC, Cheng T-L, Liu G-C, Wang Y-M (2009) Targeted herceptin–dextran iron oxide nanoparticles for noninvasive imaging of HER2/neu receptors using MRI. *JBIC Journal of Biological Inorganic Chemistry* **14**(2)**:** 253-260

Chen TJ, Cheng TH, Hung YC, Lin KT, Liu GC, Wang YM (2008) Targeted folic acid‐PEG nanoparticles for noninvasive imaging of folate receptor by MRI. *Journal of biomedical materials research Part A* **87**(1)**:** 165-175

Cherukuri P, Glazer ES, Curley SA (2010) Targeted hyperthermia using metal nanoparticles. *Advanced drug delivery reviews* **62**(3)**:** 339-345

Chithrani BD, Ghazani AA, Chan WC (2006) Determining the size and shape dependence of gold nanoparticle uptake into mammalian cells. *Nano letters* **6**(4)**:** 662-668

Choi H, Choi SR, Zhou R, Kung HF, Chen I-W (2004) Iron oxide nanoparticles as magnetic resonance contrast agent for tumor imaging via folate receptor-targeted delivery 1. *Academic radiology* **11**(9)**:** 996-1004

Chong CR, Jänne PA (2013) The quest to overcome resistance to EGFR-targeted therapies in cancer. *Nature medicine* **19**(11)**:** 1389-1400

Chou LY, Ming K, Chan WC (2011) Strategies for the intracellular delivery of nanoparticles. *Chemical Society Reviews* **40**(1)**:** 233-245

Chouly C, Pouliquen D, Lucet I, Jeune J, Jallet P (1996) Development of superparamagnetic nanoparticles for MRI: effect of particle size, charge and surface nature on biodistribution. *Journal of microencapsulation* **13**(3)**:** 245-255

Cirstoiu-Hapca A, Bossy-Nobs L, Buchegger F, Gurny R, Delie F (2007) Differential tumor cell targeting of anti-HER2 (Herceptin®) and anti-CD20 (Mabthera®) coupled nanoparticles. *International journal of pharmaceutics* **331**(2)**:** 190-196

Clogston JD, Patri AK (2011) Zeta potential measurement. In *Characterization of nanoparticles intended for drug delivery*, pp 63-70. Springer

Conner SD, Schmid SL (2003) Regulated portals of entry into the cell. *Nature* **422**(6927)**:** 37-44

Cooper G (2000) Structure of the Plasma Membrane. In *The Cell: A Molecular Approach. 2nd edition. Sunderland (MA): Sinauer Associates; 2000. Availble at* http://www.ncbi.nlm.nih.gov/books/NBK9898/.

Cumashi A, Ushakova NA, Preobrazhenskaya ME, D'Incecco A, Piccoli A, Totani L, Tinari N, Morozevich GE, Berman AE, Bilan MI (2007) A comparative study of the anti-inflammatory, anticoagulant, antiangiogenic, and antiadhesive activities of nine different fucoidans from brown seaweeds. *Glycobiology* **17**(5)**:** 541-552

Daniels TR, Bernabeu E, Rodríguez JA, Patel S, Kozman M, Chiappetta DA, Holler E, Ljubimova JY, Helguera G, Penichet ML (2012) The transferrin receptor and the targeted delivery of therapeutic agents against cancer. *Biochimica et Biophysica Acta (BBA)-General Subjects* **1820**(3)**:** 291-317

Daniels TR, Delgado T, Helguera G, Penichet ML (2006a) The transferrin receptor part II: targeted delivery of therapeutic agents into cancer cells. *Clinical Immunology* **121**(2)**:** 159-176

Daniels TR, Delgado T, Rodriguez JA, Helguera G, Penichet ML (2006b) The transferrin receptor part I: Biology and targeting with cytotoxic antibodies for the treatment of cancer. *Clinical Immunology* **121**(2)**:** 144-158

Das N, Basu MK, Das MK (1987) Suppression of liver uptake of orally fed liposomes by injection (ip) of dextran sulfate 500. *Bioscience Reports* **7**(6)**:** 465-470

Dawidczyk CM, Kim C, Park JH, Russell LM, Lee KH, Pomper MG, Searson PC (2014a) State-of-the-art in design rules for drug delivery platforms: Lessons learned from FDA-approved nanomedicines. *Journal of Controlled Release* **187**(0)**:** 133-144

Dawidczyk CM, Russell LM, Searson PC (2014b) Nanomedicines for cancer therapy: state-of-the-art and limitations to pre-clinical studies that hinder future developments. *Frontiers in chemistry* **2**

De Jong WH, Borm PJA (2008) Drug delivery and nanoparticles: applications and hazards. *International journal of nanomedicine* **3**(2)**:** 133

De Rosales RTM, Finucane C, Mather S, Blower P (2009) Bifunctional bisphosphonate complexes for the diagnosis and therapy of bone metastases. *Chemical Communications*(32)**:** 4847-4849

de Rosales RTM, Tavaré R, Glaria A, Varma G, Protti A, Blower PJ (2011) 99mTc-bisphosphonate-iron oxide nanoparticle conjugates for dual-modality biomedical imaging. *Bioconjugate Chem* **22:** 455-465

Denardo GL, Denardo SJ (2008) Turning the Heat on Cancer. *Cancer biotherapy & radiopharmaceuticals* **23**(6)**:** 671-679

Di Marco M, Sadun C, Port M, Guilbert I, Couvreur P, Dubernet C (2007) Physicochemical characterization of ultrasmall superparamagnetic iron oxide particles (USPIO) for biomedical application as MRI contrast agents. *International journal of nanomedicine* **2**(4)**:** 609

Dinndorf PA, Gootenberg J, Cohen MH, Keegan P, Pazdur R (2007) FDA drug approval summary: pegaspargase (Oncaspar®) for the first-line treatment of children with acute lymphoblastic leukemia (ALL). *The oncologist* **12**(8)**:** 991-998

Dobson J (2006) Magnetic nanoparticles for drug delivery. *Drug development research* **67**(1)**:** 55-60

Eberbeck D, Wiekhorst F, Wagner S, Trahms L (2011) How the size distribution of magnetic nanoparticles determines their magnetic particle imaging performance. *Applied physics letters* **98**(18)**:** 182502

Etheridge ML, Campbell SA, Erdman AG, Haynes CL, Wolf SM, McCullough J (2013) The big picture on nanomedicine: the state of investigational and approved nanomedicine products. *Nanomedicine: Nanotechnology, Biology and Medicine* **9**(1)**:** 1-14

EU (2011) Commission recommendation of 18 October 2011 on the definition of nanomaterial (2011/696/EU). *Official Journal of the European Union L275* **54:** 38-40

Fan C, Gao W, Chen Z, Fan H, Li M, Deng F, Chen Z (2011) Tumor selectivity of stealth multi-functionalized superparamagnetic iron oxide nanoparticles. *International journal of pharmaceutics* **404**(1)**:** 180-190

Ferrari M (2010) Frontiers in cancer nanomedicine: directing mass transport through biological barriers. *Trends in biotechnology* **28**(4)**:** 181-188

Feynman RP (1960) There's plenty of room at the bottom. *Engineering and science* **23**(5)**:** 22-36

Fischer HC, Hauck TS, Gómez‐Aristizábal A, Chan WC (2010) Exploring primary liver macrophages for studying quantum dot interactions with biological systems. *Advanced Materials* **22**(23)**:** 2520-2524

Fitton JH (2011) Therapies from fucoidan; multifunctional marine polymers. *Marine drugs* **9**(10)**:** 1731-1760

Flexner C, Barditch-Crovo PA, Kornhauser DM, Farzadegan H, Nerhood LJ, Chaisson RE, Bell KM, Lorentsen KJ, Hendrix CW, Petty BG (1991) Pharmacokinetics, toxicity, and activity of intravenous dextran sulfate in human immunodeficiency virus infection. *Antimicrobial agents and chemotherapy* **35**(12)**:** 2544

Forssen EA, Ross ME (1994) Daunoxome® treatment of solid tumors: preclinical and clinical investigations. *Journal of Liposome Research* **4**(1)**:** 481-512

Foss FM (2000) DAB 389 IL-2 (ONTAK): a novel fusion toxin therapy for lymphoma. *Clinical lymphoma* **1**(2)**:** 110-116

Frank H, Weissleder R, Brady T (1994) Enhancement of MR angiography with iron oxide: preliminary studies in whole-blood phantom and in animals. *AJR American journal of roentgenology* **162**(1)**:** 209-213

Fujishima M, Omae T, Tanaka K, Iino K, Matsuo O, Mihara H (1986) Controlled trial of combined urokinase and dextran sulfate therapy in patients with acute cerebral infarction. *Angiology* **37**(7)**:** 487-498

Fujiwara M, Baldeschwieler JD, Grubbs RH (1996) Receptor-mediated endocytosis of poly (acrylic acid)-conjugated liposomes by macrophages. *Biochimica et Biophysica Acta (BBA)-Biomembranes* **1278**(1)**:** 59-67

Gabizon AA (2001) Stealth liposomes and tumor targeting: one step further in the quest for the magic bullet. *Clinical Cancer Research* **7**(2)**:** 223-225

Gao Z, Zhang L, Hu J, Sun Y (2013) Mesenchymal stem cells: a potential targeted-delivery vehicle for anti-cancer drug loaded nanoparticles. *Nanomedicine: Nanotechnology, Biology and Medicine* **9**(2)**:** 174-184

Garris C, Pittet MJ (2013) Therapeutically reeducating macrophages to treat GBM. *Nature medicine* **19**(10)**:** 1207-1208

Gaur U, Sahoo SK, De Tapas K, Ghosh PC, Maitra A, Ghosh P (2000) Biodistribution of fluoresceinated dextran using novel nanoparticles evading reticuloendothelial system. *International journal of pharmaceutics* **202**(1)**:** 1-10

GE-Healthcare (2014) Gel Filtration Handbook (Principles and Methods). In http://www.gelifesciences.com/gehcls_images/GELS/Related Content/Files/1314807262343/litdoc18102218_20141208003707.pdf Vol. 2014. General Electric Company

Godoy B, Murgas P, Tichauer J, Von Bernhardi R (2012) Scavenger receptor class A ligands induce secretion of IL1β and exert a modulatory effect on the inflammatory activation of astrocytes in culture. *Journal of neuroimmunology* **251**(1)**:** 6-13

Goffin JR, Zbuk K (2013) Epidermal growth factor receptor: pathway, therapies, and pipeline. *Clinical therapeutics* **35**(9)**:** 1282-1303

Goldstein R, Sosabowski J, Livanos M, Leyton J, Vigor K, Bhavsar G, Nagy-Davidescu G, Rashid M, Miranda E, Yeung J (2014) Development of the designed ankyrin repeat protein (DARPin) G3 for HER2 molecular imaging. *European journal of nuclear medicine and molecular imaging***:** 1-14

Golovko DM, Henning T, Bauer JS, Settles M, Frenzel T, Mayerhofer A, Rummeny EJ, Daldrup-Link HE (2010) Accelerated stem cell labeling with ferucarbotran and protamine. *European radiology* **20**(3)**:** 640-648

Gonzales-Weimuller M, Zeisberger M, Krishnan KM (2009) Size-dependant heating rates of iron oxide nanoparticles for magnetic fluid hyperthermia. *Journal of Magnetism and Magnetic Materials* **321**(13)**:** 1947-1950

Gordon EM, Hall FL (2010) Rexin-G, a targeted genetic medicine for cancer. *Expert opinion on biological therapy* **10**(5)**:** 819-832

Gordon RT, Hines JR, Gordon D (1979) Intracellular hyperthermia a biophysical approach to cancer treatment via intracellular temperature and biophysical alterations. *Medical Hypotheses* **5**(1)**:** 83-102

Green M, Manikhas G, Orlov S, Afanasyev B, Makhson A, Bhar P, Hawkins M (2006) Abraxane®, a novel Cremophor®-free, albumin-bound particle form of paclitaxel for the treatment of advanced non-small-cell lung cancer. *Annals of Oncology* **17**(8)**:** 1263-1268

Greish K, Fang J, Inutsuka T, Nagamitsu A, Maeda H (2003) Macromolecular Therapeutics. *Clin Pharmacokinet* **42**(13)**:** 1089-1105

Gupta AK, Gupta M (2005) Synthesis and surface engineering of iron oxide nanoparticles for biomedical applications. *Biomaterials* **26**(18)**:** 3995-4021

Gupta AK, Naregalkar RR, Vaidya VD, Gupta M (2007) Recent advances on surface engineering of magnetic iron oxide nanoparticles and their biomedical applications. *Nanomedicine* **2**(1)**:** 23-39

Hall B, Dembinski J, Sasser AK, Studeny M, Andreeff M, Marini F (2007) Mesenchymal stem cells in cancer: tumor-associated fibroblasts and cell-based delivery vehicles. *International journal of hematology* **86**(1)**:** 8-16

Hamm B, Staks T, Taupitz M, Maibauer R, Speidel A, Huppertz A, Frenzel T, Lawaczeck R, Wolf KJ, Lange L (1994) Contrast enhanced MR imaging of liver and spleen: First experience in humans with a new superparamagnetic iron oxide. *Journal of Magnetic Resonance Imaging* **4**(5)**:** 659-668

Hanahan D, Weinberg RA (2000) The hallmarks of cancer. *cell* **100**(1)**:** 57-70

Hanahan D, Weinberg RA (2011) Hallmarks of Cancer: The Next Generation. *Cell* **144**(5)**:** 646-674

Hao-Yu T, Chen-Yi L, Ying-Hsia S, Xi-Zhang L, Gwo-Bin L (2007) Hyperthermia Cancer Therapy Utilizing Superparamagnetic Nanoparticles. *Nano/Micro Engineered and Molecular Systems, 2007 NEMS '07 2nd IEEE International Conference on*: 163-166

He Y, Song W, Lei J, Li Z, Cao J, Huang S, Meng J, Xu H, Jin Z, Xue H (2012) Anti-CXCR4 monoclonal antibody conjugated to ultrasmall superparamagnetic iron oxide nanoparticles in an application of MR molecular imaging of pancreatic cancer cell lines. *Acta Radiologica* **53**(9): 1049-1058

Herr JK, Smith JE, Medley CD, Shangguan D, Tan W (2006) Aptamer-conjugated nanoparticles for selective collection and detection of cancer cells. *Analytical Chemistry* **78**(9): 2918-2924

Herrington-Symes AP, Farys M, Khalili H, Brocchini S (2013) Antibody fragments: Prolonging circulation half-life special issue-antibody research. *Advances in Bioscience and Biotechnology* **4**(55): 10

Hoelzinger DB, Demuth T, Berens ME (2007) Autocrine factors that sustain glioma invasion and paracrine biology in the brain microenvironment. *Journal of the National Cancer Institute* **99**(21): 1583-1593

Högemann-Savellano D, Bos E, Blondet C, Sato F, Abe T, Josephson L, Weissleder R, Gaudet J, Sgroi D, Peters PJ (2003) The transferrin receptor: a potential molecular imaging marker for human cancer. *Neoplasia* **5**(6): 495-506

Hou Y, Liu Y, Chen Z, Gu N, Wang J (2010) Manufacture of IRDye 800 CW-coupled Fe 3 O 4 nanoparticles and their applications in cell labeling and in vivo imaging. *Journal of nanobiotechnology* **8**(Preprint)

Hsiao JK, Chu HH, Wang YH, Lai CW, Chou PT, Hsieh ST, Wang JL, Liu HM (2008) Macrophage physiological function after superparamagnetic iron oxide labeling. *NMR in Biomedicine* **21**(8): 820-829

Hsieh W-J, Liang C-J, Chieh J-J, Wang S-H, Lai I-R, Chen J-H, Chang F-H, Tseng W-K, Yang S-Y, Wu C-C (2012) In vivo tumor targeting and imaging with anti-vascular endothelial growth factor antibody-conjugated dextran-coated iron oxide nanoparticles. *International journal of nanomedicine* **7**: 2833

Hu C-MJ, Fang RH, Wang K-C, Luk BT, Thamphiwatana S, Dehaini D, Nguyen P, Angsantikul P, Wen CH, Kroll AV, Carpenter C, Ramesh M, Qu V, Patel SH, Zhu J,

Shi W, Hofman FM, Chen TC, Gao W, Zhang K, Chien S, Zhang L (2015) Nanoparticle biointerfacing by platelet membrane cloaking. *Nature* **526**(7571)**:** 118-121

Hu C-MJ, Zhang L, Aryal S, Cheung C, Fang RH, Zhang L (2011) Erythrocyte membrane-camouflaged polymeric nanoparticles as a biomimetic delivery platform. *Proceedings of the National Academy of Sciences* **108**(27)**:** 10980-10985

Huang J, Bu L, Xie J, Chen K, Cheng Z, Li X, Chen X (2010) Effects of nanoparticle size on cellular uptake and liver MRI with polyvinylpyrrolidone-coated iron oxide nanoparticles. *ACS nano* **4**(12)**:** 7151-7160

Huang X, Yi C, Fan Y, Zhang Y, Zhao L, Liang Z, Pan J (2014) Magnetic Fe 3 O 4 nanoparticles grafted with single-chain antibody (scFv) and docetaxel loaded β-cyclodextrin potential for ovarian cancer dual-targeting therapy. *Materials Science and Engineering: C* **42:** 325-332

Iio M, Wagner Jr HN (1963) Studies of the reticuloendothelial system (RES). I. Measurement of the phagocytic capacity of the RES in man and dog. *Journal of Clinical Investigation* **42**(3)**:** 417

Illum L, Thomas NW, Davis SS (1986) Effect of a selected suppression of the reticuloendothelial system on the distribution of model carrier particles. *Journal of pharmaceutical sciences* **75**(1)**:** 16-22

Ishihara K, Fukumoto K, Iwasaki Y, Nakabayashi N (1999) Modification of polysulfone with phospholipid polymer for improvement of the blood compatibility. Part 2. Protein adsorption and platelet adhesion. *Biomaterials* **20**(17)**:** 1553-1559

Ishihara Y, Honma T, Nohara S, Ito Y (2013) Evaluation of magnetic nanoparticle samples made from biocompatible ferucarbotran by time-correlation magnetic particle imaging reconstruction method. *BMC medical imaging* **13**(1)**:** 15

Ito A, Shinkai M, Honda H, Kobayashi T (2005) Medical application of functionalized magnetic nanoparticles. *Journal of bioscience and bioengineering* **100**(1)**:** 1-11

Janeway CA, Travers P, Walport M, Shlomchik MJ (2001) The structure of a typical antibody molecule. In *Immunobiology: The Immune System in Health and Disease. Available from:* http://www.ncbi.nlm.nih.gov/books/NBK27144/. New York: Garland Science

Jansen RW, Molema G, Ching TL, Oosting R, Harms G, Moolenaar F, Hardonk MJ, Meijer DK (1991) Hepatic endocytosis of various types of mannose-terminated albumins. What is important, sugar recognition, net charge, or the combination of these features. *Journal of Biological Chemistry* **266**(5)**:** 3343

Jayasena SD (1999) Aptamers: an emerging class of molecules that rival antibodies in diagnostics. *Clinical chemistry* **45**(9)**:** 1628-1650

Jeanes A, Haynes WC, Wilham CA, Rankin JC, Melvin EH, Austin MJ, Cluskey JE, Fisher BE, Tsuchiya HM, Rist CE (1954) Characterization and Classification of Dextrans from Ninety-six Strains of Bacteria1b. *Journal of the American Chemical Society* **76**(20)**:** 5041-5052

Jeon MJ, Ahn C-H, Kim H, Chung IJ, Jung S, Kim Y-H, Youn H, Chung JW, Kim YI (2014) The intratumoral administration of ferucarbotran conjugated with doxorubicin improved therapeutic effect by magnetic hyperthermia combined with pharmacotherapy in a hepatocellular carcinoma model. *J Exp Clin Cancer Res* **33**(1)**:** 1-11

Jordan A, Rheinländer T, Waldöfner N, Scholz R (2003) Increase of the specific absorption rate (SAR) by magnetic fractionation of magnetic fluids. *Journal of Nanoparticle Research* **5**(5-6)**:** 597-600

Jordan A, Scholz R, Maier-Hauff K, van Landeghem FK, Waldoefner N, Teichgraeber U, Pinkernelle J, Bruhn H, Neumann F, Thiesen B (2006) The effect of thermotherapy using magnetic nanoparticles on rat malignant glioma. *Journal of neuro-oncology* **78**(1)**:** 7-14

Jordan A, Scholz R, Wust P, Schirra H, Schiestel T, Schmidt H, Felix R (1999) Endocytosis of dextran and silan-coated magnetite nanoparticles and the effect of intracellular hyperthermia on human mammary carcinoma cells in vitro. *Journal of Magnetism and Magnetic Materials* **194**(1)**:** 185-196

Junghanns J-UA, Müller RH (2008) Nanocrystal technology, drug delivery and clinical applications. *International journal of nanomedicine* **3**(3)**:** 295

Kager L, Pötschger U, Bielack S (2010) Review of mifamurtide in the treatment of patients with osteosarcoma. *Therapeutics and clinical risk management* **6:** 279

Kajander T, Cortajarena AL, Regan L (2006) Consensus design as a tool for engineering repeat proteins. In *Protein Design*, pp 151-170. Springer

Kalber TL, Kamaly N, So P-W, Pugh JA, Bunch J, McLeod CW, Jorgensen MR, Miller AD, Bell JD (2011) A low molecular weight folate receptor targeted contrast agent for magnetic resonance tumor imaging. *Molecular Imaging and Biology* **13**(4)**:** 653-662

Kalber TL, Smith CJ, Howe FA, Griffiths JR, Ryan AJ, Waterton JC, Robinson SP (2005) A longitudinal study of R2* and R2 magnetic resonance imaging relaxation rate measurements in murine liver after a single administration of 3 different iron oxide-based contrast agents. *Investigative radiology* **40**(12)**:** 784

Kallumadil M, Tada M, Nakagawa T, Abe M, Southern P, Pankhurst QA (2009) Suitability of commercial colloids for magnetic hyperthermia. *Journal of Magnetism and Magnetic Materials* **321**(10)**:** 1509-1513

Kaluzova M, Bouras A, Machaidze R, Hadjipanayis C (2015) Targeted therapy of glioblastoma stem-like cells and tumor non-stem cells using cetuximab-conjugated iron-oxide nanoparticles. *Oncotarget* **6**(11)**:** 8788-8806

Kamaly N, Xiao Z, Valencia PM, Radovic-Moreno AF, Farokhzad OC (2012) Targeted polymeric therapeutic nanoparticles: design, development and clinical translation. *Chemical Society Reviews* **41**(7)**:** 2971-3010

Kang C, Zhang Z, Jia Z, Wang G, Qiu M, Zhou H, Yu S, Chang J, Jiang H, Pu P (2006) Suppression of EGFR expression by antisense or small interference RNA inhibits U251 glioma cell growth in vitro and in vivo. *Cancer gene therapy* **13**(5)**:** 530-538

Kang HW, Josephson L, Petrovsky A, Weissleder R, Bogdanov A (2002) Magnetic resonance imaging of inducible E-selectin expression in human endothelial cell culture. *Bioconjugate chemistry* **13**(1)**:** 122-127

Karimi Z, Karimi L, Shokrollahi H (2013) Nano-magnetic particles used in biomedicine: core and coating materials. *Materials Science and Engineering: C* **33**(5)**:** 2465-2475

Kehagias DT, Gouliamos AD, Smyrniotis V, Vlahos LJ (2001) Diagnostic efficacy and safety of MRI of the liver with superparamagnetic iron oxide particles (SH U 555 A). *Journal of Magnetic Resonance Imaging* **14**(5)**:** 595-601

Kelemen LE (2006) The role of folate receptor α in cancer development, progression and treatment: cause, consequence or innocent bystander? *International journal of cancer* **119**(2)**:** 243-250

Kelley JL, Ozment TR, Li C, Schweitzer JB, Williams DL (2014) Scavenger receptor-A (CD204): A two-edged sword in health and disease. *Critical Reviews™ in Immunology* **34**(3)

Khandare J, Calderón M, Dagia NM, Haag R (2012) Multifunctional dendritic polymers in nanomedicine: opportunities and challenges. *Chemical Society Reviews* **41**(7)**:** 2824-2848

Kidd S, Spaeth E, Dembinski JL, Dietrich M, Watson K, Klopp A, Battula VL, Weil M, Andreeff M, Marini FC (2009) Direct evidence of mesenchymal stem cell tropism for tumor and wounding microenvironments using in vivo bioluminescent imaging. *Stem cells* **27**(10)**:** 2614-2623

Kievit FM, Zhang M (2011) Surface Engineering of Iron Oxide Nanoparticles for Targeted Cancer Therapy. *Accounts of Chemical Research* **44**(10)**:** 853-862

Kim JG, Xia M, Liu H (2005) Extinction coefficients of hemoglobin for near-infrared spectroscopy of tissue. *Engineering in Medicine and Biology Magazine, IEEE* **24**(2)**:** 118-121

Kim T-Y, Kim D-W, Chung J-Y, Shin SG, Kim S-C, Heo DS, Kim NK, Bang Y-J (2004) Phase I and pharmacokinetic study of Genexol-PM, a cremophor-free, polymeric micelle-formulated paclitaxel, in patients with advanced malignancies. *Clinical cancer research* **10**(11)**:** 3708-3716

Kitano H, Suzuki H, Matsuura K, Ohno K (2010) Molecular recognition at the exterior surface of a zwitterionic telomer brush. *Langmuir* **26**(9)**:** 6767-6774

Klausz K, Berger S, Lammerts van Bueren JJ, Derer S, Lohse S, Dechant M, van de Winkel JG, Peipp M, Parren PW, Valerius T (2011) Complement‐mediated tumor‐specific cell lysis by antibody combinations targeting epidermal growth factor receptor (EGFR) and its variant III (EGFRvIII). *Cancer science* **102**(10)**:** 1761-1768

Kobe B, Kajava AV (2000) When protein folding is simplified to protein coiling: the continuum of solenoid protein structures. *Trends in biochemical sciences* **25**(10)**:** 509-515

Kondepati VR, Heise HM, Backhaus J (2008) Recent applications of near-infrared spectroscopy in cancer diagnosis and therapy. *Analytical and bioanalytical chemistry* **390**(1)**:** 125-139

Kovar JL, Simpson MA, Schutz-Geschwender A, Olive DM (2007a) A systematic approach to the development of fluorescent contrast agents for optical imaging of mouse cancer models. *Analytical Biochemistry* **367**(1)**:** 1-12

Kovar JL, Volcheck W, Sevick-Muraca E, Simpson MA, Olive DM (2009) Characterization and performance of a near-infrared 2-deoxyglucose optical imaging agent for mouse cancer models. *Analytical biochemistry* **384**(2)**:** 254-262

Kovar JL, Volcheck WM, Chen J, Simpson MA (2007b) Purification method directly influences effectiveness of an epidermal growth factor-coupled targeting agent for noninvasive tumor detection in mice. *Analytical biochemistry* **361**(1)**:** 47-54

Kowalczyk B, Lagzi I, Grzybowski BA (2011) Nanoseparations: strategies for size and/or shape-selective purification of nanoparticles. *Current Opinion in Colloid & Interface Science* **16**(2)**:** 135-148

Kresse M, Wagner S, Pfefferer D, Lawaczeck R, Elste V, Semmler W (1998) Targeting of ultrasmall superparamagnetic iron oxide (USPIO) particles to tumor cells in vivo by using transferrin receptor pathways. *Magnetic Resonance in Medicine* **40**(2)**:** 236-242

Kreyling WG, Semmler-Behnke M, Chaudhry Q (2010) A complementary definition of nanomaterial. *Nano Today* **5**(3)**:** 165-168

Krishnan KM (2010) Biomedical nanomagnetics: a spin through possibilities in imaging, diagnostics, and therapy. *IEEE Transactions on Magnetics* **46**(7)**:** 2523-2558

Kwak J-Y (2014) Fucoidan as a marine anticancer agent in preclinical development. *Marine drugs* **12**(2)**:** 851-870

Lammers T, Hennink W, Storm G (2008) Tumour-targeted nanomedicines: principles and practice. *British journal of cancer* **99**(3)**:** 392-397

Lanza GM, Winter PM, Caruthers SD, Morawski AM, Schmieder AH, Crowder KC, Wickline SA (2004) Magnetic resonance molecular imaging with nanoparticles. *Journal of nuclear cardiology* **11**(6)**:** 733-743

Lawaczeck R, Bauer H, Frenzel T, Hasegawa M, Ito Y, Kito K, Miwa N, Tsutsui H, Vogler H, Weinmann HJ (1997) Magnetic iron oxide particles coated with carboxydextran for parenteral administration and liver contrasting. *Acta Radiologica* **38**(4)**:** 584

Leckband D, Israelachvili J (2001) Intermolecular forces in biology. *Quarterly reviews of biophysics* **34**(02)**:** 105-267

Lee JH, Smith MA, Liu W, Gold EM, Lewis B, Song HT, Frank JA (2009) Enhanced stem cell tracking via electrostatically assembled fluorescent SPION peptide complexes. *Nanotechnology* **20:** 355102

Lemarchand C, Gref R, Couvreur P (2004) Polysaccharide-decorated nanoparticles. *European Journal of Pharmaceutics and Biopharmaceutics* **58**(2)**:** 327-341

Leonard R, Williams S, Tulpule A, Levine A, Oliveros S (2009) Improving the therapeutic index of anthracycline chemotherapy: Focus on liposomal doxorubicin (Myocet™). *The Breast* **18**(4)**:** 218-224

Lesniak A, Fenaroli F, Monopoli MP, Åberg C, Dawson KA, Salvati A (2012) Effects of the presence or absence of a protein corona on silica nanoparticle uptake and impact on cells. *ACS nano* **6**(7)**:** 5845-5857

Letunic I, Goodstadt L, Dickens NJ, Doerks T, Schultz J, Mott R, Ciccarelli F, Copley RR, Ponting CP, Bork P (2002) Recent improvements to the SMART domain-based sequence annotation resource. *Nucleic acids research* **30**(1)**:** 242-244

Leung K (2004) H18/7 F(ab')2 E-selectin monoclonal antibody conjugated to cross-linked iron oxide nanoparticles. In *Molecular Imaging and Contrast Agent Database (MICAD)*. Bethesda (MD): National Center for Biotechnology Information (US)

Lewin M, Carlesso N, Tung C-H, Tang X-W, Cory D, Scadden DT, Weissleder R (2000) Tat peptide-derivatized magnetic nanoparticles allow in vivo tracking and recovery of progenitor cells. *Nature biotechnology* **18**(4)**:** 410-414

Li B, Lu F, Wei X, Zhao R (2008) Fucoidan: structure and bioactivity. *Molecules* **13**(8)**:** 1671-1695

Li S, Schmitz KR, Jeffrey PD, Wiltzius JJ, Kussie P, Ferguson KM (2005) Structural basis for inhibition of the epidermal growth factor receptor by cetuximab. *Cancer cell* **7**(4)**:** 301-311

Li S-D, Huang L (2010) Stealth nanoparticles: high density but sheddable PEG is a key for tumor targeting. *Journal of controlled release: official journal of the Controlled Release Society* **145**(3)**:** 178

Li Y, Chen Z, Li F, Wang J, Zhang Z (2012) Preparation and in vitro studies of MRI-specific superparamagnetic iron oxide antiGPC3 probe for hepatocellular carcinoma. *International journal of nanomedicine* **7:** 4593

Lira M, Santos-Magalhães N, Nicolas V, Marsaud V, Silva M, Ponchel G, Vauthier C (2011) Cytotoxicity and cellular uptake of newly synthesized fucoidan-coated nanoparticles. *European Journal of Pharmaceutics and Biopharmaceutics* **79**(1)**:** 162-170

Liu D, Chen C, Hu G, Mei Q, Qiu H, Long G, Hu G (2011) Specific targeting of nasopharyngeal carcinoma cell line CNE1 by C225-conjugated ultrasmall superparamagnetic iron oxide particles with magnetic resonance imaging. *Acta biochimica et biophysica Sinica* **43**(4)**:** 301-306

Liu D, Mori A, Huang L (1992) Role of liposome size and RES blockade in controlling biodistribution and tumor uptake of GM1-containing liposomes. *Biochimica et Biophysica Acta (BBA)-Biomembranes* **1104**(1)**:** 95-101

Loebinger MR, Eddaoudi A, Davies D, Janes SM (2009a) Mesenchymal stem cell delivery of TRAIL can eliminate metastatic cancer. *Cancer research* **69**(10)**:** 4134-4142

Loebinger MR, Kyrtatos PG, Turmaine M, Price AN, Pankhurst Q, Lythgoe MF, Janes SM (2009b) Magnetic resonance imaging of mesenchymal stem cells homing to pulmonary metastases using biocompatible magnetic nanoparticles. *Cancer research* **69**(23)**:** 8862

Loebinger MR, Kyrtatos PG, Turmaine M, Price AN, Pankhurst Q, Lythgoe MF, Janes SM (2009c) Magnetic resonance imaging of mesenchymal stem cells homing to pulmonary metastases using biocompatible magnetic nanoparticles. *Cancer research* **69**(23)**:** 8862-8867

Love RJ, Jones KS (2013) The recognition of biomaterials: Pattern recognition of medical polymers and their adsorbed biomolecules. *Journal of Biomedical Materials Research Part A* **101A**(9)**:** 2740-2752

Löwa N, Knappe P, Wiekhorst F, Eberbeck D, Thünemann AF, Trahms L (2014) Hydrodynamic and magnetic fractionation of superparamagnetic nanoparticles for magnetic particle imaging. *Journal of Magnetism and Magnetic Materials* **380:** 226-270

Lunov O, Syrovets T, Loos C, Beil J, Delacher M, Tron K, Nienhaus GU, Musyanovych A, Mailander V, Landfester K (2011) Differential uptake of functionalized polystyrene nanoparticles by human macrophages and a monocytic cell line. *Acs Nano* **5**(3)**:** 1657-1669

Lunov O, Syrovets T, Röcker C, Tron K, Ulrich Nienhaus G, Rasche V, Mailänder V, Landfester K, Simmet T (2010a) Lysosomal degradation of the carboxydextran shell of coated superparamagnetic iron oxide nanoparticles and the fate of professional phagocytes. *Biomaterials* **31**(34)**:** 9015-9022

Lunov O, Zablotskii V, Syrovets T, Röcker C, Tron K, Nienhaus GU, Simmet T (2010b) Modeling receptor-mediated endocytosis of polymer-functionalized iron oxide nanoparticles by human macrophages. *Biomaterials*

Lyass O, Uziely B, Ben‐Yosef R, Tzemach D, Heshing NI, Lotem M, Brufman G, Gabizon A (2000) Correlation of toxicity with pharmacokinetics of pegylated liposomal doxorubicin (Doxil) in metastatic breast carcinoma. *Cancer* **89**(5)**:** 1037-1047

MagForce (2015) Previous clinical treatment experience with NanoTherm™ therapy. http://www.magforce.de/en/studien/uebersicht.html: MagForce AG, The Nanomedicine Company

Maier-Hauff K, Rothe R, Scholz R, Gneveckow U, Wust P, Thiesen B, Feussner A, von Deimling A, Waldoefner N, Felix R (2007) Intracranial thermotherapy using magnetic nanoparticles combined with external beam radiotherapy: results of a feasibility study on patients with glioblastoma multiforme. *Journal of Neuro-Oncology* **81**(1)**:** 53-60

Maier-Hauff K, Ulrich F, Nestler D, Niehoff H, Thiesen B, Orawa H, Budach V, Jordan A (2011) Efficacy and safety of intratumoral thermotherapy using magnetic iron-oxide nanoparticles combined with external beam radiotherapy on patients with recurrent glioblastoma multiforme. *Journal of neuro-oncology***:** 1-8

Mailänder V, Lorenz MR, Holzapfel V, Musyanovych A, Fuchs K, Wiesneth M, Walther P, Landfester K, Schrezenmeier H (2008) Carboxylated superparamagnetic iron oxide particles label cells intracellularly without transfection agents. *Molecular Imaging and Biology* **10**(3)**:** 138-146

Majumdar S, Zoghbi S, Gore J (1990) Pharmacokinetics of superparamagnetic iron-oxide MR contrast agents in the rat. *Investigative radiology* **25**(7)**:** 771-777

Mallory M, Gogineni E, Jones GC, Greer L, Simone CB (2015) Therapeutic Hyperthermia: The old, the new, and the upcoming. *Critical Reviews in Oncology/Hematology*

Maurizi L, Sakulkhu U, Gramoun A, Vallee J-P, Hofmann H (2014) A fast and reproducible method to quantify magnetic nanoparticle biodistribution. *Analyst* **139**(5)**:** 1184-1191

McClune B, Buadi F, Aslam N, Przepiorka D (2005) Intrathecal Liposomal Cytarabine (Depocyt) Is Safe and Effective for Prevention of Meningeal Disease in Patients with Acute Lymphoblastic Leukemia and High-Grade Lymphoma Treated with the HyperCVAD Regimen. *ASH Annual Meeting Abstracts* **106**(11)**:** 4594-

McNeil SE (2009) Nanoparticle therapeutics: a personal perspective. *Wiley Interdisciplinary Reviews: Nanomedicine and Nanobiotechnology* **1**(3)**:** 264-271

Mendelsohn J, Baselga J (2006) Epidermal growth factor receptor targeting in cancer. *Seminars in oncology* **33**(4)**:** 369-385

Mimura G, Fukuda M, Haraguchi Y, Jinnouchi T (1983) A clinical study of long-term administration of dextran sulfate (MDS Kowa) in patients with retinopathy. *The Tohoku journal of experimental medicine* **141:** 389

Mitragotri S, Lahann J (2009) Physical approaches to biomaterial design. *Nature materials* **8**(1)**:** 15-23

Moghimi SM, Szebeni J (2003) Stealth liposomes and long circulating nanoparticles: critical issues in pharmacokinetics, opsonization and protein-binding properties. *Progress in lipid research* **42**(6)**:** 463-478

Moore A, Marecos E, Bogdanov Jr A, Weissleder R (2000) Tumoral distribution of long-circulating dextran-coated iron oxide nanoparticles in a rodent model 1. *Radiology* **214**(2)**:** 568-574

Mukherjee A, Darlington T, Baldwin R, Holz C, Olson S, Kulkarni P, DeWeese TL, Getzenberg RH, Ivkov R, Lupold SE (2014) Development and Screening of a Series of Antibody‐Conjugated and Silica‐Coated Iron Oxide Nanoparticles for Targeting the Prostate‐Specific Membrane Antigen. *ChemMedChem* **9**(7)**:** 1356-1360

Murgas P, Cornejo F, Merino G, von Bernhardi R (2014) SR-A regulates the inflammatory activation of astrocytes. *Neurotoxicity research* **25**(1)**:** 68-80

Murry DJ, Blaney SM (2000) Clinical pharmacology of encapsulated sustained-release cytarabine. *Annals of Pharmacotherapy* **34**(10)**:** 1173-1178

Nakamizo A, Marini F, Amano T, Khan A, Studeny M, Gumin J, Chen J, Hentschel S, Vecil G, Dembinski J (2005) Human bone marrow–derived mesenchymal stem cells in the treatment of gliomas. *Cancer research* **65**(8)**:** 3307-3318

National Nanotechnology Initiative A (2000) Leading to the Next Industrial Revolution. A Report by the Interagency Working Group on Nanoscience, Engineering and Technology. *Washington, DC, Committee on Technology, National Science and Technology Council*

Ndong C, Toraya-Brown S, Kekalo K, Baker I, Gerngross TU, Fiering SN, Griswold KE (2015) Antibody-mediated targeting of iron oxide nanoparticles to the folate receptor alpha increases tumor cell association in vitro and in vivo. *International journal of nanomedicine* **10:** 2595

Nel AE, Mädler L, Velegol D, Xia T, Hoek EM, Somasundaran P, Klaessig F, Castranova V, Thompson M (2009) Understanding biophysicochemical interactions at the nano–bio interface. *Nature materials* **8**(7)**:** 543-557

Nelson AL (2010) Antibody fragments: hope and hype. *MAbs* **2**(1)**:** 77-83

Nelson AL, Reichert JM (2009) Development trends for therapeutic antibody fragments. *Nature biotechnology* **27**(4)**:** 331-337

Ni X, Castanares M, Mukherjee A, Lupold SE (2011) Nucleic acid aptamers: clinical applications and promising new horizons. *Current medicinal chemistry* **18**(27)**:** 4206

Nicholson R, Gee J, Harper M (2001) EGFR and cancer prognosis. *European Journal of Cancer* **37:** 9-15

Nohara S, Kato I, Ito Y, Honma T, Ishihara Y (2013) Separation of Ferucarbotran: A leading candidate of MPI tracer for practical use. *Magnetic Particle Imaging (IWMPI), 2013 International Workshop on***:** 23-24 March 2013.

Nunes AC, Yu Z-C (1989) Size and quality dispersion of a single preparation of colloidal magnetic particles. *Journal of magnetism and magnetic materials* **78**(2)**:** 241-246

Olynik B, Rastegar M (2012) The genetic and epigenetic journey of embryonic stem cells into mature neural cells. *Frontiers in genetics* **3:** 81

Pao W, Miller V, Zakowski M, Doherty J, Politi K, Sarkaria I, Singh B, Heelan R, Rusch V, Fulton L (2004) EGF receptor gene mutations are common in lung cancers from "never smokers" and are associated with sensitivity of tumors to gefitinib and erlotinib. *Proceedings of the National Academy of Sciences of the United States of America* **101**(36)**:** 13306-13311

Park BH, Jung JC, Lee GH, Kim TJ, Lee YJ, Kim JY, Kim YW, Jeong JH, Chang Y (2008) Comparison of labeling efficiency of different magnetic nanoparticles into stem cell. *Colloids and Surfaces A: Physicochemical and Engineering Aspects* **313:** 145-149

Parodi A, Quattrocchi N, van de Ven AL, Chiappini C, Evangelopoulos M, Martinez JO, Brown BS, Khaled SZ, Yazdi IK, Enzo MV (2013) Synthetic nanoparticles functionalized with biomimetic leukocyte membranes possess cell-like functions. *Nature nanotechnology* **8**(1)**:** 61-68

Parveen S, Misra R, Sahoo SK (2012) Nanoparticles: a boon to drug delivery, therapeutics, diagnostics and imaging. *Nanomedicine: Nanotechnology, Biology and Medicine* **8**(2)**:** 147-166

Passirani C, Barratt G, Devissaguet J-P, Labarre D (1998) Long-circulating nanopartides bearing heparin or dextran covalently bound to poly (methyl methacrylate). *Pharmaceutical research* **15**(7)**:** 1046-1050

Patel KR, Li MP, Baldeschwieler JD (1983) Suppression of liver uptake of liposomes by dextran sulfate 500. *Proceedings of the National Academy of Sciences* **80**(21)**:** 6518

Pearson S, Jia H, Kandachi K (2004) China approves first gene therapy. *Nat Biotech* **22**(1)**:** 3-4

Peer D, Karp JM, Hong S, Farokhzad OC, Margalit R, Langer R (2007) Nanocarriers as an emerging platform for cancer therapy. *Nat Nano* **2**(12)**:** 751-760

Pennock S, Wang Z (2008) A tale of two Cbls: interplay of c-Cbl and Cbl-b in epidermal growth factor receptor downregulation. *Molecular and cellular biology* **28**(9)**:** 3020-3037

Perumal OP, Inapagolla R, Kannan S, Kannan RM (2008) The effect of surface functionality on cellular trafficking of dendrimers. *Biomaterials* **29**(24)**:** 3469-3476

Platt N, Gordon S (2001) Is the class A macrophage scavenger receptor (SR-A) multifunctional?-The mouse's tale. *Journal of Clinical Investigation* **108**(5)**:** 649-654

Pleuvry BJ (2004) Pharmacology of plasma expanders. *Anaesthesia &intensive care medicine* **5**(2)**:** 59-61

Plotkin M, Gneveckow U, Meier-Hauff K, Amthauer H, Feußner A, Denecke T, Gutberlet M, Jordan A, Felix R, Wust P (2006) 18F-FET PET for planning of thermotherapy using magnetic nanoparticles in recurrent glioblastoma. *International journal of hyperthermia* **22**(4)**:** 319-325

Politi LS, Bacigaluppi M, Brambilla E, Cadioli M, Falini A, Comi G, Scotti G, Martino G, Pluchino S (2007) Magnetic resonance‐based tracking and quantification of intravenously injected neural stem cell accumulation in the brains of mice with experimental multiple sclerosis. *Stem Cells* **25**(10)**:** 2583-2592

Ponka P, Lok CN (1999) The transferrin receptor: role in health and disease. *The international journal of biochemistry & cell biology* **31**(10)**:** 1111-1137

Poon Z, Chang D, Zhao X, Hammond PT (2011) Layer-by-layer nanoparticles with a pH-sheddable layer for in vivo targeting of tumor hypoxia. *ACS nano* **5**(6)**:** 4284-4292

Quarta A, Bernareggi D, Benigni F, Luison E, Nano G, Nitti S, Cesta MC, Di Ciccio L, Canevari S, Pellegrino T (2015) Targeting FR-expressing cells in ovarian cancer

with Fab-functionalized nanoparticles: a full study to provide the proof of principle from in vitro to in vivo. *Nanoscale* **7**(6)**:** 2336-2351

Quon CY (1988) Clinical pharmacokinetics and pharmacodynamics of colloidal plasma volume expanders. *Journal of Cardiothoracic Anesthesia* **2**(6)**:** 13-23

RAD-AR Council A (2015) MDS KOWA Drug Information Sheet: RAD-AR Council, Japan. http://www.rad-ar.or.jp/siori/english/kekka.cgi?n=1860

Raschke W, Baird S, Ralph P, Nakoinz I (1978) Functional macrophage cell lines transformed by Abelson leukemia virus. *Cell* **15**(1)**:** 261-267

Raynal I, Prigent P, Peyramaure S, Najid A, Rebuzzi C, Corot C (2004) Macrophage endocytosis of superparamagnetic iron oxide nanoparticles: mechanisms and comparison of ferumoxides and ferumoxtran-10. *Investigative radiology* **39**(1)**:** 56

Regad T, Bellodi C, Nicotera P, Salomoni P (2009) The tumor suppressor Pml regulates cell fate in the developing neocortex. *Nature neuroscience* **12**(2)**:** 132-140

Reimer P, Balzer T (2003) Ferucarbotran (Resovist): a new clinically approved RES-specific contrast agent for contrast-enhanced MRI of the liver: properties, clinical development, and applications. *European radiology* **13**(6)**:** 1266-1276

Reimer P, Rummeny EJ, Daldrup HE, Balzer T, Tombach B, Berns T, Peters PE (1995) Clinical results with Resovist: a phase 2 clinical trial. *Radiology* **195**(2)**:** 489-496

Rheinländer T, Kötitz R, Weitschies W, Semmler W (2000a) Different methods for the fractionation of magnetic fluids. *Colloid and Polymer Science* **278**(3)**:** 259-263

Rheinländer T, Roessner D, Weitschies W, Semmler W (2000b) Comparison of size-selective techniques for the fractionation of magnetic fluids. *Journal of Magnetism and Magnetic Materials* **214**(3)**:** 269-275

Ricketts C (1952) Dextran sulphate—a synthetic analogue of heparin. *Biochemical Journal* **51**(1)**:** 129

Riegler J, Liew A, Hynes SO, Ortega D, O'Brien T, Day RM, Richards T, Sharif F, Pankhurst QA, Lythgoe MF (2013) Superparamagnetic iron oxide nanoparticle targeting of MSCs in vascular injury. *Biomaterials* **34**(8)**:** 1987-1994

Riehemann K, Schneider SW, Luger TA, Godin B, Ferrari M, Fuchs H (2009) Nanomedicine—challenge and perspectives. *Angewandte Chemie International Edition* **48**(5)**:** 872-897

Riemer J, Hoepken HH, Czerwinska H, Robinson SR, Dringen R (2004) Colorimetric ferrozine-based assay for the quantitation of iron in cultured cells. *Analytical biochemistry* **331**(2)**:** 370-375

Rinholm JE, Bergersen LH (2012) Neuroscience: The wrap that feeds neurons. *Nature* **487**(7408)**:** 435-436

Rodriguez PL, Harada T, Christian DA, Pantano DA, Tsai RK, Discher DE (2013) Minimal" Self" peptides that inhibit phagocytic clearance and enhance delivery of nanoparticles. *Science* **339**(6122)**:** 971-975

Romanus E, Koettig T, Prass S, Schmidl F, Heinrich J, Gopinadhan M, Berkov D, Helm C, Weitschies W, Weber P (2007) Energy barrier distributions of maghemite nanoparticles. *Nanotechnology* **18**(11)**:** 115709

Rosen JE, Chan L, Shieh D-B, Gu FX (2012) Iron oxide nanoparticles for targeted cancer imaging and diagnostics. *Nanomedicine: Nanotechnology, Biology and Medicine* **8**(3)**:** 275-290

Sahay G, Alakhova DY, Kabanov AV (2010a) Endocytosis of nanomedicines. *Journal of controlled release* **145**(3)**:** 182-195

Sahay G, Kim JO, Kabanov AV, Bronich TK (2010b) The exploitation of differential endocytic pathways in normal and tumor cells in the selective targeting of nanoparticulate chemotherapeutic agents. *Biomaterials* **31**(5)**:** 923-933

Salvati A, Pitek AS, Monopoli MP, Prapainop K, Bombelli FB, Hristov DR, Kelly PM, Åberg C, Mahon E, Dawson KA (2013) Transferrin-functionalized nanoparticles lose their targeting capabilities when a biomolecule corona adsorbs on the surface. *Nature nanotechnology* **8**(2)**:** 137-143

Sampath L, Kwon S, Ke S, Wang W, Schiff R, Mawad ME, Sevick-Muraca EM (2007) Dual-labeled trastuzumab-based imaging agent for the detection of human

epidermal growth factor receptor 2 overexpression in breast cancer. *Journal of Nuclear Medicine* **48**(9)**:** 1501-1510

Sanai N, Alvarez-Buylla A, Berger MS (2005) Neural stem cells and the origin of gliomas. *New England Journal of Medicine* **353**(8)**:** 811-822

Sandiford L, Phinikaridou A, Protti A, Meszaros LK, Cui X, Yan Y, Frodsham G, Williamson PA, Gaddum N, Botnar RM (2012) Bisphosphonate-anchored PEGylation and radiolabeling of superparamagnetic iron oxide: long-circulating nanoparticles for in vivo multimodal (T1 MRI-SPECT) imaging. *Acs Nano* **7**(1)**:** 500-512

Sands H, Jones PL (1987) Methods for the study of the metabolism of radiolabeled monoclonal antibodies by liver and tumor. *Journal of nuclear medicine: official publication, Society of Nuclear Medicine* **28**(3)**:** 390

Sarkar N, Banerjee J, Hanson AJ, Elegbede AI, Rosendahl T, Krueger AB, Banerjee AL, Tobwala S, Wang R, Lu X (2007) Matrix metalloproteinase-assisted triggered release of liposomal contents. *Bioconjugate chemistry* **19**(1)**:** 57-64

Sartor O (2003) Eligard: leuprolide acetate in a novel sustained-release delivery system. *Urology* **61**(2)**:** 25-31

Sathish JG, Sethu S, Bielsky M-C, de Haan L, French NS, Govindappa K, Green J, Griffiths CE, Holgate S, Jones D (2013) Challenges and approaches for the development of safer immunomodulatory biologics. *Nature Reviews Drug Discovery* **12**(4)**:** 306-324

Scheinberg DA, Villa CH, Escorcia FE, McDevitt MR (2010) Conscripts of the infinite armada: systemic cancer therapy using nanomaterials. *Nat Rev Clin Oncol* **7**(5)**:** 266-276

Schering A (2002) Resovist: Liver-specific contrast agent for MRI of focal liver lesions: Detection and characterisation in a single diagnostic work-up (Information for radiologists).

Schöpf B, Neuberger T, Schulze K, Petri A, Chastellain M, Hofmann M, Hofmann H, Von Rechenberg B (2005) Methodology description for detection of cellular uptake of PVA coated superparamagnetic iron oxide nanoparticles (SPION) in synovial cells of sheep. *Journal of magnetism and magnetic materials* **293**(1)**:** 411-418

Scott AM, Wolchok JD, Old LJ (2012) Antibody therapy of cancer. *Nature Reviews Cancer* **12**(4)**:** 278-287

Sedgwick SG, Smerdon SJ (1999) The ankyrin repeat: a diversity of interactions on a common structural framework. *Trends in biochemical sciences* **24**(8)**:** 311-316

Segers FM, den Adel B, Bot I, van der Graaf LM, van der Veer EP, Gonzalez W, Raynal I, de Winther M, Wodzig WK, Poelmann RE (2013) Scavenger Receptor-AI–Targeted Iron Oxide Nanoparticles for In Vivo MRI Detection of Atherosclerotic Lesions. *Arteriosclerosis, thrombosis, and vascular biology* **33**(8)**:** 1812-1819

Shaffer SA, Baker-Lee C, Kennedy J, Lai MS, de Vries P, Buhler K, Singer JW (2007) In vitro and in vivo metabolism of paclitaxel poliglumex: identification of metabolites and active proteases. *Cancer chemotherapy and pharmacology* **59**(4)**:** 537-548

Shahbazi-Gahrouei D, Abdolahi M (2013) Superparamagnetic iron oxide-C595: Potential MR imaging contrast agents for ovarian cancer detection. *Journal of medical physics/Association of Medical Physicists of India* **38**(4)**:** 198

Shamsi K, Balzer T, Saini S, Ros PR, Nelson RC, Carter EC, Tollerfield S, Niendorf HP (1998) Superparamagnetic iron oxide particles (SH U 555 A): evaluation of efficacy in three doses for hepatic MR imaging. *Radiology* **206**(2)**:** 365-371

Shanehsazzadeh S, Gruettner C, Lahooti A, Mahmoudi M, Allen BJ, Ghavami M, Daha FJ, Oghabian MA (2014) Monoclonal antibody conjugated magnetic nanoparticles could target MUC‐1‐positive cells in vitro but not in vivo. *Contrast media & molecular imaging* **10**(3)**:** 225-236

Shen T, Weissleder R, Papisov M, Bogdanov A, Brady TJ (1993) Monocrystalline iron oxide nanocompounds (MION): physicochemical properties. *Magnetic Resonance in Medicine* **29**(5)**:** 599-604

Sheng Q, Liu J (2011) The therapeutic potential of targeting the EGFR family in epithelial ovarian cancer. *British journal of cancer* **104**(8)**:** 1241-1245

Shevtsov MA, Nikolaev BP, Yakovleva LY, Marchenko YY, Dobrodumov AV, Mikhrina AL, Martynova MG, Bystrova OA, Yakovenko IV, Ischenko AM (2014) Superparamagnetic iron oxide nanoparticles conjugated with epidermal growth factor (SPION–EGF) for targeting brain tumors. *International journal of nanomedicine* **9:** 273

Shmeeda H, Tzemach D, Mak L, Gabizon A (2009) Her2-targeted pegylated liposomal doxorubicin: retention of target-specific binding and cytotoxicity after in vivo passage. *Journal of Controlled Release* **136**(2)**:** 155-160

Shubayev VI, Pisanic TR, Jin S (2009) Magnetic nanoparticles for theragnostics. *Advanced drug delivery reviews* **61**(6)**:** 467-477

Silva AC, Oliveira TR, Mamani JB, Malheiros S, Malavolta L, Pavon LF, Sibov TT, Amaro Jr E, Tannus A, Vidoto E (2011) Application of hyperthermia induced by superparamagnetic iron oxide nanoparticles in glioma treatment. *Int J Nanomedicine* **6**(3)**:** 591-603

Silverman JA, Deitcher SR (2013) Marqibo®(vincristine sulfate liposome injection) improves the pharmacokinetics and pharmacodynamics of vincristine. *Cancer chemotherapy and pharmacology* **71**(3)**:** 555-564

Smith BR, Heverhagen J, Knopp M, Schmalbrock P, Shapiro J, Shiomi M, Moldovan NI, Ferrari M, Lee SC (2007) Localization to atherosclerotic plaque and biodistribution of biochemically derivatized superparamagnetic iron oxide nanoparticles (SPIONs) contrast particles for magnetic resonance imaging (MRI). *Biomedical microdevices* **9**(5)**:** 719-727

Smith PJ, Giroud M, Wiggins HL, Gower F, Thorley JA, Stolpe B, Mazzolini J, Dyson RJ, Rappoport JZ (2012) Cellular entry of nanoparticles via serum sensitive clathrin-mediated endocytosis, and plasma membrane permeabilization. *International journal of nanomedicine* **7:** 2045

Sonia S, Mirko M, Chiara F, Marina P, Federica B, Umberto B, Marco G (2009) Ascorbic acid pre-treated quartz stimulates TNF-α release in RAW 264.7 murine macrophages through ROS production and membrane lipid peroxidation. *Respiratory Research* **10**

Sonvico F, Mornet S, Vasseur S, Dubernet C, Jaillard D, Degrouard J, Hoebeke J, Duguet E, Colombo P, Couvreur P (2005) Folate-conjugated iron oxide nanoparticles for solid tumor targeting as potential specific magnetic hyperthermia mediators: synthesis, physicochemical characterization, and in vitro experiments. *Bioconjugate chemistry* **16**(5)**:** 1181-1188

Stea B, Falsey R, Kislin K, Patel J, Glanzberg H, Carey S, Ambrad AA, Meuillet EJ, Martinez JD (2003) Time and dose-dependent radiosensitization of the glioblastoma multiforme U251 cells by the EGF receptor tyrosine kinase inhibitor ZD1839 ('Iressa'). *Cancer letters* **202**(1)**:** 43-51

Studeny M, Marini FC, Dembinski JL, Zompetta C, Cabreira-Hansen M, Bekele BN, Champlin RE, Andreeff M (2004) Mesenchymal stem cells: potential precursors for tumor stroma and targeted-delivery vehicles for anticancer agents. *Journal of the National Cancer Institute* **96**(21)**:** 1593-1603

Stumpp MT, Binz HK, Amstutz P (2008) DARPins: a new generation of protein therapeutics. *Drug discovery today* **13**(15)**:** 695-701

Stupp R, Mason WP, Van Den Bent MJ, Weller M, Fisher B, Taphoorn MJ, Belanger K, Brandes AA, Marosi C, Bogdahn U (2005) Radiotherapy plus concomitant and adjuvant temozolomide for glioblastoma. *New England Journal of Medicine* **352**(10)**:** 987-996

Sun C, Lee JSH, Zhang M (2008) Magnetic nanoparticles in MR imaging and drug delivery. *Advanced drug delivery reviews* **60**(11)**:** 1252-1265

Sun C, Sze R, Zhang M (2006) Folic acid‐PEG conjugated superparamagnetic nanoparticles for targeted cellular uptake and detection by MRI. *Journal of Biomedical Materials Research Part A* **78**(3)**:** 550-557

Sun R, Dittrich J, Le-Huu M, Mueller MM, Bedke J, Kartenbeck J, Lehmann WD, Krueger R, Bock M, Huss R (2005) Physical and biological characterization of superparamagnetic iron oxide-and ultrasmall superparamagnetic iron oxide-labeled cells: a comparison. *Investigative radiology* **40**(8)**:** 504-513

Suwa T, Ozawa S, Ueda M, Ando N, Kitajima M (1998) Magnetic resonance imaging of esophageal squamous cell carcinoma using magnetite particles coated with anti‐epidermal growth factor receptor antibody. *International Journal of Cancer* **75**(4)**:** 626-634

Tagami T, Nakamura K, Shimizu T, Yamazaki N, Ishida T, Kiwada H (2010) CpG motifs in pDNA-sequences increase anti-PEG IgM production induced by PEG-coated pDNA-lipoplexes. *Journal of Controlled Release* **142**(2)**:** 160-166

Takamatsu S, Matsui O, Gabata T, Kobayashi S, Okuda M, Ougi T, Ikehata Y, Nagano I, Nagae H (2008) Selective induction hyperthermia following transcatheter arterial embolization with a mixture of nano-sized magnetic particles (ferucarbotran) and embolic materials: feasibility study in rabbits. *Radiation Medicine* **26**(4)**:** 179-187

Tamaskovic R, Simon M, Stefan N, Schwill M, Plückthun A (2012) Designed ankyrin repeat proteins (DARPins) from research to therapy. *Methods Enzymol* **503:** 101-134

Tang Q, An Y, Liu D, Liu P, Zhang D (2014) Folate/NIR 797-conjugated albumin magnetic nanospheres: synthesis, characterisation, and in vitro and in vivo targeting evaluation. *PLoS One* **9**(9)**:** e106483

Tenzer S, Docter D, Kuharev J, Musyanovych A, Fetz V, Hecht R, Schlenk F, Fischer D, Kiouptsi K, Reinhardt C (2013) Rapid formation of plasma protein corona critically affects nanoparticle pathophysiology. *Nature nanotechnology* **8**(10)**:** 772-781

Thelen T, Hao Y, Medeiros AI, Curtis JL, Serezani CH, Kobzik L, Harris LH, Aronoff DM (2010) The class A scavenger receptor, macrophage receptor with collagenous structure, is the major phagocytic receptor for Clostridium sordellii expressed by human decidual macrophages. *The Journal of Immunology* **185**(7)**:** 4328-4335

Thermo Fisher Scientific Inc. A (2011) Thermo Scientific immunoassays plate guide. http://thermo.dirxion.com/immunoassaybrochure/WebProject.asp?CodeId=7.5.1.2&BookCode=imu11flx&from=2

Thiesen B, Jordan A (2008) Clinical applications of magnetic nanoparticles for hyperthermia. *International Journal of Hyperthermia* **24**(6)**:** 467-474

Thorek DLJ, Tsourkas A (2008) Size, charge and concentration dependent uptake of iron oxide particles by non-phagocytic cells. *Biomaterials* **29**(26)**:** 3583-3590

Thünemann AF, Rolf S, Knappe P, Weidner S (2008) In situ analysis of a bimodal size distribution of superparamagnetic nanoparticles. *Analytical chemistry* **81**(1)**:** 296-301

Toumey C (2009) Plenty of room, plenty of history. *Nature nanotechnology* **4**(12)**:** 783-784

Tse BW-C, Cowin GJ, Soekmadji C, Jovanovic L, Vasireddy RS, Ling M-T, Khatri A, Liu T, Thierry B, Russell PJ (2015) PSMA-targeting iron oxide magnetic nanoparticles enhance MRI of preclinical prostate cancer. *Nanomedicine* **10**(3)**:** 375-386

Tseng HY, Lee GB, Lee CY, Shin YH, Lin XZ (2009) Localised heating of tumours utilising injectable magnetic nanoparticles for hyperthermia cancer therapy. *Nanobiotechnology, IET* **3**(2)**:** 46-54

van der Meel R, Vehmeijer LJ, Kok RJ, Storm G, van Gaal EV (2013) Ligand-targeted particulate nanomedicines undergoing clinical evaluation: current status. *Advanced drug delivery reviews* **65**(10)**:** 1284-1298

van Landeghem FKH, Maier-Hauff K, Jordan A, Hoffmann KT, Gneveckow U, Scholz R, Thiesen B, Brück W, von Deimling A (2009) Post-mortem studies in glioblastoma patients treated with thermotherapy using magnetic nanoparticles. *Biomaterials* **30**(1)**:** 52-57

Vauthier C, Tsapis N, Couvreur P (2011) Nanoparticles: heating tumors to death? *Nanomedicine* **6**(1)**:** 99-109

Verma A, Stellacci F (2010) Effect of surface properties on nanoparticle–cell interactions. *Small* **6**(1)**:** 12-21

Vigor KL, Kyrtatos PG, Minogue S, Al-Jamal KT, Kogelberg H, Tolner B, Kostarelos K, Begent RH, Pankhurst QA, Lythgoe MF (2010) Nanoparticles functionalised with recombinant single chain Fv antibody fragments (scFv) for the magnetic resonance imaging of cancer cells. *Biomaterials* **31**(6)**:** 1307-1315

Wade CE, Kramer GC, Grady JJ, Fabian TC, Younes RN (1997) Efficacy of hypertonic 7.5% saline and 6% dextran-70 in treating trauma: A meta-analysis of controlled clinical studies* 1. *Surgery* **122**(3)**:** 609-616

Wang AZ, Bagalkot V, Vasilliou CC, Gu F, Alexis F, Zhang L, Shaikh M, Yuet K, Cima MJ, Langer R (2008) Superparamagnetic iron oxide nanoparticle–aptamer bioconjugates for combined prostate cancer imaging and therapy. *ChemMedChem* **3**(9)**:** 1311-1315

Wang Z, Tiruppathi C, Minshall RD, Malik AB (2009) Size and dynamics of caveolae studied using nanoparticles in living endothelial cells. *ACS nano* **3**(12)**:** 4110-4116

Weissig V, Guzman-Villanueva D (2015) Nanopharmaceuticals (part 2): products in the pipeline. *International journal of nanomedicine* **10:** 1245

Weissig V, Pettinger TK, Murdock N (2014) Nanopharmaceuticals (part 1): products on the market. *International journal of nanomedicine* **9:** 4357

Weissleder R, Elizondo G, Wittenberg J, Lee A, Josephson L, Brady T (1990) Ultrasmall superparamagnetic iron oxide: an intravenous contrast agent for assessing lymph nodes with MR imaging. *Radiology* **175**(2)**:** 494-498

Weissleder R, Nahrendorf M, Pittet MJ (2014) Imaging macrophages with nanoparticles. *Nature materials* **13**(2)**:** 125-138

Wetzel SK, Ewald C, Settanni G, Jurt S, Plückthun A, Zerbe O (2010) Residue-resolved stability of full-consensus ankyrin repeat proteins probed by NMR. *Journal of molecular biology* **402**(1)**:** 241-258

Wetzel SK, Settanni G, Kenig M, Binz HK, Plückthun A (2008) Folding and unfolding mechanism of highly stable full-consensus ankyrin repeat proteins. *Journal of molecular biology* **376**(1)**:** 241-257

Wildeboer R, Southern P, Pankhurst Q (2014) On the reliable measurement of specific absorption rates and intrinsic loss parameters in magnetic hyperthermia materials. *Journal of Physics D: Applied Physics* **47**(49)**:** 495003

Wilhelm C, Billotey C, Roger J, Pons JN, Bacri JC, Gazeau F (2003) Intracellular uptake of anionic superparamagnetic nanoparticles as a function of their surface coating. *Biomaterials* **24**(6)**:** 1001-1011

Wust P, Hildebrandt B, Sreenivasa G, Rau B, Gellermann J, Riess H, Felix R, Schlag PM (2002) Hyperthermia in combined treatment of cancer. *The lancet oncology* **3**(8)**:** 487-497

Xu X, Ho W, Zhang X, Bertrand N, Farokhzad O (2015) Cancer nanomedicine: from targeted delivery to combination therapy. *Trends in molecular medicine* **21**(4)**:** 223-232

Yang CY, Tai MF, Lin CP, Lu CW, Wang JL, Hsiao JK, Liu HM (2011) Mechanism of Cellular Uptake and Impact of Ferucarbotran on Macrophage Physiology. *PloS one* **6**(9)**:** e25524

Yang L, Mao H, Wang YA, Cao Z, Peng X, Wang X, Duan H, Ni C, Yuan Q, Adams G (2009) Single chain epidermal growth factor receptor antibody conjugated nanoparticles for in vivo tumor targeting and imaging. *Small* **5**(2)**:** 235-243

Yoshida T, Othman N, Enpuku K (2013) Characterization of magnetically fractionated magnetic nanoparticles for magnetic particle imaging. *Journal of Applied Physics* **114**(17)**:** 173908

Yoshinobu T, Takuya F, Hisao F, Makiya N, Hitoshi S, Mitsuru H (1994) Pharmacokinetics of succinylated proteins and dextran sulfate in mice: Implications for hepatic targeting of protein drugs by direct succinylation via scavenger receptors. *International journal of pharmaceutics* **105**(1)**:** 19-29

Zahnd C, Wyler E, Schwenk JM, Steiner D, Lawrence MC, McKern NM, Pecorari F, Ward CW, Joos TO, Plückthun A (2007) A designed ankyrin repeat protein evolved to picomolar affinity to Her2. *Journal of molecular biology* **369**(4)**:** 1015-1028

Zalipsky S, Hansen CB, Oaks JM, Allen TM (1996) Evaluation of blood clearance rates and biodistribution of poly (2‐oxazoline)‐grafted liposomes. *Journal of pharmaceutical sciences* **85**(2)**:** 133-137

Zhang L, Yamane T, Satoh E, Amagasaki K, Kawataki T, Asahara T, Furuya K, Nukui H, Naganuma H (2005) Establishment and partial characterization of five malignant glioma cell lines. *Neuropathology* **25**(2)**:** 136-143

Zimmer C, Wright S, Engelhardt R, Johnson G, Kramm C, Breakefield X, Weissleder R (1997) Tumor cell endocytosis imaging facilitates delineation of the glioma–brain interface. *Experimental neurology* **143**(1)**:** 61-69

Zwicke GL, Mansoori GA, Jeffery CJ (2012) Utilizing the folate receptor for active targeting of cancer nanotherapeutics. *Nano reviews* **3**

Appendix 5

Faraday Discussions Publication

Maha Abdollah